UNIVERSITY OF BLIDA 1
Faculty of Technology
Department of Civil Engineering

DOCTORAT THESIS

In Civil Engineering

QUANTIFICATION OF SEISMIC PERFORMANCE FACTORS FOR COLD-FORMED STEEL STRUCTURES

By

Smail KECHIDI

Thesis committee composed by:

M. Abed	Professor (full), University of Blida 1	President
Y. Bouafia	Professor (full), University Mouloud Mammeri of Tizi-Ouzou (UMMTO)	Examiner
N. Ihaddoudène	Associate Professor, University of Sciences and Technology Houari Boumediene (USTHB)	Examiner
R. TALEB	Associate Professor, University of Blida 1	Examiner
N. Bourahla	Professor (full), University of Blida 1	Supervisor
J.M. Castro	Assistant Professor, University of Porto (FEUP)	Co-supervisor

Blida, March 2018

ABSTRACT

Shear wall panel (SWP) made of cold-formed steel (CFS) is one of the lateral load resisting systems adopted in light gauge steel constructions. It is composed of CFS C-shaped framing members (studs and tracks) attached to steel or wood sheathing using screw fasteners.

The objective of the research study addressed in this thesis is to define a seismic design and verification procedure for CFS framed buildings that can integrate the current seismic design framework of Eurocode 8. The approach comprises the definition of a set of design criteria, the selection and design of a set of archetype buildings, the development of nonlinear building models in the OpenSees finite element (FE) software followed by the conduction of nonlinear static (pushover) and Incremental Dynamic Analyses (IDA) of the archetype buildings following the Federal Emergency Management Agency (FEMA) P695 methodology.

Two hysteresis models that take into account strength and stiffness deterioration as well as pinching, have been developed and implemented in the official OpenSees release (version 2.4.5 and above) as uniaxialMaterials entitled "CFSSSWP and CFSWSWP" for steel- and wood-sheathed CFS-SWP, respectively. The proposed deteriorating models are validated using the experimental test results obtained from the literature, where a good agreement has been achieved.

A seismic design procedure for CFS framed structures employing sheathed SWPs, compatible with the framework of the Eurocodes, is proposed. In order to assess the structural behaviour and generate the required data for the appraisal of the seismic design procedure, the OpenSees FE environment was used to simulate the nonlinear behaviour of CFS-SWP adopting a novel deteriorating hysteresis model. Pushover analyses and IDA have been carried out on 54 CFS-SWP frames having 2-, 4- and 5-storey designed with varying seismic intensity levels. Fragility curves based on buildings collapse probability have been developed following the FEMA P695 methodology. Based on the defined design requirements, the CFS structural system evaluated in this study is shown to meet the acceptance criteria for a behaviour factor (q) equal to 2 for low- and moderate-seismicity. Further, the probabilistic seismic performance and risk assessment of CFS-SWP structures is presented adopting conventional steel moment-resisting frame systems as a benchmark with the aim of exploring the viability of using CFS-SWP as a new structural solution in seismic prone regions. Based on probabilistic seismic hazard analyses (PSHA), a site-specific selection of ground motion records for IDA has been carried out adopting the Conditional Spectrum (CS) as a more realistic target response spectrum.

Subsequently, the seismic risk was evaluated over the structure lifetime (*i.e.*, 50 years) in terms of the annual probability of exceeding the Damage Limitation, No-Local Collapse and Near Collapse limit states. The importance and usefulness of the risk metrics are highlighted and adopted as an indicator to explore the behavioural features of both structural systems. Overall, the assessment procedure showed that both systems present an acceptable seismic performance and therefore the CFS-SWP can be seen as a reliable structural solution to achieve performance-based objectives in seismic regions.

Subsequently, a FE modelling protocol for screw connected, back-to-back built-up CFS columns is developed and validated using results from experiments conducted at Johns Hopkins University as part of a collaborative project. The motivations for the effort are (1) to provide modelling results to augment experiments directed at improving design guidance for built-up CFS columns, and (2) to provide a simulation path for modelling built-up CFS columns in shear wall chords that commonly experience cyclic demands. Shell FE-based models were created in ABAQUS and include monotonic loading, nonlinear geometric and material behaviour, geometric imperfections based on laser scanned measurements of tested specimens, and a contact model that includes friction. Additionally, the screw fasteners were integrated into the modelling protocol using user-defined element (UEL) subroutines capable of reproducing strength and stiffness deterioration under monotonic load as well as the pinching that occurs when screw fasteners are subjected to cyclic loads. Monotonic, concentric compression tests on 17 back-to-back CFS columns using two cross section sizes and varying fastener layouts with sheathing conditions, were simulated. Buckling deformations, strength and collapse mechanisms obtained by the models were in close agreement with the experimental results. An assessment of the loading demand on screw fasteners reveals the conservatism in built-up column fastener layout and design as required by the North American Specification for the Design of Cold-Formed Steel Structural Members (AISI S100-16 section I1.2). Also, under the tested semi-rigid column end conditions, there is little boost in axial capacity with the addition of member end fastener groups (EFGs) at the top and bottom of the columns. The developed modelling protocol will also be used, in future work, to characterise the monotonic and cyclic behaviour of axially-loaded columns so that chord stud buckling limit states could be captured in seismic simulations of CFS framed shear walls.

Keywords: Cold-formed steel, Seismic design, Behaviour factor, Seismic performance assessment, FEMA P695, Seismic risk, Columns, Built-up cross sections, Experimental, Finite element analysis.

ملخص

جدار القص المصنوع من الحديد المشكل على البارد هو أحد الأنظمة الرئيسية لمقاومة الحمولات الجانبية في المنشآت الفولاذية الخفيفة. يتكون هذا الأخير من أعضاء تأطير على شكل C (أعمدة و عوارض) و عليهم توضع لوحات تغليف من حديد أو خشب باستخدام عناصر الربط.

الهدف من الدراسة البحثية المعالجة في هذه الأطروحة هو تحديد طريقة تصميم ضد الزلازل و إجراء التحقق, للمباني المنجزة من الحديد المشكل على البارد, التي يمكن أن تندمج في إطار النظام الحالي للتصميم الزلزالي Eurocode 8 . النهج المتبع يتألف من تعريف مجموعة معايير تصميم, اختيار و تصميم مجموعة مباني وتطوير نماذج غير خطية لهياكل هذه المباني باستعمال برنامج العناصر المنتهية OpenSees و يليها اداء تحليلات ستاتيكية غير خطية و تحليلات ديناميكية تدريجية (IDA) اتباعا لمنهجية FEMA P695.

تم تطوير ودمج نموذجين تباطؤ يأخذان بعين الاعتبار تدهور المقاومة والصلابة مع المعسر في برنامج OpenSees (الاصدار 2.4.5 فما فوق) كمواد معرفة من طرف المستخدم ملقبة ب ”CFSSSWP و CFSWSWP“ لجدران قص بلوحات تغليف مصنوعة من الحديد والخشب, على التوالي. تم التحقق من النموذجين المقترحين عن طريق نتائج التجارب المتوفرة حاليا و لقد تم الحصول على توافق جيد.

تم اقتراح تصميم زلزالي منسجم مع إطار Eurocodes للهياكل المنجزة من الحديد المشكل على البارد التي تعتمد على جدران القص المغلفة. من اجل تقييم السلوك الهيكلي و توفير البيانات اللازمة لتثمين اجراء التصميم الزلزالي, تم استخدام برنامج OpenSees لمحاكاة السلوك الغير خطي لجدران القص اعتمادا على نموذج تباطؤ طورت مؤخرا. تحليلات نفذت على 54 اطار من 2 ,4 و 5 طوابق مصممة لمقاومة شدة زلزال ذات مستويات مختلفة. وقد أنشأت منحنيات الهشاشة بناءا على احتمال انهيار المباني اتباعا لمنهجية FEMA P695. بناءا على متطلبات التصميم المعرفة تبين أن النظام الهيكلي المصنوع من الحديد المشكل على البارد الذي تم تقييمه في هذه الدراسة يلبي معايير القبول بمعامل سلوك (q) يساوي 2 في حالة زلزال ذو شدة منخفضة و معتدلة. وعلاوة على ذلك, تم تقديم الأداء الزلزالي الاحتمالي و المخاطر لنظام جدران القص المصنوعة من الحديد المشكل على البارد استنادا إلى نظام الأطر المقاومة للعزوم المصنوع من الصلب التقليدي بهدف استكشاف إمكانية استخدام نظام الحديد المشكل على البارد كحل هيكلي جديد في المناطق المعرضة للزلازل. بناء على التحليلات الاحتمالية للمخاطر الزلزالية (PSHA) تم اختيار, و لمواقع محددة, سجلات الهزات الارضية من اجل اجراء تحليلات ديناميكية تدريجية (IDA) اعتمادا على ”Conditional Spectrum“ كطيف استجابة مرجعي أكثر واقعية. و في وقت لاحق, تم تقيم مخاطر الزلزال على مدى عمر الهيكل (أي 50 سنة) من حيث الاحتمال السنوي لتجاوز حالات الحد التالية: الحد من الأضرار، لا- انهيار محلي و القرب من الانهيار. و يسلط الضوء على أهمية و فائدة مقاييس المخاطر التي اعتمدت كمؤشر لاكتشاف السمات السلوكية لكلا النظامين الهيكلين.عموما, أظهر إجراء التقييم ان كلا النظامين يقدمان أداء زلزالي مقبول, و بالتالي يمكن اعتبار النظام الهيكلي المصنوع من الحديد المشكل كحل يمكن الاعتماد عليه لتحقيق الأهداف القائمة على الأداء في المناطق المعرضة للزلازل.

و في وقت لاحق, تم تطوير نموذج العناصر المنتهية لمحاكاة سلوك الأعمدة المصنوعة من الحديد المشكل على البارد ذات المقطع العرضي المركب والتحقق من صحته باستخدام نتائج التجارب التي أجريت في جامعة جونز هوبكنز كجزء من مشروع تعاوني. الدوافع وراء هذه الدراسة تتمثل في: (1) تقديم نتائج النمذجة لزيادة التجارب الموجهة نحو تحسين المبادئ

التوجيهية لتصميم الأعمدة ذات المقطع العرضي المركب المصنوعة من الحديد المشكل على البارد, و (2) لتوفير مسار محاكاة لنمذجة الأعمدة ذات المقطع العرضي المركب المصنوعة من الحديد المشكل على البارد المستعملة في جدران القص و التى تخضع عادة لقوى دورية. تم إنشاء نماذج رقمية عن طريق برنامج العناصر المنتهية ABAQUS التي تضم السلوك الهندسي و المادي الغير خطي و العيوب الهندسية التي تم قياسها عن طريق الليزر على عينات اخذت من نفس الصلب المستعمل في إنشاء الأعمدة, و نموذج تلامس الذي يأخذ بعين الاعتبار الاحتكاك. ميزة إضافية لهذه النماذج الرقمية تتمثل في نماذج المسامير باستخدام عناصر معرفة من طرف المستخدم (UEL) التي بإمكانها محاكاة تدهور مقاومة وصلابة المسامير بالإضافة إلى المعسر عندما تكون هذه العناصر تحت أحمال دورية. تمت محاكاة اختبارات الضغط التي أجريت على 17 عمود مصنوع من الحديد المشكل على البارد باستخدام مقطعين عرضين, مخططات ربط وشروط تغليف مختلف. تشوهات الالتواء, مقاومة وآليات الانهيار المحصل عليها من النماذج الرقمية كانت على توافق جيد مع النتائج التجريبية. تقييم الحمولات المطبقة علي المسامر يكشف ان تصميم و مخطط عناصر الربط المشروط من طرف AISI S100 (2016) section I1.2 يعطي نتائج محافظة. كذلك, هناك ارتفاع طفيف في مقاومة الأعمدة عند إضافة عناصر الربط (EFGs) في قاعدة و قمة الأعمدة. النماذج الرقمية التي تم تطويرها سوف تستعمل مستقبلا في دراسة بحثية لتوصيف السلوك الرتيب والدوري للاعمدة المحملة محوريا من اجل اعطاء امكانية التقاط الحالات الحدية للاعمدة الجانبية في جدران القص في نماذج محاكاة الزلزال للأطر المصنوعة من الحديد المشكل على البارد.

الكلمات الرئيسية : حديد مشكل على البارد, تصميم زلزالي, معامل السلوك, تقييم الأداء الزلزالي, FEMA P695, مخاطر الزلازل, أعمدة, مقاطع مركبة, تجارب, تحليلات العناصر المنتهية.

RESUME

Le mur de cisaillement (SWP) en profilés d'acier formés à froid (CFS) est l'un des systèmes de contreventement adopté dans les constructions en acier léger. Ce dernier est constitué d'un cadre en profilés CFS sous forme de C (poteaux et poutres) sur lequel sont attachées des plaques (sheathing) en acier ou en bois au moyen d'éléments de fixation (vis).

Cette thèse s'inscrit dans le contexte de la définition d'une procédure de conception sismique et de vérification, pour les bâtiments en profilés CFS, pouvant intégrer le cadre de conception sismique actuel de l'Eurocode 8. L'approche adoptée comprend la définition d'un ensemble de critères de conception, la sélection et la conception d'un ensemble de bâtiments types, le développement de leurs modèles numériques non-linéaires dans le logiciel de modélisation par éléments finis OpenSees suivi par l'exécution d'analyses statiques non-linéaires (Pushover) et d'analyses dynamiques incrémentales (IDA) suivant la méthodologie de Federal Emergency Management Agency (FEMA) P695.

Deux modèles hystérésis tenant en compte la détérioration de la résistance et de la rigidité ainsi que le pincement ont été développés et implémentés dans le logiciel OpenSees (version 2.4.5 et ultérieure) sous forme des matériaux intitulés "CFSSSWP et CFSWSWP" pour CFS-SWPs ayant des plaques de revêtement en acier et en bois, respectivement. Les modèles ainsi développés ont été validés par les données expérimentales disponibles dans la littérature, une concordance acceptable a été atteinte.

Par la suite, une procédure de conception sismique compatible avec le cadre des Eurocodes est présentée pour les bâtiments en profilés CFS employant des SWPs. Afin d'examiner le comportement structurel et de générer les données requises pour l'évaluation de la procédure de conception sismique, le logiciel OpenSees a été utilisé pour simuler le comportement non-linéaire du CFS-SWP en adoptant un modèle hystérésis développé récemment. Des analyses Pushover et IDA ont été effectuées sur 54 portiques CFS-SWP de 2, 4 et 5 étages conçus avec différents niveaux d'intensité sismique. En se basant sur la probabilité d'effondrement des bâtiments, des courbes de fragilité ont été développées suivant la méthodologie de FEMA P695. Sur la base des exigences de conception définies, le système structurel en profilés CFS, évalué dans cette étude, répond aux critères d'acceptation avec un coefficient de comportement (q) égal à 2 pour une sismicité faible et modérée. En outre, une évaluation probabiliste de la performance et de risque sismique du système structurel CFS-SWP est présentée en utilisant des portiques auto-stables en charpente métallique classique comme un système référence dans

le but d'explorer la viabilité d'utiliser CFS-SWP en tant qu'une nouvelle solution structurelle dans les régions sismiques. Sur la base des analyses probabilistes de l'aléa sismique (PSHA), une sélection des enregistrements de mouvement du sol, spécifiques au site, a été réalisée pour effectuer IDA moyennant "Conditional Spectrum" comme un spectre de réponse cible plus réaliste. Par la suite, le risque sismique a été évalué sur la durée de vie de la structure (à savoir, 50 ans) en termes de la probabilité annuelle de dépassement des exigences de limitation des dommages, non-effondrement local et près de l'effondrement. L'importance et l'utilité des mesures de risque sont mises en évidence et adoptées comme un indice afin d'explorer les caractéristiques du comportement des deux systèmes structuraux. Dans l'ensemble, la procédure d'évaluation a montré que les deux systèmes ont présenté une performance sismique acceptable et par conséquent le système CFS-SWP peut être considéré comme une solution structurelle fiable pour atteindre les objectifs basés sur la performance dans les régions sismiques.

Subséquemment, un protocole de modélisation par éléments finis pour les poteaux en CFS à section composée dos-à-dos a été développé et validé en utilisant des résultats d'essais effectués à l'Université de Johns Hopkins faisant partie d'un projet de cooperation. Les motivations sont (1) de fournir des résultats de modélisation pour augmenter les essais visant à améliorer la conception des poteaux CFS à section composée, et (2) de fournir un chemin de simulation pour la modélisation du comportement hystérésis non-linéaire des poteaux CFS à section composée dans les CFS-SWPs. Les modèles en éléments finis ont été développés moyennant le logiciel ABAQUS et qui incluent le chargement monotone, la non-linéarité géométrique et matérielle, les imperfections géométriques basées sur des mesures effectuées sur les spécimens testés moyennant un scanner laser ainsi qu'un modèle de contact qui prend en considération le frottement. Une caractéristique supplémentaire qui est la modélisation des vis à l'aide des subroutines (UEL) qui peuvent reproduire la détérioration de la résistance et de la rigidité sous charge monotone ainsi que le pincement qui se produit lorsque les vis sont soumises à un chargement cyclique. Des essais de compression monotone sur 17 poteaux CFS à section composée dos-à-dos ont été simulés en utilisant deux types de la section transversale et différentes dispositions des éléments de fixation et conditions de revêtement. Les déformations des flambements, les forces et les mécanismes d'effondrement obtenus numériquement correspondent aux résultats expérimentaux avec une erreur acceptable. Une évaluation de la demande en termes d'effort de cisaillement sur les vis révèle le conservatisme dans la disposition et la conception des vis exigées par the North American CFS design specification

(AISI S100-16 section I1.2). Egalement, sous les conditions aux limites semi-rigides des poteaux testés, il y a peu d'augmentation de la capacité axiale quand les deux groupes d'éléments de fixation (EFGs) sont ajoutés aux extrémités (sommet et base) du poteau. Le protocole de modélisation ainsi développé sera utilisé, dans un futur travail de recherche, afin de caractériser le comportement monotonique et cyclique des poteaux chargés axialement de sorte que les états limites des poteaux à section composée pourraient être capturés dans les simulations sismiques des CFS-SWPs.

Mots clés : Acier forme à froid, Conception parasismique, Coefficient de comportement, Evaluation de la performance sismique, FEMA P695, Risque sismique, Poteaux, Sections composées, Expérimental, Analyse par éléments finis.

ACKNOWLEDGMENTS

I thank the Almighty (Allah) for bringing me to this stage in my life, blessed me with this achievement and for giving the health to be able to do this work.

There is probably a philosopher who once said something along these lines: “It seems forever while you are living a challenge, but it seems so short when you look back on it.” While I still have the vivid memories of the “forever” I would like to acknowledge all the people who have helped me.

I would like to acknowledge my sincere gratitude to my supervisor, Nouredine Bourahla Professor at the University of Blida 1, for believing in me since the early ages of my academic career, more than six years ago. I did not know that I could do so much. Your excitement for research is amazing. Please never lose it; you are a source of energy to all of your students. And thanks for your friendship. Our talks and emails will remain forever in my memory.

To my co-supervisor, José Miguel Castro Professor at the University of Porto, thank you for the opportunity to be part of your research group, the fruitful discussions about Earthquake Engineering and for many ideas.

I am grateful to Professor Benjamin William Schaffer for the collaboration with The Thin-Walled Structures Group at Johns Hopkins University within the framework of the project entitled “Experiments, Analysis, and Design of Built-Up Cold-Formed Steel Columns”.

I sincerely thank the members of my thesis committee for reviewing and giving me constructive comments and criticisms on my work that would enhance the quality of my thesis. In addition to professors of the Civil Engineering Department of the University of Blida 1 for their quality of teaching.

My family has never let me down. In fact, the inconveniences of life made me rediscover them. My parents, thanks for everything; nobody could ever do better than you two. Brothers and sisters, thank you for your love, gratitude and respect. To all of you, this thesis is dedicated.

My friends and colleagues at University of Blida 1, University of Porto and Johns Hopkins University, thank you for your companionship and kindness.

Lastly, I would like to acknowledge the financial support provided by Erasmus Mundus Battuta project through a PhD mobility Scholarship (BT15DM2716).

CONTENTS

LIST OF FIGURES

LIST OF TABLES

LIST OF APPENDICES

INTRODUCTION

1. Research problem and motivation

In constructional steel practice, conventional steel moment-resisting and concentrically-braced frames (MRFs and CBFs, respectively) as well as more recent dissipative eccentric bracing schemes represent the most common solutions for buildings to withstand lateral loads (wind and earthquake). The reliability of these lateral load resisting systems was confirmed and improved by their performance observed in past earthquake events and also from significant past research activities that have culminated in detailed seismic design provisions adopted worldwide. In recent years, new innovative systems to ensure high structural and environmental performance have emerged. Among others, cold-formed steel (CFS) shear wall panel (SWP), is becoming an effective structural system to resist lateral loads for low- and mid-rise CFS buildings, offering a potential benefit from using lightweight framing components, thus, limiting the seismic mass. Nevertheless, conventional steel MRFs and CBFs are still preferred due to the more complex analysis and design procedures required when dealing with thin-walled CFS framing members, which develop local instabilities and several failure mechanisms.

The CFS-SWP using steel or wood sheathing is a code approved lateral load resisting system for low- and mid-rise CFS buildings in North America. It is composed of CFS C-shaped framing members (chord studs, studs and tracks) attached to sheathing using screw fasteners. The overall behaviour of this structural component is governed by the inelastic behaviour that develops in the connection zone between the CFS frame and the sheathing. This structural component should be designed to provide adequate lateral shear strength and stiffness to the global structure.

At present, there is no code for the design of CFS buildings in Algeria, and the current version of the European code for seismic design, Eurocode 8 (EC8) [1], does not provide any guidance for CFS-SWP, consequently, a modest level of adoption of this lateral load resisting system has been recorded in Europe and North Africa. The North American Standard for Seismic Design of Cold-Formed Steel Structural Systems AISI S400 (2015) [2] represents the main reference for the lateral design of this type of structures. Since there is no Algerian code for CFS design and the RPA99 V2003 [3] and CCM97 [4] (Algerian code for seismic design and steel code, respectively) are mainly inspired from EC8 [1] and Eurocode 3 [5], respectively, a new seismic design procedure for CFS framed structures based on existing information, but tailored to fit the Eurocode requirements and typical European design practices would be beneficial for both, the Eurocode and a perspective Algerian CFS code.

Modern seismic design requires the establishment of proper seismic performance factors, such as response modification factor, displacement modification factor and system overstrength, which are needed for practicing engineers. Since these factors are related to the performance of the overall structure, they cannot be obtained directly from experimental tests of individual walls, but through nonlinear dynamic analyses of the whole building structural system.

In order to achieve a more rational seismic resistant structural design procedure, research in the CFS framed building system, made up of wall panels (*i.e.*, partition, bearing and shear walls), is moving toward the performance-based seismic design approach. The central challenge in performing such a design approach, is the development of robust, yet computationally efficient, models that can be used to represent structural response in highly nonlinear dynamic analyses at different seismic intensity levels.

2. Thesis objectives

The goal of the research study conducted herein is to develop a procedure and tools for seismic design and verification of CFS framed buildings employing sheathed SWP. The procedure is based on the Federal Emergency Management Agency (FEMA) P695 (2009) methodology [6] and integrates the current seismic design framework of EC8 [1]. The tools involve the development of constitutive models capable of simulating as accurately as possible the response of the lateral load resisting system (CFS-SWP) when subjected to lateral loading (wind and earthquake). Furthermore, in order to explore the relative potentialities of CFS framed structures in seismic prone regions, a comparison of the probabilistic seismic performance and risk assessment between CFS-SWP and conventional steel MRF systems is sought in terms of the annual probability of exceeding the Damage Limitation (DL), No-Local Collapse (NLC) and Near Collapse (NC) limit states over the structure lifetime (*i.e.*, 50 years).

At the element level, an in-depth study on the behaviour and design of screw connected built-up back-to-back CFS columns as constructed and installed in a SWP (chord studs) is of paramount importance. For this purpose, an extensive numerical study has been carried out in tight cooperation with an experimental work that has been conducted by a research team in Johns Hopkins University (USA) [7] to analyse the composite action, prevailing buckling modes, post-peak behaviour and failure modes of a series of 17 CFS columns. The goal of this study is to contribute to the improvement of the existing design guidelines of CFS structural members towards more precise calculations in which, all relevant failure modes (local, distortional and global buckling) are considered in the design of built-up CFS columns. In addition, the characterisation of the monotonic and cyclic behaviour of built-up CFS columns is intended in future work such that chord stud buckling limit states could be captured in the seismic simulation of the CFS-SWP frames.

3. Thesis outline

This thesis starts with a general description of the research topic followed by a critical review of the relevant literature including the CFS-SWP lateral behaviour and the performance-based seismic design methods.

The development of hysteresis models for steel- and wood-sheathed CFS-SWP that take into account strength and stiffness deterioration with pinching, in addition to their implementation process into the OpenSees finite element (FE) software, are presented in Chapter 2.

In Chapter 3, a seismic design and verification procedure for CFS framed buildings employing sheathed SWP, is defined. A description of the building design for seismic hazard regions of low, moderate and moderate-to-high, is provided. The model of the archetype buildings is also explained in terms of applied elements and corresponding materials.

Chapter 4 discusses the assessment of the proposed seismic design procedure following the FEMA P695 methodology [6]. The evaluation of the seismic performance for the serviceability limit state is performed as well.

In Chapter 5, a probabilistic framework for structural performance assessment and a comparison between CFS-SWP and conventional steel MRF systems in terms of seismic risk, are presented. In order to provide insights into the relative performance of both structural systems, the seismic risk is evaluated over the structure lifetime (*i.e.*, 50 years) in terms of the annual probability of exceeding DL, NLC and NC limit states under a set of ground motion records selected based on the Conditional Spectrum.

Subsequently, numerical studies together with an associated experimental program to analyse the composite action, prevailing buckling modes, post-peak behaviour and failure modes of a series of 17 CFS columns, are detailed in Chapter 6. Advanced FE models, validated based on tests results, are built using ABAQUS 6.14-5 (Simulia 2014) software [8] with nonlinear geometry, material, fastener and contact behaviour.

The last part of the thesis concludes the research findings and explores areas of future research.

The detailed description of C++ source codes of the developed hysteresis models (CFSSSWP.h and CFSSSWP.cpp), are attached to this thesis as an appendix. IDA and fragility curves of the archetype buildings designed with a q factor equal to 2 are provided as well. The coupon tests results of the steel used for the experimental campaign conducted on built-up columns and the comparison between the measured monotonic response and that predicted by the FE simulation for all specimens are also attached as appendices.

CHAPTER 1

LITERATURE REVIEW

1.1. Introduction

Cold-formed steel (CFS) is structural steel rolled into a thin sheet (~1 to 3 mm thick) and gradually cold bent into desired cross-sections. The result of this manufacturing process is light steel members that may be used as wall studs, joists, headers, jamb studs, chord studs and others. A construction site and common CFS cross-sections are shown in Fig. 1.1. Several desirable features, like high strength-to-weight ratio, low shipping cost and easiness of construction, expedite the use of CFS members in many countries as both structural and non-structural members (Schafer (2011) [9]). In Algeria, the use of CFS profiles as primary structural members in buildings is in its beginning, the first CFS multi-storey buildings were erected late last decade.

a) b)

Fig. 1.1. a) Photograph of CFS framed residential building located in Setif, Algeria (photo credit: ALRIM), b) drawing of common CFS cross-sections.

This chapter presents a literature review on the behaviour and failure modes of steel- and wood-sheathed CFS shear wall panels (SWPs) representing one of the lateral load resisting systems in CFS framed buildings. The first part is devoted to failure modes of SWPs and the parameters that have a significant effect on their shear strength and post-elastic behaviour when subjected to lateral loadings. In addition, details of two hysteresis models previously used to simulate the response of SWPs, are discussed. The second part sheds light on the probabilistic method of assessing the seismic performance factors. Finally, the current research studies related to testing, modelling and design of CFS framed buildings, are outlined.

1.2. Lateral load resisting system in CFS framed buildings

The CFS-SWP using steel or wood sheathing is a code approved lateral load resisting system for low- and mid-rise CFS buildings in North America. It is composed of CFS C-shaped framing members (chord studs, studs and tracks) attached to sheathing using screw fasteners as shown in Fig. 1.2. This structural component dissipates energy by taking advantage of the inelastic behaviour that develops in the connection zone between the CFS frame and sheathing.

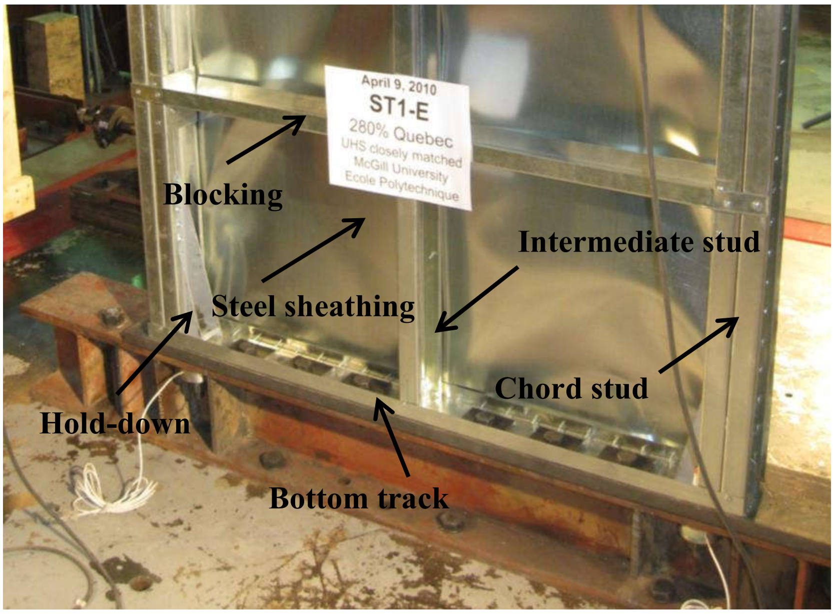

Fig. 1.2. Details of a steel-sheathed CFS-SWP [10].

The focus in this thesis is on the above described SWP, nevertheless, other types of lateral load resisting system do exist for CSF framed buildings such as strap-braced and truss framed walls, which are beyond the scope of the research study conducted herein.

1.3. Characteristics of the CFS-SWP hysteresis

Every lateral load resisting system when submitted to cyclic lateral loading exhibits a hysteresis behaviour. The factors that influence the hysteresis loops can be attributed not only to external variables such as the type and the velocity of loading history, but also to material and structural characteristics of the system itself.

The hysteresis loops of a typical wood-sheathed CFS-SWP having height-to-width aspect ratio of 2:1 (2440 x 1220 mm) is shown in Fig. 1.3. From this figure, one can visually assess the asymmetrical shape characterised by the narrowing of the shear strength amplitude near the origin. These loops are characterised by the minimal energy dissipation in the 2nd and 4th quadrants of the chart.

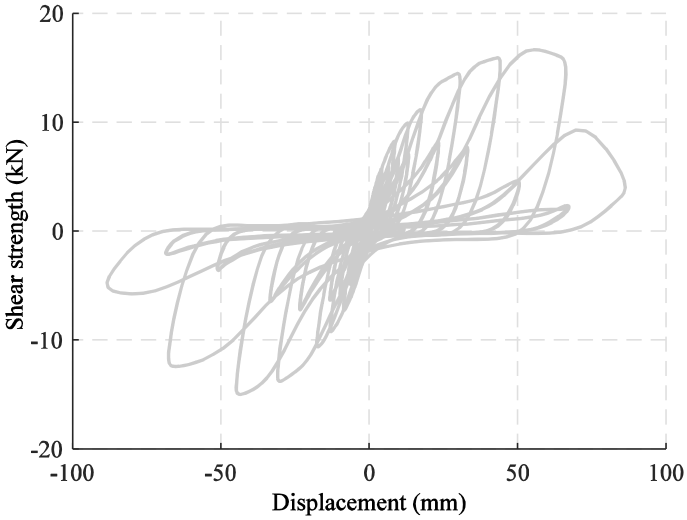

Fig. 1.3. Hysteresis loops of specimen 12A tested by Branston et al. (2006) [11].

In recent years, several experimental quasi-static tests have been carried out on SWP specimens having different configurations. A common observation in these tests was that the nonlinear behaviour of the SWP depends considerably on the complex behaviour that occurs at each location of sheathing-to-framing screw fasteners, resulting from bearing between the sheathing and fasteners as well as tilting of the fasteners themselves.

Memory effect occurs when the SWP response in terms of shear strength-lateral displacement curve of a given cycle is directly influenced by the strength and displacement of the previous cycle. This particular characteristic makes modelling the SWP behaviour under cyclic loading more complex than when it is subjected to a progressive (monotonic) loading.

The most important characteristics of SWP hysteresis loops are: nonlinearity at low levels of loading, strength and stiffness deterioration as well as pinching.

1.3.1. Nonlinearity

As opposed to lateral load resisting systems made of conventional steel or reinforced concrete, where the behaviour is linear at low levels of loading, CFS-SWPs exhibit nonlinear behaviour at very low shear demands (Fig. 1.4). This feature is mainly due to the behavioural complexity of the SWP components and their interaction. Therefore, the applicability of the equal displacement theory for CFS-SWP frames is arguable.

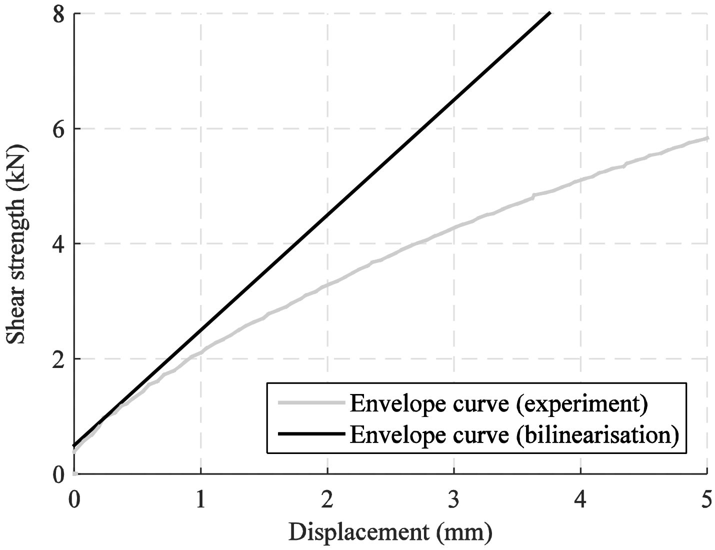

Fig. 1.4. Nonlinear shear strength-lateral displacement curve of a typical CFS-SWP at a low shear demand [11].

The equal displacement principle assumes that for a given seismic intensity level, the perfectly elastic system and the equivalent elastic-plastic bilinear system have the same maximum lateral displacement (see Fig. 1.5a). This Newmark's assumption, applies to structures having structural elements behaving linearly at low level of loading. The seismic codes provisions have been developed by applying the equal displacement assumption in defining the behaviour factor, "Lateral deflections obtained from an elastic analysis using the loads given by design response spectrum shall be multiplied by *R* (or *q* in the European context) to give realistic values of anticipated deflections".

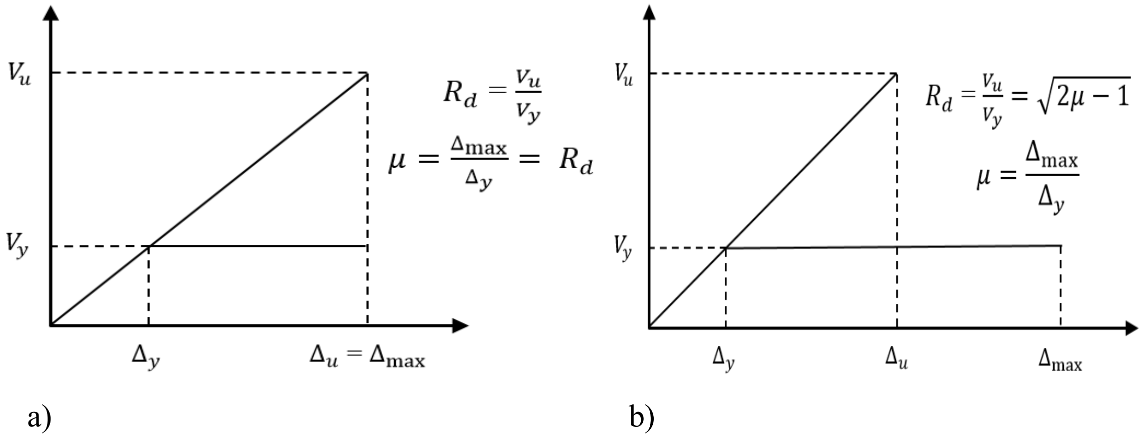

Fig. 1.5. a) Equal displacement and b) equal energy rule (Gad (1997) [12]).

However, if a system is stiffer, and therefore has a much shorter fundamental period of vibration than the dominant period (T) of the response spectrum (acceleration), the equal displacement assumption can no longer be used. Stewart (1987) [13] and Dolan (1989) [14] observed that when a stiff system yields, its period becomes longer as a result of partial damage and can enter in a quasi-resonance state as it approaches T on the acceleration spectrum. For such systems, which have a relatively short period of vibration (between 0.1 sec and 0.5 sec), the equal energy principle applies. This principle, as illustrated in Fig. 1.5b, states that the strain energy of an inelastic system must be equal to the strain energy of the corresponding elastic system.

1.3.2. Strength deterioration

The cyclic response in Fig. 1.6 shows that the shear strength of a CFS-SWP deteriorates as a function of the amplitude and the number of loading cycles, where even prior to the attainment of the ultimate shear capacity this effect is clearly noticed. This deterioration in strength is assumed to occur in the plastic domain, however, a SWP could experience light deteriorations at low displacement amplitudes in the elastic range due to repeated cyclic displacements, this phenomenon is well known as low cycle fatigue.

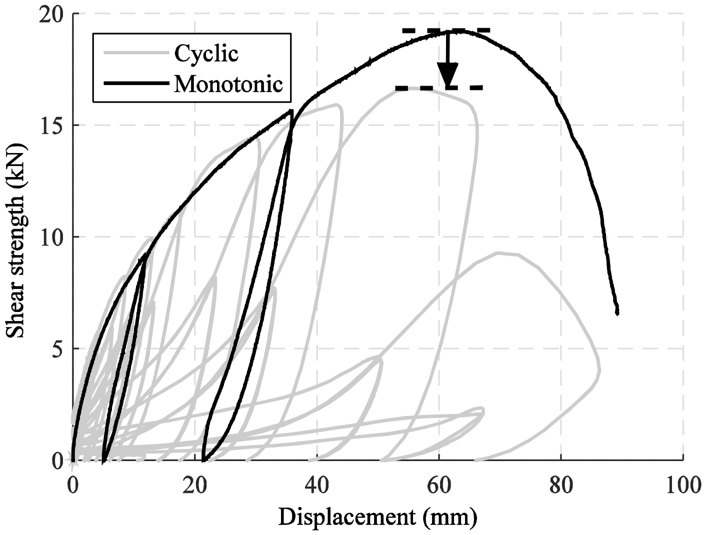

Fig. 1.6. Strength deterioration representation between monotonic and cyclic responses [11].

At the fastener scale, the formation of play around the screw head during the first excursion in a given direction results in a lower capacity for successive loops at the same displacement level simply because we can expect less resistance from a damaged part of the sheathing around the fastener. Although strength deterioration is a noticeable feature of a SWP hysteresis shear strength-lateral displacement curve (see Fig. 1.6), it is considered by many researchers such as Ibarra et al. (2005) [15] and Vigh et al. (2013) [16] to play a lesser role in the response of whole structure compared to other characteristics such as un- and re-loading stiffness deterioration as well as pinching.

1.3.3. Un- and re-loading stiffness deterioration

The effective stiffness is expressed as the slope of the hysteresis loop with respect to the horizontal axis. Over successive load cycles, the un- or re-loading stiffness decreases as well as the area enclosed within the loop. The latter represents the energy dissipated by the SWP. Therefore, the un- or re-loading stiffness deterioration lead to less energy dissipation capacity. Knowledge of this feature is crucial to avoid an overestimation of stiffness and energy dissipation capacity in numerical models.

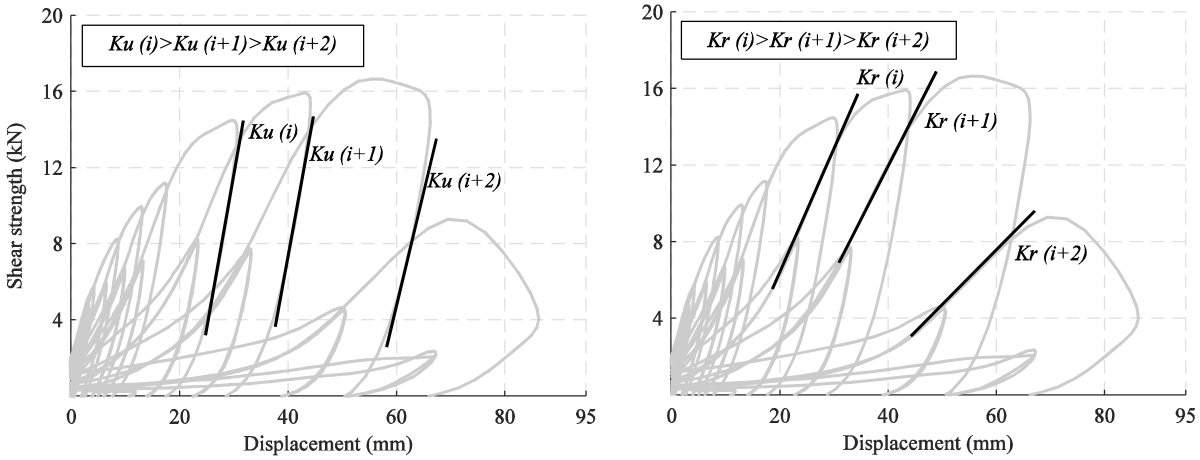

a) b)

Fig. 1.7. Stiffness deterioration: a) un-loading and b) re-loading [11].

1.3.4. Pinching

Pinching is the most important characteristic of the hysteresis loops of a CFS-SWP. The pinching is caused by the loss of stiffness at the interface between screw fasteners-sheathing, where a gap creates around the screw fastener due to the damage of the sheathing. With each reversed displacement of the SWP, the shear strength is significantly reduced as the screw fasteners move freely through the gap, once a contact with the sheathing takes place, an increase of the stiffness occurs. When moving through the gap, the screw fastener is free to tilt without the support of the sheathing and the contact between the thread and the thin steel layer (framing member) provides a residual strength to the applied load. This residual strength can be observed to be quite constant even after consecutive loops as shown in Fig. 1.8 where the intercept strength is represented.

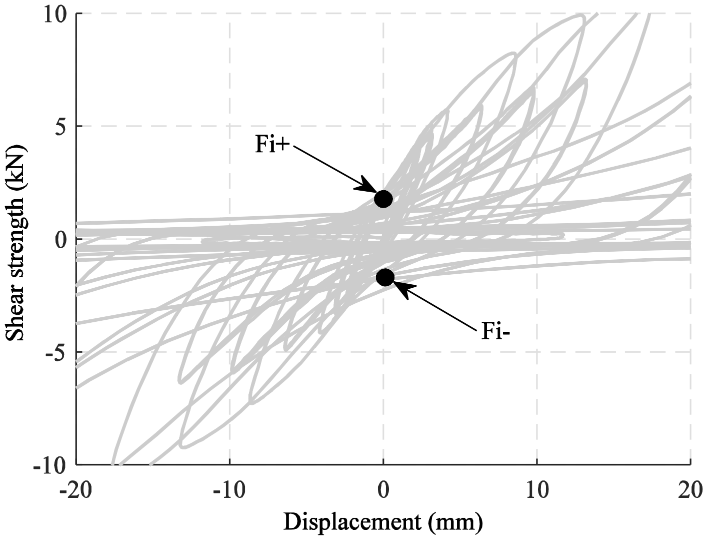

Fig. 1.8. Intercept strength at zero displacement [11].

Different levels of pinching may be observed. At very low displacement levels, the sheathing of the SWP is not damaged, therefore, the pinching is not yet visible (Fig. 1.9a). As the displacement increases, inflection points appear and consequently the area enclosed within the loop, which is a direct measure of seismic energy dissipation due to hysteresis, diminishes (Figs. 1.9b and 1.9c). Thus, neglecting the pinching in modelling SWPs cyclic behaviour, would lead to an overestimation of their energy dissipation ability and a permissive response assessment.

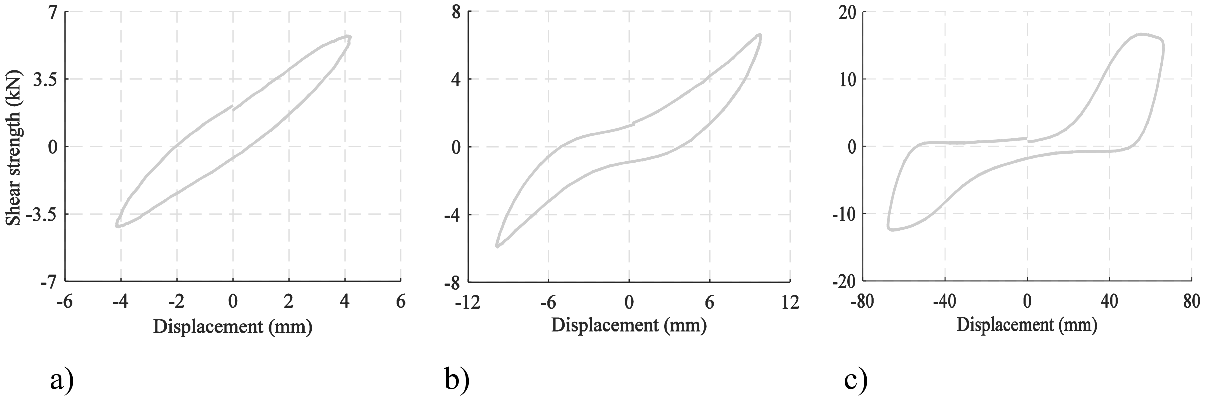

a) b) c)

Fig. 1.9. Evolution of pinched hysteresis loops with increased displacement level: a) no pinching, b) moderate pinching and c) sever pinching [11].

1.4. Failure modes of CFS-SWPs

1.4.1. Single CFS-SWPs

At the ultimate limit state, the failure of a CFS-SWP under a lateral loading occurs when the latter has no further strength to resist the applied lateral load. Many researchers (Branston et al. (2006) [11], Nisreen Balh (2010) [17], Cheng Yu (2010) [18], Yu and Chen (2011) [19], Liu et al. (2014) [20], Jamin DaBreo (2012) [21] and Iman Shamim (2012) [10]) have shown in previous experimental studies that the behaviour of screw fasteners, connecting the CFS framing members and sheathing, provides the key energy dissipation mechanism in the SWP.

The failure in boundary studs (chord studs) and hold-downs (uplift anchorages) could be successfully prevented if the designer follows the capacity design principle given by The North American Standard for Seismic Design of Cold-Formed Steel Structural Systems AISI S400 (2015) [2] which requires that the chord studs and uplift anchorages have a nominal capacity capable of resisting the expected loading demand and remain elastic and undamaged. Hence, the lateral load resisting system would keep its structural integrity and, thus, the vertical load carrying capacity.

a) Steel-sheathed CFS-SWP

Cheng Yu (2010) [18], Yu and Chen (2011) [19], Nisreen Balh (2010) [17] Jamin DaBreo (2012) [21], Iman Shamim (2012) [10] and Mohebbi et al. (2015) [22] conducted experimental programs on CFS-SWPs sheathed with flat steel sheets. It was found that the shear strength of a SWP is mainly generated by the sheathing through a diagonal tension field (Fig. 1.10). The observed failure modes are screw failures within the diagonal tension field (Fig. 1.11) and, under particular conditions (a dense concentration of screw fasteners and/or a relatively large thickness of the sheathing), local buckling of the compressed chord stud could happen (Fig. 1.12). As shown in Fig. 1.10, the sheathing does not contribute to the lateral strength evenly across the entire width of the SWP. A partial width of the sheathing is counted to withstand the majority of the tensile force in the system. Thus, in most tests, failure of the screw fasteners occurs at the corners of the SWP, more precisely inside the tension field region.

Fig. 1.10. Tension field action of steel-sheathed CFS-SWPs [18].

Fig. 1.11. Typical sheathing-to-framing screw failure modes: at top left: bearing of sheathing, at top right: fastener pull-through and at bottom: fastener pull-out [17].

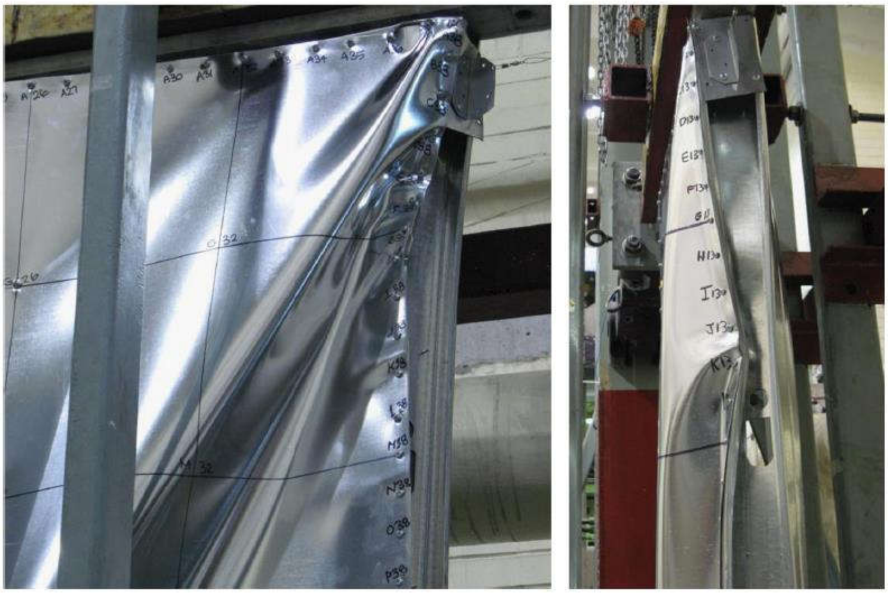

Fig. 1.12. Torsional failure of chord studs in un-blocked walls due to horizontal component of tension field force, at left: face view of 1220 x 2440 mm SWP (monotonic loading) and at right: end view of 610 x 2440 mm SWP (monotonic loading) [17].

As for CFS-SWPs sheathed with corrugated steel sheets, previous experimental tests conducted by Fülöp and Dubina (2004) [23], Vigh et al. (2013) [16] and Berediafe-Bourahla et al. (2015) [24] revealed that the eventual pulling out/through of the screw fasteners due to warping of the sheathing were the main failure modes (see Figs. 1.13 and 1.14). Particularly, when the SWPs are subjected to cyclic loading, the screw fasteners would eventually elongate holes in the studs and/or sheathing (see Fig. 1.13a). As the lateral loading increased, warping of the corrugated steel sheet became more pronounced and simultaneous diagonal tension and compression fields developed across the SWP. As the holes in the studs and/or sheathing enlarged, the tensile capacity of the screw fasteners was reduced and eventually the screws failed in tension due to the warping of the corrugated steel sheet and pulled out/through. It is also interesting to note the location of the screw fasteners that first pulled out/through, where in all cases, the first screws to pull out/through were in the boundary members. The location of the screw fasteners that pulled along the boundary members was random. The locations varied from top to bottom on both the left and right boundary members (see Fig. 1.13b and c). The screws fastened into the top track, the bottom track and the horizontal seams were never the first to fail (see Fig. 1.13c).

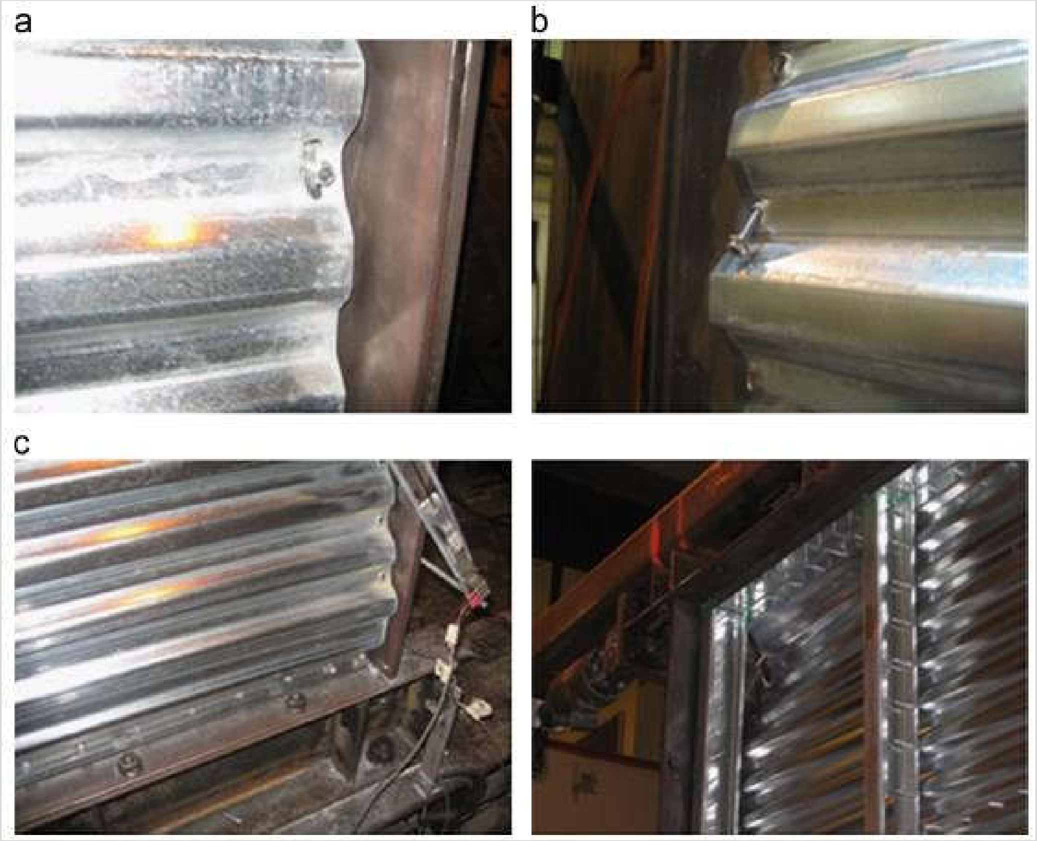

Fig. 1.13. Observed failure sequence: a) bearing, b) screws pull-out/tilt and c) buckling and warping of corrugated steel sheet after screws pull-out [16].

Fig. 1.14. Screws pull-through and tear out-bearing [24].

b) Wood-sheathed CFS-SWP

According to experimental tests that have been conducted by Gad et al. (1999) [25], Branston et al. (2006) [11], Serrette et al. (2002) [26] and Liu et al. (2014) [20], it has been noticed that the failure mechanism in wood-sheathed CFS-SWPs is often initiated at the sheathing-to-framing screw fasteners as well. However, when the thickness of the CFS chord studs is relatively small (*e.g.*, thickness ≤ 0.84 mm), the failure of the SWP could be initiated by the local buckling of the chord studs. The failure of the chord studs can also occur when the sheathing board is installed on both sides of the SWP so as to double the sheathing thickness and thereby enhance the SWP shear strength. However, the resulting axial forces in the chord studs are amplified, which can lead to chord stud failure in compression, prior to failure of the sheathing-to-framing screw fasteners.

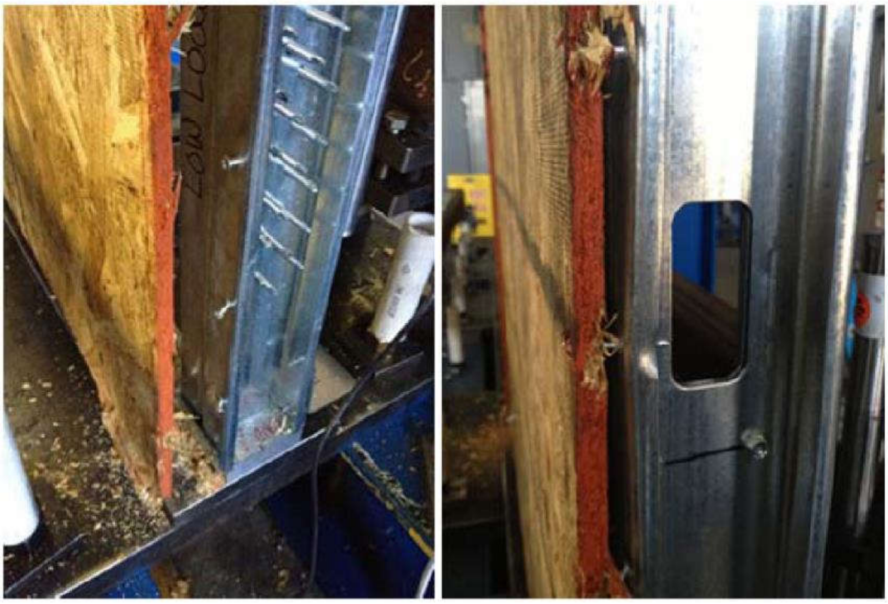

Fig. 1.15. Typical failure modes of the sheathing-to-framing screw fasteners in wood-sheathed CFS-SWP: a) pull through and b) tear out-bearing [11].

Fig. 1.16. Local buckling of the chord stud [11].

1.4.2. Double-storey CFS shear walls

An experimental study on isolated steel- and wood-sheathed CFS-SWPs (Fig. 1.17a) has been carried out through dynamic tests on a shake table [10]. The aims were to evaluate the seismic performance, uncover whether the behaviour of SWPs under dynamic loads is similar to the one observed during past quasi-static cyclic tests, and to measure the damping ratio as well as the fundamental period of vibration of this lateral load resisting system.

The influence of a second storey on the overall behaviour of a lateral load resisting system consisting of two-storey shear wall (Fig. 1.17b), has been studied as well. The tests outcomes showed that the shear capacity and failure modes of SWPs under dynamic loading are not significantly different from those observed during the previous quasi-static tests conducted on SWPs having identical physical and mechanical characteristics.

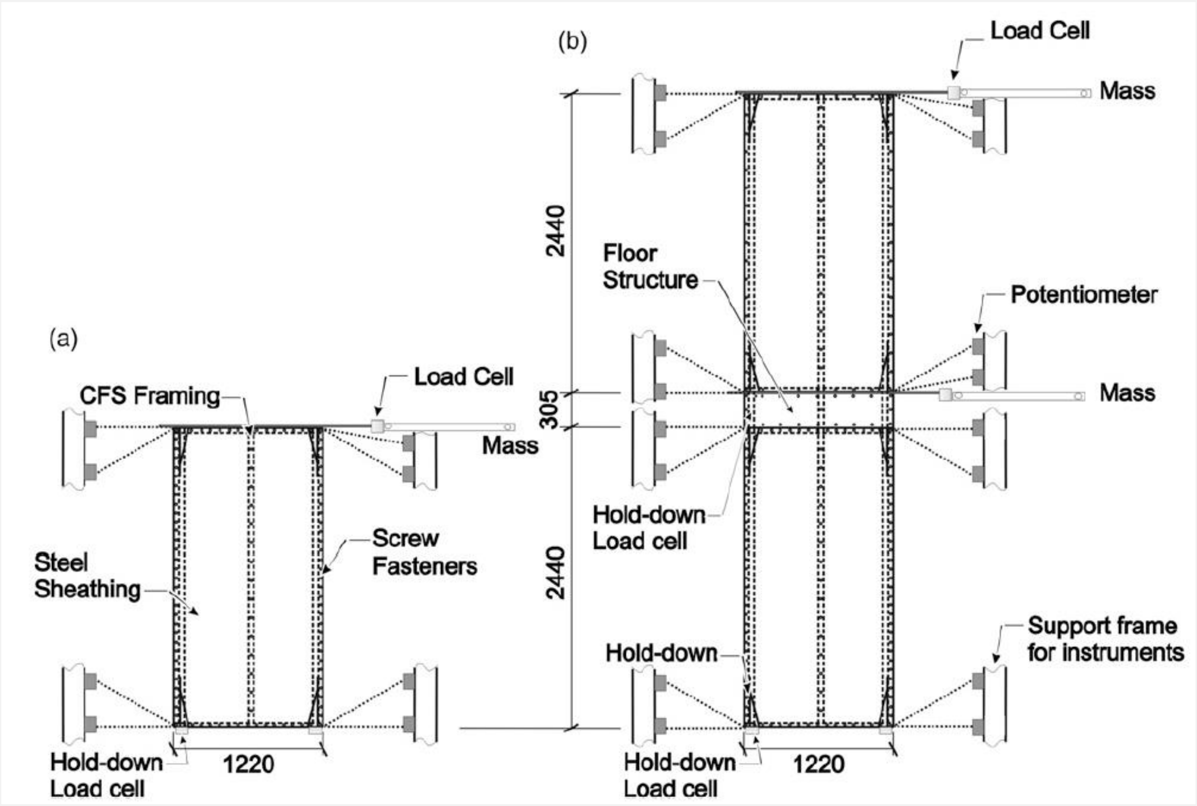

Fig. 1.17. a) Single- and b) double-storey shear walls [10].

In practice, there are two different approaches in designing shear walls, so-called type I and type II. As long as both types have the same screws configuration, the difference in CFS framing do not make significant difference in the overall performance of the system unless the CFS frame undergoes plastic deformations or shows high degree of elongation (which increases the participation of CFS framing action in the amount of the lateral displacement of a SWP). In the above described experimental campaign, since SWPs are connected with anchor rods they are also influenced by the anchor rods' elongation and behaviour which in turn increases the lateral displacement due to the SWP rigid rotation.

1.4.3. Full scale CFS structures

Shake table tests have been conducted by Kara Perterman (2014) [27] on two full-scale CFS framed buildings at the University of Buffalo, Structural Engineering Earthquake

Simulation Laboratory. The two-story buildings, approximately 7 x 15.3 m in plan and 5.8 m in height, were tested in two different configurations. In the first (Phase I), the engineered lateral load resisting system, consisting of oriented strand board (OSB) sheathed shear walls, and OSB sheathed floors/diaphragms was tested, gravity walls were left unsheathed and interior gypsum on the shear walls and interior walls were absent. In the second configuration (Phase 2), the building was completely fit-out. All sub-phases within Phase 2 construction are shown in Fig. 1.18.

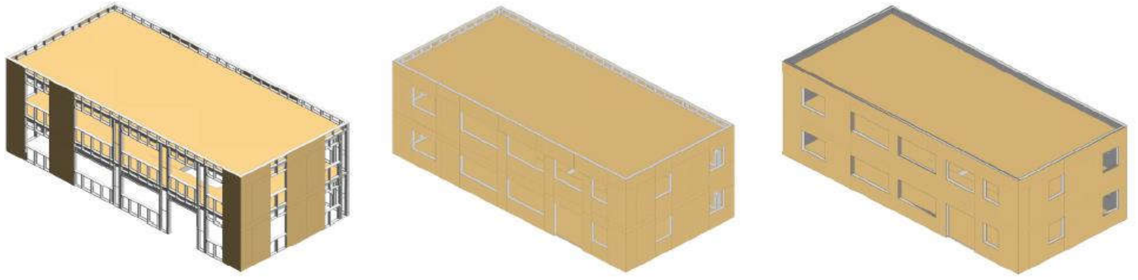

Phase 2a: steel skeleton and shear walls **Phase 2b:** add exterior OSB **Phase 2c:** add interior gypsum

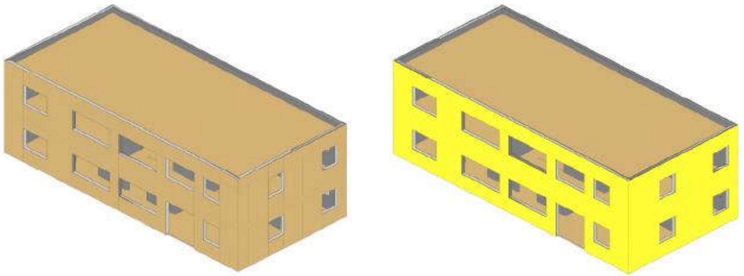

Phase 2d: add ceilings, floor, interior walls, finishing **Phase 2e:** add exterior DensGlass

Fig. 1.18. Construction sub phases, ending with fully finished Phase 2e [27].

Phase 2a Phase 2b Phase 2c

Phase 2d Phase 2e

Fig. 1.19. As built construction sub phases [27].

This full-scale testing provides the first examination of the full system effect for buildings framed from CFS and the main findings were as follows: the building is stiffer and stronger than engineering designs suggest; the building responds as a system, not as a set of uncoupled SWPs (type I) and the gravity system contributes to the lateral response.

1.5. Parameters contributing to the CFS-SWP shear capacity

Various factors can affect the behaviour and strength of CFS-SWP such as material properties, geometrical dimensions and construction details.

1.5.1. Effect of wall length

Previous research studies revealed that the CFS-SWP behaviour is sensitive to aspect ratio, where the 4:1 SWP is characterised by a low shear strength and more ductile behaviour compared to a SWP with an aspect ratio of 2:1 and 1:1. The stocky SWP (2:1 and 1:1) reached their maximum strength capacity at nearly the same deflection level. However, the deflection of the 4:1 SWP (slender), at its ultimate strength level, was almost twice that of the two longer SWPs. AISI S400-15 specifies a reduction factor of 2w/h (where w and h are the width and height of the SWP, respectively) in case of a SWP with an aspect ratio greater than 2:1 and not exceeding 4:1, this factor leads to a conservative design, nevertheless, researchers recommend to keep using the 2w/h reduction factor for slender SWPs.

1.5.2. Effect of screw spacing

For both steel- and wood-sheathed CFS-SWPs, previous experimental comparative studies [11, 17] revealed that a steady increase in shear strength is associated with the reduction of screw spacing. Moreover, the idealised initial stiffness (K_e) increases when the screw spacing decreases, nevertheless, designers should always apply capacity design method to mitigate buckling limit states that could occur in chord studs.

1.5.3. Effect of openings

In order to assess the effect of openings (*i.e.*, doors and windows) on wood-sheathed (OSB) CFS-SWPs shear capacity, experimental monotonic and cyclic tests have been carried out at National Association of Home Builders (NAHB) centre [28]. Comparison between tested CFS-SWPs resistances and predictions using Sugiyama's equations which is initially developed for wood framed SWPs, revealed a conservative nature of predictions at all levels of monotonic and cyclic loading. Moreover, even though long fully sheathed SWPs were significantly stiffer and stronger, but less ductile than SWPs with openings.

1.5.4. Effect of sheathing thickness

Given the fact that CFS-SWPs designed per the AISI S400-15 provisions, have failure mechanism represented by the inelastic behaviour that develops in the connection zone between CFS frame and steel (or wood) sheathing, resulting from bearing between the sheathing and fasteners and tilting of the fasteners themselves. Therefore, an increase in sheathing thickness results in a higher SWP shear capacity. This assumption has been proved by previous experimental test results [18], where the thicker the sheathing is the better the SWP shear capacity becomes.

1.5.5. Effect of framing thickness

The assumptions given in Paragraph 1.5.4 hold true, however, for steel-sheathed CFS-SWPs, when the thickness of framing and sheathing are closed in value, the measured response was negatively affected as some of the forces were dissipated in form of damage in chord studs [17]. This behaviour should be avoided using framing elements that are thicker than the sheathing steel sheet in order to prevent the collapse of the framing system and to maintain the post-earthquake gravity loading capacity (serviceability). The above described trend is not usually observed in case of wood-sheathed CFS-SWPs, this is due to the fact that the sheathing board dominates the SWP lateral behaviour.

1.6. Hysteresis models that incorporate deterioration

In this section, details of two hysteresis models which, when appropriately calibrated, have been proved to reasonably capture the CFS-SWP response up to the onset of collapse, are described.

1.6.1. Ibarra-Medina-Krawinkler

The original Ibarra-Medina-Krawinkler model [15] is based on a backbone curve that represents the behaviour for monotonic loading and defines the limits for cyclic deterioration modes which are: basic strength, post-capping strength, un- and re-loading stiffness as well as pinching (see Fig. 1.20).

The deterioration algorithm of the modified Ibarra-Medina-Krawinkler model first defines the reference hysteresis energy dissipation capacity of the considered structural element E_t as:

$$E_t = \gamma M_y \theta_y \tag{1.1}$$

Where M_y (F_y) is the yield moment (strength) and θ_y (δ_y) is the yield rotation (displacement) of the considered structural element.

The rates of cyclic deterioration are controlled by a characteristic total hysteresis energy dissipation capacity E_t and an energy-based rule β_i developed by Rahnama and Krawinkler (1993) [29] given by the following expression:

$$\beta_i = \left(\frac{E_i}{E_t - \sum_{j=1}^{i} E_j}\right)^c \tag{1.2}$$

E_i is the hysteresis energy dissipated in the i^{th} excursion, β_i is the deteriorated rate after the i^{th} excursion occurrence and c is an exponent commonly set to unity. In summary, the higher the value of γ, the larger the capacity of the reference hysteresis energy dissipation of the structural element, therefore, the slower the rate of deterioration and vice versa.

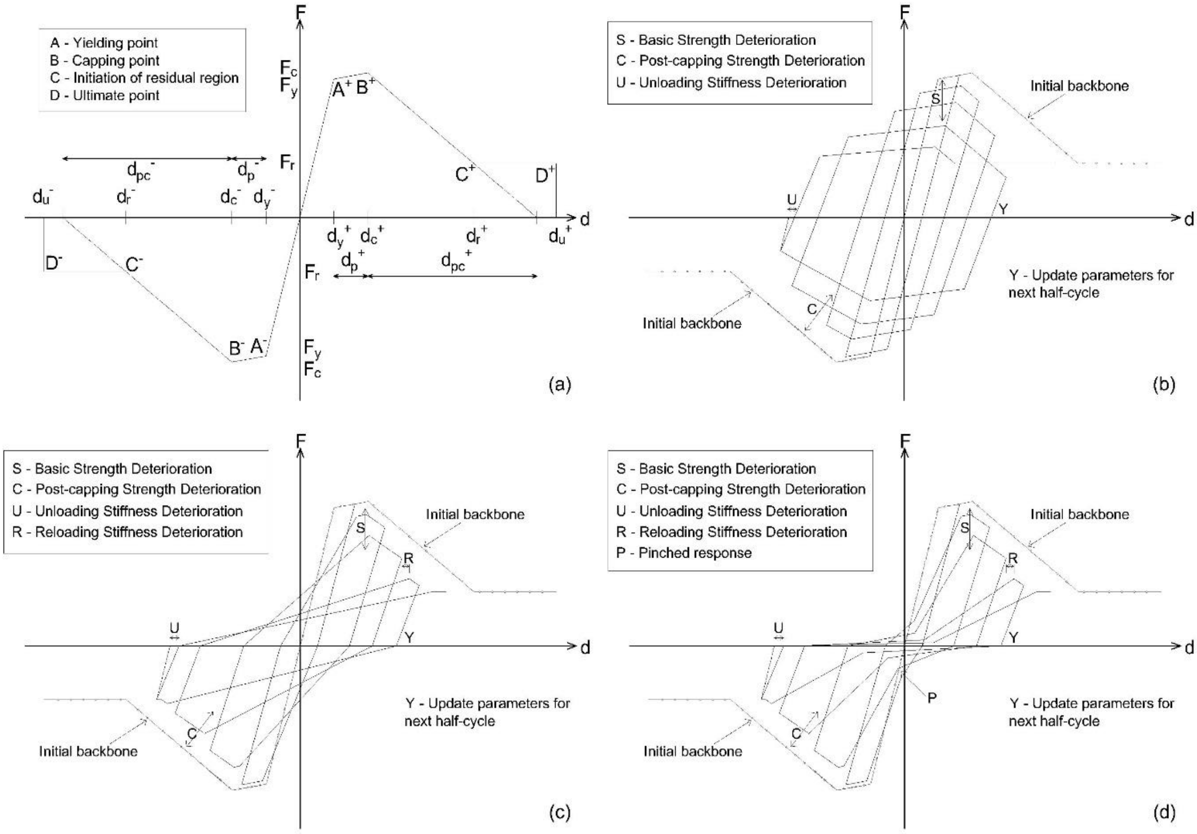

Fig. 1.20. Backbone curve and deteriorating modes of the Ibarra-Medina-Krawinkler model.

In general, a parameter X, which can represent any of the five deterioration modes and can include stiffness or strength parameter, is updated through the following expression:

$$X_i = (1 - \beta_i)X_{i-1} \tag{1.3}$$

The reader is referred to Ibarra et al. (2005) [15] for a detailed description of the model.

1.6.2. Pinching4

The Pinching4 model consists of a multilinear envelop curve (backbone), two trilinear un- and re-loading paths (pinching) and three deterioration rules controlling the evolution of these paths.

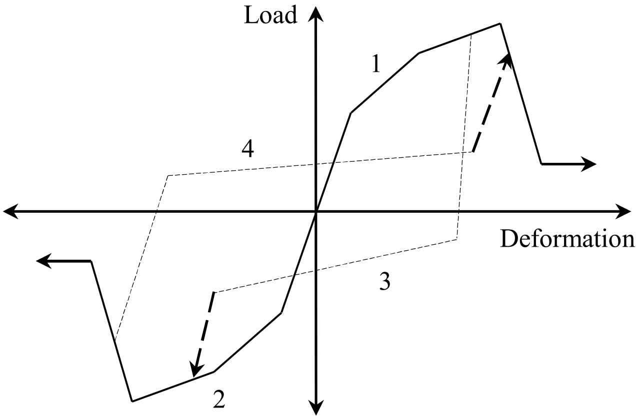

Fig. 1.21. Pinching4 material backbone curve (solid lines) and pinching paths (dashed lines).

a) Backbone curve and pinching paths

Fig. 1.21 shows the four material states that define the Pinching4 model. Load-deformation paths for states 1 and 2 are defined at the beginning of the analysis and modified during the analysis to simulate hysteresis strength loss. For states 3 and 4, the load path is redefined each time there is a deformation reversal. The load-deformation point at which the reversal occurs defines one endpoint for state 3 (state 4); the state 3–state 2 (state 4–state 1) transition defines the other. Two additional load-deformation points define the state 3 (state 4) load path: the point reached once substantial unloading has occurred and the point at which substantial reloading occurs. For state 3 (state 4), the load developed upon unloading is defined as a fraction of the minimum (maximum) strength that can be developed. With the unloading stiffness defined, this establishes the end of the substantial unload phase. The load-deformation point at which substantial reloading occurs for state 3 (state 4) is defined as a fraction of the minimum (maximum) historic deformation demand and a fraction of the load developed at the minimum (maximum) deformation demand. Fig. 1.22 illustrates the connectivity rules which dictate the change of the above described states [30].

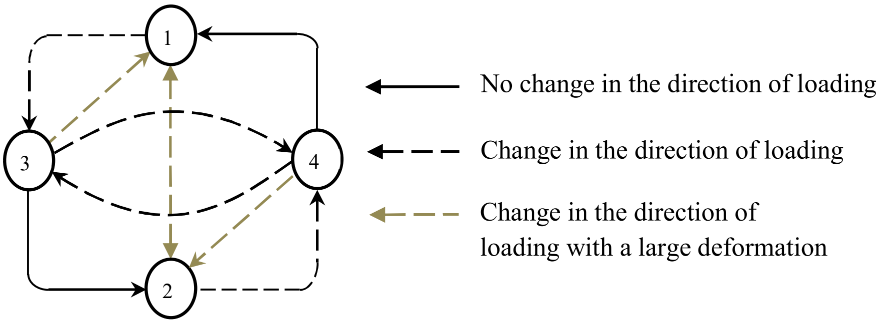

Fig. 1.22. State connectivity.

b) Damage criteria

Due to the irreversible and unrecoverable characteristics of the deterioration of structural components (*e.g.*, reinforced concrete elements) caused by deformation history, three damage rules control deterioration in strength, un- and re-loading stiffness. Fig. 1.23 shows the impact of these three different deterioration modes on the load-deformation response.

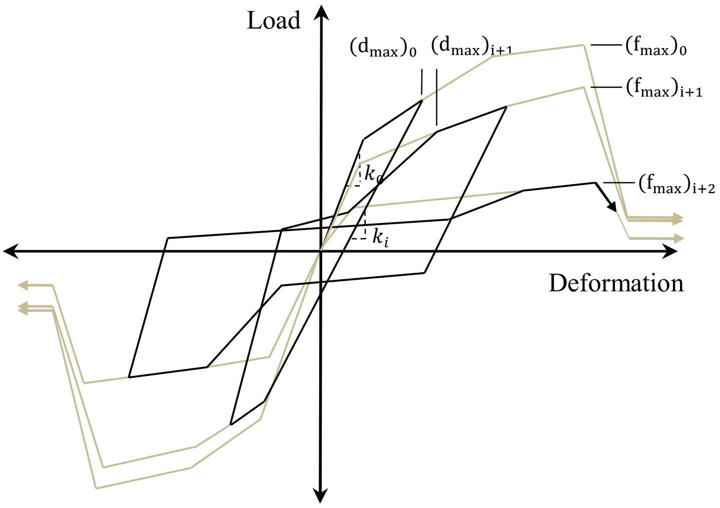

Fig. 1.23. Impact of hysteresis damage on load-deformation response.

Each of these deterioration modes employs a damage index δ proposed by Park and Ang (1985) [31], defined as follows:

$$\delta_i = \left(\alpha_1 (d_{max})^{\alpha_3} + \alpha_2 \left(\frac{E_i}{E_{monotonic}}\right)^{\alpha_4}\right) \le \delta_{limit} \tag{1.4}$$

Where:

$$d_{max} = \max\left[\frac{(d_{max})_i}{ePd_3}, \frac{(d_{min})_i}{eNd_3}\right] \tag{1.5}$$

$$E_i = \int_{\text{Load history}} dE \tag{1.6}$$

$$E_{\text{monotonic}} = gE\left(\int_{\text{monotonic load history}} dE\right) \tag{1.7}$$

Stiffness and strength are assumed to deteriorate due to the imposed load history. The same basic equations are used to describe deterioration in strength, un- and re-loading stiffness:

$$k_i = k_0.\left(1 - \delta_i^k\right) \tag{1.8}$$

Where k_i is the un-loading stiffness at time t_i, k_0 is the initial unloading stiffness (for the case of no damage), and δ_i^k (defined above) is the value of the stiffness damage index at time t_i.

$$d_{\max,i} = d_{\max 0}.\left(1 + \delta_i^d\right) \tag{1.9}$$

Where $d_{\max,i}$ is the deformation demand that defines the end of the reload cycle for increasing deformation demand, $d_{\max 0}$ is the maximum historic deformation demand (which would be the deformation demand defining the end of the reload cycle if deterioration of re-loading stiffness is ignored), and δ_i^d (defined above) is the value of re-loading stiffness damage index at time t_i.

$$f_{\max,i} = f_{\max 0}.\left(1 - \delta_i^f\right) \tag{1.10}$$

Where $f_{\max,i}$ is the current envelope maximum strength at time t_i, $f_{\max 0}$ is the initial envelope maximum strength for the case of no damage, and δ_i^f (defined above) is the value of strength value index at time t_i.

1.7. Probabilistic seismic performance assessment

The foundation of probabilistic structural performance analysis is performance-based earthquake engineering (PBEE) that became an element of standards in the United States in the late 1990s [32, 33]. In PBEE, the realistic nonlinear response of the structure is analysed at several ground motion intensity levels. A specific design option is judged by comparing the expected losses during the lifetime of the structure to the cost of the given design. The so-called first generation PBEE procedures had limited consideration of the inherent uncertainty in the input data and numerical models [34]. Considered uncertainty was typically limited to the probabilistic definition of the seismic hazard.

The Pacific Earthquake Engineering Research Center proposed an advanced performance assessment framework in the early 2000s [35]. The framework is based on four separate processes that provide an explicit and transparent approach to PBEE. The first step is seismic hazard analysis, where the hazard at a given site is described by an intensity measure (IM). The second step is structural analysis; the evaluation of engineering demand parameters (EDPs) such as maximum inter-storey drift or component forces based on the IM that describes the hazard. Damage is expressed as a function of EDPs in the third step, while the final phase calculates the decision variables such as expected loss and risk from the experienced damage.

By 2009, a group of experts developed a procedure for the quantification of seismic performance factors of structures using the above framework for PBEE [6]. The procedure describes structural performance through nonlinear collapse simulation on finite element (FE) models of archetype structures. The archetypes should be designed with the procedure under evaluation and their set shall capture the variability of the performance characteristics of the structural system under consideration. In literature, the procedure is typically cited as the FEMA P695 (ATC-63) methodology (2009), its main components are introduced in Chapter 4.

1.8. Performance-based earthquake engineering in EC8

The seismic design concepts and the specific requirements of EC8 [1] primarily intend to prevent structural collapse. However, failure prevention and the preservation of life should not be the only concerns especially if the earthquake is weaker than the one considered during the design phase. On one hand maintaining the operation of some building types is more important than of others *e.g.*, hospitals, military facilities and schools. On the other hand, in case of more frequent earthquakes, the damages of non-structural members should be prevented making the continuous occupancy possible. The Structural Engineers Association of California (SEAOC) [36] proposed the performance requirements depicted by Fig. 1.24. In the concept of PBEE, four performance requirements are proposed to four seismic action levels defined by their probability of exceedance. In EC8 both the requirements and the action levels are less detailed but the concept in principal correlates with the presented figure. The differences of the importance of the buildings are considered at the definition of the seismic action as the PGA is scaled by the importance factor. For buildings of extraordinary or critical importance 20% or 40% increase of the seismic effect is recommended. In order to reasonably couple the seismic hazard and the performance target, EC8 imposes two fundamental requirements that are approximately indicated by the red dots in Fig. 1.24.

No-collapse requirement: the primary structural members have to be verified that they have adequate strength and ductility so that structural integrity is retained after the seismic action. The reference earthquake associated with this state has a return period equal to 475 years.

Damage Limitation requirement: the structure should withstand earthquakes of smaller return period without extensive damage that may limit the use or the cost-of-which would be disproportionally high. The reference earthquake associated with this state has a return period equal to 95 years.

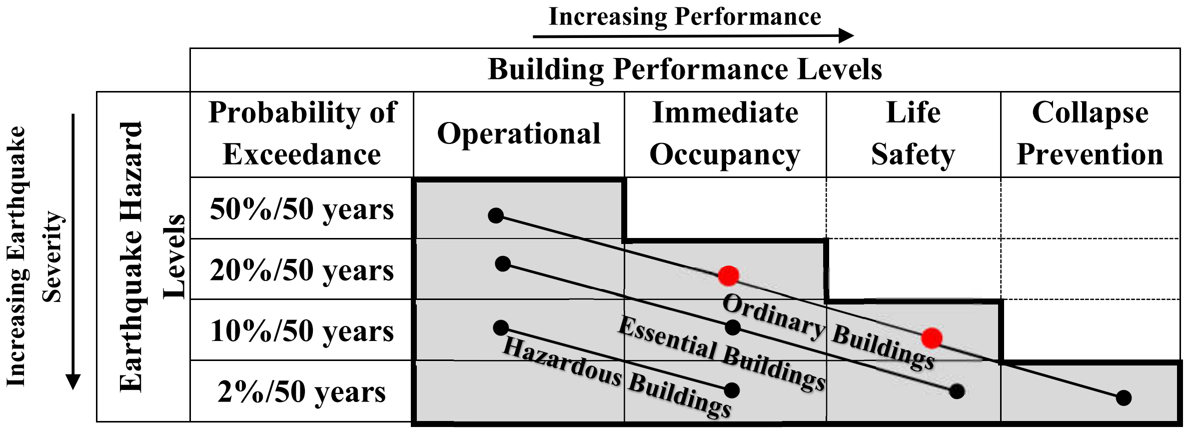

Fig. 1.24. Performance requirements for buildings of various importance.

In the damage limitation design state, performance targets are imposed upon the inelastic relative drifts of adjacent floors *i.e.*, the inter-storey drifts. The main difference between the different requirement levels is whether or not the non-structural elements, the damage of which is intended to be limited, are brittle, ductile or flexibly connected to the primary members. Considering a building with no particular sensitivity of its non-structural elements, the conservative, but for steel buildings commonly used limitation of the maximum inelastic inter-storey drift, d_r is:

$$d_r \upsilon = 0.01h \qquad (1.11)$$

where h is the storey height and υ is the reduction factor considering the lower return period of the seismic effect as d_r is to be computed with the seismic action associated with the no-collapse limit state. The recommended value of the reduction factor for buildings of ordinary importance is $\upsilon = 0.5$, though national annexes may give even less rigorous values *e.g.*, 0.4.

1.9. State of the art in modelling, analysis and design of CFS structures

In this section, details regarding the previous testing and modelling of steel- and wood-sheathed CFS-SWPs, are presented. Previous research studies on the development of seismic design provisions for lateral load resisting systems of CFS framed buildings as well as up to date studies on the design of CFS built-up columns, are critically reviewed.

1.9.1. Modelling of steel- and wood-sheathed CFS-SWPs

Several research activities on CFS have been carried out in North America by Branston et al. (2006) [11], Cheng Yu (2010) [18], Yu and Chen (2011) [19], Nisreen Balh (2010) [17], Liu et al. (2014) [20] and Jamin DaBreo (2014) [21] through quasi-static experimental tests on CFS-SWP as well as a dynamic test program conducted by Shamim et al., (2013) [37] on two-storey SWPs. Many experimental and numerical research activities were also undertaken in Europe with the aim of gaining a deep understanding of the behaviour of CFS components and broaden their use as a new structural solution. Fülöp and Dubina (2004) [38], Landolfo et al. (2006) [39], Iuorio et al. (2014) [40] and Fiorino et al. (2016) [41] performed monotonic and cyclic tests on different configurations of sheathed SWPs and diagonal strap-braced walls. The test outcomes underscored the impact of SWP physical and mechanical characteristics on its hysteresis behaviour. The main parameters which have been identified are: the fastener spacing, the sheathing thickness, the height-to-width aspect ratio and the framing thickness of the panel. As far as the numerical aspect is concerned, many FE models have been developed to simulate the hysteresis behaviour of the CFS-SWP. Nisreen Balh (2010) [17] used Stewart model (1987) [13] which accounts for the pinched behaviour and the stiffness deterioration; however, the strength deterioration has not been considered. Jiazhen Leng (2015) [42] modelled CFS-SWP using Pinching4 hysteresis model based on test results carried out on isolated SWP, then, two-storey CFS framed building was modelled for the assessment of its seismic performance employing the calibrated SWP model parameters. The Bouc–Wen–Baber–Noori (BWBN) (1993) [43] model was used by Nithyadharan and Kalyanaraman (2013) [44] to capture the deteriorating behaviour, in terms of the strength and stiffness deterioration with severe pinching, which has been observed in the screw fasteners between the CFS framing members and the sheathing under cyclic loading. Based on the dynamic tests results of two-storey SWP obtained by Shamim and Rogers (2013) [45], the Pinching4 model has been calibrated. Vigh et al. (2014) [46] presented model development and calibration to tests results through a simplified strut model to represent the CFS corrugated steel-sheathed SWP in global structural analysis. The calibration of nonlinear model parameters to experimental data uses genetic algorithms optimization method. The model allows to capture the monotonic as well as the cyclic performance of the SWP. In order to take into account the simulation of the effect of cyclic deteriorations, the Ibarra-Medina-Krawinkler model is applied. Buonopane et al. (2015) [47] developed and validated a FE model for the simulation of CFS-SWPs using OpenSees software; it consists of beam-column elements for the CFS framing and a rigid diaphragm for the sheathing. The sheathing-to-framing connections are modelled using CoupledZeroLength elements having nonlinear uniaxialMaterial (Pinching4) model which captures the sheathing material damage in the area surrounding the fastener. This modelling technique provides detailed information on forces in the framing members and developed strengths at individual fasteners. David Padilla-Llano (2015) [48] proposed a numerical framework for CFS-SWPs that captures the nonlinear cyclic behaviour of critical components including axial members as well as screw fasteners. Firstly, the cyclic experimental and characterisation of axial members was incorporated into a uniaxialMaterial model which follows the same format of the original Pinching4 model introduced by Lowes and Altoontash (2003) [30] with redefined variables to make damage accumulation independent for negative and positive excursions. Then, nonlinear behaviour in critical components (chord studs) was included in the model developed by Buonopane et al. (2015) [47]. The results from the SWP study highlighted the need to include local buckling behaviour and any other nonlinear behaviour in components when analysing structural systems with thin walled members as it can reveal additional limit states and failure mechanisms that may go unnoticed if not included. All the above mentioned hysteresis models have parameters which are depending on the conditions and results of the experimental tests and do not refer explicitly to the physical and mechanical characteristics of the CFS-SWP.

Besides, Martínez and Xu (2010) [49] developed a simplified approach for analysing CFS framed buildings using FE method where the SWP is modelled by a 16-node shell element having equivalent material properties. The nonlinear behaviour of SWP is characterised by a stiffness deterioration factor which is a function of the spacing of sheathing-to-framing screw fasteners located at the edge of the SWP. However, with no un-loading and re-loading paths defined, the latter could merely be used for a pushover analysis (monotonic loading) rather than a nonlinear dynamic or cyclic loading analysis.

1.9.2. Seismic design provisions for CFS structures

Over recent years, researchers have carried out several experimental and numerical studies aiming at evaluating the collapse safety of CFS structures designed according to specific provisions. By conducting nonlinear dynamic analyses, Denise Morello (2009) [50] validated seismic reduction factors and height limits provided in the AISI S213 (2007) [51] (AISI S400-15 today) for wood-sheathed CFS framed SWP with and without gypsum sheathing board. Four-, 6- and 7-storey CFS framed buildings have been designed for two different cities in Canada implementing the equivalent static force method with the ductility (Rd) and the overstrength (Ro) modification factors taken equal to 1.5 and 1.7, respectively. Using the ATC-63 Federal Emergency Management Agency methodology FEMA P695 [6], the outcomes showed that the modelled structures exhibited an acceptable seismic performance. Nisreen Balh (2010) [17] adopted the FEMA P695 methodology to assess a seismic design procedure for steel-sheathed CFS-SWP frames; it has been shown that the initial test-based seismic force modification factors were not able to provide an acceptable level of safety against collapse. Subsequent analyses conducted by the same author resulted in a recommendation of Rd value of 2.0 and Ro value of 1.3. A maximum height limit of 15 m was also recommended. Jamin DaBreo (2012) [21] carried out dynamic analyses on a 2-storey CFS framed building model to validate the test-based seismic force modification factors for ductility, Rd=2.0, and for overstrength, Ro=1.3 following a methodology adopted from FEMA P695, where the acceptance criteria set, given in this document for assessing response modification factors, were not met. More recently, and based on shake table test results, a numerical study has been undertaken by Shamim and Rogers (2015) [52] to evaluate the seismic performance of 2-, 4- and 5-storey CFS framed buildings with steel-sheathed SWP. The authors did not account for the strength deterioration due to repeated cycles in the modelling of the CFS-SWP, which led to recommended values of Rd=2 and Ro=1.3. Further investigation on the inclusion of non-structural gypsum sheathing boards showed that they could increase the collapse limit of buildings. It is worth noting that all the above-described studies have been carried out to provide seismic design provisions for CFS-SWP frames specific to Canada. Vigh et al. (2013) [16] evaluated the seismic performance factors for a newly proposed CFS corrugated steel-sheathed SWP for use in midrise residential and commercial CFS framed buildings. The archetype buildings evaluated in the study, which were designed according to ASCE 7-10 [53] with a response modification factor (R) equal to 4, met the FEMA P695 acceptance criteria. In Europe, many experimental and numerical research activities on CFS structures were undertaken. Landolfo et al. (2006) [39], Iuorio et al. (2014) [40] and Fiorino et al. (2016) [41] performed monotonic and cyclic tests on different configurations of sheathed SWPs and diagonal strap-braced walls. Fülöp and Dubina (2004) [38], Corte et al. (2006) [54] and Vincenzo et al. (2014) [55] conducted numerical and theoretical studies on sheathed SWPs and diagonal strap-braced walls. Fiorino et al. (2009) [56], Landolfo et al. (2010) [57], Fiorino et al. (2012) [58] and Fiorino et al. (2014) [59] proposed a seismic design method for a 1-storey CFS framed building. Although, some of these studies focused on the seismic behaviour of CFS sheathed SWPs and diagonal strap-braced walls, whilst others allowed the sheathed SWP components to be designed using sub-system level criteria. However, more research work on the use of advanced analysis methods for frames and further investigation of seismic design, for a setting other than the North American one, at the global building level as opposed to simply SWPs, is deemed necessary.

It is noteworthy that in all the above-described works the numerical models were calibrated based on the sub-system level behaviour of the CFS lateral load resisting system. As far as the full structure behaviour is concerned, Kara Peterman (2014) [27] has conducted shake table tests on two full-scale CFS framed 2-storey buildings. The results highlighted the adequate structural performance under seismic loads where the buildings showed to be stiffer and stronger than what they were designed for (sub-system level design). A subsequent numerical study performed by Jiazhen Leng (2015) [42] which addressed the advanced 3D modelling of 2-storey CFS buildings' structure adopting experimental data spanning from fastener to full scale shake table level tests. Based on fragility analyses, similar conclusions as extracted experimentally by Kara Peterman (2014) [27] have been drawn regarding the structural performance where acceptable levels of collapse safety were achieved.

Although a major understanding of the behaviour of CFS structures under seismic loading conditions has been learned, the potential of CFS systems has not been fully evaluated yet in terms of risk assessment, based on a probabilistic method incorporating uncertainties that arise from the occurrence and intensity of earthquakes for limit states probability of exceedance. Therefore, it is deemed necessary to incorporate much of the previous research findings into the context of structural reliability to identify the performance of CFS buildings in seismic regions lacking proper standardised specifications for seismic design and verification.

1.9.3. Design of CFS built-up columns

Built-up CFS sections are often assembled and used in low to mid-rise CFS framed buildings where higher axial capacity or greater local system rigidity is required. They can also be designed as chord studs in CFS framed shear walls. Within the past decade, there has been a push towards studying the behaviour of built-up CFS columns since design rules for these types of members are limited in the current North American cold-formed steel specification AISI S100 (2016) [60] as well as Part 1.3 of Eurocode 3 [61]. A limited set of column experiments with back-to-back CFS channel sections found that the AISI S100 modified slenderness ratio can be conservative and that the end connections are critical for maintaining overall column strength (Stone and LaBoube (2005) [62]). Young and Chen (2008) [63] conducted experiments on built-up CFS sections with intermediate stiffeners and concluded that using the Direct Strength Method (DSM) for calculating nominal local and distortional capacities using single section properties provided reliable and conservative estimates; composite action was not significant in their tests.

Other experimental tests, conducted in parallel with numerical analysis at KU Leuven in a large research thrust, on various types of built-up CFS column cross-sections using Z-shaped studs have been completed (Georgieva et al. (2012) [64, 65]). Axial capacities were compared with DSM-based equations, calibrated to account for buckling interactions. Similar testing of varying cross-sections and DSM calibration was completed by Jiahui Zhang (2014) [66] at the University of Hong Kong, and efficient attempts to model web interconnections are explored. Also from the same research group in Hong Kong, the behaviour and strength of built-up beams with back-to-back and box-section types made with varying screw arrangements, web perforations and intermediate stiffeners were studied; parallel numerical models were completed and DSM design approaches were proposed. Global-local buckling interactions were closely observed and studied in Loughlan and Yidris (2014) [67]. Anbarasu et al. (2015) [68] conducted similar experimental and numerical analyses on battened built-up CFS columns and assessed the conservatism of two DSM approaches, while also closely studying local and global deformations. Dabaon et al. (2015) [69, 70] also conducted experiments and numerical analyses on pin-ended, back-to-back battened columns, concluding that AISI provisions are non-conservative for specimens failing in local buckling and conservative for those failing in flexural buckling. Reyes and Guzmán (2011) [71] tested 48 weld-connected "box" sections and showed that the modified slenderness ratio of AISI S100 (2012) [72] (AISI S100-16 today) is not necessary when the base metal thickness is less than 2 mm and if the seam weld spacing is greater than 600 mm for box sections with any type of end condition tested. Li et al. (2014) [73] completed experimental and numerical analyses of 2 types of built-up CFS sections made with both lipped and web-stiffened channel sections; one type had a back-to-back web configuration while the other was a screw-connected "box" section. They extended existing AISI S100-12 [72] design provisions for flexural and distortional buckling, and offered suggestions for optimal built-up member fastener spacing.

Sheathed built-up columns have not been extensively studied, but work on the axial compressive capacity of sheathed single studs (Luiz Vieira (2011)) [74] has been completed with emphasis on sheathing-braced design and quantification of both local and diaphragm stiffnesses for foundation springs used in elastic buckling analyses. Ye et al. (2016) [75] conducted 16 full-scale single and "I" section built-up column tests with OSB sheathing and observed a prevalence of local and flexural-torsional buckling deformations, which are not accounted for in current design codes; these results are mostly confirmed by the experimental results reported in this thesis (see Chapter 6).

1.10. Conclusion

In literature, significant campaigns of laboratory testing have been performed on lateral load resisting systems adopted in CFS framed buildings, which includes single- and double-storey shear walls as well as whole CFS framed building shake table tests. Results of these tests have served the identification of the SWP response, which is strongly influenced by the behaviour of the sheathing-to-framing screw fasteners which is in turn characterised by strength and stiffness deterioration as well as pinching.

Currently, the North American Standard for Seismic Design of Cold-Formed Steel Structural Systems “AISI S400-15” represents the main reference for the lateral design of this type of structures, where the design guidelines for SWP are based on data obtained from quasi-static tests carried out under both monotonic and reversed cyclic loading protocols. While many studies have investigated the cyclic behaviour of individual SWPs, the dynamic demands on the structural system, under various seismic hazard levels, needs additional studies in order to enable engineers to practice seismic performance-based design and to spur innovation in the seismic design of CFS framed buildings. In addition, modern seismic design requires the establishment of proper seismic performance factors, such as response modification factor, displacement modification factor and system overstrength, which are needed in design. Since these factors are related to the performance of the overall building, they cannot be obtained directly from experimental tests of individual SWPs, but nonlinear dynamic analysis of the whole structure would be necessary where accurate modelling tools are needed. Several numerical works have been carried out by researchers with the objective of evaluating seismic design provisions and deriving seismic performance factors for CFS structures, in the context of American and Canadian design practice, following the FEMA P695 methodology. However, assessment of the results in accordance to European standards would require the adaptation of each component of the methodology to the European environment. Based on our preliminary research, update of the uncertainty (modelling, quality of knowledge, etc.) treatment method, ground motion records and adaptation of the Eurocode safety level into the process, are required.

In the following chapter, proper modelling tools that enable numerical simulation of steel- and wood-sheathed CFS-SWP frames are developed and implemented in OpenSees software. These modelling tools would also open doors, through nonlinear dynamic analyses, for the assessment of seismic design provisions and deriving seismic performance factors.

CHAPTER 2

DETERIORATING HYSTERESIS MODELS FOR COLD-FORMED STEEL SHEAR WALL PANELS

2.1. Introduction

As discussed in Chapter 1, appropriately designed cold-formed steel (CFS) shear wall panels (SWPs) dissipate energy by the inelastic behaviour of its framing-to-sheathing screw fasteners. When subject to repeated cyclic loading, the formed hysteresis loops are characterised by severe strength and stiffness deterioration as well as pinching. These phenomena, which affect most the post-elastic behaviour, must be taken into account in modelling full CFS framed structures for the purpose of performing dynamic nonlinear analyses. The basic requirement to perform such analyses is the availability of a constitutive model capable of simulating as accurately as possible the SWP response when subjected to complex cyclic deformation paths such as those induced by earthquakes.

Although nonlinear models in the Open System for Earthquake Engineering Simulation (OpenSees) software [76] provide significant improvement over simple bilinear representations, there was still room for improvement of numerical CFS-SWP behaviour under realistic dynamic loading. Only one of the built-in materials, Pinching4 [30], supports CFS-SWP behaviour (see Section 1.6.2); the latter has been used in several research studies (Jiazhen Leng (2015) [42], Peterman et al. (2014) [77], Iman Shamim (2012) [10] and Buonopane et al. (2015) [47]) which takes into account both strength and stiffness deterioration as well as pinching. However, it lacks a direct relationship between the physical and mechanical characteristics of the CFS-SWP and its parameters, as well as smooth shaped hysteresis loops. Further to developments undertaken in previous work [78], the abovementioned shortcomings were addressed and new uniaxialMaterial models were elaborated and implemented in OpenSees software version 2.4.5 and above, as user-defined uniaxialMaterials entitled “CFSSSWP and CFSWSWP” for steel- and wood-sheathed CFS-SWP, respectively. The accuracy of the proposed models is then revalidated against experimental results obtained from the literature and the effect and sensitivity of the main analytical parameters of the models have been parametrically examined.

2.2. Hysteresis models development

Smooth round shaped hysteresis models for steel- and wood-sheathed CFS-SWP, based on the model proposed by Lowes and Altoontash (2003) [30] that takes into account strength and stiffness deterioration with pinching, have been developed. The uniaxial hysteresis models of steel- and wood-sheathed CFS-SWP consist of three parts: backbone curve of the hysteresis loops (states 1 and 2), hysteresis criteria (un- and re-loading paths: states 3 and 4) and deterioration criteria (Fig. 2.1). The following sections will respectively introduce the expressions of the three parts.

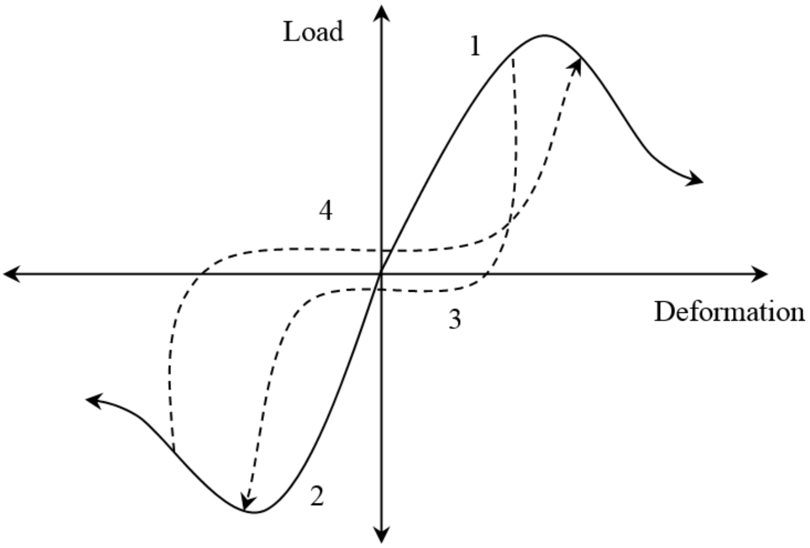

Fig. 2.1. Uniaxial hysteresis model states.

These models can represent characteristics observed in experiments such as the response at time/instance that depends not only on the instantaneous displacement, but also on its history, such as the input and response at earlier times.

2.2.1. Backbone curve

Maximum lateral shear strength and the associated displacement are assessed using two analytical methods for steel- and wood-sheathed CFS-SWP proposed by, respectively, Yanagi and Yu (2014) [79] and Xu and Martinez (2006) [80] which take into account a wide range of factors that affect the behaviour and strength of a SWP, namely: material properties, thickness and geometry of sheathing and framing, spacing of studs, construction details such as size and spacing of sheathing-to-framing connections.

Equivalent energy elastic-plastic (EEEP) multi-linear model, as shown in Fig. 2.2, is used to determine the key points' coordinates through which the envelop curve passes. This model assumes an envelope curve that is capable of dissipating an equivalent amount of energy as the real shear wall does when it is tested experimentally (equal energy principle: area $A_1=A_2$).

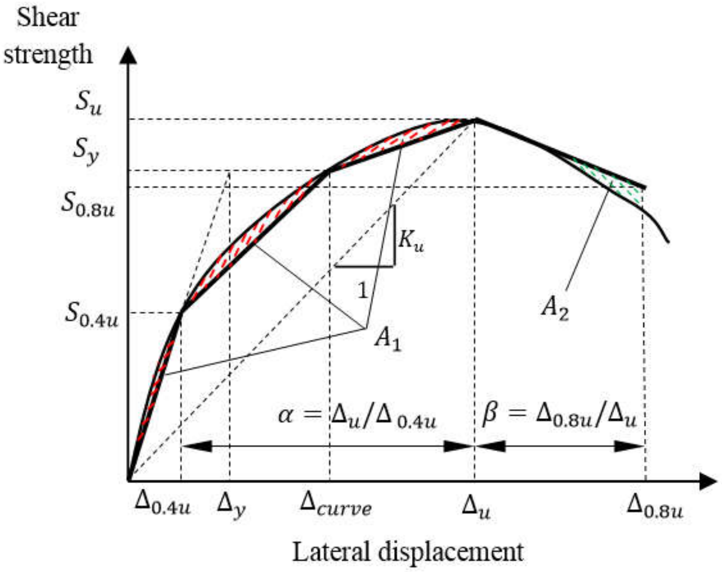

Fig. 2.2. Multi-linear envelope curve.

Where:

- $\mathrm{S_u}$: Ultimate shear strength;
- Δ_u : Displacement corresponding to $\mathrm{S_u}$;
- $\mathrm{S_{0.4\,u}}$: Strength corresponding to 40% of the ultimate shear strength value;
- $\Delta_\mathrm{0.4\,u}$: Displacement corresponding to $\mathrm{S_{0.4u}}$;
- $\mathrm{S_{0.8\,u}}$: Strength corresponding to 20% drop of the ultimate shear strength value;
- $\Delta_\mathrm{0.8\,u}$: Displacement corresponding to $\mathrm{S_{0.8u}}$;
- $\mathrm{S_y}$: Yield strength limit idealised as 85% of the ultimate shear strength value;
- Δ_y : Displacement corresponding to $\mathrm{S_y}$;
- $\mathrm{k_e} = \frac{\mathrm{S_{0.4\,u}}}{\Delta_\mathrm{0.4\,u}}$: Elastic stiffness;
- Δ_curve : Displacement adjusted so that the area ($\mathrm{A_{multi}}$) limited by the x-axis and the multi-linear curve till the failure point is equal to that limited by the experimental curve.

$$\Delta_\mathrm{curve} = \frac{\mathrm{S_y}.(\Delta_\mathrm{u}+\Delta_\mathrm{y}-2.\Delta_\mathrm{0.8\,u}-\Delta_\mathrm{0.4\,u})+\mathrm{S_u}.\Delta_\mathrm{0.8\,u}+\mathrm{S_{0.8\,u}}.(\Delta_\mathrm{0.8\,u}-\Delta_\mathrm{u})}{0.6\ \mathrm{x}\ \mathrm{S_u}} \qquad (2.1)$$

According to the experimental results of tests conducted by Serrette et al. (2009) [81] on CFS-SWPs with wood sheathing attached by pins, the displacement ratio α of the ultimate displacement Δ_{u} to the elastic displacement $\Delta_{0.4u}$ value varies from 8.61 to 10.29, with an average value of 9.25. The ratio β of the failure displacement limit $\Delta_{0.8u}$ to ultimate displacement Δ_{u} varies from 1.0 to 1.63 with an average value of 1.40. Given the similarity between pins and screws nonlinear behaviour, for the simplicity, the author applied the abovementioned factors in SWP with screw fasteners.

Given the key points shown in Fig. 2.2, a curved envelope is adjusted by applying the B-Spline algorithm; this achieves the curvature for the states 1 and 2 of the hysteresis models.

2.2.2. Pinching

In addition to the envelope curve, the proposed hysteresis models require the introduction of parameters that define the strength and stiffness deterioration, as well as the pinching under cyclic loading. On the basis of information deduced from the steel- and wood-sheathed CFS-SWP experimental database, empirical relationships to assess the hysteresis criteria and the deterioration parameters are proposed hereafter.

Experimental results show pinched shear strength-lateral displacement loops. The pinching is caused by the loss of stiffness at the connection level, where a gap or slot is formed around the screw head when the sheathing is damaged; this phenomenon is represented using the uniaxialMaterial models with parameters defined as follow:

- Un-loading stiffness: assumed equal to the elastic stiffness;
- Shear displacements at which re-loading occurs: defined to be 0.448 of maximum historic shear displacement demand in both positive and negative directions;
- Shear strengths at which re-loading occurs: defined to be 0.183 and 0.244 of maximum historic shear strength demand, respectively, in positive and negative direction;
- The ratio of strength developed upon un-loading from negative and positive loads to, respectively, the maximum and minimum strengths developed under monotonic loading: defined to be -0.08.

Based on experimental results [11, 17], the above parameters were determined using median values of deflection points’ coordinates through which the un- and re-loading curves pass, in order to ensure that two important modelling parameters, shear strength-lateral displacement and cumulative energy dissipated, are captured as accurately as possible.

The curvature for the states 3 and 4 is obtained with the monotone cubic spline algorithm as the generated curve always passes through the 4 points defined in the un-loading and the re-loading paths in states 3 and 4 while ensuring the monotony of the curve. When applying the monotone cubic spline, a fifth point is taken into account in order to improve the derivability of the curve when it is attached to the envelope curve (states 1 and 2), this fifth point is added after the last point of the state with a chosen offset of (20, 1) in the positive quadrant and (-20, -1) in the negative quadrant.

The above-defined un- and re-loading paths are shown in Fig. 2.3.

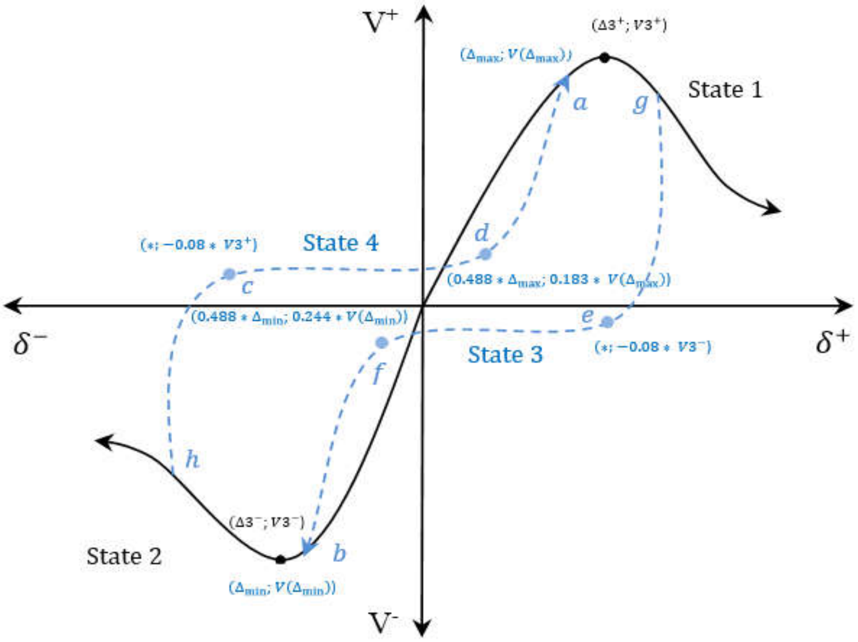

Fig. 2.3. Un-loading and re-loading paths of the proposed hysteresis models.

2.2.3. Strength and re-loading stiffness deterioration

Compared to the monotonic test result, the hysteresis response of wood-sheathed CFS-SWP exhibits strength deterioration (Fig. 2.4a) before reaching the peak strength. This deterioration is attributed to the formation of a gap around the screw head during the first excursion in a given direction which results in a lower strength capacity, simply because we can expect less resistance from crushed wood around the fastener. As far as the steel-sheathed SWP is concerned, this difference in strength capacity was not noticed due to the fact that the failure mode of such a type of wall is initiated by the elastic buckling of steel sheet. Therefore, the cyclic nature of loading enables the SWP to regain its shape which allows the latter to generate the same strength as if it were loaded monotonically (Fig. 2.4b).

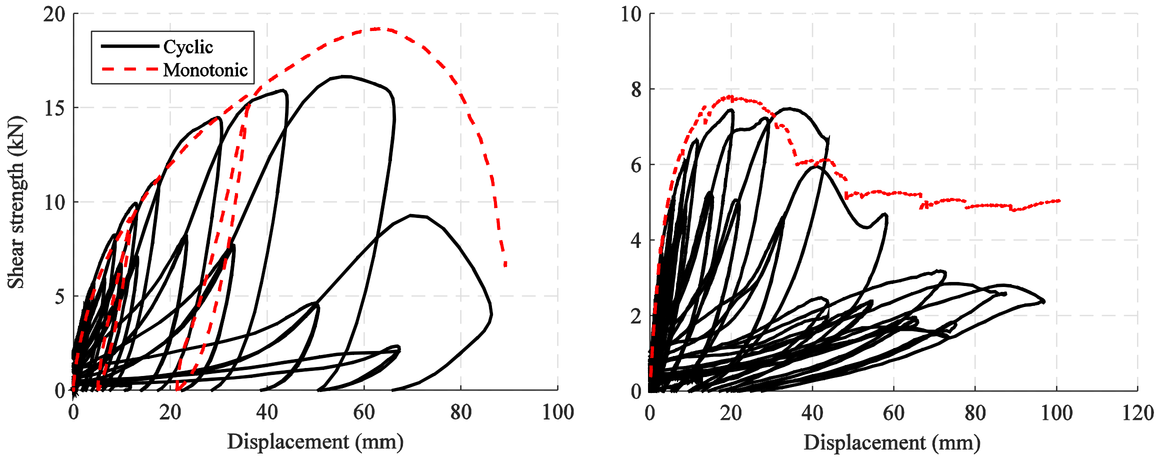

a) b)

Fig. 2.4. Comparison between monotonic and cyclic test results: a) wood-sheathed CFS-SWP tested by Branston et al. (2006) [11], b) steel-sheathed CFS-SWP tested by Nisreen Balh (2010) [17].

Re-loading stiffness values were obtained by fitting a line to the re-loading paths of the cyclic responses. The re-loading stiffness is therefore the slope of segments d-a and f-b as shown in Fig. 2.3. Re-loading stiffness deterioration rate in negative side rapidly increases compared to the one of the positive side of loading direction.

The above described deterioration modes are assumed to occur in the nonlinear domain. However, the CFS-SWP could experience light deteriorations at low displacement amplitudes in the elastic range due to repeated cyclic displacement. The effect of low cycle fatigue is included in CFSSSWP and CFSWSWP by using load cycle counting through the rain flow process. There is also an efficient substitute solution for this phenomenon in the OpenSees software, the Fatigue material developed by Uriz and Mahin (2008) [82] is a wrapper function that can be used on any other uniaxialMaterial to include the effects of low cycle fatigue in its formulation.

The rates of deterioration are related to the physical and mechanical characteristics of SWP as follows:

$$\delta_{i}^{(f/d)+} = \left(\frac{E_i}{10 \text{ x } E_{monotonic}}\right) \leq \delta_{limit} \; \forall \; E_i > E_{elastic} \tag{2.2}$$

$$\delta_{i}^{(f/d)-} = \left(\frac{E_i}{10 \text{ x } E_{monotonic}}\right) \tag{2.3}$$

Where:

$$\delta_{limit} = 0.10 \text{ x } \left(\left(\frac{H}{2.W}\right).\left(\frac{S_c}{152}\right)\right) \tag{2.4}$$

$\delta_i^{(f/d)+}$ and $\delta_i^{(f/d)-}$: strength/stiffness deterioration rate values for the positive and negative excursions, respectively;

δ_{limit} : maximum deterioration rate value in positive direction;

H and W: height and width of the SWP, respectively;

S_c : screw spacing at SWP perimeter;

E_i, $E_{monotonic}$, and E_e: accumulated hysteresis energy, energy required to achieve displacement at failure under monotonic loading, and recoverable elastic strain energy, respectively.

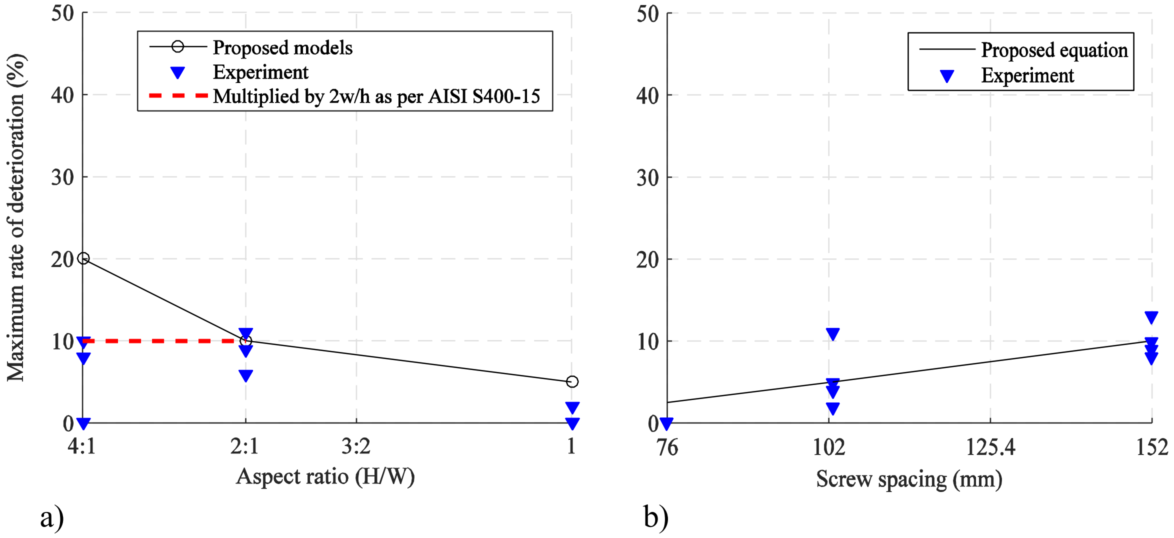

Fig. 2.5. Dependence of strength deterioration rate on: a) aspect ratio and b) edge screw spacing.

The re-loading stiffness deterioration of the proposed models is related to strength deterioration, and is defined in a same way as the strength deterioration.

The strength deterioration was calculated as the positive difference between the initial envelope maximum strength for the case of no damage $f_{max\,0}$ and the current envelope maximum strength at time t_i ($f_{max,i}$). As for the re-loading stiffness deterioration, the latter was calculated as the positive difference between the deformation demand that defines the end of the reload cycle for increasing deformation demand $d_{max,i}$ and the maximum historic deformation demand $d_{max\,0}$ (which would be the deformation demand defining the end of the reload cycle if deterioration of re-loading stiffness is ignored).

The re-loading stiffness and strength deterioration are defined as follow:

$$f_{max,i} = f_{max\,0} \cdot \left(1 - \delta_i^f\right) \tag{2.5}$$

$$\mathrm{d}_{\max,\mathrm{i}} = \mathrm{d}_{\max 0}.\left(1 + \delta_{\mathrm{i}}^{\mathrm{d}}\right) \tag{2.6}$$

Where $\delta_{\mathrm{i}}^{\mathrm{f}}$ is the strength deterioration index, $\delta_{\mathrm{i}}^{\mathrm{d}}$ is the re-loading stiffness deterioration index, and subscripts i and 0 refer, respectively, to load step i (deterioration at time t) and the initial load step (where no damage has already taken place).

2.3. uniaxialMaterial models implementation in OpenSees software

OpenSees is an open source software for finite element (FE) analysis applications in structural and geotechnical engineering. The OpenSees platform is designed around an object-oriented architecture (Fig. 2.6) which facilitates, using existing classes, the development of new components (material, element and/or integrator). Most of its modules are developed on an open-source basis and implemented using C++ programming language.

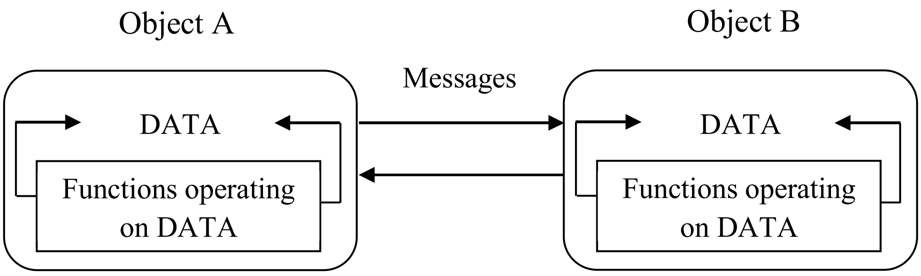

Fig. 2.6. Principle of the object-oriented architecture.

The hierarchical nature of the OpenSees architecture allows new material models to be seamlessly added to the framework by keeping element and material implementations separate. The programming language C++ directly supports the data encapsulation (Fig. 2.6) and run-time binding which are necessary to achieve this complete separation.

Scott and Fenves (2001) [83] documented the procedures of adding a new uniaxialMaterial model into the platform of OpenSees software. As shown in Fig. 2.7, there are three major material abstractions in OpenSees, each of which is a subclass of Material. The Material class is a subclass of both the TaggedObject and MovableObject classes. The TaggedObject class allows materials to be identified through a tag. The MovableObject class allows parallel processing and database programming.

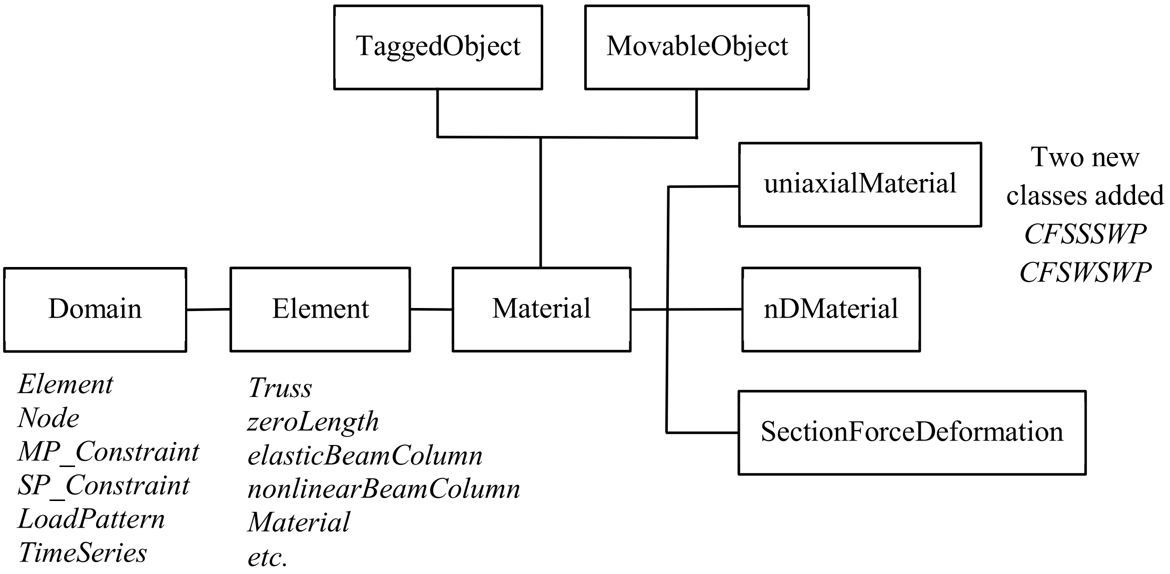

Fig. 2.7. Material class hierarchy.

The proposed hysteresis models for steel- and wood-sheathed CFS-SWP are formulated as user-defined materials named, respectively, CFSSSWP and CFSWSWP using C++ programming language [84] based on the uniaxialMaterial main class available in OpenSees library. OpenSees main program calls CFSSSWP/CFSWSWP class at each material integration point before each load increment. As subjected to a current load increment ΔP, [K] is identified when the resulting structural load converges to the applied load, then the next incremental step initiates. The program flowchart of CFSSSWP/CFSWSWP in OpenSees software is shown in Fig. 2.8.

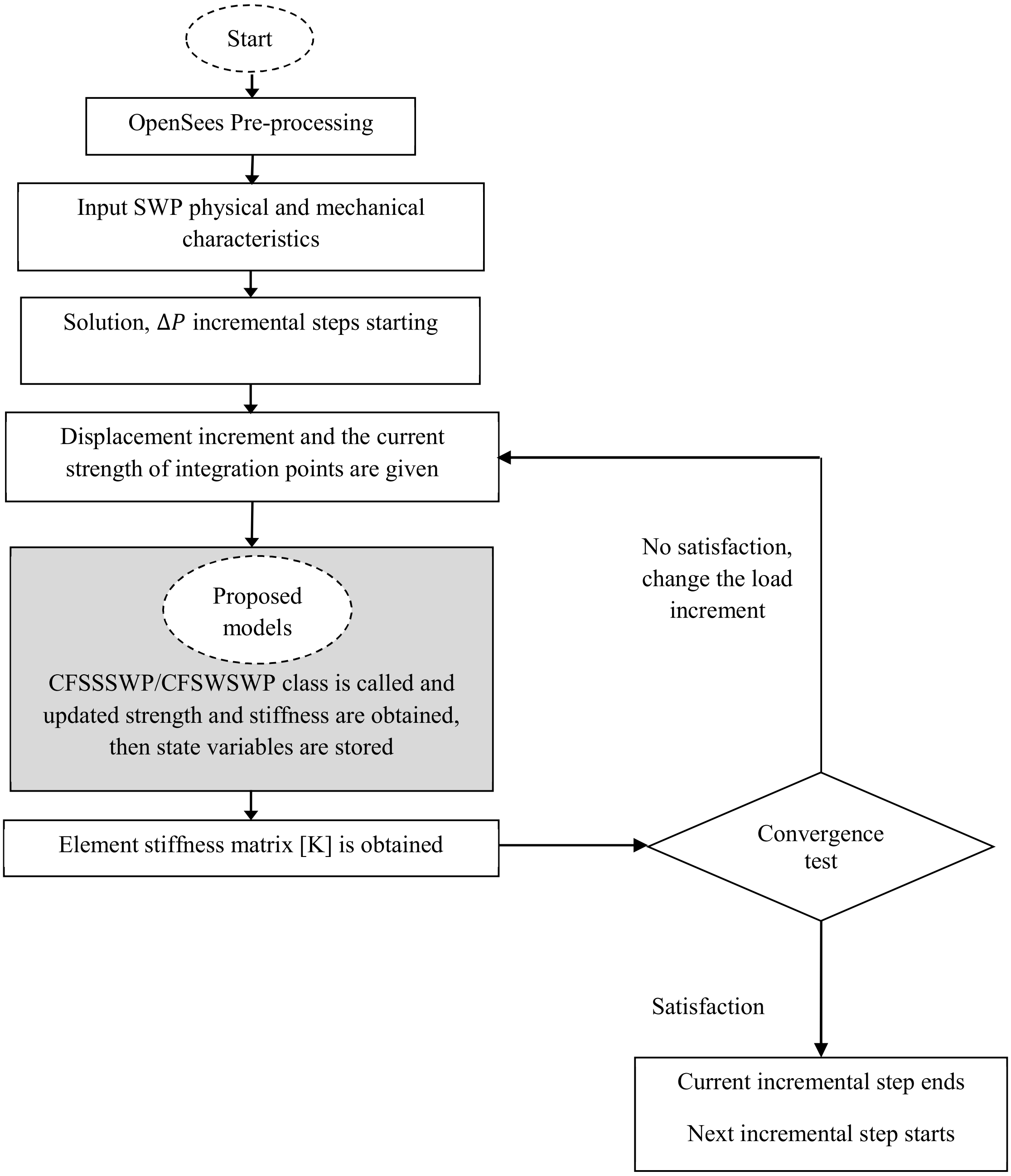

Fig. 2.8. Basic call relations and processes of CFSSSWP and CFSWSWP classes.

Constructor and methods in the uniaxialMaterial class interface

The uniaxialMaterial main class provides default implementations for methods to be used in creating a new subclass material model. However, when the methods are "pure virtual", *i.e.*, "(void)", they must be defined by subclasses because the uniaxialMaterial main class does not provide a default implementation. The methods' declaration in the interface files "CFSSSWP.h and CFSWSWP.h" are provided in Appendix B.

The constructor of the uniaxialMaterial main class takes a tag as its argument and passes it to CFSSSWP/CFSWSWP constructor. The following four methods are pure virtual and therefore they must be implemented in the new uniaxialMaterial subclasses (CFSSSWP and CFSWSWP): *setTrialStrain()*, *getStrain()*, *getStress()*, and *getTangent()*. The method, *setTrialStrain()*, takes an updated displacement vector and defines the state of the CFS-SWP strength-displacement response; the methods *getStrain()*, *getStress()*, and *getTangent()*, return the current displacement vector, strength vector and tangent stiffness matrix, respectively. The method, *commitState()*, is invoked to inform a uniaxialMaterial object that its current state is on the converged solution path and its internal history variables should be updated accordingly; the method *revertToLastCommit()* is provided to let a uniaxialMaterial object know that it should return to its last committed state. These methods are coded in the implementation files "CFSSSWP.ccp and CFSWSWP.cpp" which are provided in Appendix B as well.

Table 2.1 lists and briefly describes the main methods that make up CFSSSWP and CFSWSWP classes. The dependency between these methods is shown in the flowchart of Fig. 2.9. For further details, the reader is referred to Appendix B.

Table 2.1. Methods of the uniaxialMaterial classes CFSSSWP and CFSWSWP.

Class: CFSSSWP/CFSWSWP	
Constructor	
Public: CFSSWP/CFSWSWP (…)	Initialises an object of the class
Destructor	
Public: ~CFSSWP/CFSWSWP (…)	Performs dynamic storage deallocation
Inquiry and access methods	
Public: virtual double getStrain ()	Returns the current converged displacement of the material model
Public: virtual double getStress ()	Returns the current converged force of the material model
Public: virtual double getTangent ()	Returns the current converged tangent of the material model
Public: virtual UniaxialMaterial* getCopy ()	Performs a deep copy of the material object
Private: lateralShearStrength (…)	Computes the ultimate shear strength of the SWP and the associated displacement
Private: SetSpline ()	Defines the curvature that passes through key points of the material model
Public: virtual int setTrialStrain (…)	Sets the displacement demand on the material model
Private: void setEnvelope ()	Sets the initial positive and negative backbone envelope for the material model based upon inputs introduced by the user
Private: void getState ()	Determines the state of the material model based upon the material history and current force demand
Private: double posEnvlpStrength (…) & Private: double negEnvlpStrength (…)	Return positive/negative damaged strength of the material model
Private: double posEnvlpTangent (…) & Private: double negEnvlpTangent (…)	Return positive/negative damaged tangent of the material model
Private: void getState3 (…) & Private: void getState4 (…)	Form the backbone envelop of state 3/state 4 of the material model
Private: double Envlp3Strength (…) & Private: double Envlp4 Strength (…)	Determine the strength of the envelope curve at state 3/state 4 of the material model
Private: double Envlp3Tangent (…) & Private: double Envlp4Tangent (…)	Determine the tangent of the envelope curve at state 3/state 4 of the material model
Private: updateDmg (…)	Updates the damages at a particular state of the material model
Public: virtual int commitState (…)	Commits the history variables of the material model after the state-check has been done
Public: virtual int revertToLastCommit ()	Returns to last committed state in case the analysis fails
Public: virtual int revertToStart ()	Initialisation process for the material model at start
Private: double GetTangentFromCurve (…)	Returns the current tangent of the material model associated with states 1 and 2
Private: double GetTangentFromCurve3(…) Private: double GetTangentFromCurve4(…)	Return the current material model stiffness matrix associated with state 3/state 4
Private: double GetStressFromCurve (…)	Returns the current strength vector associated with states 1 and 2
Private: double GetStressFromCurve3(…) Private: double GetStressFromCurve4(…)	Return the current strength vector associated with state 3/state 4

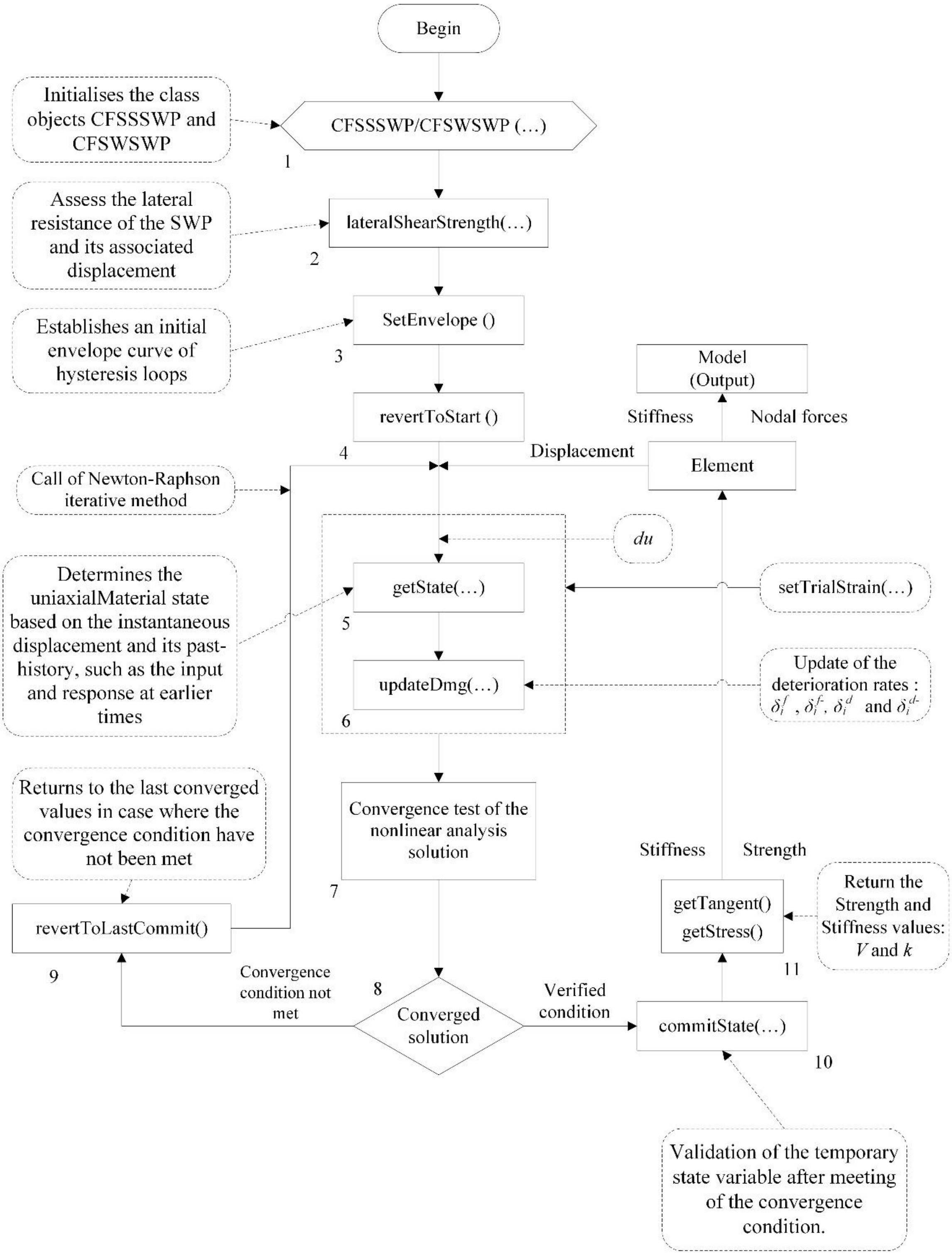

Fig. 2.9. Nonlinear analysis flowchart using CFSSSWP and CFSWSWP uniaxialMaterials.

CFSSSWP and CFSWSWP allow to evaluate the lateral response of steel- and wood- sheathed CFS-SWP, respectively, under quasi-static and dynamic lateral loading. As a first step, the classes parameters are set by the constructor *CFSSSWP (...)/CFSWSWP (...)*; then, the method named *lateralShearStrength ()* is called in order to assess the ultimate shear strength of the SWP and the correspondent displacement.

The development of the envelop curve of hysteresis loops is done by *setEnvelope ()* method. Then, at the beginning of the analysis, temporary state variables are initialised to zero using the *revertToStart ()* method.

The *setTrialStrain (...)* method, at first, records the loading level in terms of displacement (experienced by the element). Then its *getState (...)* method is called to determine the current state of the hysteresis model based on the strength and displacement of the previous iteration, as well as on the load increment *(du)*. An update of the deterioration rate is performed through *updateDmg (...)* method.

If the convergence test condition during a nonlinear analysis is met, the temporary state variables (trial variables) are assigned to the converged state variables; the stiffness and strength deterioration rules are thus applied. Otherwise, solver algorithms keep operating in order to reach numerical convergence.

The stiffness and strength generated by the uniaxialMaterial is provided to the overall FE model using *GetTangentFromCurve (...)* and *GetStressFromCurve (...)* methods, respectively.

2.4. OpenSees finite element modelling and validation of CFSSSWP and CFSWSWP uniaxialMaterials

The programming language Tcl (John Ousterhout (1994) [85] and Welch et al. (2003) [86]) is the basic user interface of OpenSees where FE models are created through a series of Tcl commands that execute the analysis. As shown in Fig. 2.10, users construct their models from the module ModelBuilder and the program adds the related objects to the Domain. In Domain, the program holds the state of the model at each time step. In the meantime, users can exploit a Recorder to register these states for response monitoring purpose. The Analysis module computes the responses of the model as it moves from the current state to the next state.

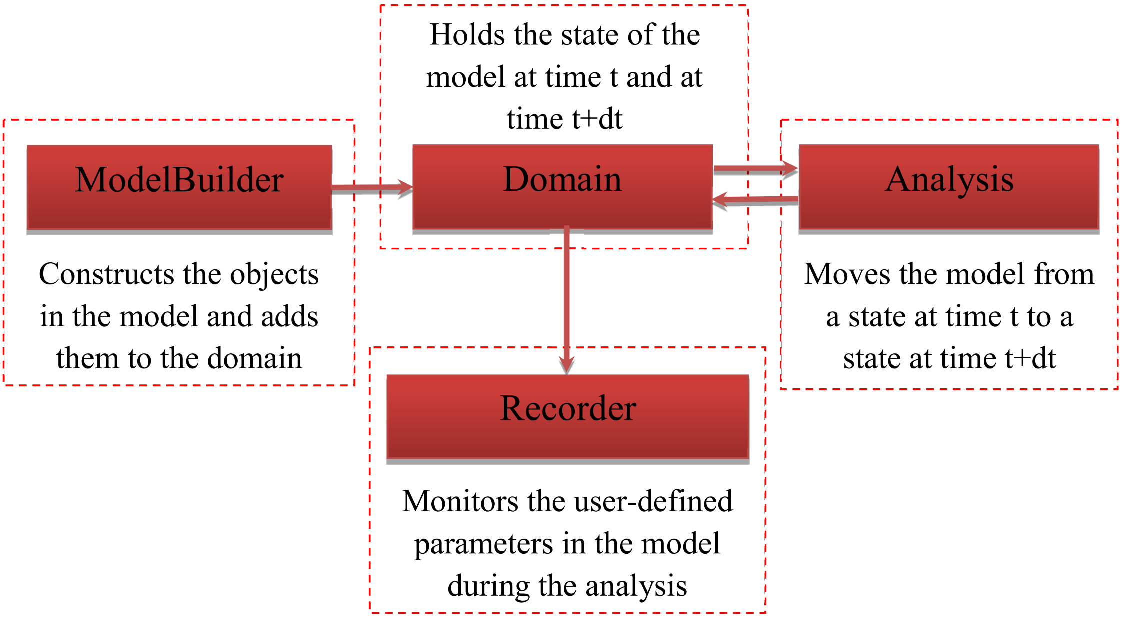

Fig. 2.10. Functional diagram of OpenSees software.

In order to account for the overall lateral stiffness and strength of the SWP, an equivalent simple nonlinear zeroLength element, connected to rigid truss or shell elements which transmit the force to the boundary studs that resist the uniaxial tension and compression stress, is used [87, 88]. This modelling tip leads to a considerable reduction in terms of elements number constituting the SWP. The boundary members form a mechanism and the lateral stiffness and strength are derived directly from the zeroLength element. The SWP components as well as the schematic representation with the element types of the FE model are illustrated in Fig. 2.11.

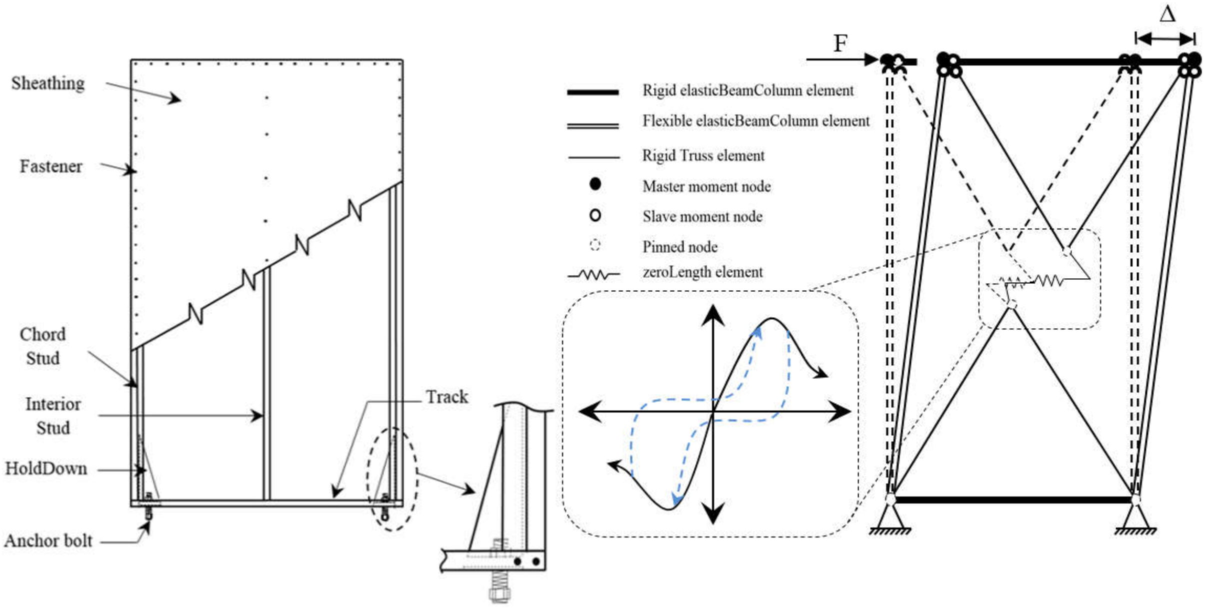

a) b)

Fig. 2.11. CFS-SWP system: a) components and b) OpenSees FE model using concentrated plasticity approach.

In order to check the accuracy of the proposed models, quasi-static nonlinear analyses of CFS-SWPs have been carried out using OpenSees software.

2.4.1. Nonlinear monotonic analyses

Pushover analyses were performed for the sake of comparison between the numerical and experimental monotonic test results. The monotonic loading procedure followed ASTM E564-12 (2012) [89]. As can be seen in Fig. 2.12, a good agreement between the envelope curves of a SWP developed numerically and those derived from monotonic tests [11, 17].

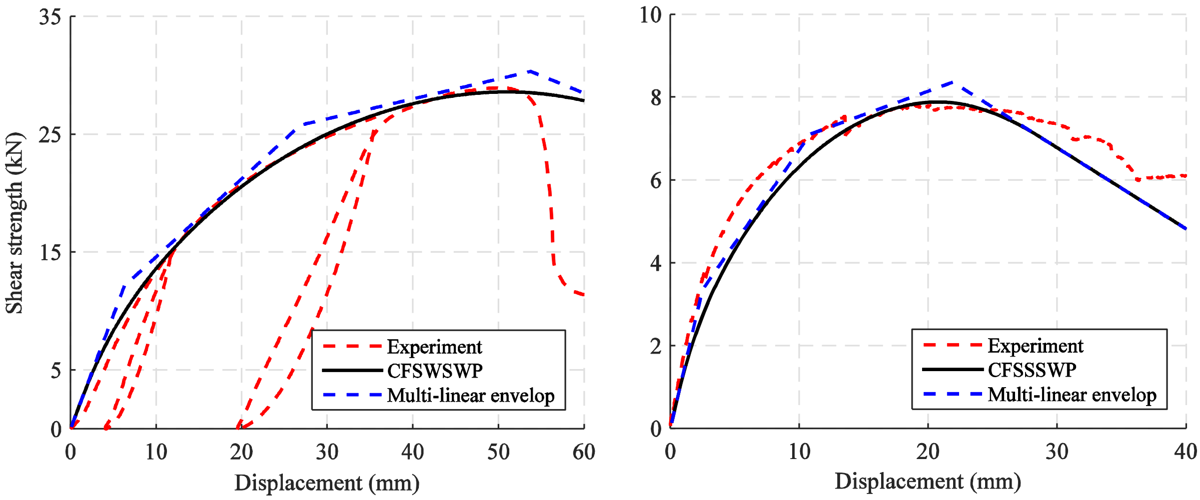

a) b)

Fig. 2.12. Comparison between analytical and experimental monotonic curves: a) wood-sheathed CFS-SWP specimen n° 25 tested by Branston et al. (2006) [11], b) steel-sheathed CFS-SWP specimen n° 1Mc tested by Nisreen Balh (2010) [17].

2.4.2. Nonlinear cyclic analyses

For this purpose, specimens No 12 and No 14 tested by Aaron Branston (2004) [90], specimens No 26 and No 32 tested by Chang Chen (2004) [91], and specimens 1C-b and 3C-a tested by Nisreen Balh (2010) [17] were selected from the literature and analysed under similar loading conditions. This set of specimens covers a range of variation in physical and mechanical characteristics (see Tables 2.2 and 2.3) such as: spacing, number, shear strength, diameter of screw fasteners (s_c, n_c, V_s and d_s); height-to-width aspect ratio (H/W); frame thickness, chord stud moment of inertia, chord stud cross section area, interior stud moment of inertia, yield and ultimate strengths of steel frame (t_f, I_{fe}, A_f, I_{fi}, F_{yf} and F_{uf}); type of sheathing steel/wood, sheathing thickness, yield and ultimate strengths of sheathing (type, t_s, F_{ys} and F_{us}); as well as the anchor bolt diameter of the hold-down (d_t).

Table 2.2. Steel-sheathed CFS-SWP specimens.

Specimen	H/W (mm)	t_s (mm)	F_{us} (MPa)	F_{ys} (Mpa)	t_f (mm)	F_{uf} (Mpa)	F_{yf} (MPa)	S_c (mm)	V_s (N)
1C-b	2440/1220	0.46	395	300	1.14	496	346	150	1560
3C-a	2440/1220	0.46	395	300	0.87	391	342	150	1560

Table 2.3. Wood-sheathed CFS-SWP specimens.

Specimen	H/W (mm)	Type of wood sheathing panel*	Sheathing thickness (mm)	Screw spacing (mm)	Number of screw
12	2440/1220	DFP	12.5	152	50
14	2440/1220	DFP	12.5	76	98
16	2440/610	OSB	11	152	40
26	2440/1220	CSP	12.5	76	98
32	2440/2440	CSP	12.5	102	98

*DFP: Douglas Fir Plywood, OSB: Oriented Strand Board and CSP: Canadian Soft Plywood.

Each SWP was subjected to the Consortium of Universities for Research in Earthquake Engineering (CUREE) protocol with 0.2 Hz loading frequency which is in accordance with the method C in ASTM E2126-12 (2012) [92]. The CUREE basic loading history adopted in this research, shown in Fig. 2.13, includes 40 cycles with specified displacement amplitudes, Δ.

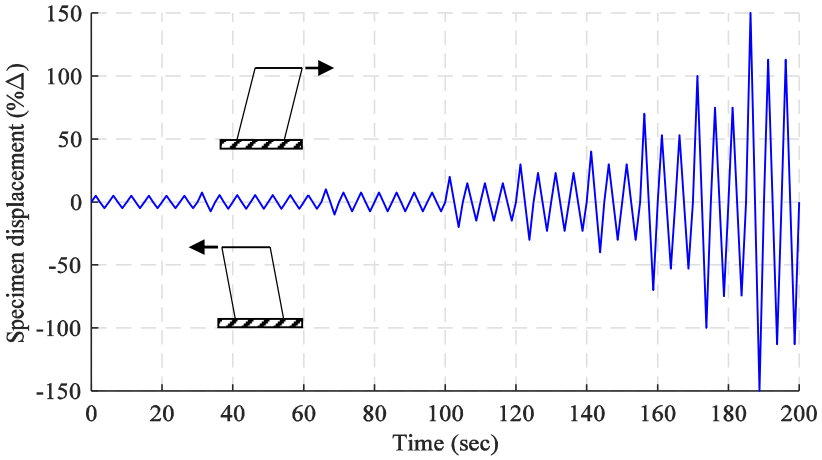

Fig. 2.13. CUREE basic loading history (0.2 Hz).

The specified displacement amplitudes are based on the ultimate displacement capacity determined from the monotonic tests ($\Delta=0.60\Delta_{0.8u}$). If the SWP has not failed at the end of the 40 cycles, additional loading cycles would be added. Each progressive primary cycle added would include an increase of 50% over the previous primary cycle. Two trailing cycles would follow each primary cycle with an added magnitude of 75% of the primary cycle. The large number of various load cycles in the protocol gives essential information for numerical modelling about SWP under different levels of cyclic loading.

The models are assessed by comparing the shear strength-lateral displacement hysteresis curves and the cumulative energy dissipation of the steel- and wood-sheathed CFS-SWP. The results from tests are plotted together with the FE responses of the models in Figs. 2.14 and 2.15.

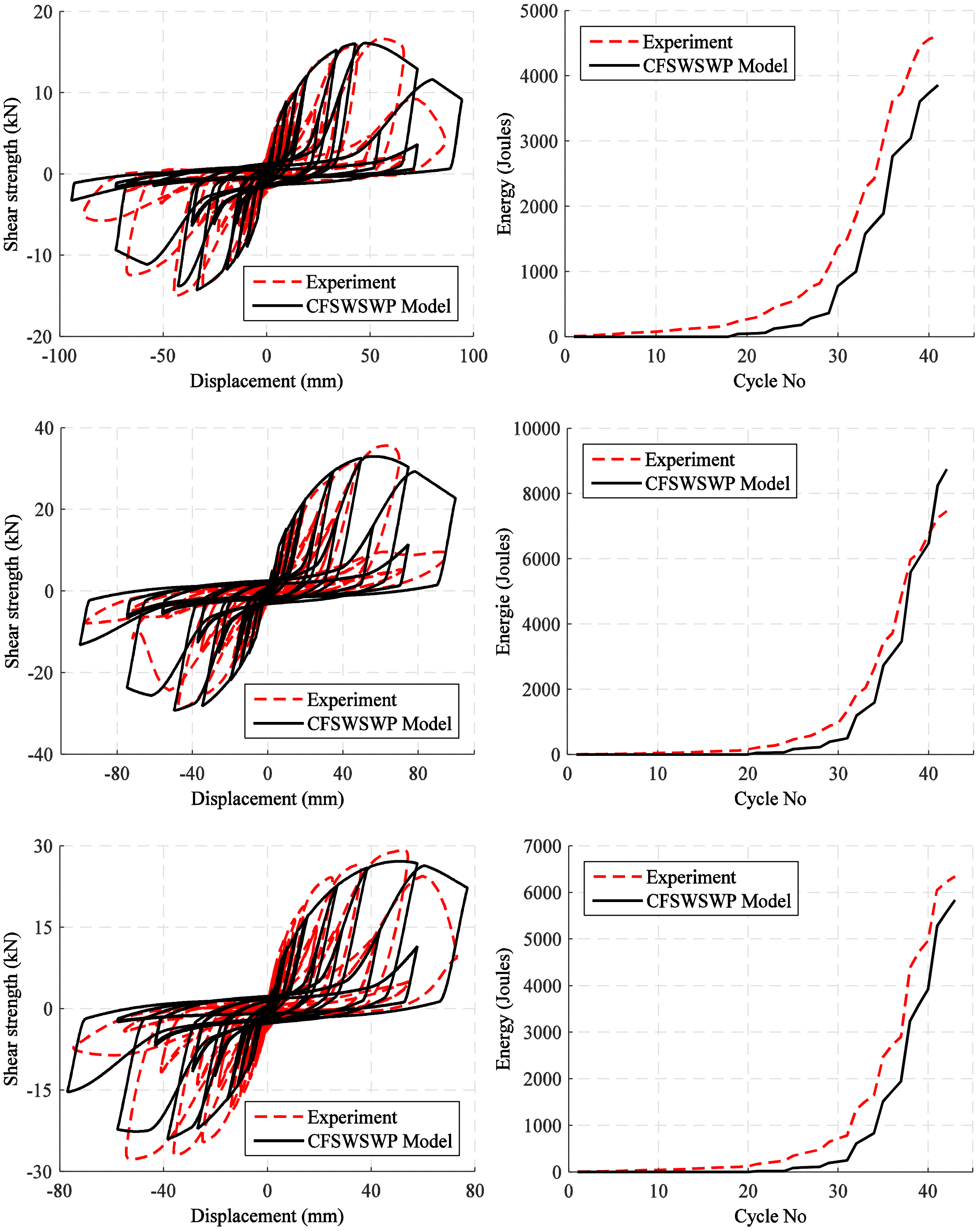

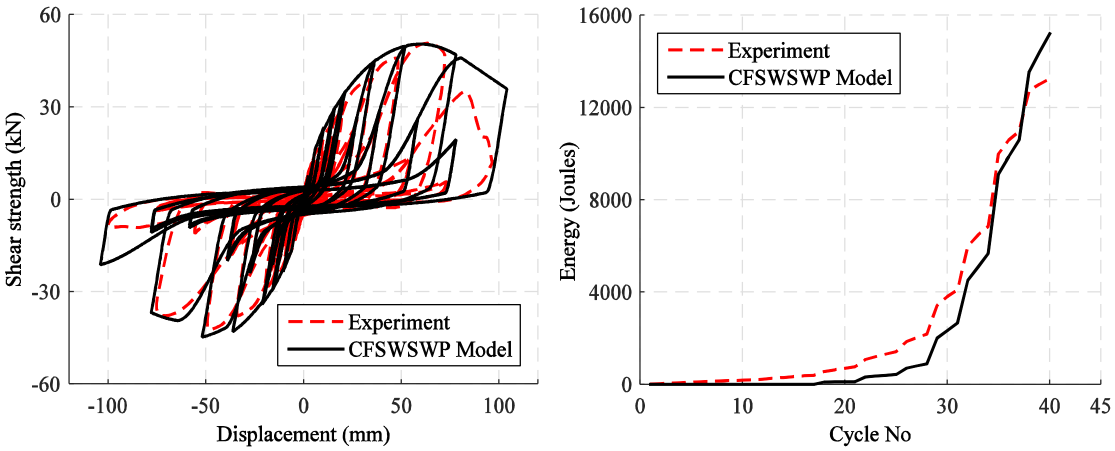

a) b)

Fig. 2.14. Comparison between wood-sheathed CFS-SWP experimental and numerical results (specimens No 12, 14, 26, and 32 [11] from top to bottom): a) Shear strength-lateral displacement, b) Cumulative energy dissipated over cycles.

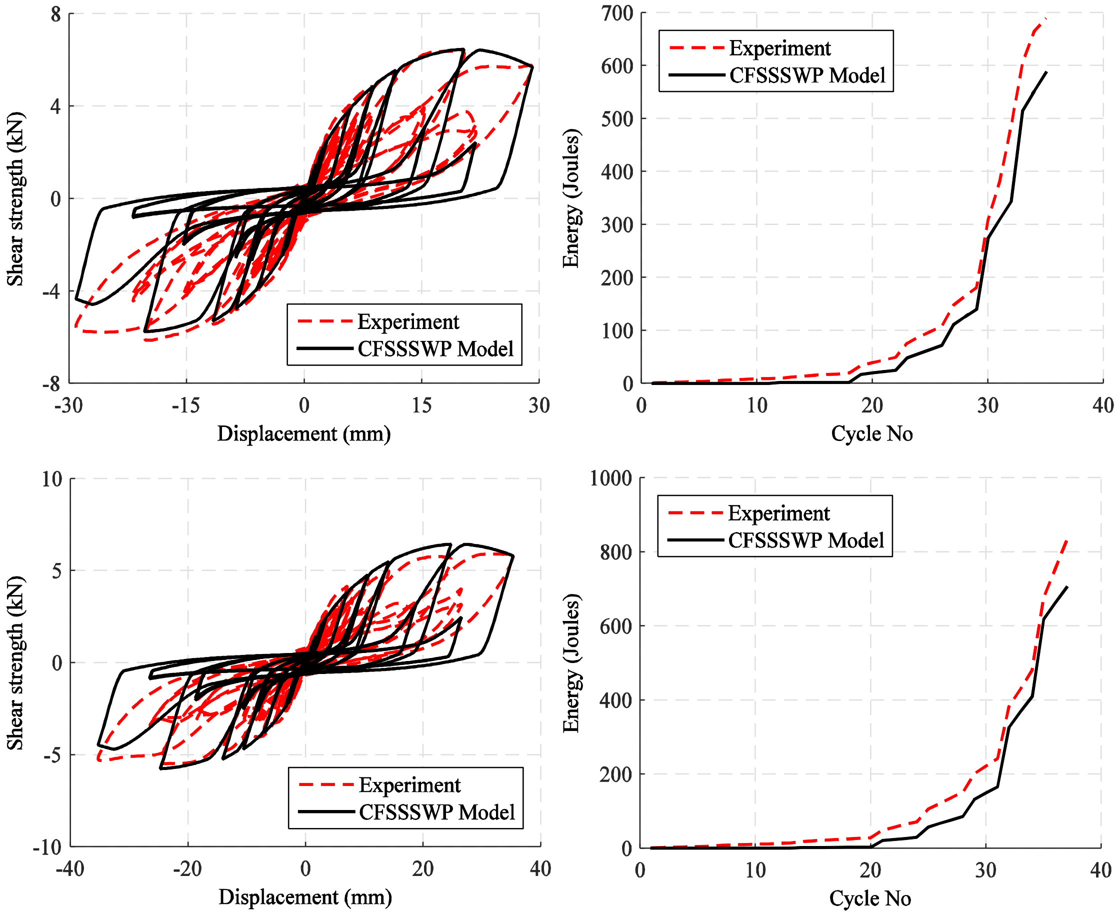

a) b)

Fig. 2.15. Comparison between steel-sheathed CFS-SWP experimental and numerical results (specimens No 1C-b and 3C-a [17]): a) Shear strength-lateral displacement, b) Cumulative energy dissipated over cycles.

a) Shear strength-lateral displacement hysteresis response

In general, a good agreement is observed between the experimental and numerical results (Figs. 2.14a and 2.15a). It is noticed from these figures that the CFSSSWP/CFSWSWP model simulates the fundamental response characteristics of the CFS-SWP, such as: strength and stiffness deterioration, as well as pinching, reasonably well. The positive loops performance of the cyclic response is better than negative ones in terms of strength capacity; this is due to the fact that the SWP is first loaded in the positive direction, hence, the ability of the SWP to resist shear load in the negative side becomes weaker due to the deteriorations experienced during positive incursions (Baushinger effect). This behaviour is well captured using CFSSSWP and CFSWSWP uniaxialMaterials.

Discrepancies in post-peak point at which the specimens experienced a sudden decrease in shear resistance are attributed to the detachment, at the connections of the sheathing from CFS frame. Once the sheathing had become detached from the frame during testing, lateral stiffness and strength of the wall become substantially lower showing no clear trend due to the change in load transfer mechanism in the wall, and hence, the proposed models are not as accurate. Therefore, the main limitation of the proposed models that are not able to simulate the post failure behaviour that has a random trend (inelastic behaviour possibility of chord studs after the exhaustion of CFS-SWP strength and stiffness). Besides, the limited number of laboratory tests continued after the capping point and thus considerable uncertainty associated with the post-failure region of shear strength-lateral displacement diagram is the other noteworthy source of approximation in the work of this thesis.

The ultimate values of the positive and negative strength (F^+ and F^-, respectively) for specimen No 16 tested by Chang Chen (2004) [91] in every complete cycle, as obtained numerically (CFSWSWP model) and the correspondent experimental values are compared and shown in Table 2.4 and Fig. 2.16, respectively. It is observed that during the first 7 cycles of the hysteresis loops (linear elastic range), the CFSWSWP model underestimates the peak strength values by 8% (a good initial elastic stiffness assessment) and for the 14th cycle CFSWSWP model overestimates the peak strength value by around 4%. From cycle n° 21 up to the 38th cycle, the CUREE loading protocol consists of displacement cycles wherein each increase in displacement (primary cycles) is followed by two trailing cycles having amplitudes equal to 75% of the primary cycle's amplitude. During this cyclic loading range, the CFSWSWP model estimates the peak strength values in positive direction of the hysteresis loops with an average error of 6 %. In the same way, in negative direction the CFSWSWP model estimates the peak strength values with an average error of 7 %.

Table 2.4. Comparison of the peak positive and negative force in each cycle from experiment and CFSWSWP model of test specimen No 16 tested by Chang Chen (2004) [91].

Cycle N°	F^+ (kN)		Difference (%)	F^- (kN)		Difference (%)
	Experiment	CFSWSWP		Experiment	CFSWSWP	
7	1.8084	1.7719	2.02	-2.0754	-1.7618	15.11
14	2.1746	2.3139	-6.41	-2.3501	-2.3079	1.80
21	3.0521	3.7254	-22.06	-3.4718	-3.6784	-5.95
25	3.6320	3.8326	-5.52	-4.2196	-3.8074	9.77
29	4.3035	4.4999	-4.56	-4.8071	-4.4224	8.00
32	6.0966	5.9937	1.69	-6.0508	-5.7348	5.22
35	6.7376	6.4981	3.55	-6.3026	-5.8369	7.39
38	6.9512	6.8483	1.48	-5.7075	-5.1146	10.39

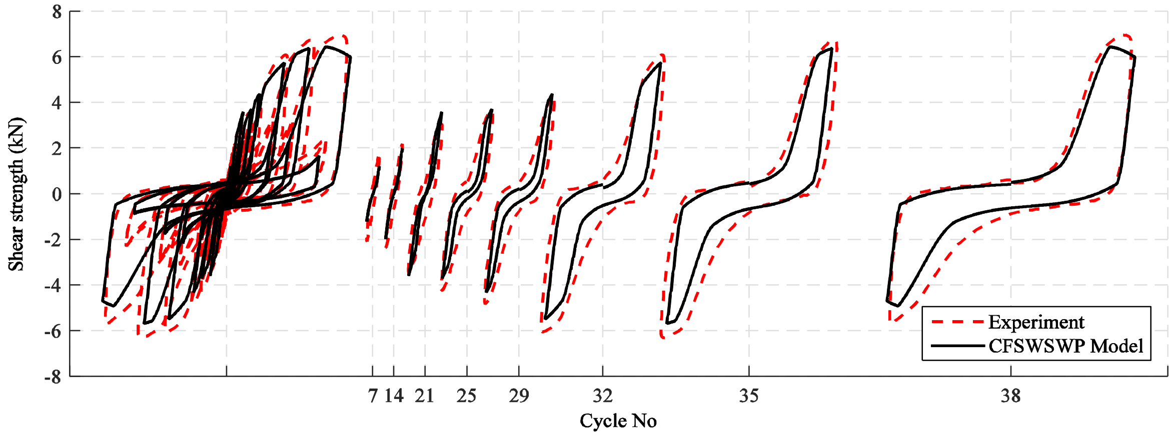

Fig. 2.16. Cycle-by-cycle comparison between experimental and numerical hysteresis loops (specimen No 16 tested by Chang Chen (2004) [91]).

b) Cumulative energy dissipation

Figs. 2.14b and 2.15b show the time histories of the numerical and experimental cumulative energy dissipation of the selected specimens. The simulated results are slightly underestimated compared to the correspondent test results. The differences, fall within a relative average error of 15%, this misalignment is due to the fact that the CFSSSWP/CFSWSWP remains elastic till $\Delta_{0.4\,u}$ (the idealised elastic limit) is attained. In other words, the model does not dissipate energy below this threshold, whereas the experimental test results exhibit energy dissipation at displacement level well below the estimated value of $\delta_e$which is illustrated by an oval shaped hysteresis loops. On the other hand, the numerical model overestimates the dissipated energy during the last cycles after the strength peak has been reached (particularly in the hysteresis loops located in the positive side).

Overall, the CFSSSWP and CFSWSWP model predict the key structural responses of the CFS-SWP subjected to lateral quasi-static loading with an acceptable correlation rate. When the hysteresis model is used in conjunction with the macro-element technique, it offers a powerful tool to model entire CFS framed buildings that run faster with less convergence issues compared to detailed cumbersome FE models. More importantly, is that the parameters of the models are directly input in terms of the physical and mechanical characteristics of the SWP. Thereby, the developed models are validated for use in further parametric studies.

2.5. Model parameters effect on the CFS-SWP lateral response (parametric study)

In order to assess the influence of the parameters related to the proposed hysteresis models, two numerical examples have been taken from previous section, namely; steel-sheathed SWP specimen No 3C-a and wood-sheathed SWP specimen No 26 tested by, respectively, Nisreen Balh (2010) [17] and Aaron Branston (2004) [90] having the following parameters values:

Steel-sheathed SWP: H = 2440 mm; W = 1220 mm; f_{uf} = 391 MPa; f_{yf} = 342 MPa; t_f = 0.87 mm; A_f = 436.22 mm²; f_{us} = 395 MPa; f_{ys} = 300 MPa; t_s = 0.46 mm; n_p = 1; d_s = 4.166 mm; V_s = 1560 N, s_c = 150 mm; d_t = 22.2 mm; opening_Area = 0; opening_Length = 0.

Wood-sheathed SWP: H = 2440 mm, W = 1220 mm, f_{uf} = 344 MPa, t_f = 1.12 mm, I_{fe} = 181600 mm^4, I_{fi} = 51240 mm^4, np = 1, d_s = 4.064 mm, V_s = 3256 N, s_c = 76 mm, n_c = 98, type = 2 (OSB 11mm), opening_Area = 0, opening_Length =0.

A parametric study has been performed by changing the magnitude of each parameter individually one after another, while other parameters are kept constant. Figs. 2.17-2.22 display the effect of each parameter variation (H/W, s_c, Openings, t_s, d_s, and t_f) on the hysteresis loops.

2.5.1 Effect of wall length

Fig. 2.17 shows hysteresis loops of representative SWP specimens which reveal that the wood sheathed specimen is very sensitive to the aspect ratio where the 4:1 wall is characterised by a low shear strength and very pinched loops. The 1:1 and 2:1 walls reached their maximum strength capacity at nearly the same deflection level. However, the deflection of the 4:1 wall was almost twice that of the two longer walls at its ultimate strength position. This indicates that the 4:1 walls are much more flexible than the 1:1 and 2:1 walls due to the higher aspect ratio.

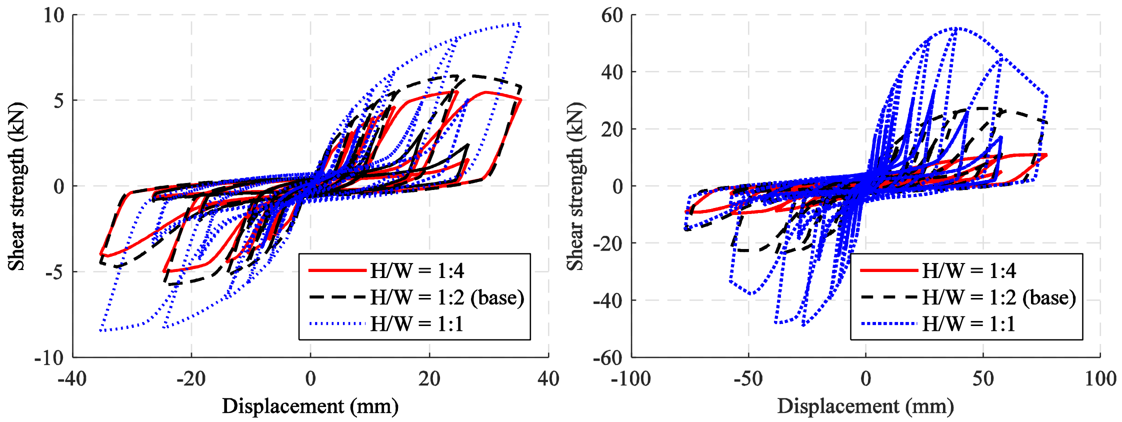

Fig. 2.17. Effect of wall length variation on the hysteresis loops of steel- (left) and wood- (right) sheathed CFS-SWP.

2.5.2 Effect of screw spacing

For both steel- and wood-sheathed CFS-SWP, a steady increase in shear resistance is associated with screw spacing reduction as illustrated in Fig. 2.18. The idealised initial stiffness K_e increases when the screw spacing decreases, however, the variation is not linear and in some cases it decreases when putting additional screw fasteners on the perimeter. It should be noted that ductility values are almost unaffected.

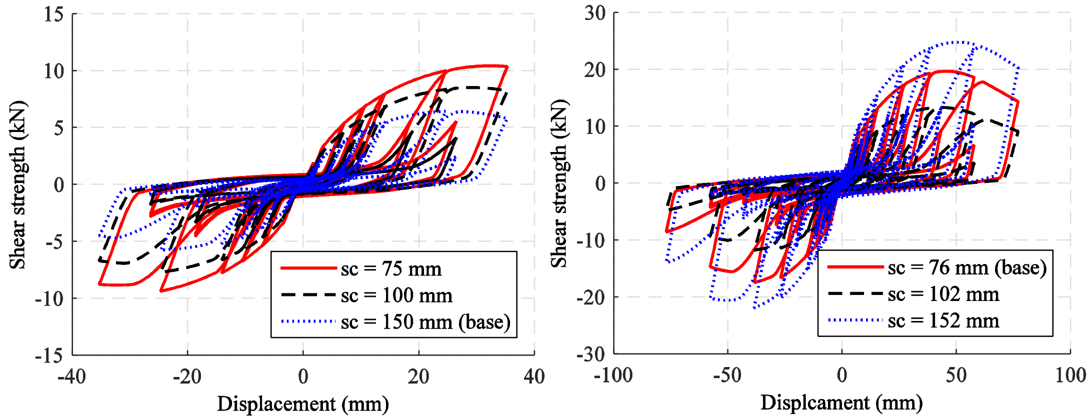

Fig. 2.18. Effect of screw spacing variation on the hysteresis loops of steel- (left) and wood- (right) sheathed CFS-SWP.

2.5.3 Effect of openings

The effect of opening on the steel-sheathed CFS-SWP is relatively significant where 5% and 10% opening ratio (percentage of the wall area) can reduce the elastic stiffness K_e by around 9.1% and 17%, respectively, and the ultimate strength is also decreased by 16.7% and 28.6%, respectively (Fig. 2.19), but ductility values are essentially unaffected. For the wood-sheathed CFS-SWP, the opening effect results in different behaviour where the elastic stiffness is almost unaffected underlying probably the invariance of the overall stiffness of the wood sheathing with opening and the weakening of the strength which decreases about 28% and 45% for 10% and 20% opening ratios, respectively. Ductility values are also faintly affected.

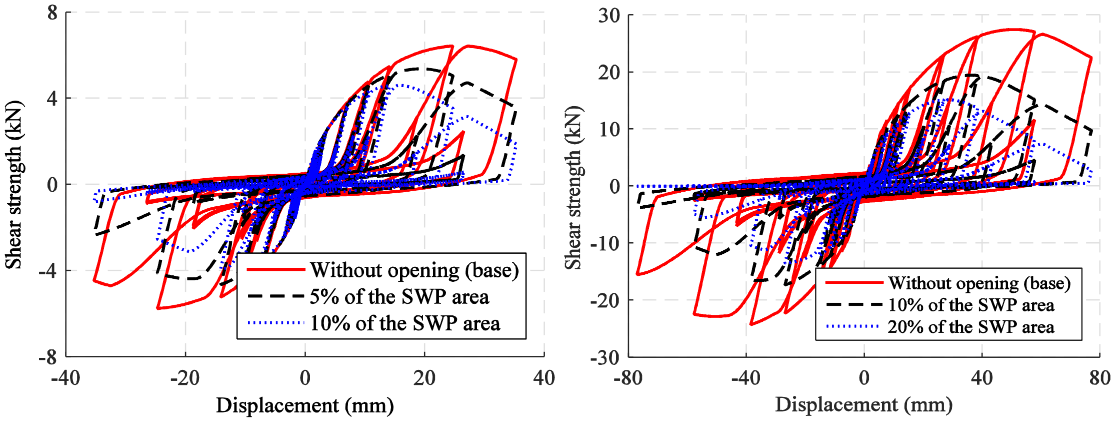

Fig. 2.19. Effect of opening size variation on the hysteresis loops of steel- (left) and wood- (right) sheathed CFS-SWP.

2.5.4 Effect of sheathing thickness

As can be seen in Fig. 2.20 the relationship between the nominal shear strength and the sheathing thickness is almost linear. In this parametric study, sheathing thickness of 0.460 mm, 0.686 mm and 0.762 mm for steel-sheathed SWPs, and sheathing thickness of 10 mm, 11 mm and 12 mm for wood-sheathed SWPs were investigated. It should be also noted that the initial stiffness and the ductility are not affected.

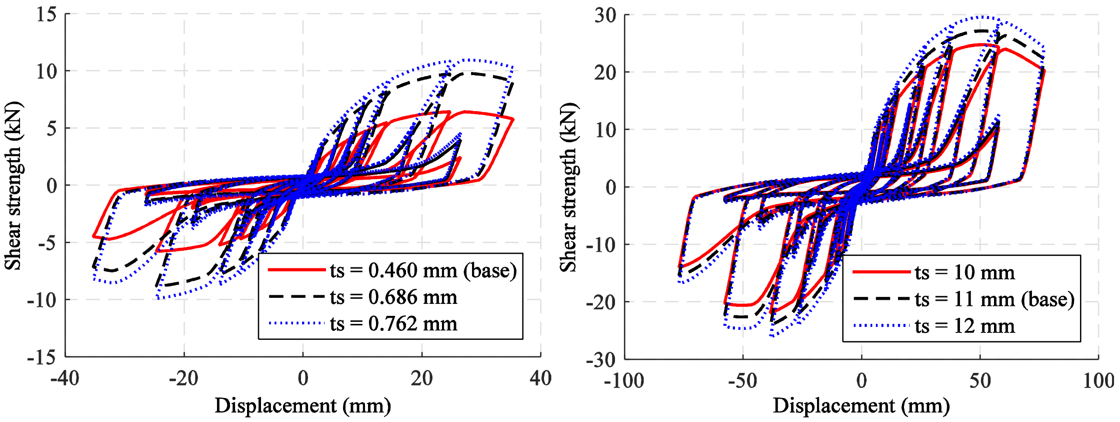

Fig. 2.20. Effect of sheathing thickness variation on the hysteresis loops of steel- (left) and wood- (right) sheathed CFS-SWP.

2.5.5 Effect of screw diameter

In this parametric study, screw diameters of 4.064 mm, 4.828 mm (19% larger) and 5.486 mm (35% larger) for wood-sheathed SWPs, and diameters of 0.460 mm, 0.686 mm (50% larger) and 0.762 (66% larger) for steel-sheathed SWPs were investigated. As can be seen in Fig. 2.21 the relationship between the nominal shear strength and the screw diameter is almost linear. Larger diameters tend to slightly enhance the shear strength of the SWP.

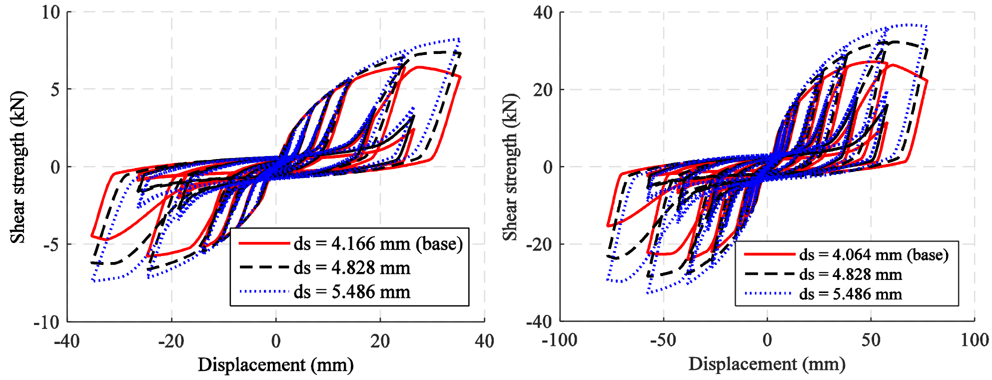

Fig. 2.21. Effect of screw diameter variation on the hysteresis loops of steel- (left) and wood- (right) sheathed CFS-SWP.

2.5.6 Effect of framing thickness

The framing thickness affects mainly the displacement capacity of the steel-sheathed CFS-SWP. As can be seen on Fig. 2.22, thicker framings exhibit shorter maximum displacement. Hence, the SWP having 0.87 mm framing thickness is much more flexible than those having 1.00 mm and 1.50 mm framing thickness. However, no effect was observed on the hysteresis loops of the wood-sheathed CFS-SWP. This is due to the fact that the wood sheathing dominates the SWP lateral behaviour (the assumption that the failure mode is always initiated at sheathing-to-framing connection is verified).

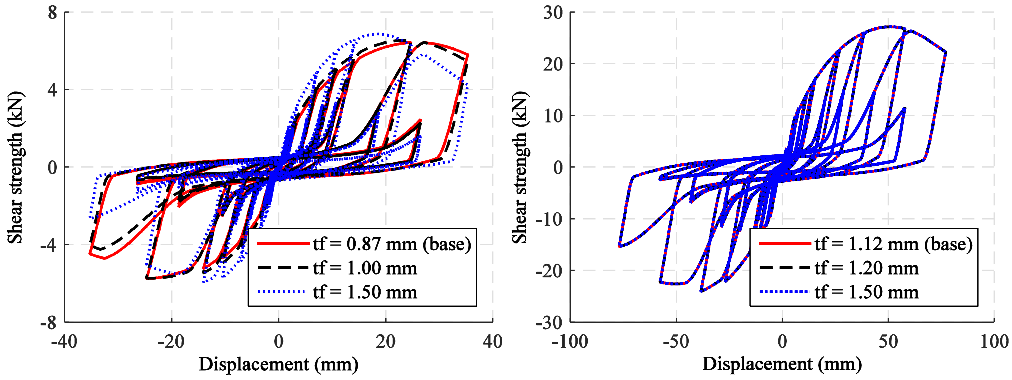

Fig. 2.22. Effect of framing thickness variation on the hysteresis loops of steel- (left) and wood- (right) sheathed CFS-SWP.

The influence of these factors on the lateral strength of a SWP gives a useful insight during the design of SWPs (see Chapter 3), the factors that most affect their lateral strength must be considered so that the strength can be effectively increased. The following are typical modifications that have a major impact on the lateral strength of a SWP: increasing the sheathing thickness, attaching sheathing on the two sides of the SWP (if it is being used only on one side), reducing the spacing of the sheathing-to-framing screw fasteners at the edge of the SWP, and increasing their diameter. The modifications that are considered to have a minor impact on the lateral strength of a SWP include increasing the thickness and depth of the CFS studs and reducing the spacing between studs.

2.6. Sensitivity analysis

Successful modelling requires an in-depth understanding of the model inputs and their sensitivity. In this section, the sensitivity of the main parameters of CFSSSWP and CFSWSWP uniaxialMaterials, is assessed.

Let [Y] be the response of a CFS-SWP for a given loading. Then, each parameter was offseted with -10% to +10% of its original amplitude. Now, if due to the variation of a parameter, say screw spacing (sc), the hysteresis response in terms of shear strength becomes [Y'], then the root mean square error e_{sc} will be as:

$$e_{sc} = \sqrt{\frac{1}{N}\left(\sum_{1}^{N}(Y - Y')^2\right)} \tag{2.7}$$

Where:

N: number of data points for input loading function.

The maximum error relates to the variation of s_c, termed as $| e_{sc} |$ can be obtained by the following expression:

$$| e_{sc} | = \text{maximum}\ (e_{sc}) \tag{2.8}$$

The maximum root mean square (RMS) error associated with each parameter variation is summarised in Tables 2.5 and 2.6. The parameter with the highest magnitude of maximum RMS error is ranked as 1 based on its sensitivity. By plotting the RMS error for any parameter within the range of its variation, spider diagrams are obtained as shown in Fig. 2.23.

Table 2.5. Parameters sensitivity ranking for CFSSSWP uniaxialMaterial.

Parameter	Maximal sensitivity	Ranking
W	0.1691	2
s_c	0.0981	3
t_s	0.0956	4
Opening	0.0801	5
d_s	0.1966	1

Table 2.6. Parameters sensitivity ranking for CFSWSWP uniaxialMaterial.

Parameter	Maximal sensitivity	Ranking
W	7.0720	1
s_c	3.7198	4
t_s	0.0799	5
Opening	4.8682	2
d_s	4.5365	3

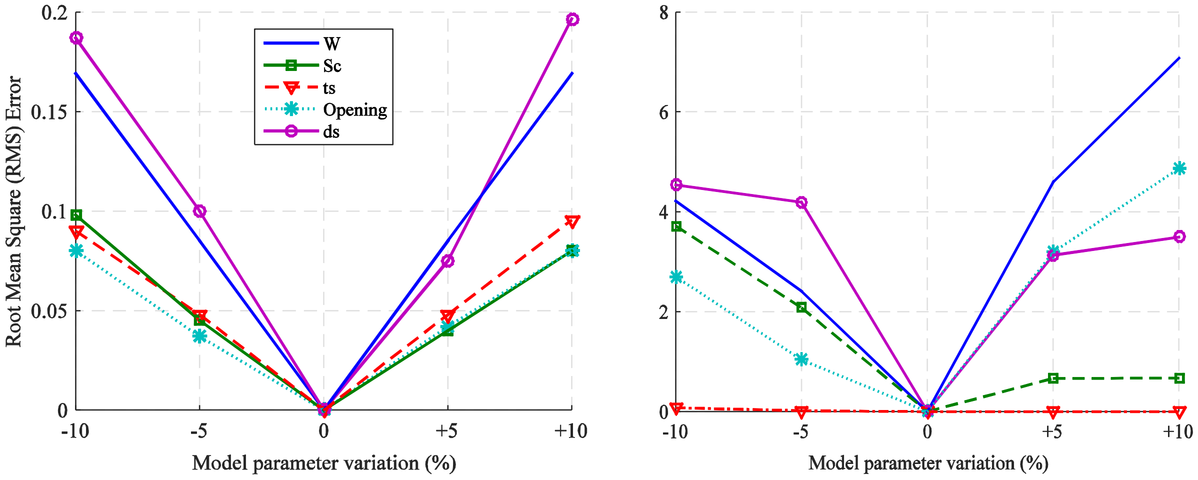

a) b)

Fig. 2.23. Diagram of RMS error versus the percentage of variation of the main parameters of: a) CFSSSWP and b) CFSWSWP uniaxialMaterials.

This sensitivity analysis of the main parameters of CFSSSWP and CFSWSWP uniaxialMaterials is vital especially when it comes to the assessment of the SWP physical and mechanical characteristics. A sensitive parameter when deviated from its nominal magnitude will show a relatively significant error. Thus, by underestimate or overestimate the magnitude of sensitive parameters, better correlation cannot be achieved. On the other hand, less sensitive parameters, even when they are fluctuated from their real magnitude, can produce a reasonable response as their contribution to the final response is relatively less. Therefore, users should focus on the sensitive parameters during the identification process, and as for the less sensitive parameters, they could be attributed standard values provided by the manufacturer without affecting the quality of results.

2.7. Conclusion

Throughout this chapter, analytical approaches to predict the hysteresis behaviour of steel- and wood-sheathed CFS-SWP, were detailed and validated. Two analytical methods have been used for the lateral strength assessment and the correspondent displacement. A multi-linear envelop curve of the hysteresis loops based on the EEEP model was adopted. The hysteresis models incorporate load path dependent (memory effect), strength and stiffness deterioration as well as pinching. The models input parameters are explicitly introduced in terms of the SWP physical and mechanical characteristics. The models have been integrated into the FE software OpenSees version 2.4.5 and above as user-defined uniaxialMaterials. The accuracy and efficiency of the models is validated through a correlation with available experimental results. Subsequently, the influence of the key physical and mechanical characteristics on the lateral stiffness, strength and ductility as well as the shear strength sensitivity, have been investigated. The outcomes revealed the parameters which have most affected the cyclic response such as: height-to-width aspect ratio, edge screw spacing and sheathing thickness.

In summary, the CFSSSWP and CFSWSWP deteriorating models allow the simulation of the asymmetric hysteresis behaviour of steel- and wood-sheathed CFS-SWP, respectively, including different rates of cyclic deterioration in both loading directions. Therefore, these hysteresis models are considered to be reliable for the purpose of the research aims of this thesis.

The proposal of a seismic design and verification procedure for CFS framed structures is the subject of the following chapter.

CHAPTER 3

PROPOSAL OF A SEISMIC DESIGN AND VERIFICATION PROCEDURE FOR COLD-FORMED STEEL SHEATHED SHEAR WALL FRAMES BASED ON EUROCODE APPROACH

3.1. Introduction

The North American Standard code of practice for Seismic Design of Cold-Formed Steel Structural Systems AISI S400 (2015) [2] represents the main reference for the lateral design of this type of structures. The current version of the European code for seismic design, Eurocode 8 (EC8) [1], does not provide any guidance for cold-formed steel (CFS) shear wall panel (SWP) system, which hinders the use of this lateral load resisting system in construction practice. Since most of Algerian codes for construction practice especially the CCM97 [4] (Algerian steel code) is mainly based on the Eurocode 3 [5], a seismic design procedure for CFS framed structures based on existing information, but tailored to fit the Eurocode (EC) requirements would be of paramount importance for future adaptation to the Algerian context.

The main objective of this chapter is to propose a seismic design and verification procedure for CFS framed buildings employing sheathed SWP that can integrate the current seismic design framework of EC8. The approach comprises the definition of a set of design criteria as well as the selection and design of a set of archetype buildings.

3.2. Definition of design provisions and guidelines for CFS framed structures

In CFS framed structures, SWP is the primary lateral load resisting system; it is composed of CFS C-shaped framing members (chord studs, studs and tracks as shown in Fig. 2.11) attached to steel or wood sheathing using screw fasteners. The inelastic behaviour that develops in the connection zone between the CFS frame and the sheathing, resulting from bearing between the sheathing and the fasteners and tilting of the fasteners themselves, is the main mechanism of energy dissipation, providing that inelastic behaviour of the chord studs is prevented through capacity design. This structural component should be designed to provide adequate lateral shear strength and stiffness to the global structure.

Given the fact that EC8 does not provide guidelines for design of CFS-SWP system, in this study the latter is designed, in terms of strength criterion, in accordance with AISI S400-15 [2] adopting Load Resistance Factor Design (LRFD) method, which requires that this system have to resist the shear demand according to the following expression:

$$\phi R_n \geq \text{lateral design factored loads applied to SWP} \tag{3.1}$$

Where:

ϕ: Resistance factor;

R_n: Nominal shear capacity of the SWP.

A reliability analysis was carried out to assess the resistance factor for the ultimate limit state design with a target reliability index, β, of 2.5 following the provisions given in Chapter F of AISI S100 (2012) [72]. For this purpose, the results of 106 wood-sheathed CFS-SWP tests carried out by Branston et al. (2006) [11] have been adopted and the resulted value of the resistance factor, ϕ, was 0.74. On the other hand, the values provided by AISI S400-15 (ϕ=0.65 and 0.60 for wind and seismic design, respectively) are deemed conservative since several research findings, such as those reported by Yanagi and Yu (2014) [79] and Balh et al. (2014) [93] confirmed this conservatism. On the basis of these two works, the authors recommended a value of ϕ equal to 0.70 for sheathed CFS-SWP. Moreover, given the fact that Eurocodes do not provide guidance on the design of CFS-SWP lateral load resisting system, from the author's perspective, it would be more consistent and accurate if the AISI S100-12 standard approach is adopted in calculating the value of ϕ using substantial experimental data rather than directly adopting the standard values of AISI S400-15.

$$\phi = C_\phi (M_m F_m P_m) e^{-\beta\sqrt{V_M^2 + V_F^2 + C_P V_P^2 + V_Q^2}} \tag{3.2}$$

Where:

C_ϕ = Calibration coefficient (1.52 for LRFD);

M_m = Mean value of material factor (1.05);

F_m = Mean value of fabrication factor (1.0);

P_m = Mean value of professional factor (1.0);

e = Natural logarithmic base (2.718);

V_M = Coefficient of variation of material factor (0.1);

V_F = Coefficient of variation of fabrication factor (0.05);

C_p = Correction factor for sample size (1.022);

V_P = Coefficient of variation of professional factor (0.114);

V_Q = Coefficient of variation of load effect (0.21 for LRFD).

The values of M_m, V_M, F_m, and V_F has been taken from Table F1 in AISI S100-12 [72] for wall studs with combined axial load and bending.

The EC8 seismic design provisions require that the designed structure, when subjected to earthquake events, meets strength, drift and stability criteria [94]. According to the European seismic code, two limit states should be verified, namely the damage limitation and the ultimate limit states. With regard to the former limit state, EC8 establishes that inter-storey drifts occurring for a frequent earthquake event should comply with the following expression:

$$d_r \upsilon = \psi h \tag{3.3}$$

Where d_r refers to the inter-storey drift developing for the earthquake intensity corresponding to the ultimate limit state; υ is a reduction factor applied for the smaller, more-frequent, earthquakes associated with serviceability limit state (SLS); ψ is suggested as 0.5%, 0.75% and 1.0% for brittle, ductile and non-interfering non-structural components, respectively, and h refers to the inter-storey height [95]. As for the ultimate limit state, in addition to strength design check, second-order stability effects need to be addressed using the following expression proposed in EC8:

$$\theta = \frac{P_{tot}\, d_r}{V_{tot}\, h} \tag{3.4}$$

In the above expression, P_{tot} and V_{tot} are the total cumulative gravity load and seismic shear applied at the storey under consideration; h is the inter-storey height; and d_r is the design inter-storey drift. In case $\theta < 0.1$, second order effects could be neglected. However, if $0.1 < \theta < 0.2$, the second-order effect may be approximately taken into account by multiplying the relevant seismic action effects by a factor equal to $1/(1-\theta)$ and, in no case, the value of θ shall exceed 0.3 [1]. In this study, the θ coefficient was limited to 0.2.

When the SWP selection satisfies the strength, drift and stability criteria, the latter should likewise meet the overstrength regularity condition in order to obtain a uniform dissipative behaviour along the structure’s height. This proposal is similar to that prescribed in EC8 for concentrically and eccentrically brace frames. In case of buildings with more than 2-storey, EC8 requires that the maximum overstrength factor does not differ from the minimum one by more than 25%, which directly affects the design of the lateral load resisting system. However, this condition in some cases is seldom satisfied since the shear demand that develops in archetype buildings’ top storey is relatively smaller in comparison to the one acting in intermediate storeys. A less stringent limit was set as follows:

$$\frac{\Omega_{\max}}{\Omega_{\min}} - 1 \leq 0.50 \tag{3.5}$$

Where Ω_{max} and Ω_{min} are, respectively, the maximum and the minimum values of the structural overstrength factors for SWPs.

The design of the non-dissipative elements (tracks, studs and chord studs) was carried out according to the prescriptions of Part 1.3 of Eurocode 3 (EC3) [61], applicable to thin-walled members. Cross-section design checks were performed for the vertical members (chord studs as illustrated in Fig. 3.1a), subjected to combined biaxial bending with compression, according to the following expression:

$$\frac{\mathrm{N_{Ed}}}{\mathrm{N_{c,Rd}}} + \frac{\mathrm{M_{x,Ed}} + \Delta\mathrm{M_{x,Ed}}}{\mathrm{M_{cx,Rd,com}}} + \frac{\mathrm{M_{y,Ed}} + \Delta\mathrm{M_{y,Ed}}}{\mathrm{M_{cy,Rd,com}}} \leq 1.0 \tag{3.6}$$

Where:

$$\Delta\mathrm{M_{x,Ed}} = \mathrm{N_{Ed}} \cdot \mathrm{e_{yw}} \text{ and } \Delta\mathrm{M_{y,Ed}} = \mathrm{N_{Ed}} \cdot \mathrm{e_{xw}} \tag{3.7}$$

$\Delta\mathrm{M_{x,Ed}}$ and $\Delta\mathrm{M_{y,Ed}}$: the additional moments resulting from the shift of the centroid in Class 4 cross-sections;

$\mathrm{e_{xw}}$ and $\mathrm{e_{yw}}$: shift of the relevant centroidal axes when the cross-section is subjected to compression only;

$\mathrm{N_{Ed}}$, $\mathrm{M_{x,Ed}}$ and $\mathrm{M_{y,Ed}}$: the design axial force and bending moments about x- and y-axes, respectively;

$\mathrm{N_{c,Rd}}$, $\mathrm{M_{cx,Rd,com}}$ and $\mathrm{M_{cy,Rd,com}}$: the resistance of the cross-section to axial force and bending moments about x- and y-axes, respectively.

Since CFS framing members are generally made of slender cross-sections (Class 4, according to EC3 classification), either the Effective Width Method “EWM” or the more accurate Direct Strength Method “DSM” [60] could be used to evaluate their axial and flexural design strengths in order to take into account the reduction resulting from buckling limit states. Furthermore, based on tested SWPs [37, 96], it was found that the sheathing boards and the blocking elements effectively prevent global and distortional buckling about the minor axis (y-axis) of the built-up I-sections and have an important role in limiting torsion (Fig. 3.1). Furthermore, a study which aims to examine the buckling, peak and post-peak behaviour of sheathed built-up CFS chord studs, with both an experimental and a numerical approach to improve existing design guidelines, is presented in Chapter 6.

The total compression load in the chord studs at each storey is defined as the axial load (compression) induced by the ultimate shear capacity of the SWP at each storey, in addition to the gravity load applied on the tributary area related to the chord stud. The bending moments were determined taking into account the shift of the centroid in Class 4 cross-sections due to the consideration of local/distortional buckling phenomena. It is noteworthy that in case of double-sided sheathed CFS-SWP, the chord stud elements are more stable due to the additional constraint provided by the sheathing boards.

Since the gravity and the tensile loads in hold-downs are in opposite directions, the tensile demand in these elements is calculated using the same approach as for the chord studs but with the gravity load having negative sign.

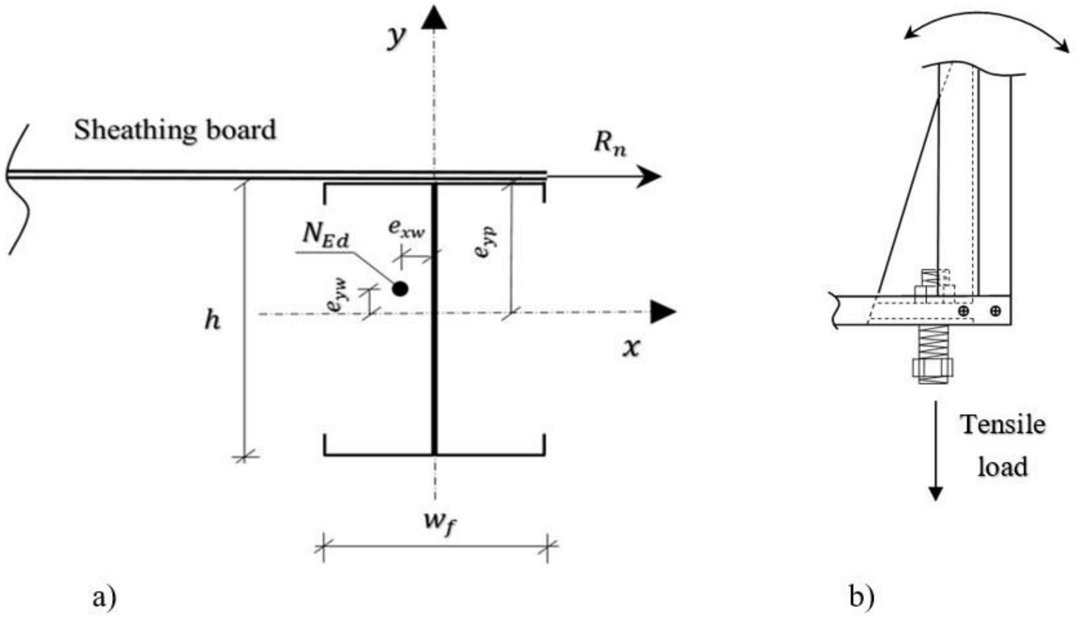

Fig. 3.1. Scheme of forces produced in: a) chord stud of a single-sided sheathed CFS-SWP and b) hold-down element.

Ultimately, the hold-downs and the thickness of plates composing the chord studs should be selected based on a capacity design principle, in such a way to promote the sheathing-to-framing fasteners energy dissipation mode, which is a basic assumption of this research and safeguards the overall integrity of the structure. It is worth pointing out that the stiffness continuity of the chord studs of CFS-SWP system is not considered during the design process; functionally, this results in isolated (type I) rather than coupled (type II) SWPs behaviour according to AISI S213 (2007) [51] commentary. As it will be discussed, this assumption has a major influence on the seismic performance of the structural system.

The diaphragm effect provided by the floor slabs is considered by coupling the horizontal movement of points on the same storey. This approach significantly reduces the seismic load on the tracks; therefore, their design is governed by gravity loading.

3.3. Selection and design of the archetype buildings

3.3.1. Selection of the archetypes

In order to cover a wide range of sheathed CFS-SWP frames structural characteristics, 54 archetypes have been defined. Table 3.1 summarises the parameters used to describe the design space where two levels of gravity load were considered. Three sites located in Portugal, namely Porto (north), Lisbon (centre) and Lagos (south) were assumed to reflect regions of, respectively, low, moderate and moderate-to-high seismicity (Fig. 3.5). The storey height of the frames was considered as 2.74 m. All structures are low- to mid-rise buildings having 2-, 4- and 5-storey. The architectural drawings as well as the structural system of the two-story archetype building are shown in Figs. 3.2 and 3.3, respectively. The dead and live loads are given in the subsequent paragraphs.

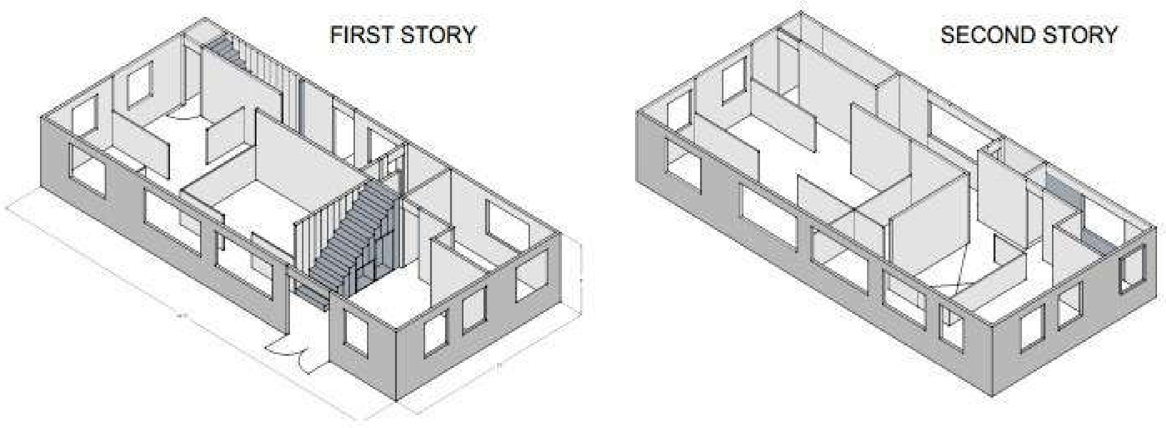

Fig. 3.2. Architectural drawings of the two-story archetype building.

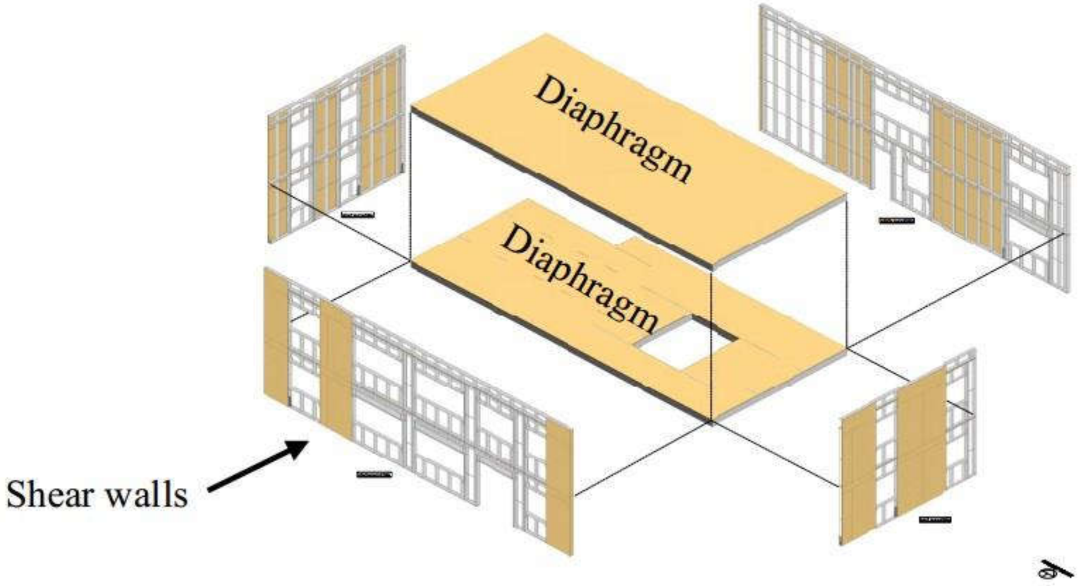

Fig. 3.3. Structural system of the two-story archetype building.

Rectangular buildings with 4 SWP lines that withstand lateral loads in each direction were selected for the research reported in this study. As depicted in Fig. 3.4, the archetype structures were analysed in the longitudinal (horizontal) direction.

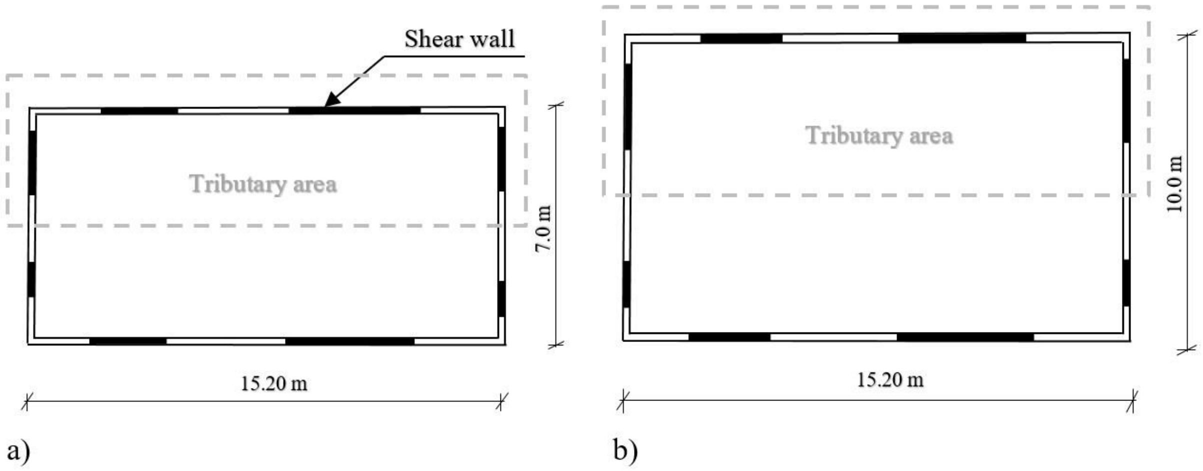

Fig. 3.4. Typical plan views of the archetypes: a) residential and b) office buildings.

Table 3.1. Parameters of the design space for CFS-SWP frame archetype buildings.

Group No.	Archetype ID	Storeys	Design load level	
			Occupancy	Seismicity
[a]PG1/7/13	[a]1/19/37	2	Residential	Low (PGA = 0.8 m/s^2, soil class B)
	2/20/38	4		
	3/21/39	5		
PG2/8/14	4/22/40	2		Moderate (PGA = 1.5 m/s^2, soil class C)
	5/23/41	4		
	6/24/42	5		
PG3/9/15	7/25/43	2		Moderate-to-high (PGA = 2.5 m/s^2, soil class C)
	8/26/44	4		
	9/27/45	5		
PG4/10/16	10/28/46	2	Office	Low (PGA = 0.8 m/s^2, soil class B)
	11/29/47	4		
	12/30/48	5		
PG5/11/17	13/31/49	2		Moderate (PGA = 1.5 m/s^2, soil class C)
	14/32/50	4		
	15/33/51	5		
PG6/12/18	16/34/52	2		Moderate-to-high (PGA = 2.5 m/s^2, soil class C)
	17/35/53	4		
	18/36/54	5		

[a] Three separated numbers correspond to performance group and archetype ID designed with q=2, 3 and 4, respectively.

These archetypes were established according to the requirement of Chapter 4 of the Federal Emergency Management Agency (FEMA) P695 [6], and separated into performance groups

(PGs) according to Section 4.3 of the same document, considering longer period and PGs with varying gravity loads. Nevertheless, since significant variability of period of vibration (*e.g.*, first-mode) and gravity load is not common for CFS structural system, it is expected that the results of this study, in terms of period variability, should be representative of the behaviour of sheathed CFS-SWP frames [16]. Additionally, according to Section 5.3 of the same document, two-dimensional archetype models, not accounting for torsional effects, are considered acceptable because the intended use of the methodology is to verify the performance of a full class of building, rather than one specific building with a unique torsional issue.

3.3.2. Design spectra

The seismic design spectra are specified based on locations (seismic zones) the archetype buildings are designed for. Since the assessment of the proposed seismic design and verification procedure will be carried out based on FEMA P695 methodology (see Chapter 4), the latter has been developed to accord with the loading provisions in the United States (US) (ASCE 7-10 [53]); which for earthquake loading are written in terms of the seismic design category "SDC", that represent the range of the maximum considered earthquake (MCE) having a return period of 2475 years for the US seismic design categories B, C and D. In contrast, the European provisions only refer to the design intensity level which, for ordinary buildings (importance class II in EC8), corresponds to a 10% probability of exceedance in 50 years (return period of 475 years). To be as much consistent as possible with the FEMA P695 methodology, the selection of the three cities was also made to reflect the regions of the lowest to the highest seismicity. The seismic spectra considered in the design of the three sites are shown in Fig. 3.5.

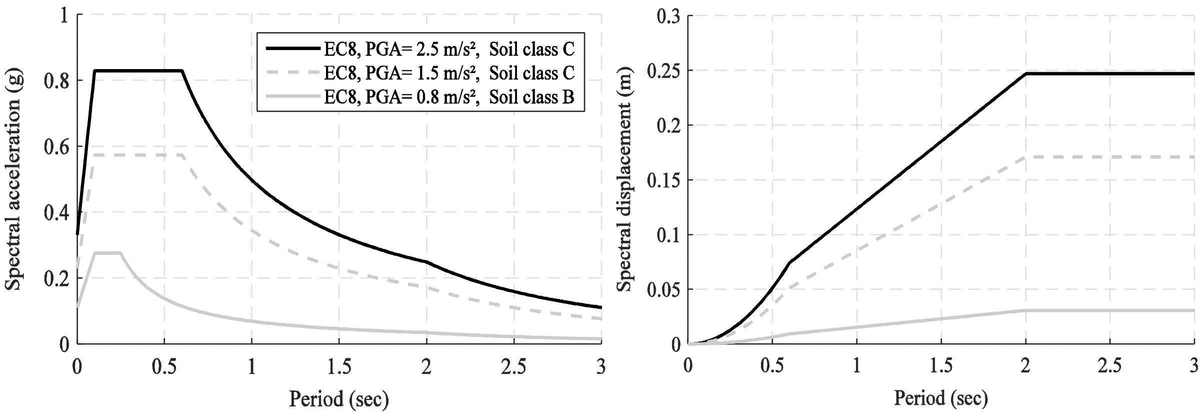

a) b)

Fig. 3.5. Elastic spectrum of three seismic intensity levels according to EC8: a) acceleration and b) displacement.

3.3.3. Seismic design of sheathed CFS-SWP systems

The CFS-SWP frames were designed based on the above described seismic design provisions proposed in Section 3.2. Since the structures satisfy EC8 regularity conditions in plan and elevation, equivalent lateral seismic loading has been followed by calculating the design base shear using the following expression [1]:

$$F_b = S_d(T_1).m.\lambda \tag{3.8}$$

Where $S_d(T_1)$ is the design spectral acceleration at the fundamental period assessed considering different behaviour factors: q=2, 3 and 4; m the seismic mass of the building and λ is the correction factor (λ=1) [1].

The calculation of the lateral displacements according to EC8 relies on an adequate estimate of the elastic stiffness of the structural elements. Whilst this information is readily available for most structural steel components, there is a lack of data regarding sheathed CFS-SWP elements. Therefore, a strategy was adopted in order to derive the elastic stiffness of this type of elements which consisted of using, for each individual SWP, the capacity curve obtained with the finite element (FE) model developed by the author [97] using concentrated plasticity hinge approach as described in Section 2.4. As shown in Fig. 3.6, the equivalent energy elastic-plastic approach has been adopted to derive the "elastic" stiffness for the SWP, which is represented by the first branch slope of the bilinear curve. This approach assumes a bilinear envelope curve that is capable of dissipating an equivalent amount of energy, up until the collapse, as the real SWP does when it is tested experimentally.

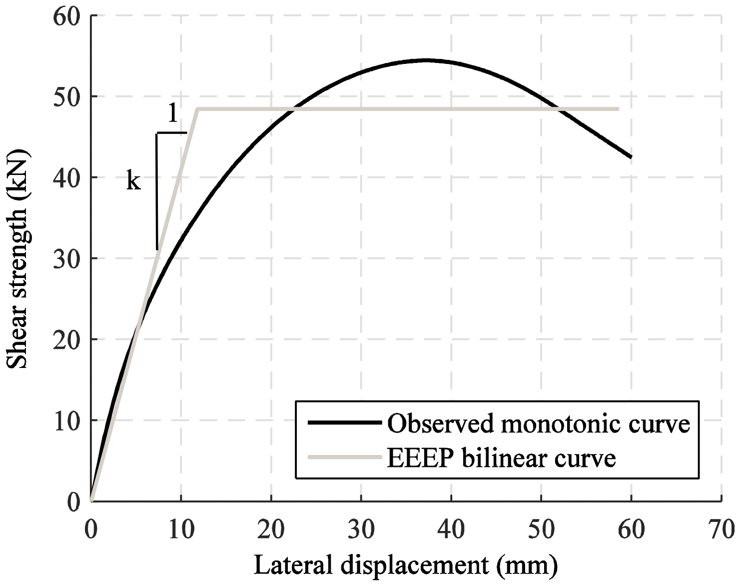

Fig. 3.6. Equivalent energy elastic-plastic model.

The methodology adopted here to estimate the elastic stiffness of SWP is clearly advanced to be used in engineering practice and hence combined efforts should be made to provide this parameter, for example, in a tabulated format.

The design base shear was then distributed along the height of the building in accordance with:

$$\mathrm{F_i} = \mathrm{F_b} \frac{\mathrm{z_i m_i}}{\sum_{\mathrm{j}} \mathrm{z_j m_j}} \tag{3.9}$$

Where $\mathrm{F_i}$ is the horizontal force acting on floor i; $\mathrm{F_b}$ is the design base shear; $\mathrm{m_i}$ and $\mathrm{m_j}$ are the floor masses; z_i and z_j are, respectively, the heights of the masses $\mathrm{m_i}$ and $\mathrm{m_j}$ [1].

The earthquake loading was combined with gravity loading according to the EC8 prescriptions. Dead loads of 2.87 kN/m² and 1.19 kN/m² were applied on all intermediate floors and on the roof, respectively. The imposed loads considered were those prescribed in Eurocode 1 [98], namely 3.0 kN/m² and 2.0 kN/m² floor live loads were applied on buildings with office and residence occupancies, respectively. As for the roofs, a live load of 1.0 kN/m² was applied for both occupancy types. Loads from the quasi-permanent combination need to be considered as seismic mass during the analysis. Each SWP frame supports half of the total mass of the structure. The SWP frame was loaded vertically according to the tributary floor area that corresponds to the SWP. The remaining vertical load that is resisted by the gravity resisting components of the frame which are not explicitly modelled are applied directly to the leaning column (Section 4.3).

A solution to minimise the length of SWPs is to employ double-sided sheathing. However, the axial force demand on chord studs will be increased; thus, there was a need for thicker framing members (2.583 mm) in comparison to the common range (0.879 to 1.438 mm). The challenging issue was to delay the chord studs' failure.

The physical and mechanical properties of built-up I-sections made by two lipped C-sections 362S162 per AISI S200 (2012) nomenclature [99] (nominal dimensions: 92.08 mm (web) x 41.28 mm (flange) x 12.7 mm (lip)) connected back-to-back (Table 3.2) have been adopted to design chord stud elements. Material properties of the CFS members are as follows: for members with thickness lower than 1.146 mm, the minimum yield strength of steel was 228 N/mm². Members having thickness greater or equal to 1.438 mm were considered to be made from steel with minimum yield strength of 340 N/mm². As for wood sheathing material, physical and mechanical characteristics are as follows: thickness=12.5 mm; bearing strength=4.5 N/mm²; Young's modulus=10445 N/mm² and shear modulus=825 N/mm².

Table 3.2. Chord stud cross-sections properties.

Chord stud sections ID	Thickness (mm)	f_y (N/mm²)	A_f (mm²)	I_x (mm⁴)	I_y (mm⁴)
1	1.146	228	438.4	590868	295434
2	1.438	340	544.4	726506	363253
3	1.811	340	675.7	889635	444817
4	2.583	340	934.2	1194415	597207

Tables 3.4, 3.5 and 3.6 summarise the design base shear, the resulting sheathed CFS-SWP configurations and the chord stud cross-sections for each archetype designed with a behaviour factor *q* equal to 2, 3 and 4, respectively. The design process primarily consisted in selecting the SWP in terms of the required configuration (Table 3.3) that satisfies all the above proposed design provisions as well as the capacity design of the chord studs and hold-downs.

Table 3.3. Design parameters for wood-sheathed CFS-SWPs.

Test Label	Wall Size H/W[a] (mm/mm)	Fastener spacing[b] (mm)	Track thickness (mm)	Ultimate shear strength (kN)	ASD[c] design strength (kN)	LRFD[d] design shear strength (kN)
1	2440/3660	152/305	1.12	60.763	30.3815	42.5341
2	2440/3660	102/305	1.12	87.002	43.501	60.9014
3	2440/3660	76/305	1.12	115.555	57.7775	80.8885
4	2440/3660	50/305	1.12	169.445	84.7225	118.6115
5	2440/2440	152/305	1.12	35.915	17.9575	25.1405
6	2440/2440	102/305	1.12	54.431	27.2155	38.1017
7	2440/2440	76/305	1.12	72.061	36.0305	50.4427
8	2440/2440	50/305	1.12	105.761	52.8805	74.0327

[a] Height-to-width aspect ratio (see Fig. 4.3);
[b] Screws spacing at perimeter/centre of the SWP;
[c] Design strength for Allowable Stress Design (ASD);
[d] Design strength for Load and Resistance Factor Design (LRFD).

3.4. Results and discussion

The design of the sheathed CFS-SWP frames listed in Table 3.4 was mostly governed by strength requirements imposed to structural members. Particularly, in case of archetype buildings designed for low seismicity regions, the calculated shear demand was much smaller than the minimum possible SWP shear capacity. For the cases where *q* was taken equal to 3 and 4 (Table 3.5 and 3.6), the design capacity of the SWP was mainly controlled by stiffness requirements. Consequently, the final sizing of the elements converged to the dimensions of the cases designed for *q* equal to 2. Therefore, these structures are associated with a significant reserve of lateral strength.

Table 3.4. Building archetypes design parameters for *q*=2.

q=2 Group No.	Archetype ID	Storeys	Occupancy type	A_{floor} (m²)	T_1 (sec)	Design base shear (kN)	SWP types (defined in Table 3.3)		Chord stud sections (defined in Table 3.2)
							1st bay	2nd bay	
PG1	1	2	Residence	106.28	0.35	16.72	6[a]/5	NA[c]	1[a]/1
	2	4			0.93	20.24	6/6/5/5	NA	2/1/1/1
	3	5			1.14	19.78	7/6/5/5/5	NA	2/2/1/1/1
PG2	4	2			0.27	73.81	6/5	2/1	2/1
	5	4			0.44	175.98	8/8/7/5	4/4/3/1	3/3/2/1
	6	5			0.49	227.07	77[b]/77/8/7/5	33/33/4/3/1	3/3/2/1/1
PG3	7	2			0.25	106.47	7/5	3/1	2/1
	8	4			0.37	253.86	77/77/8/5	33/33/4/1	4/3/2/1
	9	5			0.42	327.55	88/88/77/8/5	44/44/33/4/1	4/4/3/2/1
PG4	10	2	Office	151.6	0.6	21.18	6/5	NA	1/1
	11	4			1.12	26.02	6/6/5/5	NA	2/2/1/1
	12	5			1.28	30.04	8/7/5/5/5	NA	2/2/1/1/1
PG5	13	2			0.3	110.51	6/5	2/1	2/1
	14	4			0.41	266.71	77/66/8/5	33/22/4/1	4/3/2/1
	15	5			0.45	344.81	88/88/77/66/5	44/44/33/22/1	4/4/3/2/1
PG6	16	2			0.28	159.42	7/5	3/1	2/1
	17	4			0.37	384.73	88/77/66/6	44/33/22/2	4/3/2/1
	18	5			0.43	497.39	88/88/88/66/6	44/44/44/22/2	4/4/3/2/1

[a] From the bottom to the top of the building;

[b] Double number means double-sided sheathing in SWPs;

[c] Not applicable: lateral load resisting system composed of only one SWP line.

Table 3.5. Building archetypes design parameters for *q*=3.

q=3	**Archetype ID**	**Storeys**	**Occupancy type**	**A_{floor} (m²)**	**T_1 (sec)**	**Design base shear (kN)**	**SWP types (defined in Table 3.3)**		**Chord stud sections (defined in Table 3.2)**
Group No.							**1st bay**	**2nd bay**	
PG7	19	2	Residence	106.28	0.36	14.22	5[a]/5	NA[c]	1[a]/1
	20	4			0.94	14.64	6/5/5/5	NA	1/1/1/1
	21	5			1.07	14.97	8/7/6/5/5	NA	2/1/1/1/1
PG8	22	2			0.25	48.51	5/5	1/1	1/1
	23	4			0.51	116.51	7/7/6/5	3/3/2/1	2/2/1/1
	24	5			0.58	134.75	8/8/7/6/5	4/4/3/2/1	3/2/2/1/1
PG9	25	2			0.27	70.10	6/5	2/1	2/1
	26	4			0.41	168.36	66[b]/66/7/5	22/22/3/1	3/2/1/1
	27	5			0.47	217.49	77/77/77/7/5	33/33/33/3/1	4/3/2/1/1
PG10	28	2	Office	151.6	0.43	18.74	5/5	NA	1/1
	29	4			0.99	19.40	8/7/6/5	NA	2/1/1/1
	30	5			1.09	22.61	77/8/8/7/5	NA	2/2/1/1/1
PG11	31	2			0.32	76.15	5/5	1/1	1/1
	32	4			0.45	185.32	66/55/6/5	22/11/2/1	2/2/1/1
	33	5			0.56	221.06	66/66/8/6/5	22/22/4/2/1	3/2/2/2/1
PG12	34	2			0.30	110.04	6/5	2/1	1/1
	35	4			0.40	267.79	77/66/55/5	33/22/11/1	4/3/2/1
	36	5			0.46	346.66	88/77/77/66/5	44/33/33/22/1	4/4/3/2/1

[a] From the bottom to the top of the building;

[b] Double number means double-sided sheathing in SWPs;

[c] Not applicable: lateral load resisting system composed of only one SWP line.

Table 3.6. Building archetypes design parameters for *q*=4.

q=4	Archetype ID	Storeys	Occupancy type	A_{floor} (m²)	T_1 (sec)	Design base shear (kN)	SWP types (defined in Table 3.3)		Chord stud sections (defined in Table 3.2)
Group No.							**1st bay**	**2nd bay**	
PG13	37	2	Residence	106.28	0.36	10.67	5[a]/5	NA[c]	1[a]/1
	38	4			0.71	12.81	5/5/5/5	NA	1/1/1/1
	39	5			0.89	13.4	5/5/5/5/5	NA	1/1/1/1/1
PG14	40	2			0.37	36.32	5/5	NA	1/1
	41	4			0.64	70.76	7/7/6/5	NA	2/2/1/1
	42	5			0.73	80.38	8/8/7/6/5	NA	2/2/1/1/1
PG15	43	2			0.35	52.58	6/5	NA	2/1
	44	4			0.56	120.17	66[b]/8/7/5	NA	4/3/1/1
	45	5			0.61	136.32	77/77/8/7/5	NA	4/3/2/2/1
PG16	46	2	Office	151.6	0.43	13.95	5/5	NA	1/1
	47	4			0.82	17.46	77/66/7/5	NA	3/2/1/1
	48	5			0.94	20.47	88/77/66/7/5	NA	2/2/2/1/1
PG17	49	2			0.96	31.10	6/5	NA	1/1
	50	4			1.31	53.36	8/7/5/5	NA	2/2/1/1
	51	5			1.27	61.54	8/7/6/5/5	NA	3/2/2/1/1
PG18	52	2			0.92	46.65	6/5	NA	1/1
	53	4			1.26	82.47	8/7/6/6	NA	3/2/1/1
	54	5			1.38	97.97	8/8/8/6/5	NA	3/3/2/2/1

[a] From the bottom to the top of the building;
[b] Double number means double-sided sheathing in SWPs;
[c] Not applicable: lateral load resisting system composed of only one SWP line.

The use of a low behaviour factor resulted in higher seismic force demands and thus larger members were required for proper resistance. Application of behaviour factors equal to 3 and 4 resulted in lighter and more flexible structures developing larger inter-storey drifts that made the structure more susceptible to P-Δ effects, which is penalized by EC8 through an increase in seismic action effects. Furthermore, horizontal displacements of 4- and 5-storey structures could reach such unacceptable levels that the buildings needed to be stiffened in order to fulfil the damage limitation criterion prescribed in EC8. These phenomena, which are directly related with the lateral stiffness design requirement, counterbalanced the advantages of using a high value of the *q* factor. Moreover, although the SWP selection satisfied the resistance criterion, it did not satisfy the condition of the overstrength regularity outlined in Section 3.2. The preliminary shear wall design had to be re-evaluated to meet the overstrength regularity criterion whereby the lateral stiffness of the CFS-SWPs at a given storey must not be less than 50% of the stiffness of any adjacent storey. Hence the configurations of the SWPs were altered to increase their lateral stiffness.

Further, the influence of the behaviour factor on the design outcomes is well illustrated in Section 4.9 through fragility curves of archetype buildings designed with three different behaviour factors: *q* equal to 2, 3 and 4.

3.5. Conclusion

The objective of this chapter is to propose a seismic design and verification procedure for CFS frames using sheathed SWP as a lateral load resisting system. The approach involved the definition of a set of design provisions consistent with current European design standards, the selection and design of 54 archetype buildings considering three different levels of seismic intensity and two different types of occupancy.

The quantification of performance factors of the proposed seismic design procedure, based on fragility analyses following the FEMA P695 methodology forms the subject of Chapter 4. Further, the performance of the archetype buildings for the limit states considered in the design process, particularly in terms of the compliance of the structures with the SLS inter-storey drift limit, is studied as well.

CHAPTER 4

EVALUATION OF THE PROPOSED SEISMIC DESIGN AND VERIFICATION PROCEDURE USING FEMA P695 (ATC-63) METHODOLOGY

4.1. Introduction

A design procedure must be an effective methodology that can be applied by practicing engineers to calculate the geometric and material properties of structural members and ensure the advantageous behaviour of the resulting structural system. It is typically a set of rules and limits prescribed in the applicable standard. In order to provide guidance for a wide range of design cases, the specifications are composed of a series of conditional tasks and relatively simple formulae that often provide conservative approximations to complex phenomena. These underlying assumptions pose some interesting questions about the reliability of the seismic design procedure. If the defined seismic design provisions are efficient, will the structural response, under a major earthquake, be similar to the expected response of the code? and more importantly, will the structural design perform satisfactorily? Since the seismic design requirements in the codes are related, in part, to the past performance of buildings which formed the database containing the actual behaviour of buildings, is it realistic to expect good performance of new building systems that are not represented in this historical database such as CFS framed buildings?

It is a common belief that assurance of a sufficiently low failure probability with high confidence and economy should be the primary targets of a good design procedure. Therefore, its merits can merely be judged by robust and reliable evaluation of collapse probability. This requires a framework for probabilistic assessment of the performance of a large number of typical structural solutions under various seismic hazard scenarios. Extensive generalisation and extrapolation from small samples is not recommended, because of the inherent nonlinear relationship between realistic structural behaviour and design variables. In addition, the large number of design variables and the nonlinearity of the problem make seismic design difficult to evaluate with sufficient accuracy.

In this chapter, the assessment of the seismic design and verification procedure proposed in Chapter 3, is carried out through the application of the Federal Emergency Management Agency (FEMA) P695 methodology (2009) [6]. In order to generate the required data for the appraisal of the seismic design procedure, the OpenSees finite element (FE) environment [76] was used to simulate the nonlinear behaviour of CFS-SWP adopting an enhanced deteriorating hysteresis model developed in Chapter 2. Nonlinear static progressive collapse analyses (pushover) and incremental dynamic analyses (IDA) have been carried out on 54 CFS-SWP frames having 2-, 4- and 5-storey designed with varying seismic intensity levels. For the purpose of validating the proposed seismic design procedure and to examine whether the adopted behaviour factors could provide a sufficient margin against collapse under Maximum Considered Earthquake (MCE) ground motions, fragility curves based on buildings probability of collapse are subsequently developed. The seismic performance assessment of the archetype buildings for the serviceability limit state is addressed as well.

4.2. Overview of FEMA P695 (ATC-63) Methodology

The FEMA P695 methodology is a procedural method where the inelastic response characteristics and seismic performance factors of typical structures could be quantified. The adequacy of the structural seismic design procedure to meet the design performance objectives are verified as well. This methodology achieves the life safety performance objective by requiring an acceptably low probability of collapse of the lateral load resisting system for MCE ground motions. The methodology of FEMA P695 is illustrated in Fig. 4.1. It requires the use of a ground motion set, analysis methods, test data and design requirements.

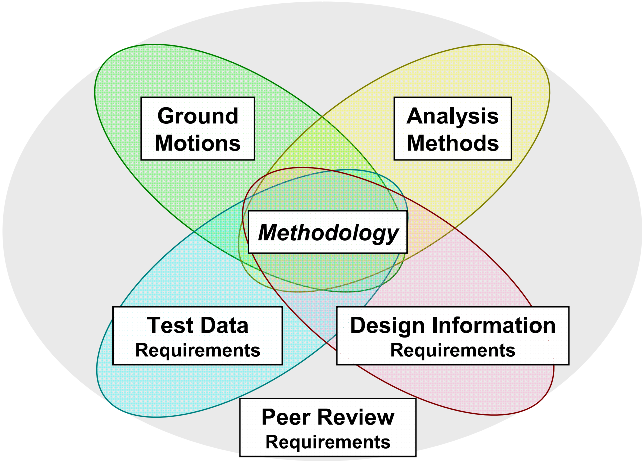

Fig. 4.1. Illustration of the key elements of FEMA P695 (ATC-63) methodology.

The process begins with gathering the required information and characteristics of the system such as design provisions under which the system is dimensioned and information related to component material properties (nonlinear load-deformation behaviour). The collapse safety of each archetype building is evaluated through dynamic analyses of nonlinear simulation models under a set of specified earthquake ground motions (44 records). In addition, nonlinear static analyses are also performed to evaluate ductility and overstrength parameters (μ_T and Ω_0, respectively). The simulation model for the nonlinear static and dynamic analyses is calibrated to experimental test results for key nonlinearity targeted in the models which is generally the response of the lateral load resisting system. The results of the nonlinear response history analyses are used to quantify statistics representing the collapse capacity of the archetype's structure *i.e.*, collapse margin ratio (CMR). The resulting collapse statistics are adjusted to account for the effect of spectral shape of the ground motion records (frequency content) which results in the adjusted collapse margin ratio (ACMR). As far as the collapse fragility curve is concerned, the uncertainties associated with a) interpretation and application of the design requirements β_{DR}, b) knowledge of the structural behaviour based on available test data β_{TD}, c) modelling assumptions made in structural analyses β_{MDL}, and d) the record-to-record variability β_{RTR}, are taken into account. The methodology then provides, based on all the above mentioned uncertainty sources (total uncertainty β_{TOT}), the seismic performance criteria to be fulfilled ($ACMR_{20\%}$ and $ACMR_{10\%}$). If the computed collapse capacities are too small (or, equivalently, the probabilities of collapse are too large), the seismic design parameters should be modified and the process would be repeated. Determination of seismic parameters through this procedure ensures that the resulting structural system, designed according to a given seismic design procedure, has an acceptable low probability of collapse.

4.3. Nonlinear modelling of the archetype structures

In this study, the OpenSees FE software has been used to model the archetype buildings and perform nonlinear analyses.

The central challenge in performing the assessment of the seismic design procedure is the development of robust, yet computationally efficient, models that can be used to accurately simulate the structural response at different seismic intensity levels.

Since capacity design has been adopted for the framing members of the sheathed CFS-SWP, the nonlinear behaviour of this structural system observed in past test campaigns, depends considerably on the complex behaviour that occurs at each location of sheathing-to-framing fasteners. Chapter 2 has resulted in a concentrated plasticity model which is capable of simulating strength deterioration (both cyclic and in-cycle), stiffness deterioration as well as pinching of sheathed CFS-SWP, associated with the highly nonlinear behaviour of the sheathing-to-framing fasteners (Kechidi and Bourahla (2016) [97]). This hysteresis model, which is implemented in OpenSees version 2.4.5 and above [100] as a uniaxialMaterial designated CFSWSWP, has been validated against experimental test data [11].

As shown in Fig. 4.2, an important feature of this model is that its parameters are directly related to physical and mechanical characteristics of the SWP that are easily identifiable by the user.

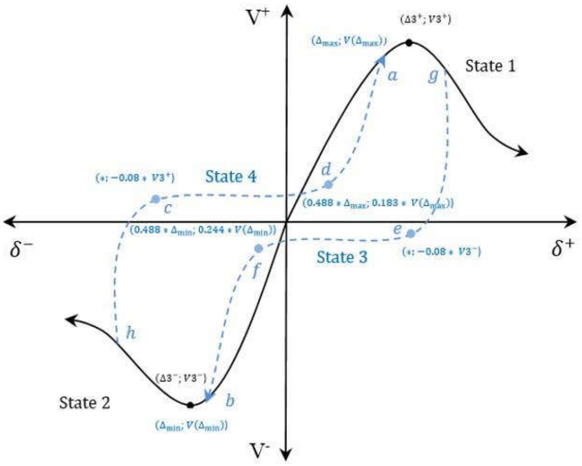

H (mm):	SWP's height
W (mm):	SWP's width
F_{uf}(MPa):	Tensile strength of framing members
t_f (mm):	Framing thickness
I_{fe} (mm^4):	Moment of inertia of the chord studs
I_{fi} (mm^4):	Moment of inertia of the intermediate studs
t_s (mm):	Sheathing thickness
np:	Sheathing number
d_s (mm):	Screws diameter
V_s (N):	Screws shear strength
s_c (mm):	Screw spacing on the sheathing perimeter
$n_{c:}$	Number of screw on the sheathing edge
Type:	wood sheathing type (DFP=1, OSB=2, CSP=3)
Opening_A (mm^2):	Total area of openings
Opening_L (mm):	Cumulative length of openings

Fig. 4.2. Parameters of the CFSWSWP uniaxialMaterial available in OpenSees.

The overall lateral stiffness and strength of the CFS-SWP are modelled using a concentrated plasticity hinge approach. An equivalent zeroLength element is located at the centre of the SWP and is assigned a CFSWSWP uniaxialMaterial connected to rigid truss elements that transmit the force to the chord studs. The framing members have pinned ends so that they do not develop any resistance to lateral loads. This modelling approach leads to a significant reduction in terms of the number of elements used to model a sheathed CFS-SWP, which results in a reduced number of degrees of freedom (DOF) without compromising the accuracy. The CFS-SWP components as well as the schematic representation with the element types of the FE model are illustrated in Fig. 2.11.

Fig. 4.3 shows an example of a CFS-SWP archetype model. The structural members not contributing to the lateral stiffness (bearing and partition walls) are considered by connecting one leaning column to the CFS-SWP frame. As mentioned in Section 3.2, Type I SWPs are considered to be totally decoupled in the whole system due to the fact that there is a limited knowledge on the behaviour of multi-storey CFS-SWP system. Hence, the continuity of chord studs along the height of the structure is not considered in the developed FE models.

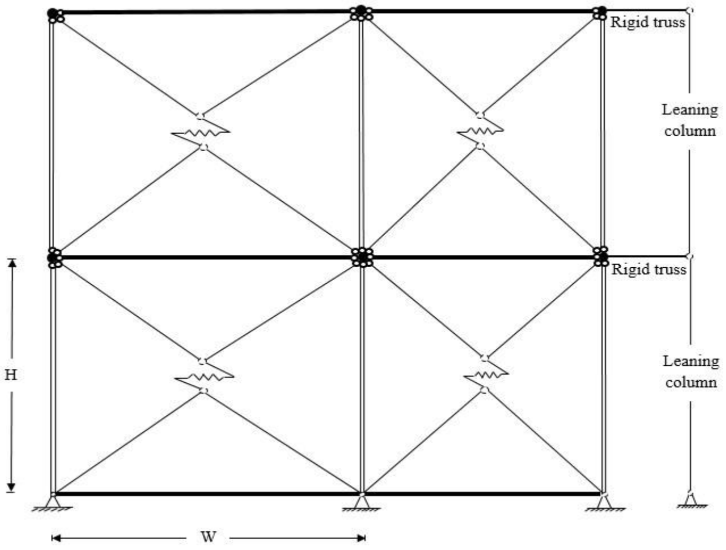

Fig. 4.3. Example of CFS-SWP 2-storey frame archetype model.

In order to ensure a proper distribution of seismic forces among all SWPs, a multipoint constraint is used to slave the horizontal DOF at each floor level to simulate a rigid diaphragm. P-delta geometric transformation available in OpenSees is applied for proper consideration of geometrical nonlinear effects. The connection between the leaning column and the SWP components is established by utilising rigid truss elements that are hinged around the SWPs (Fig. 4.3); this is required to ensure that the gravity load resisting system does not contribute to lateral stiffness while accounting for P-delta effects.

The seismic mass corresponding to gravity loads was evenly distributed at the top corners of each SWP since a uniform distribution of these loads was assumed. The gravity load was computed based on the tributary area of each SWP, and then applied to the columns as concentrated nodal loads. Rayleigh damping including both tangent stiffness and mass proportional damping has been assigned to the first and second vibration modes. A damping ratio of ξ=5% has been adopted which is in accordance with data provided by Dan Dubina (2008) [101] and Shamim and Rogers (2013) [45].

Uncertainties related to the model parameters and their effect on the collapse assessment will be incorporated later in this chapter through adjustments to the fragility function.

4.4. Ground motion record selection (FEMA P695)

The current trend of describing structural performance consists in performing a large number of nonlinear dynamic response history analyses with a set of ground motion records scaled to several seismic intensity levels. In this study, the FEMA P695 far field record set has been selected which consists of 22 pairs of ground motion records (44 records) available on the

PEER strong ground motion database [102]. The record set was selected to provide an unbiased suite of motions that represent strong ground motion shaking with earthquake magnitudes of 6.5 to 7.9 (see Table 4.1). Based on FEMA P695, scaling the ground motion records includes two main steps. The first step consists of normalising the ground motion records based on their Peak Ground Velocity (PGV) to reduce the scatter while preserving variations that are consistent with those observed in Ground Motion Prediction Equations "GMPEs" previously known as attenuation relations.

Table 4.1. Summary of earthquake events and corresponding normalisation factors for the far field FEMA P695 record set.

EQ ID	**Earthquake**			**Component[a] 1**	**Component[a] 2**	**Normalisation Factor[b] (NF)**
	Magnitude	**Year**	**Name**			
12011	6.7	1994	Northridge	NORTHR/MUL009	NORTHR/MUL279	0.65
12012	6.7	1994	Northridge	NORTHR/LOS000	NORTHR/LOS270	0.83
12041	7.1	1999	Duzce, Turkey	DUZCE/BOL000	DUZCE/BOL090	0.63
12052	7.1	1999	Hector Mine	HECTOR/HEC000	HECTOR/HEC090	1.09
12061	6.5	1979	Imperial Valley	IMPVALL/H-DLT262	IMPVALL/H-DLT352	1.31
12062	6.5	1979	Imperial Valley	IMPVALL/H-E11140	IMPVALL/H-E11230	1.01
12071	6.9	1995	Kobe, Japan	KOBE/NIS000	KOBE/NIS090	1.03
12072	6.9	1995	Kobe, Japan	KOBE/SHI000	KOBE/SHI090	1.10
12081	7.5	1999	Kocaeli, Turkey	KOCAELI/DZC180	KOCAELI/DZC270	0.69
12082	7.5	1999	Kocaeli, Turkey	KOCAELI/ARC000	KOCAELI/ARC090	1.36
12091	7.3	1992	Landers	LANDERS/YER270	LANDERS/YER360	0.99
12092	7.3	1992	Landers	LANDERS/CLW-LN	LANDERS/CLW-TR	1.15
12101	6.9	1989	Loma Prieta	LOMAP/CAP000	LOMAP/CAP090	1.09
12102	6.9	1989	Loma Prieta	LOMAP/G03000	LOMAP/G03090	0.88
12111	7.4	1990	Manjil, Iran	MANJIL/ABBAR--L	MANJIL/ABBAR--T	0.79
12121	6.5	1987	Superstition Hills	SUPERST/B-ICC000	SUPERST/B-ICC090	0.87
12122	6.5	1987	Superstition Hills	SUPERST/B-POE270	SUPERST/B-POE360	1.17
12132	7.0	1992	Cape Mendocino	CAPEMEND/RIO270	CAPEMEND/RIO360	0.82
12141	7.6	1999	Chi-Chi, Taiwan	CHICHI/CHY101-E	CHICHI/CHY101-N	0.41
12142	7.6	1999	Chi-Chi, Taiwan	CHICHI/TCU045-E	CHICHI/TCU045-N	0.96
12151	6.6	1971	San Fernando	SFERN/PEL090	SFERN/PEL180	2.10
12171	6.5	1976	Friuli, Italy	FRIULI/A-TMZ000	FRIULI/A-TMZ270	1.44

[a] Two horizontal components of a record pair; the components are perpendicular;

[b] NF = Median (PGVPEER, i)/PGVPEER, i;

Where: PGVPEER, i = Peak ground velocity of the ith record (geometric mean of PGV of the two horizontal components of the record);

Median (PGVPEER, i) = Median of PGVPEER, i values of records in the set.

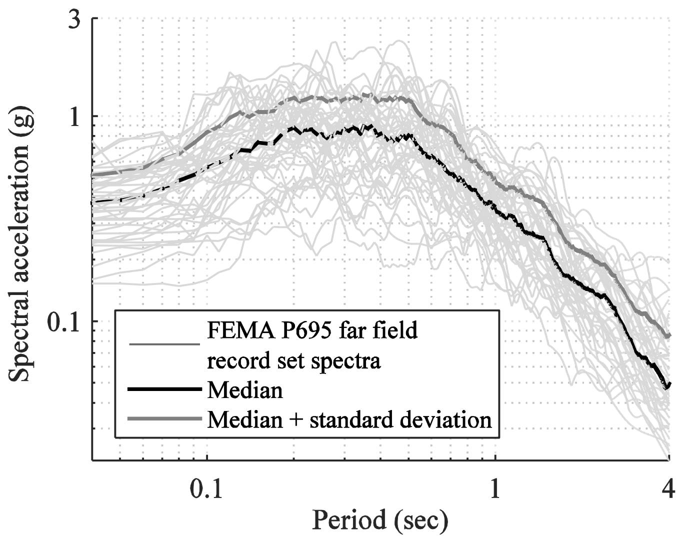

Fig. 4.4. FEMA P695 normalised far field record set response spectra.

The second step consists of adjusting the median of the records to a predefined spectral acceleration. For this purpose, the response spectrum of all the normalised earthquake records and their median are plotted in Fig. 4.4; then, the median spectrum was anchored at the first-mode spectral acceleration of the response spectrum provided by EC8 of the archetype structure under consideration (Fig. 4.5). In other words, the records represent the probabilistic nature of earthquake intensity around the design acceleration level.

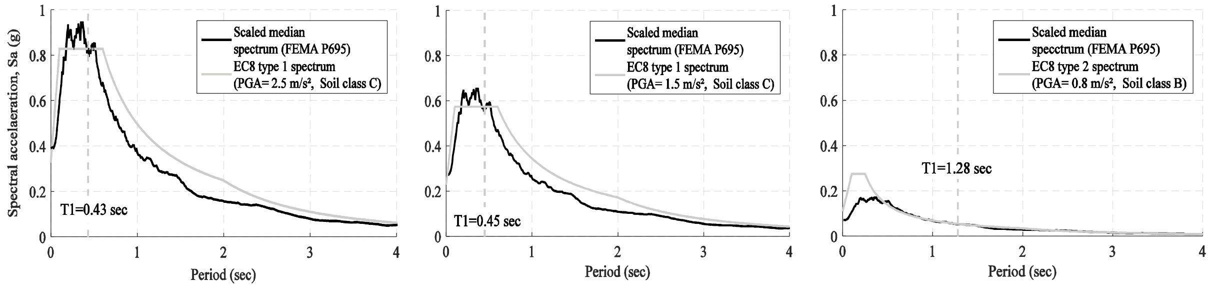

a) b) c)

Fig. 4.5. Median spectra of the far field record set anchored to the elastic response spectra at the fundamental period of the 5-storey buildings design for: a) moderate-to-high, b) moderate and c) low seismicity regions.

4.5. Nonlinear analysis using OpenSees environment

In OpenSees, one of the primary advantages of using a scripting language as a user interface is the facility with which multiple analyses can be run to investigate the impact of variation in model parameters and/or ground motion records on the structural behaviour. However, no built-in functions to perform the analyses or post-process the results. Therefore, Tcl and MATLAB

[103] custom-built programs have been written to, respectively, carry out the analyses and post process the output data.

An important aspect in the estimation of the structural response is the capabilities of the numerical simulation software used for the analysis. Factors such as algorithms used to solve the nonlinear equations, integration algorithm and tolerances adapted in the analysis are all important in the prediction of the model behaviour. While analysing nonlinear structures, convergence issues could be encountered. To ensure accuracy of the numerical solution, when using OpenSees software, a Solution Algorithm object should be defined. The latter determines a sequence of steps to be used to solve the nonlinear equations. In the event of non-convergence, multiple root-finding algorithms could be used to attempt to reach convergence. The effectiveness of this approach relies on establishing a correct order for these algorithms with an increased level of complexity. In this study, Newton algorithm command is used to construct a Newton Raphson algorithm which is a robust method for solving nonlinear equations. However, sometimes due to the roughness of the residual equation, convergence is slow or even out of reach; therefore, by using a more effective command such as Newton with Initial Tangent Algorithm, the convergence would be obtained. This trend is continued by using more complicated algorithms such as Newton with Line Search, Krylov-Newton and Broyden algorithm to assure that ultimately the results are as accurate as possible. The convergence is checked on energy basis with a tolerance of 10E-8.

4.6. Nonlinear static analyses (pushover)

According to FEMA P695 methodology, the evaluation of the effect of spectral shape requires the quantification of the structural period-based ductility (μ_T) and static overstrength (Ω_0) factors. This was achieved by conducting nonlinear static analyses (pushover) on all archetype buildings. To initiate the analysis, the lateral loads were distributed along the height of the building structures following a load pattern consistent with the distribution of the base shear adopted at the design stage. Since the backbone curve of the CFSWSWP uniaxialMaterial has a post-peak drop, a displacement control analysis was carried out. Before running the analysis, the models have been subjected to initial loads corresponding to the gravity loads associated with the seismic loading combination referred in Section 3.3.3.

As described in FEMA P695, the static overstrength factor for a given archetype model is defined as the ratio of the maximum base shear strength (V_{max}) to the design base shear

(V_{design}). As for the period-based ductility factor, it is defined as the ratio of roof displacement corresponding to 20% drop in the capacity (δ_u) to the effective yield roof displacement (δ_y).

Fig. 4.6 shows an example of pushover curves for archetypes 1 and 18. The shape of the capacity curve is of primary importance where in Fig. 4.6b there is a steep decline in the pushover capacity curve after peak.

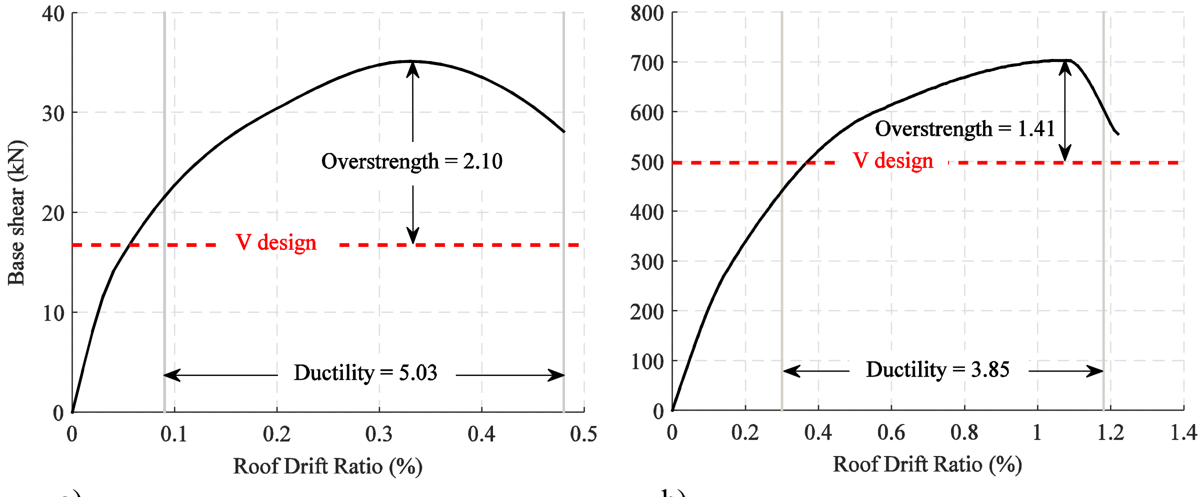

a) b)

Fig. 4.6. Pushover capacity curves: a) archetype 1 and b) archetype 18.

Results of the pushover analyses (μ_T and Ω_0) are provided in Table 4.2, where it is possible to conclude about the reduced values of Ω_0. This was a result of the concentration of damage at specific storeys, which can be attributed to the design and modelling assumption that the chord studs of different SWP units are not continuous along the height of the structure. Therefore, the behaviour of such configuration results in independent rotation of upper and lower SWP chord studs. This contributes to a low level of redundancy of the structural system, which significantly results in a concentration of inelastic demands, notably after failure of one SWP, causing additional limitation on the redistribution of shear demand between storeys. If chord studs were continuous over the structure height, the stiffness and strength of the gravity columns would contribute to limit the concentration of drift deformations at specific storeys [104].

Higher values of static overstrength were observed for those cases where the lateral deformation was relatively uniform along the height of the building and for those cases where there was some concentration of drifts at lower storeys.

4.7. Incremental dynamic analyses (IDA)

The main objective of the IDA [105] prescribed in FEMA P695 is to check whether the modelled archetype structures are appropriately designed to endure, to some extent, a suite of ground motion records taking into account several sources of uncertainty. In order to represent the various characteristics of low and high shaking intensities, the archetype models have been subjected to the above described 44 records, linearly scaled with a factor varying from 0.2 to 3.0 (in some cases up to 5.0) with a constant increment step of 0.2. The term failure used herein is synonymous with the exceedance of a predefined inter-storey drift limit. As pointed out by Kara Peterman (2014) [27], this damage parameter represents the local and global collapse and can be used as a reliable damage measure (DM). The latter was defined as the lateral displacement at the onset of SWP's failure, which is about 2.5% of its height. This value was based on the study performed by Joel Martinez (2007) [106]. Moreover, the lateral drift of a SWP might be less than the limit value but the applied loads on chord studs might exceed their strength; therefore, both the SWP lateral drift and strength on chord studs have been checked for possible collapse, based, respectively, on displacement and force demands obtained from the analysis.

The FEMA P695 methodology defines the median collapse intensity (S_{CT}) as the value for which half of the ground motion records that trigger the collapse of the structure. The collapse margin ratio (CMR) is the quotient of S_{CT} and the MCE demand level (S_{MT}). It is important to note that FEMA P695 has been developed to be compatible with the American seismic loading provisions (ASCE 7-10 [53]) where S_{MT} refers to the MCE intensity level with 2% exceedance probability in 50 years (return period of 2475 years). In contrast, the European provisions only refer to the design intensity level which, for ordinary buildings (importance class II in EC8), correspond to a 10% probability of exceedance in 50 years (return period of 475 years); therefore, the application of FEMA P695 in this investigation requires the transformation of the seismic intensity considered in the design of the archetypes to the intensity corresponding to a return period of 2475 years. This transformation is typically carried out based on the site-specific hazard whilst in ASCE 7-10 it is simply obtained by multiplying the design intensity by 3/2. This latter approach was adopted in this study. It is worth noting that the use of such a factor (3/2) is consistent with the information provided in a background document of EC8 (Fardis et al. (2005) [107]). According to this document, compliance of a structure with the no-(local-)collapse performance level, which is a performance requirement that characterises the ultimate limit state defined in the European provisions, is associated with "a safety factor between 1.5 and 2 against substantial loss of lateral load resistance".

Since the median of the ground motion records set has been scaled to the elastic response spectrum (Section 4.4), the S_{MT} was set equal to 1.50; therefore, the CMR was directly linked to S_{CT} and the scaling factor (SF) was adopted as an intensity measure (IM). This approach allows establishing a relationship between the seismic hazard defined in the building code, the IDA results and the probability of collapse [52].

Fig. 4.7a shows the IDA curves for archetype building 18 where S_{CT} is equal to 1.51, which means that for a scaling factor of 151% of the ground motion records, 50% of the records caused exceedance of one of the failure criteria, which in this particular case was the inter-storey drift limit. The main IDA parameters obtained for all archetype buildings are listed in Table 4.2.

The probability of collapse was calculated based on the IDA results, as the ratio of ground motion records that caused failure for each intensity level to the total number of ground motion records (44). Since the collapse capacity is assumed as a lognormal distributed variable, a lognormal cumulative distribution function “CDF” was used to define a fragility curve (Fig. 4.7 right). The evaluation of the fragility curve parameters was based on the maximum likelihood fitting procedure proposed by Jack Baker (2015) [108]. Then, the resulting collapse statistics are adjusted to account for the total uncertainty (Section 4.8) and the effect of spectral shape (SSF), which results in the Adjusted Collapse Margin Ratio (ACMR=CMRxSSF) [6].

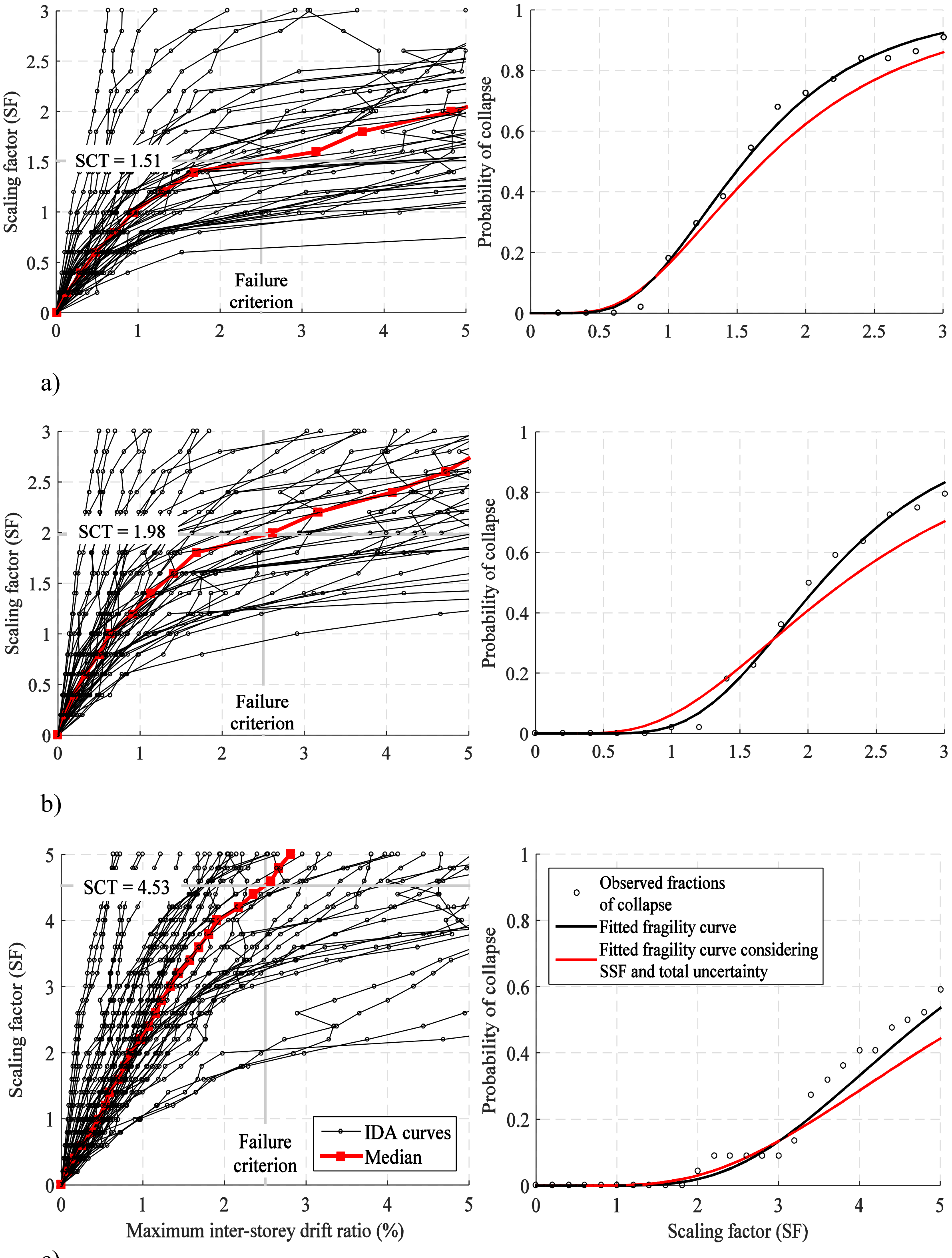

a)

b)

c)

Fig. 4.7. IDA curves (left), observed fractions of collapse and fragility curves (right) for archetypes: a) 18, b) 14 and c) 10.

The results presented in Fig. 4.7 show that the archetype building designed in a low seismicity region (Fig. 4.7c) has higher ACMR in comparison to those designed in moderate and moderate-to-high seismic intensity level (Fig. 4.7a and b). In other words, the ACMR parameter increases as the seismicity of the site decreases (all results of the archetypes design with *q* equal to 2 are provided in Appendix C). This results from the fact that the structure of archetype 10 exhibited higher static overstrength which has a significant influence on the probability of collapse. A plot of the ACMRs against the values of static overstrength of the frames designed with values of behaviour factor, *q*, equal to 2, 3 and 4 is shown in Fig. 4.8. In general, the ACMR tends to increase with an increase in static overstrength, but the trend is not well defined. A similar conclusion has been drawn by Vigh et al. (2013) [16] based on a sensitivity study in which the SWP shear strength capacity had a significant influence on the collapse performance of CFS framed structures, where 40% larger shear strength led to 30% increase in the value of the collapse seismic intensity level.

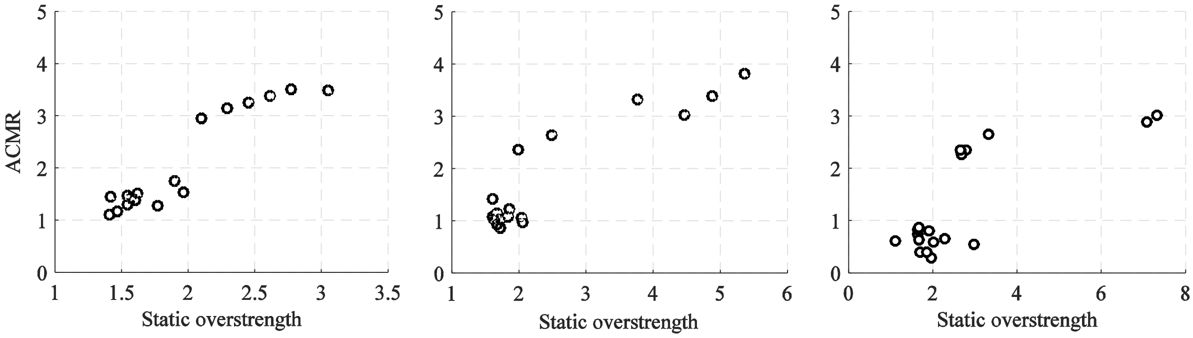

a) q=2 b) q=3 c) q=4

Fig. 4.8. Relationship between static overstrength and ACMR for all archetype buildings.

4.8. Assessment of the design procedure based on FEMA P695 (ATC-63) methodology

In order to evaluate the collapse risk of the archetype buildings, there is a need for the determination of the acceptable collapse margin ratios. The latter require characterisation of uncertainties associated with (a) interpretation and application of the design requirements (β_{DR}), (b) knowledge of the structural behaviour as confirmed by the available test data (β_{TD}), (c) modelling assumptions made in structural analyses (β_{MDL}), and (d) the record-to-record variability (β_{RTR}). According to Section 7.3 of FEMA P695, a fixed value of $\beta_{RTR} = 0.40$ is assumed in the performance evaluation of systems with significant period elongation (*i.e.*, period based ductility, $\mu_T \geq 3$).

For the uncertainty associated with test data, the experimental tests carried out by Branston et al. (2006) [11], revealed the wood-sheathed CFS-SWP behaviour under different level of lateral loading through which common deterioration and failure modes have been identified. Hence, test data was rated as Good (β_{TD}=0.2). Given the fact that the CFSWSWP uniaxialMaterial simulates the deteriorating behaviour that leads to collapse of the wood-sheathed CFS-SWP with an acceptable reliability, the nonlinear analytical models developed in this research are rated as Good (β_{MDL}=0.2). The design requirements uncertainty was rated as Good (β_{DR}=0.2) since the design procedure was defined based on EC8 provisions, in addition to AISI S400-15 design standard.

β_{TOT} describing the total collapse uncertainty is assessed as the square root of the sum of squares of all sources of uncertainty. Given the values of β_i, the resulting value of β_{TOT} is equal to 0.53. According to FEMA P695, the acceptable ACMR for 10% and 20% probability of collapse under MCE ground motions ($ACMR_{10\%}$ and $ACMR_{20\%}$) are 1.97 and 1.56, respectively. To validate the procedure used in the seismic design as well as the *q* factor, FEMA P695 requires that, for each PG, the individual ACMRi and their average must be greater than or equal to $ACMR_{20\%}$ and $ACMR_{10\%}$, respectively.

Table 4.2. Summary of performance evaluation according to FEMA P695 for archetype buildings designed with *q*=2.

Group ID	**Archetype ID**	**Storeys**	**T_1 (sec)**	**μ_T**	**Ω_0**	**SSF**	**S_{MT}**	**S_{CT}**	**CMR**	**ACMR**	**Accepted ACMR**	**Check**
PG1	1	2	0.35	5.03	2.10	1.11	1.5	3.97	2.65	2.94	1.56	pass
	2	4	0.93	3.77	2.77	1.15	1.5	4.58	3.05	3.51	1.56	pass
	3	5	1.14	3.42	3.05	1.16	1.5	4.5	3.00	3.48	1.56	pass
									Mean	**3.31**	**1.97**	**pass**
PG2	4	2	0.27	5.54	1.96	1.13	1.5	2.06	1.37	1.55	1.56	pass
	5	4	0.44	3.93	1.58	1.11	1.5	1.97	1.31	1.46	1.56	near-pass
	6	5	0.49	3.93	1.6	1.11	1.5	1.9	1.27	1.41	1.56	near-pass
									Mean	**1.47**	**1.97**	**fail**
PG3	7	2	0.25	5.44	1.77	1.11	1.5	1.74	1.16	1.29	1.56	fail
	8	4	0.37	3.65	1.54	1.10	1.5	2.04	1.36	1.50	1.56	near-pass
	9	5	0.42	3.35	1.54	1.10	1.5	1.8	1.20	1.32	1.56	fail
									Mean	**1.37**	**1.97**	**fail**
PG4	10	2	0.6	4.54	2.61	1.12	1.5	4.53	3.02	3.38	1.56	pass
	11	4	1.12	4.04	2.29	1.19	1.5	3.95	2.63	3.13	1.56	pass
	12	5	1.28	3.28	2.45	1.19	1.5	4.1	2.73	3.25	1.56	pass
									Mean	**3.25**	**1.97**	**pass**
PG5	13	2	0.3	5.13	1.62	1.13	1.5	2.04	1.36	1.54	1.56	pass
	14	4	0.41	3.48	1.57	1.08	1.5	1.98	1.32	1.43	1.56	near-pass
	15	5	0.45	3.66	1.9	1.09	1.5	2.4	1.60	1.74	1.56	pass
									Mean	**1.56**	**1.97**	**fail**
PG6	16	2	0.28	5.16	1.47	1.11	1.5	1.59	1.06	1.18	1.56	fail
	17	4	0.37	3.73	1.42	1.10	1.5	2	1.33	1.47	1.56	near-pass
	18	5	0.43	3.85	1.41	1.10	1.5	1.51	1.01	1.11	1.56	fail
									Mean	**1.25**	**1.97**	**fail**

Based on the results reported in Table 4.2, as the ACMR decreases substantially with the increase of design seismic intensity, this caused the archetype buildings that belong to PGs designed for moderate-to-high seismicity location (PG3 and PG6) to have unacceptable individual and average ACMR. The performance of these PGs could be significantly enhanced if the continuity of the chord studs along the height was considered in both the design and modelling of the corresponding archetype structures.

Moreover, as revealed by the shake table tests conducted by Kara Peterman (2014) [27] and the numerical evaluations performed by Shamim and Rogers (2015) [52] and Jiazhen Leng (2015) [42], the non-structural components of the structural system, including exterior gravity wall sheathing and interior gypsum sheathing boards for fire protection, can have a significant contribution to the building system's lateral stiffness, which can therefore enhance the probability of collapse. Furthermore, two possible adjustments can be applied to improve collapse performance: (*i*) reducing the system collapse total uncertainty factor (β_{TOT}) by adopting more optimistic individual uncertainty factors (β_i), and (*ii*) accounting for the spectrum shape effect through the selection of ground motion records based on the Conditional Spectrum (CS) proposed by Jack Baker (2011) [109], which requires an accurate description of the site-specific seismic hazard.

4.9. Sensitivity analysis

The influence of the behaviour factor on the probability of collapse is illustrated through the fragility curves of the archetype buildings designed with three different behaviour factors: q equal to 2, 3 and 4. The performances of the three alternatives are compared in Figs. 4.9 and 4.10 for different archetype buildings.

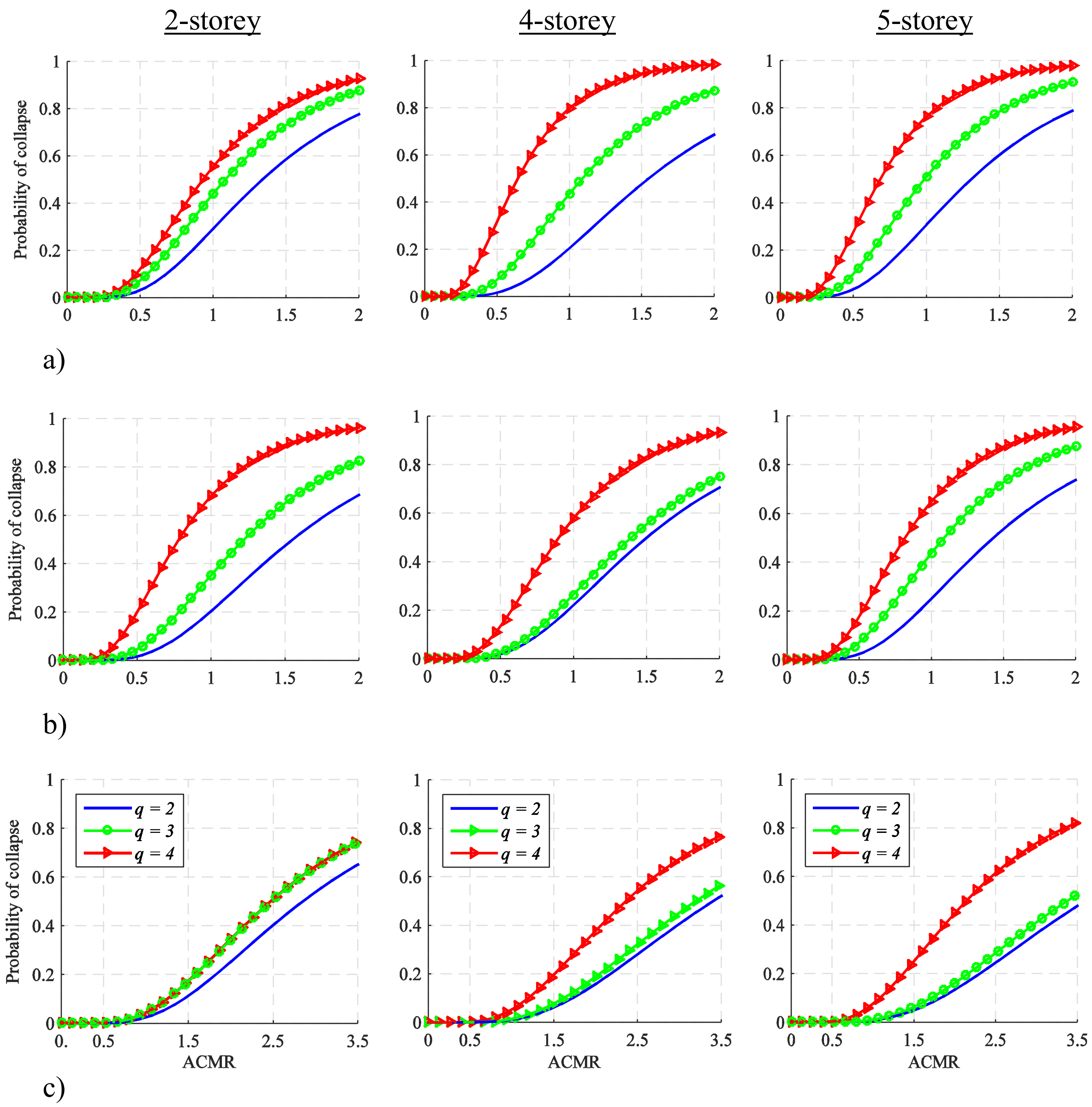

Fig. 4.9. Collapse fragility curves of archetype buildings with residence occupancy located in: a) moderate-to-high, b) moderate and c) low seismicity regions.

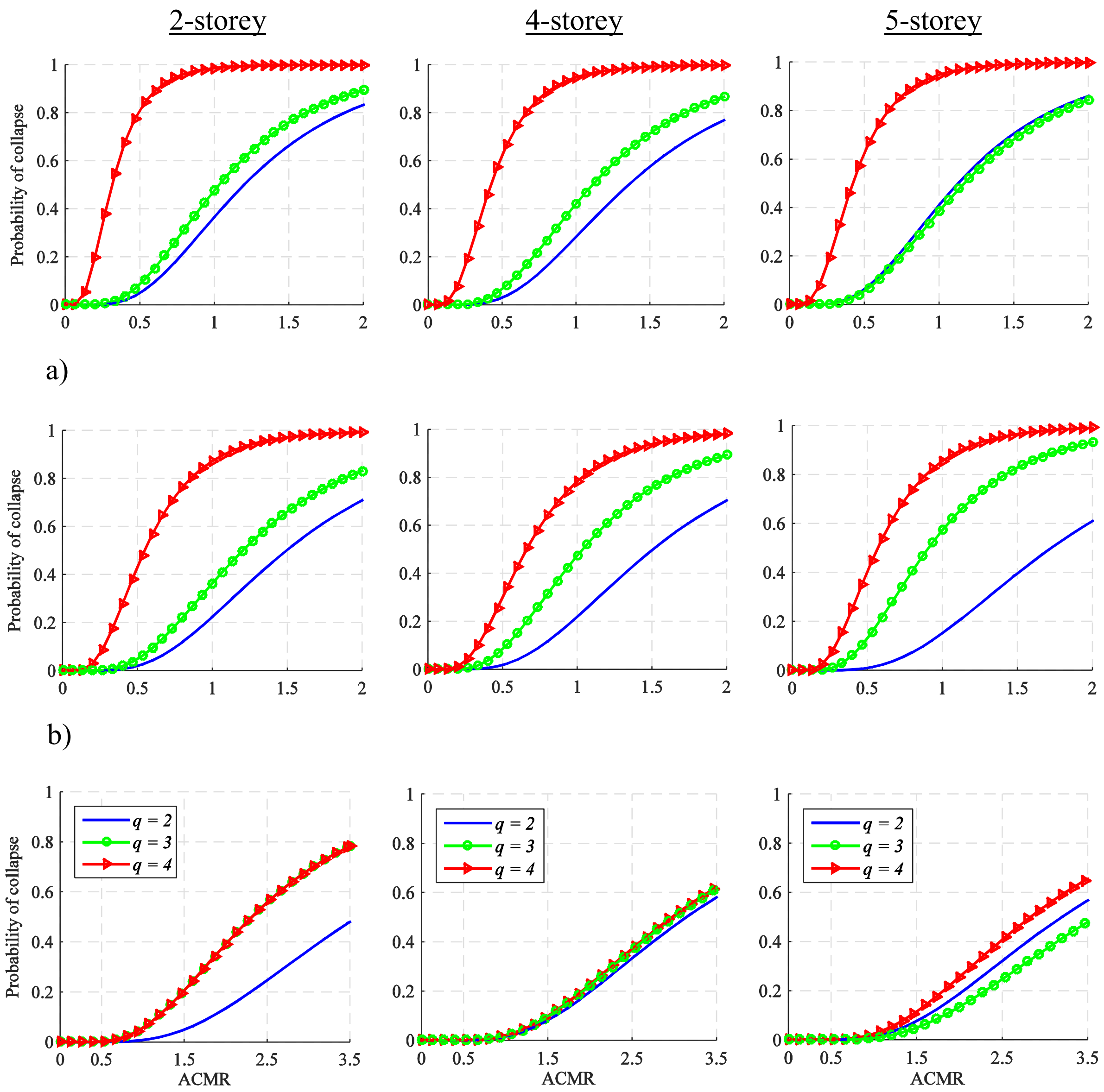

a)

b)

c)

Fig. 4.10. Collapse fragility curves of archetype buildings with office occupancy located in: a) moderate-to-high, b) moderate and c) low seismicity regions.

Figs. 4.9 and 4.10 clearly show the increase of the probability of collapse for increasing values of the adopted behaviour factor. However, it is obvious from Figs. 4.9c and 4.10c that the range of variation of the probability of collapse is lower in comparison to that observed for the archetypes designed for moderate and moderate-to-high seismic intensity levels. This confirms once again the significant impact of the static overstrength which has stemmed essentially from: the drift constraints regarding the damage limitation limit state, the second-order effects as well as the use of oversized SWP components.

Furthermore, some fragility curves are superimposed even though they correspond to archetypes designed with different q values; this is due to the aforementioned drift constraints that require stiffening of the structure, which led to an increase of the buildings lateral strength, resulting in a final structure similar to the one that has been designed with a lower *q* factor. These results demonstrate the reliability and effectiveness of the proposed seismic design procedure and, importantly, the suitability of using the lowest value of behaviour factor (q=2) considered in this study.

Fig. 4.11 illustrates the fragility curves for archetypes 18, 14 and 10 designed based on both numerical and empirical fundamental periods of vibration.

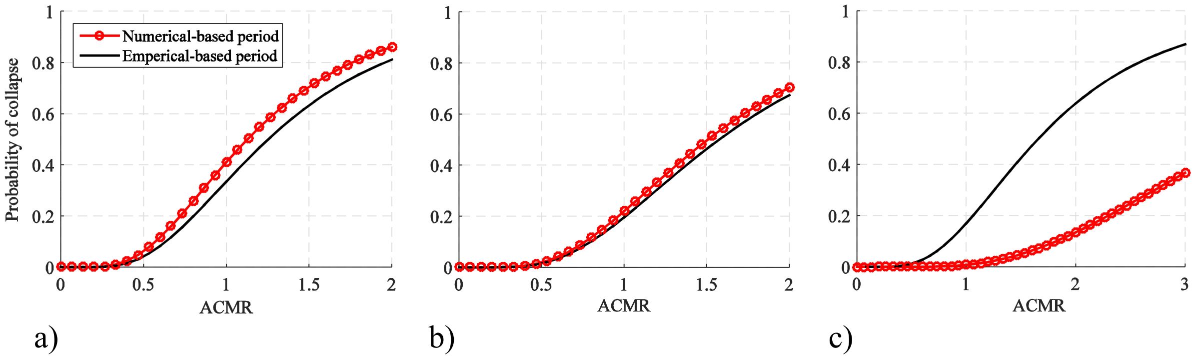

a)
b)
c)

Fig. 4.11. Influence of fundamental period on the collapse fragility curves of archetype buildings: a) 18, b) 14 and c) 10.

It can be seen that the probability of collapse could vary with the fundamental period adopted in the design process; thus, the violation of FEMA P695 performance requirements could be unnoticed in case the fundamental period adopted in the design is based on the simplified expressions provided in design codes (*e.g.*, $T_1=C_t \cdot H^{3/4}$, where $C_t=0.05$ and H is the height of the building in meters). However, a definite conclusion regarding this issue cannot be drawn since Fig. 4.11c shows that the probability of collapse increases when the structure is designed based on an empirical fundamental period. These results prove the importance of seeking a coherence between design and nonlinear FE modelling concerning the dynamic characteristics of the structure.

In Fig. 4.12, the ratio between the CMR, at the onset of failure (2.5% maximum inter-storey drift), obtained based on linear model and the corresponding nonlinear FE model for each archetype building is greater than unity which confirms the invalidity of the equal displacement rule for structures having short period of vibration. However, in Fig. 4.12c the trend is not the same since the archetype building has a relatively higher fundamental period (T_1=0.6 sec) where the equal displacement rule applies.

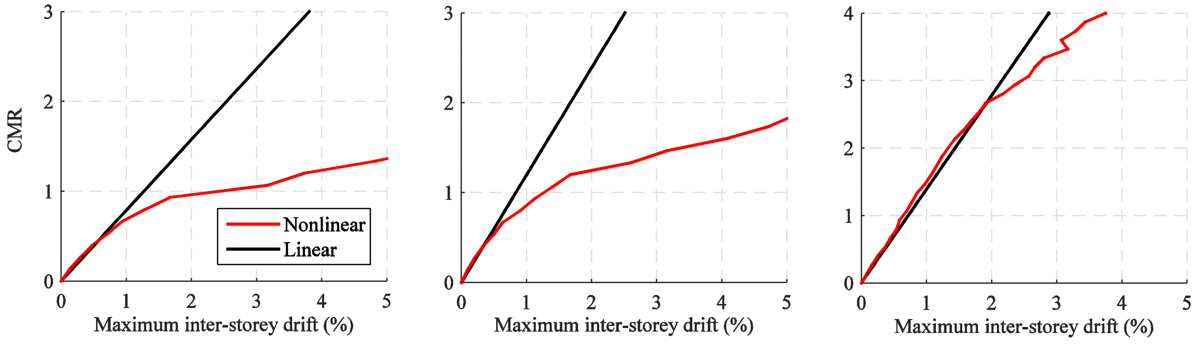

a) b) c)

Fig. 4.12. Median of IDA curves resulted from nonlinear and linear FE models for archetypes: a) 18, b) 14 and c) 10.

4.10. Serviceability performance assessment

In this study, the archetype buildings have been designed for ultimate and serviceability limit states (ULS and SLS, respectively) and then their seismic performance was evaluated for a third limit state "collapse" which is not prescribed in EC8. Therefore, the drift limit that has been considered in the verification of the SLS of the archetype structures is adopted in this section as an index to examine their performance at serviceability level and confirm the suggestions made for the evaluation of the elastic stiffness and the lateral displacement. For this purpose, the interpretation of the results provided by response history analyses under groups of seismic records that are compatible with a target spectrum obtained from EC8, is presented hereafter.

4.10.1. EC8-based ground motion record selection

In the context of demand-based assessments of buildings, Part 1 of EC8 establishes the following criteria for the selection and scaling of ground motion records: (*i*) the mean of the zero period spectral response acceleration values calculated from the individual time histories should not be smaller than the value of a_g S for the site under study, a_g being the design ground acceleration on rock and S the soil parameter; (*ii*) and, in the range of periods between $0.2T_1$ and $2.0T_1$, where T_1 is the fundamental period of the structure in the direction where the record will be applied, no value of the mean 5% damping elastic spectrum, calculated from all time histories, should be less than 90% of the corresponding value of the 5% damping elastic response spectrum of EC8.

The real ground-motion sets were defined using the SelEQ tool (Macedo and Castro (2017) [110]), which consists of a software application for record selection developed at the Faculty of Engineering of the University of Porto (FEUP). SelEQ makes use of the adaptive harmony search meta-heuristic optimization algorithm in order to significantly minimize computational cost and analysis time, whilst still meeting the imposed selection constraints. In this study, 10 records per group compatible with the elastic spectrum obtained from EC8 multiplied by the reduction factor ν [1] which was adopted in the verification of the Damage Limitation performance level *i.e.*, SLS. A maximum deviation of 10% of the average spectrum from the EC8 target spectrum was imposed in the period range of interest. Fig. 4.13 shows spectra of the 10 records and their average along with the EC8 target spectrum for moderate and moderate-to-high seismicity regions. Moreover, and with the aim of finding a simple and efficient way of reducing the record-to-record variability of each set, an additional criterion was considered in the selection, which consisted of imposing spectral mismatch limits relative to the target spectrum of ±50% for each individual record.

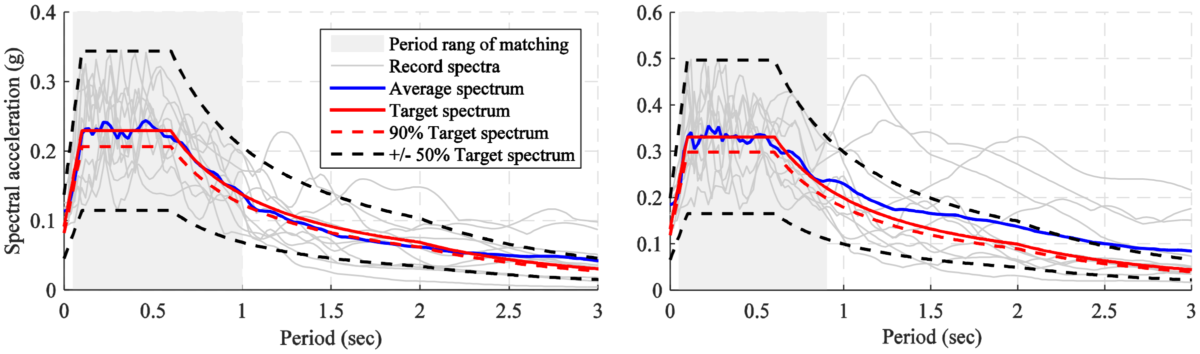

a) b)

Fig. 4.13. Target and different ground motion records spectra for: a) moderate and b) moderate-to-high seismicity regions.

4.10.2. Demand-based assessment

Fig. 4.14 shows the values of the maximum inter-storey drift ratio (dashed blue) along with the correspondent mean (black) recorded in each floor of archetype buildings designed for moderate-to-high seismicity regions subjected to ground motion records selected based on the above described method, in addition to drifts estimated during the verification of the SLS (red).

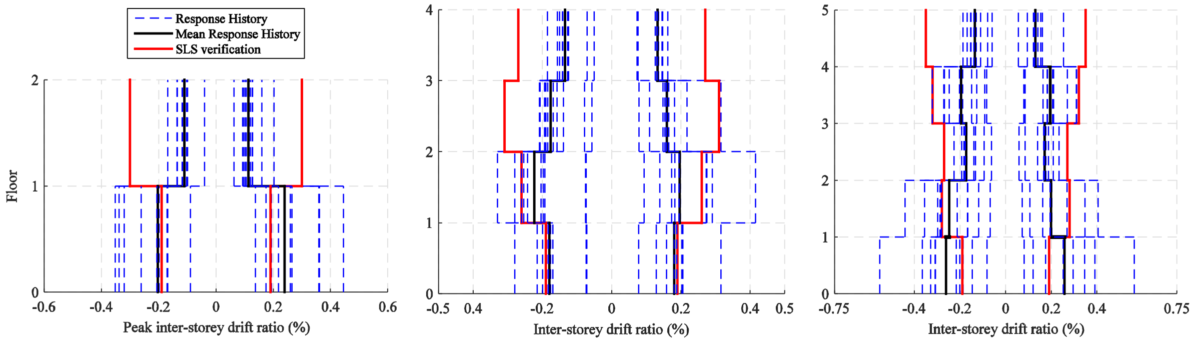

a) b) c)

Fig. 4.14. Peak inter-storey drift ratios obtained from response history analyses for archetypes: a) 16, b) 17 and c) 18.

It can be observed in Fig. 4.14 that these archetype buildings that did not fulfil FEMA P695 criteria under MCE ground motions (see Section 4.8) do comply with the inter-storey drift limit of 1% adopted for the verification of the SLS under a set of ground motion records compatible with the EC8 target spectrum. One can also compare the inter-storey drifts estimated during the design check of the SLS with the average inter-storey drifts from response history analyses where some discrepancies confirm the invalidity of the equal displacement rule for CFS framed structures having a short period of vibration and a deteriorating hysteresis behaviour of their lateral load resisting system. Therefore, the approach adopted in the evaluation of the elastic stiffness and the lateral displacement during the design stage can be considered as acceptable. Moreover, the performance of the studied structures under serviceability earthquake level affirms the adequacy of the proposed seismic design procedure with a behaviour factor *q* equal to 2 and 3, where they performed within the envelop of drift ratios that have been predicted at the design stage and hence are more likely to comply with performance based objectives (Damage Limitation, No-Local Collapse and Near Collapse) of EC8 which are assessed in Chapter 5. However, results related to archetype buildings designed with *q* equal to 4 violate the serviceability limit which confirms that this behaviour factor is not appropriate for the studied lateral load resisting system.

In addition, these results support the fact that not meeting the FEMA P695 criteria, under MCE ground motions, stemmed from the raisons detailed in Section 4.8 rather than design deficiency.

4.11. Conclusion

The seismic performance assessment of the design and verification procedure, proposed in the previous chapter, has been conducted following the methodology prescribed in FEMA P695, which consisted in performing IDA on FE models developed in OpenSees using a novel constitutive model that tracks the history of damage until the onset of collapse incorporating the effect of deterioration.

Fragility curves have been developed to investigate the impact of the design criteria on safety margins and to establish a perspective on seismic performance of sheathed CFS-SWP frame buildings. The outcomes from the archetypes designed with a behaviour factor, q, equal to 2, ascertained that the proposed seismic design procedure met the acceptance criteria defined in FEMA P695 and resulted in an acceptable collapse safety under MCE ground motions for archetype buildings designed for low and moderate seismicity regions. The overstrength revealed to have a significant impact on the collapse safety of the studied system. Therefore, some group of archetypes designed with higher q factors still satisfied the collapse criteria. This was due to the lateral overstrength that resulted from member sizing associated with the need to fulfil drift requirements. Additionally, the results demonstrate that it is crucial to ensure consistency between the design process and the advanced nonlinear FE models in what concerns the dynamic characterisation of the structures.

It was suggested that improvement of the seismic performance of the studied CFS archetype buildings, particularly those designed for moderate-to-high seismicity, could be achieved by imposing continuity of the CFS elements along the height of the structure and accounting for the contribution of non-structural components to the lateral stiffness and strength to the global structure. If these considerations are taken into account, it is expected that the FEMA P695 acceptance criteria would be passed for all archetype buildings, including those designed for the moderate-to-high seismicity regions.

Based on results presented in this chapter, it is proposed that a behaviour factor q equal to 2 can be adopted for the type of CFS-SWP system addressed in this study, but limited to structures located in regions of low-to-moderate seismicity. An extension of this proposal to structures located in high seismicity regions should only be made based on additional research that could involve addressing the issues of continuity of CFS-SWP chord studs and the contribution of non-structural components.

However, assessment of the results in accordance to European standards should have been done with the adaptation of each component of the FEMA P695 methodology to European environment. Based on our preliminary research, update of the seismic record database and adaptation of the Eurocode safety level into the process are required. Moreover, reliability analysis is required which is an additional evaluation that is not part of the FEMA P695 methodology. Its assessment is complicated by the fact that the Eurocode does not provide seismic specific target value of the reliability index.

A hazard-consistent procedure for a ground motion records selection based on the Conditional Spectrum to reflect, with more accuracy, the site-specific seismic hazard will be adopted in Chapter 5 to study, among others, the effect of spectral shape on the structural performance as well as the risk-based assessment of the building archetypes studied in this chapter.

CHAPTER 5

SEISMIC RISK ASSESSMENT OF COLD-FORMED STEEL SHEAR WALL SYSTEMS LOCATED IN LOW AND MODERATE-TO-HIGH SEISMICITY REGIONS

5.1. Introduction

In this chapter, a probabilistic framework for structural performance assessment of cold-formed steel (CFS) shear wall panel (SWP) structures with reference to conventional steel moment-resisting frame (MRF) systems in terms of seismic risk, is presented. For this purpose, 2-, 4- and 5-storey buildings of each structural system have been designed for two seismic intensity levels and then modelled using the OpenSees finite element (FE) software [76]. Incremental Dynamic Analyses (IDA) were performed to generate the required data for the development of fragility curves adopting the Conditional Spectrum (CS) [109] method to select site-specific ground motion records. Subsequently, in order to provide insights into the relative performance of both structural systems, the seismic risk is evaluated over the structure lifetime (*i.e.*, 50 years) in terms of the annual probability of exceeding the Damage Limitation (DL), No-Local Collapse (NLC) and Near Collapse (NC) limit states following the probabilistic SAC/FEMA closed-form framework [111], assuming a biased hazard fitted with a second-order power-law function [112].

5.2. Overview of the spectral shape effect on structural response

Dynamic structural analysis is commonly used in performance-based earthquake engineering (PBEE) to predict the response of a structure subjected to ground motion records consistent with the seismic hazard for which the design was performed. This consistency could be merely guaranteed if ground motion records are chosen to reflect the earthquake magnitudes (M) and distances (R) that would likely cause a given intensity of ground motion measure *e.g.*, spectral acceleration (Sa). The reason is that the magnitude and distance affect the duration and frequency content (spectral shape) of the ground motion record, which in turn affects the dynamic structural response history.

During the last decade, several researchers have drawn attention to the fact that the spectral shape of an earthquake ground motion with high spectral intensity at a given return period could vary significantly from another with lower intensity at the same return period [113-117]. Therefore, using the same records set (*e.g.*, FEMA P695 records set), scaled to several ground motion intensities, for a wide range of structures and seismic environments (sites) remains arguable. As seen in Chapter 4, FEMA P695 methodology addresses the spectral shape effect through the modification of fragility curves (increasing the median collapse capacity), the values of the spectral shape factor (SSF), given in Table 7.1 of FEMA P695 document [6], resulted from detailed analyses on a large number of reinforced concrete frames and wooden structures in a Californian setting [118, 119]. Its value is based on the ductility and the dominant period of the structure and it also accounts for the influence of seismic intensity on the spectral shape. Although this procedure is adopted literally in Chapter 4 as well as in previous FEMA P695-based studies [16, 104, 120-124], its direct applicability has not yet been verified for regions of seismicity other than California and structural systems other than the ones used for its calibration. Therefore, a detailed investigation of this topic is performed in cooperation with the research group of Professor José Miguel Castro at the University of Porto (FEUP) [125]. Such a study requires a more accurate description of the seismic hazard using advanced target spectra. In this study, the CS is adopted.

5.3. Conditional Spectrum-based ground motion record selection

In order to provide hazard-consistent ground motion records for dynamic structural analyses, a selection methodology based on a more realistic target spectrum is presented in the flowchart of Fig. 5.1. First, a probabilistic seismic hazard analysis (PSHA) is performed to derive the hazard curves given the local seismic source models and ground motion prediction equations (GMPEs). Then disaggregation of the PSHA is carried out to identify the earthquake characteristics such as magnitudes (M) and distances (R) that contributed to the occurrence of a given ground motion intensity level. Next, the CS is computed based on multiple causal earthquakes from PSHA disaggregation data and multiple GMPEs that are often considered in the PSHA computation. Lastly, ground motion records are selected from the PEER strong ground motion database [102] and their response spectra are scaled to match the CS.

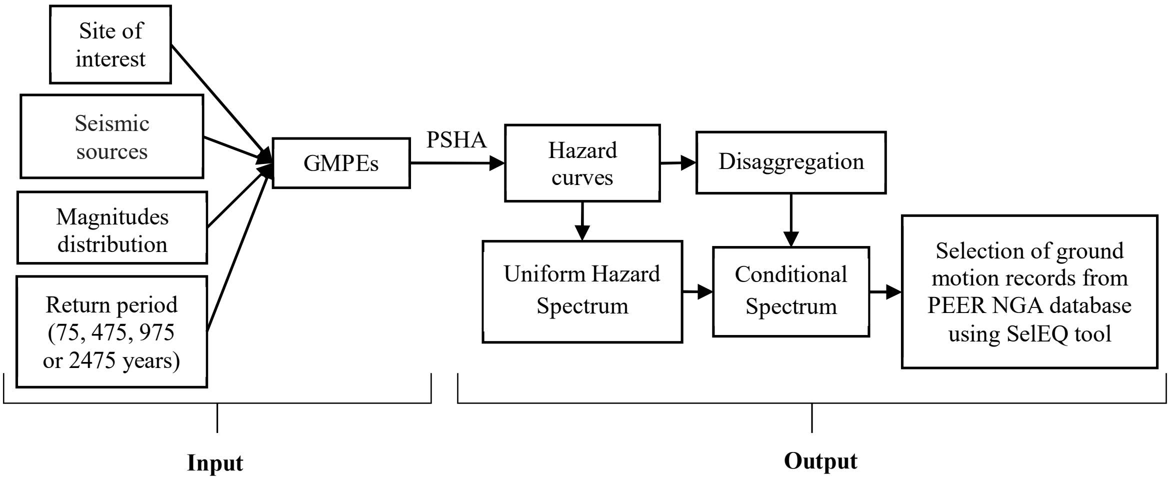

Fig. 5.1. Flowchart of the site-specific ground motion record selection procedure.

5.3.1. Probabilistic seismic hazard analysis and disaggregation

PSHA is used to estimate the hazard curve which describes the probability of exceeding a given ground motion intensity level (*e.g.*, damped elastic first-mode spectral acceleration Sa (T_1, 5%)) over the structure lifetime (*i.e.*, 50 years) at any site. Hazard curves are influenced by the characteristics of active faults; thus, they are site dependent. Because they describe spectral intensities, the curves are also period dependent and influenced by the type of soil at the site. The hazard curves in this study are obtained from PSHA computation using OpenQuake hazard engine version 1.0 [126] with an embedded database provided by the research project of the European Facility for Earthquake Hazard and Risk EFEHR entitled "SHARE" [127]. The probability of exceedance (PoE) can be expressed in terms of return period, for instance, an intensity level with 5% PoE in 50 years corresponds to a Sa value with a return period of 975 years under a Poissonian assumption of ground motion occurrence [128].

To illustrate, we obtained hazard curves and disaggregation data for two sites with characteristic PGA of 0.8 and 2.5 m/s^2 and shear wave velocity in the top 30 meters of the soil "V_{s30}" of 200 and 600 m/s which have been adopted in agreement with, respectively, soil B and C defined in Part 1 of Eurocode 8 (EC8) [1]. Since there is no GMPE valid for soft soil, the soil class at both sites is considered by increasing the spectral acceleration values based on the acceleration difference between the EC8 response spectral ordinates at T_1 for rock and soft soil type. Fig. 5.2 displays the hazard curve for both seismicity regions and different fundamental periods of the studied structures (see Section 5.5.2).

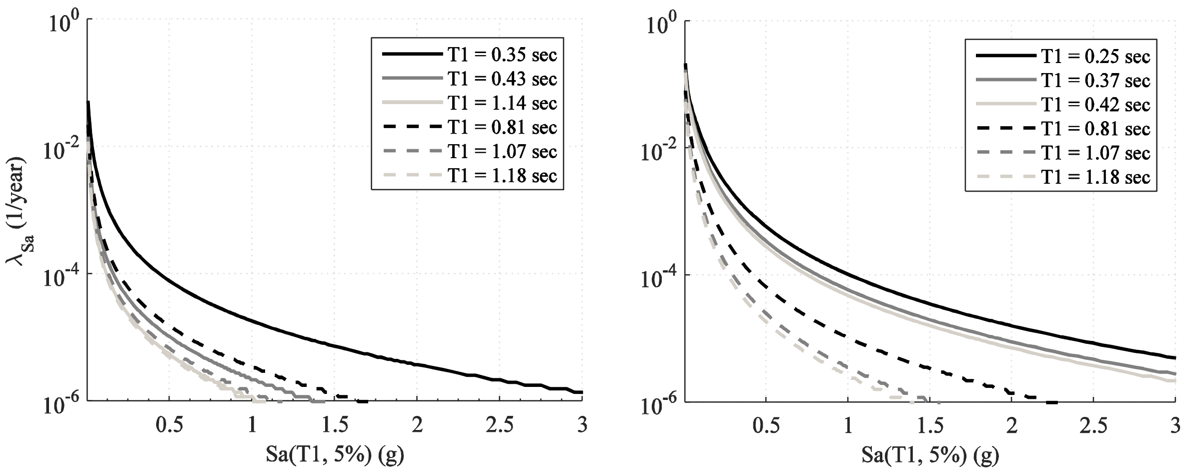

a) b)

Fig. 5.2. Seismic hazard curves for: a) low and b) moderate-to-high seismicity regions.

Disaggregation of PSHA is used to identify the M, R and epsilon (ε) associated with the occurrence of a given ground motion intensity level. The variable ε is used to express the difference between the spectrum of interest and the median spectrum from the same seismic source (further details are provided in Section 5.3.2). Fig. 5.3 shows the disaggregation data for Sa (1.14 sec) and Sa (1.18 sec) with 5% PoE in 50 years. These figures tell us what is the distribution of M and R, and which types of earthquake that are likely to cause high ground motion amplitude in the sites being studied.

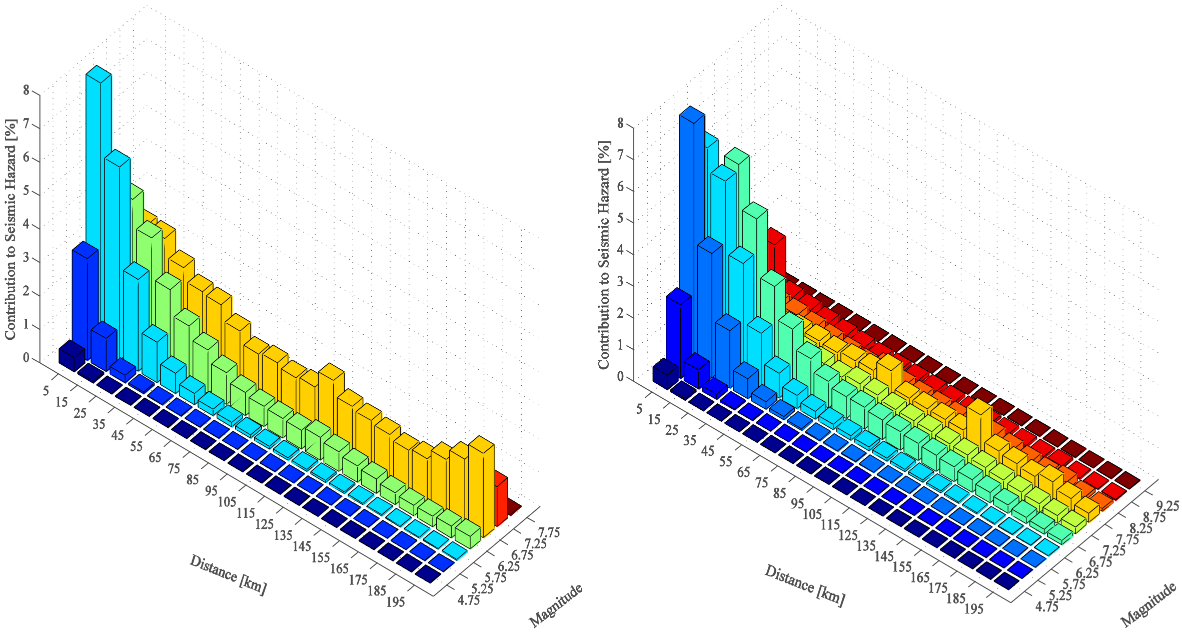

a) b)

Fig. 5.3. Seismic hazard disaggregation with 5% PoE in 50 years for: a) low (T_1=1.14 sec) and b) moderate-to-high (T_1=1.18 sec) seismicity regions.

5.3.2. Conditional Spectrum

The seismic risk over the structure lifetime is evaluated by coupling seismic hazard curves with the results of dynamic structural analyses (*e.g.*, probabilistic drift-hazard analysis). Hence, in order to obtain consistent structural responses, the selection of ground motion records should be associated with a target spectrum that is derived from PSHA results. One commonly used target spectrum is the Uniform Hazard Spectrum (UHS). As shown in Fig. 5.4, the construction of the UHS, is a collection of Sa values at different periods. UHS has this name because, at any period, the amplitude of Sa has the same PoE (*i.e.*, consistent PoE at all periods).

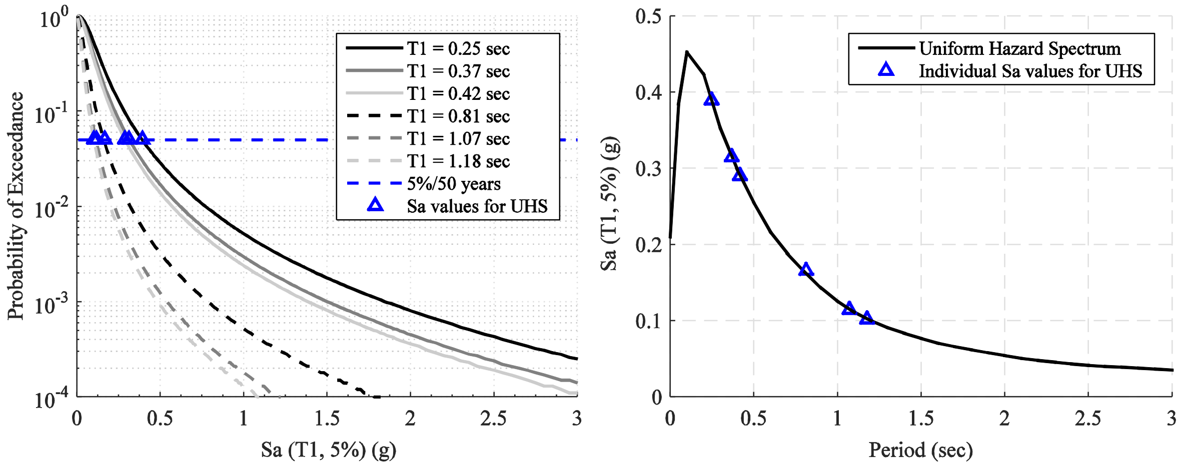

a) b)

Fig. 5.4. Individual Sa values: a) from hazard curves to b) UHS.

In practice, the UHS is more commonly used, especially in building codes. However, shortcomings of the UHS include a lack of hazard consistency as it assumes equal probabilities of Sa exceedance at all periods. Previous studies, such as the one reported by Baker and Cornell (2006) [113], indicated that traditional PSHA ignores the joint PoE of Sa at periods other than the period of interest. Therefore, once the Sa corresponding to a certain PoE has been determined, it is conservatively assumed that expected Sa at other periods are exceeded with the same probability. As shown in Fig. 5.5 the UHS (black dashed line) would not be a real representation of an individual ground motion spectrum (blue line) throughout the full range of periods.

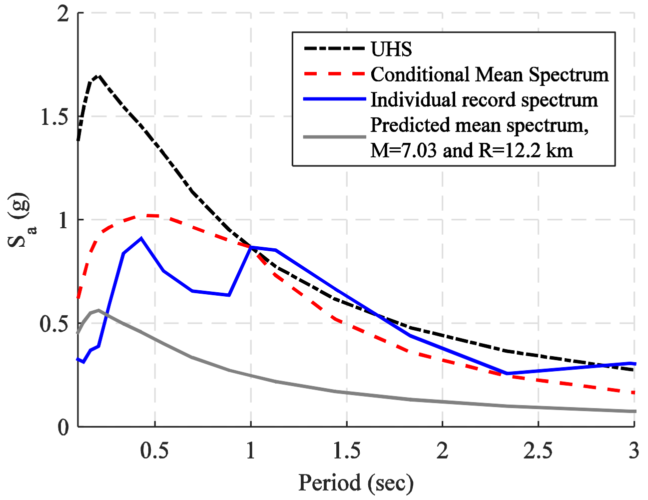

Fig. 5.5. Response spectrum from real ground motion record having approximately M = 7.03 and R = 12.2 km along with the conditional mean spectrum and UHS.

The reason why the UHS does not represent a spectrum caused by a single earthquake at a given site is typically explained by the fact that the high-frequency portion of the UHS is often dominated by small nearby earthquakes, while the low-frequency portion is dominated by larger, more distant earthquakes. Since high- and low-frequency portions come from different events, no single earthquake will produce a response spectrum as high as the UHS throughout the full range of frequencies. Therefore, subjecting structures to ground motion records selected based on the UHS would lead to a poor risk-based (conservative) assessment.

A more accurate approximation of the spectral shape could be reached with the adoption of the CS [109]. The CS incorporates correlation across periods to estimate the expected Sa values at all periods T_i (Sa (T_i)) given the target Sa value at the period of interest T* (commonly adopted as the fundamental period of vibration). Additional information regarding the correlation coefficient between pairs of ε values at two periods $\rho(\varepsilon(T_i), \varepsilon(T^*))$ (hereafter referred to as $\rho(T_i, T^*)$) can be found in Baker and Jayaram (2008) [129]. $\rho(T_i, T^*)$ is needed to compute the conditional mean of Sa at other periods T_i, $\mu_{\ln Sa_{j,k}(T_i)|\ln Sa(T^*)}$ using the following expression:

$$\mu_{\ln Sa_{j,k}(T_i)|\ln Sa(T^*)} = \mu_{\ln Sa_k}\left(M_j, R_j, T_i\right) + \rho(T^*, T_i).\,\varepsilon(T^*).\,\sigma_{LnSa_k}\left(M_j, R_j, T_i\right) \qquad (5.1)$$

Similarly, the conditional standard deviation of Sa at period T_i, $\sigma_{\ln Sa_{j,k}(T_i)|\ln Sa(T^*)}$, can be computed as:

$$\sigma_{\ln Sa_{j,k}(T_i)|\ln Sa(T^*)} = \sigma_{\ln Sa_k}\left(M_j, T_i\right).\sqrt{1-\rho^2(T^*, T_i)} \qquad (5.2)$$

The conditional mean and standard deviation target response spectrum are given by:

$$\mu_{\ln Sa(T_i)|\ln Sa(T^*)} = \sum_k \sum_j P^d_{j,k}\, \mu_{\ln Sa_{j,k}(T_i)|\ln Sa(T^*)} \qquad (5.3)$$

$$\sigma_{\ln \mathrm{Sa}(\mathrm{T_i})|\ln \mathrm{Sa}(\mathrm{T^*})} = \sqrt{\sum_{\mathrm{k}} \sum_{\mathrm{j}} \mathrm{P}^{\mathrm{d}}_{\mathrm{j,k}} \left(\sigma^2{}_{\ln \mathrm{Sa}\,{\mathrm{j,k}}(\mathrm{T_i})|\ln \mathrm{Sa}(\mathrm{T^*})} + (\mu_{\ln \mathrm{Sa}\,{\mathrm{j,k}}(\mathrm{T_i})|\ln \mathrm{Sa}(\mathrm{T^*})} - \mu_{\ln \mathrm{Sa}(\mathrm{T_i})|\ln \mathrm{Sa}(\mathrm{T^*})})^2\right)} \tag{5.4}$$

Where $P^d_{j,k}$ indicates the contribution of each $\mathrm{M_j} \mid \mathrm{R_j}$ pair and $\mathrm{GMPE_k}$ to the exceedance of the Sa of interest.

The GMPE can be used to obtain the logarithmic mean and standard deviation of Sa at all periods $\mathrm{T_i}$, denoted as $\mu_{\ln Sa}(\mathrm{M}, \mathrm{R}, \mathrm{T_i})$ and $\sigma_{\ln \mathrm{Sa_k}}(\mathrm{M_j},\ \mathrm{T_i})$, respectively. For any $\mathrm{Sa}(\mathrm{T_i})$ value, $\varepsilon(\mathrm{T_i})$ is computed as the number of standard deviations by which $\ln \mathrm{Sa}(\mathrm{T_i})$ differs from the mean spectral ordinate predicted by GMPE, $\mu_{\ln Sa}(\mathrm{M}, \mathrm{R}, \mathrm{T_i})$, at $\mathrm{T_i}$. Hence, $\varepsilon(\mathrm{T_i})$ depends on the GMPEs used and is mathematically defined by the following equation:

$$\varepsilon(\mathrm{T_i}) = \frac{\ln Sa\,(\mathrm{T_i}) - \mu_{\ln Sa}(\mathrm{M}, \mathrm{R}, \mathrm{T_i})}{\sigma_{\ln Sa}(\mathrm{M},\ \mathrm{T_i})} \tag{5.5}$$

The target $\varepsilon(\mathrm{T^*})$ (for the target $\mathrm{Sa}(\mathrm{T^*})$ value) can also be computed using Equation (5.5). In this study, the $\varepsilon(\mathrm{T_i})$ value has been obtained directly from PSHA disaggregation data.

The conditional standard deviation $\sigma_{\ln \mathrm{Sa}(\mathrm{T_i})|\ln \mathrm{Sa}(\mathrm{T^*})}$ from Equation (5.4), when combined with the conditional mean $\mu_{\ln \mathrm{Sa}(\mathrm{T_i})|\ln \mathrm{Sa}(\mathrm{T^*})}$ from Equation (5.3), specifies a distribution of Sa values at all periods. The resulting spectrum distribution is termed as a “Conditional Spectrum”, to be distinguished from the Conditional Mean Spectrum (CMS) that does not consider the variability specified by Equation (5.4).

By utilising the correlation of Sa values across periods, the CS removes the conservatism from the UHS when used as a target for ground motion record selection, and more realistically captures the Sa distributions away from the conditioning period.

The exact CS, incorporating aleatory uncertainties from ground motion parameters and epistemic uncertainties from multiple GMPEs, have been computed and used as more realistic target response spectra that are fully consistent with the PSHA calculations upon which they are based. Further details regarding the calculation of the exact CS can be found in the work of Lin et al. (2013) [130]. Fig. 5.6 shows how changing the spectral acceleration and the target period affects the CS shape. Unlike the UHS, the CS has a varied spectral shape at different conditioning periods. The Sa values of the CS, at their respective conditioning periods, are equal those of the UHS, in other words, the UHS is an envelope of all CS.

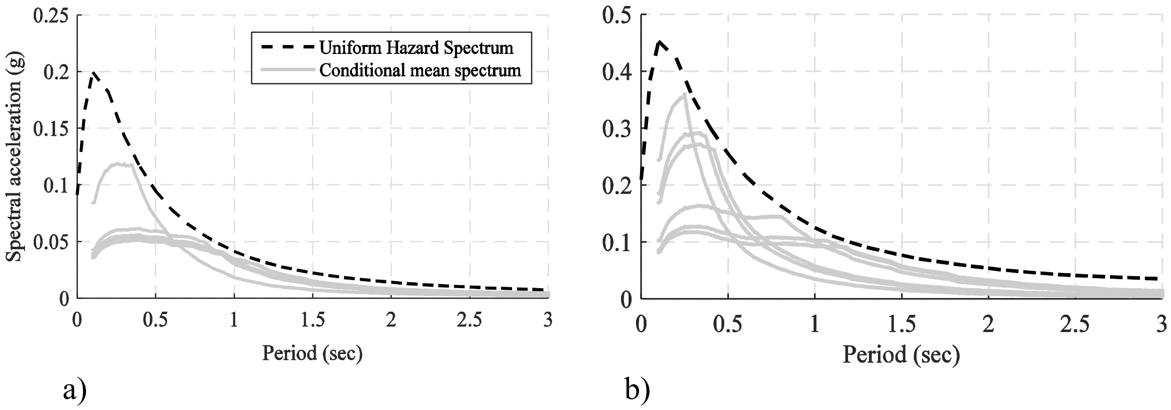

Fig. 5.6. CS conditioned on Sa values at several periods having equal PoE for: a) low and b) moderate-to-high seismicity regions.

Comparing these spectra tells us that, at the conditioning period, both UHS and CS have the same Sa but at longer and shorter periods the UHS is higher in amplitude than the CS. At longer periods, the higher amplitude of the UHS will imply greater loading on the structure as its period lengths and steps into nonlinearity due to the deteriorating behaviour (see Chapter 2); thus, the nonlinear response would be more excited when using ground motions matching the UHS. On the other hand, over shorter periods the difference between both spectra implies that ground motions matching the UHS will excite higher modes in the structure to greater extent than ground motions that match the CS. In other words, response of structures with higher modes of vibration as well as those characterised by period elongation will be overestimated when the UHS is adopted as a target spectrum for ground motion record selection instead of the CS. Therefore, in both cases it is expected to observe larger structural response amplitude (less performance). The impact of this change in target spectrum on the resulting structural response is summarised in Section 5.4.

The response spectrum prescribed in current building codes is often a UHS. Fig. 5.7 shows the UHS for low (left) and moderate-to-high (right) seismicity regions along with the elastic response spectra of EC8 as well as the CMS obtained in this study. The UHS have been validated against the results of the SHARE project which are available at EFEHR [127].

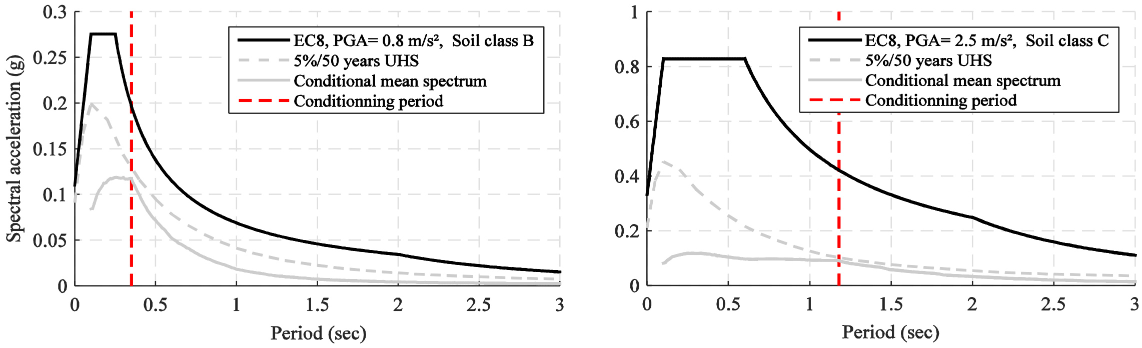

a) b)

Fig. 5.7. EC8 elastic response spectrum, 5%/50 years UHS and CS for: a) low and b) moderate-to-high seismicity regions.

One can notice discrepancies between the elastic response spectra defined in EC8 for low and moderate-to-high seismicity regions and the UHS (5%/50 years). This is because the Hazard Models and GMPEs used in the UHS computation are different from the background data adopted in the development of the elastic response spectra of EC8 for the Portuguese territory. It is worth noting that the data employed in the UHS computation is based on the most recent and available hazard models developed for Europe [127].

5.3.3. Ground motion record selection procedure

Having the target spectra identified and computed, ground motions can then be selected from a ground motion database to match each target spectrum. Suites of ground motions can be selected and scaled using a computationally efficient algorithm so that they collectively match the entire distribution of the CS. The SelEQ tool (Macedo and Castro (2017)) [110] was employed to build the CS for each of the selected sites and structures, for a probability of occurrence of 5% in 50 years (return period of 975 years). Since the spectral shape changes with the intensity level, a selection of multiple sets of records at multiple intensity measure (IM) levels is required to account for such changes in the spectral shape and use multiple stripe analysis “MSA” instead of IDA. In this study, a simplified approach was assumed adopting a single intensity level of 5% in 50 years corresponding to an intermediate level between 2% and 10% in 50 years (return period of 2475 and 475 years, respectively). It is worth noting that, for the Portuguese territory, the seismic hazard model developed in the SHARE research project [127] was used in combination with additional hazard (Vilanova and Fonseca (2007)) [131]. The GMPEs considered were Atkinson and Boore (2006) [132] and Akkar and Bommer (2010) [133] with a weight of 70% and 30%, respectively (Vitor Silva (2013) [134]).

Sets of 40 ground motion records obtained from real earthquake events were selected for each structure from the PEER strong ground motion database [102] and scaled to match the mean and standard deviation of the previously calculated CS. Both linear and logarithmic scale plots are presented in Fig. 5.8 to orient the reader familiar with either format. The response spectra are computed using 5% damping.

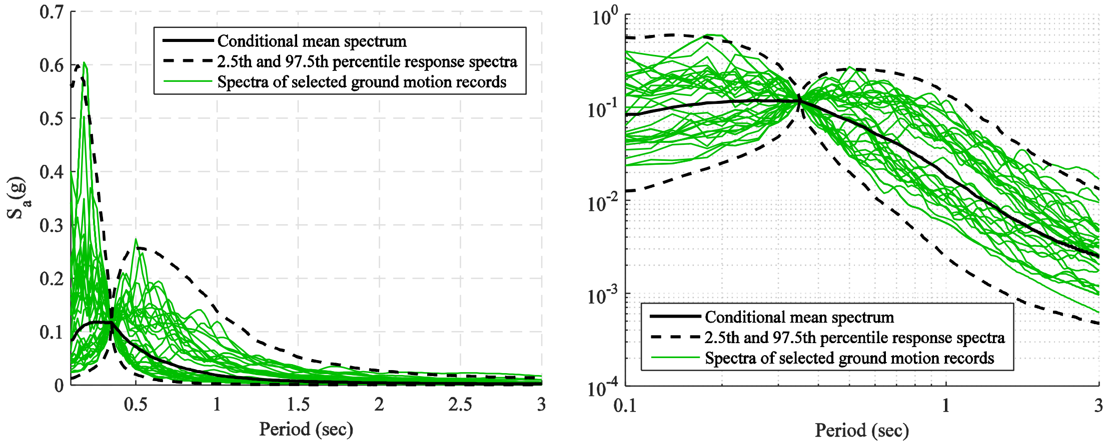

a) b)

Fig. 5.8. Example of response spectra of selected ground motion records along with CS for Sa (T_1=0.35 sec) having 5%/50 years PoE: a) linear and b) logarithmic scale.

When we look at Fig. 5.9 from the upper right to the down left, we can notice as the intensity level increases, so does the disaggregated mean ε value and the spectral shape of the CS becomes more peaked at the conditioning period. Therefore, it is deemed necessary to select a separate set of ground motion records at each amplitude to reflect those target spectra. This draws the attention to the importance of matching the whole spectrum instead of paying attention to only the vicinity of the dominant structural period of vibration (*i.e.*, the fundamental period for low- and mid-rise buildings) because the structures will be driven to high levels of nonlinearity which may cause significant effective-period lengthening (see Section 5.5.4b).

For a hazard-consistent ground motion record selection, rather than trying to model target M, R and ε values, one might use M, R and ε to determine a target spectral shape and select records based on this target alone. This should increase the number of available records, because some records with *incorrect* M, R and/or ε values may have the *correct* spectral shape. Following the above-described approach, only scaling of records is employed, the frequency content of the records is not modified as opposed to other technics such as the one based on wavelets algorithm proposed by Abrahamson (1992) [135] and Hancock et al. (2006) [136].

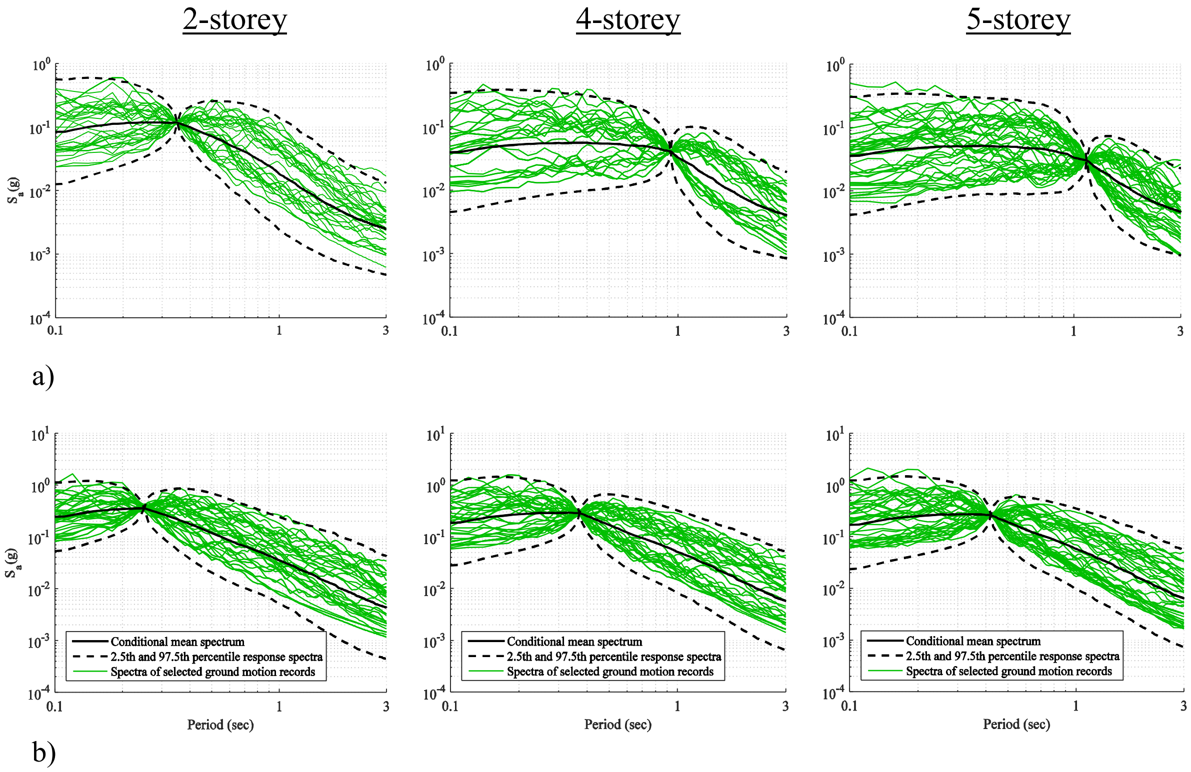

Fig. 5.9. Response spectra of ground motion records selected based on CS for Sa having 5%/50 years PoE for different conditional periods: a) low and b) moderate-to-high seismicity regions.

5.4. Effect of ground motion record selection procedure on the performance of sheathed CFS-SWP system

In order to reveal the effect of spectral shape on the structural response, the same FE models of some archetype structures studied in Chapter 3 (PG1 and PG3) were selected, therefore, an opportunity is provided for comparison and verification and make sure that the difference in the results would stem from the differences in input seismic loads rather than from the modelling aspect.

In Fig. 5.10, the IDA curves for archetype 9 of PG 3 (see Chapter 4) based on FEMA P695 far field records set are shown together with to the IDA curves corresponding to records set selected following the strategy presented in Section 5.3. Because of the omission of spectral variability in ground motion histories around the conditioning period, a reduced scatter is observed particularly at the elastic region, this is due to the fact that, at the fundamental period, all ground motion records have the same spectral acceleration. This smaller dispersion implies the median can be estimated more efficiently (*i.e.*, with fewer dynamic response analyses).

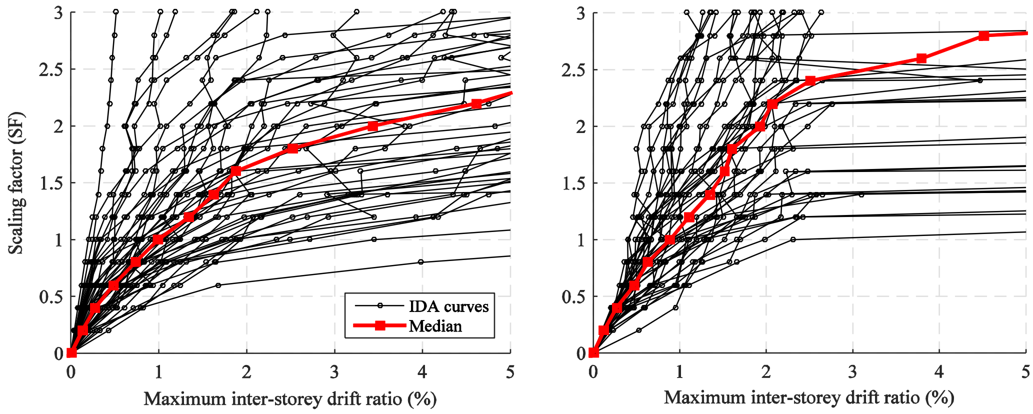

a) b)

Fig. 5.10. IDA curves: a) FEMA P695 far field and b) CS records set.

As for the probability of collapse, fragility curves derived based on both ground motion record selection strategies are shown in Fig. 5.11. For a given spectral acceleration level, there is much lower probability of collapse when using ground motion records selected based on the CS than when adopting FEMA P695 far field records set. However, the FEMA P695-based results culminate in lower standard deviation than the CS-based results. This is explained by the fact that ground motions selected to match the CS additionally account for the spectral variability at longer and higher-modes periods unlike those of FEMA P695 far field set.

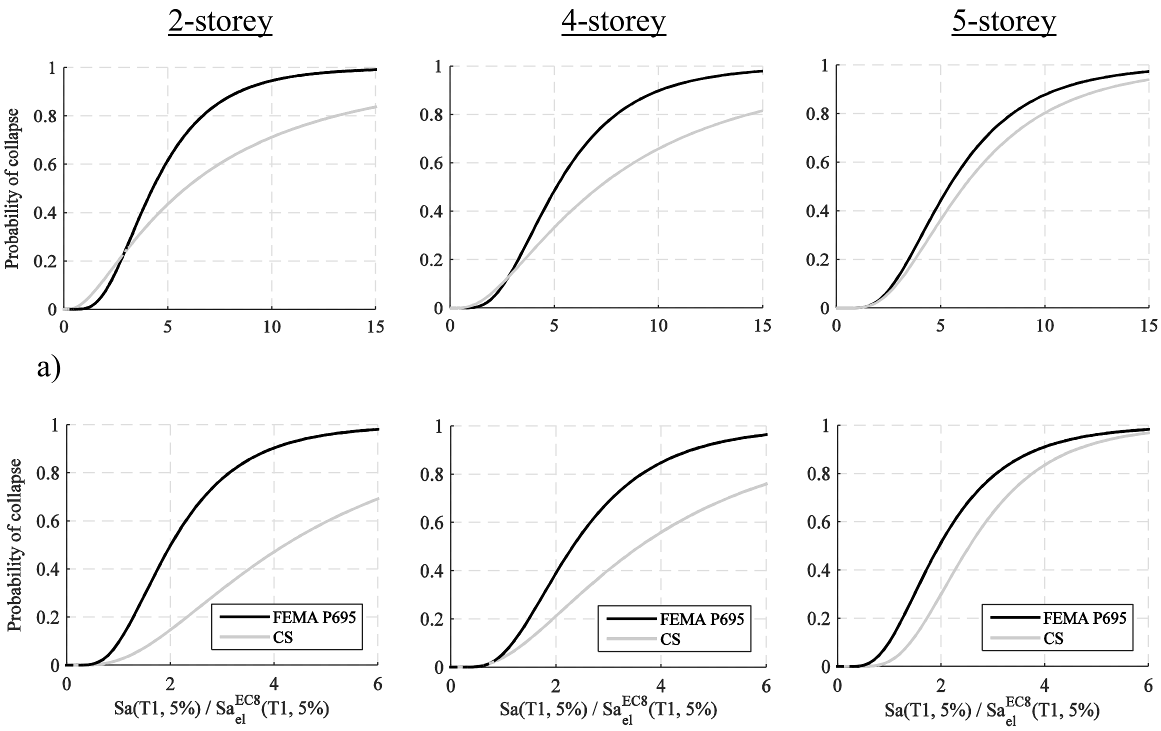

a)

b)

Fig. 5.11. Comparison of FEMA P695- and CS-based fragility curves for: a) low and b) moderate-to-high seismicity regions.

These results demonstrate the reliability and effectiveness of the proposed seismic design procedure and the suitability of adopting a behaviour factor q equal to 2 for the CFS-SWP system as suggested in the work of Kechidi et al. (2017) [137], where performance groups designed for moderate-to-high seismicity regions have not fulfilled the FEMA P695 acceptance criteria under Maximum Considered Earthquake level. Following the CS approach in selecting ground motion records set, showed a superior structural performance when compared to FEMA P695-based results. This proves the influence of the spectral shape effect on the seismic performance of the buildings and draws attention to the consequences of deviating from the target CS when selecting sets of ground motion records. A similar conclusion has been drawn by Haselton and Baker (2006) [138]. Findings from these analyses have potentially important implications for seismic assessments in both future building codes and PBEE.

5.5. Probabilistic seismic performance and risk assessment of CFS-SWP structures compared to MRF systems

In this section, a comparison of the probabilistic seismic performance and risk assessment between CFS-SWP and steel MRF systems, is presented as follows:

- A set of 12 building structures of both systems, with 2-, 4- and 5-storey, have been designed for two seismic intensity levels. To simulate their nonlinear behaviour, the structures were modelled adopting recently developed deteriorating hysteresis models.
- Based on PSHA, structure- and site-specific selection of ground motion records for IDA is performed adopting the CS as a more realistic target response spectrum.
- Subsequently, the seismic risk is evaluated over the structure lifetime (*i.e.*, 50 years) in terms of the annual probability of exceeding the DL, NLC and NC limit states.

It is to note that the design and modelling aspects of the CFS-SWP system, for a brevity, are not detailed in this chapter since the reader has become familiar with via Chapters 3 and 4.

5.5.1. Seismic design provisions for conventional steel MRFs

The response of a conventional steel MRF depends on the characteristics of its fundamental components namely the columns, beams and connections (*e.g.,* beam-to-column connection). In this structural system, the shear yielding of the panel zone as well as the flexural yielding of the beams represent the main source of energy dissipation. In this study, the MRFs have been firstly designed to resist gravity loads in accordance with the provisions of Eurocode 3 (EC3) [5] for sectional resistance, stability checks and deflection serviceability limits.

Afterwards, seismic design was performed in accordance with the EC8 provisions considering a behaviour factor (*q*) equal to 4. Two limit states were verified, namely DL and ultimate limit states (*i.e.*, NLC). Although it is not specifically defined in EC8 [1], it is considered by the author that the first step of the design process should be the DL limit state checking, particularly in the case of flexible structures located in moderate-to-high seismicity regions (see Section 5.5.2). Regarding the NLC limit state, the design process consists of checking the dissipative elements followed by capacity design of non-dissipative elements. The capacity design of the non-dissipative members was conducted according to the EC8 criteria with the modifications proposed by Ahmed Elghazouli (2010) [139]. As for the design of the panel zone, a "balanced" design approach was adopted in this study [140] which establishes that panel zones should be proportioned such that yielding of these elements occurs at similar load levels that develop flexural plastic hinges in the beams. The potential influence of second-order P-Δ effects should be checked through the calculation of the inter-storey sensitivity coefficient θ. In this study, the θ coefficient was limited to 0.2, meaning that an amplification of the lateral load had to be performed during the design process [1]. Furthermore, the DL performance requirement was considered in the seismic design by limiting the inter-storey drift ratio during a frequent earthquake event to 1% of the storey height.

5.5.2. Description of the study

Two-, 4- and 5-storey CFS-SWP and MRF buildings have been selected and then designed. Table 5.1 summarises the parameters used to describe the design space where two sites located in Portugal, namely Porto (north) and Lagos (south) were considered to reflect, respectively, low and moderate-to-high seismicity regions. The acceleration and displacement elastic response spectra are plotted in Fig. 5.12. The storey heights of CFS-SWP and MRF systems are 2.74 m and 3.50 m, respectively, with a MRF first floor height equal to 4.50 m.

Table 5.1. Parameters of the design space for CFS-SWP and MRF systems.

Building	**Number of storeys**	**Design load level**	
		Occupancy	**Seismicity**
1	2	Residential	Low (PGA = 0.8 m/s², soil class B)
2	4		
3	5		
4	2		Moderate-to-high (PGA = 2.5 m/s², soil class C)
5	4		
6	5		

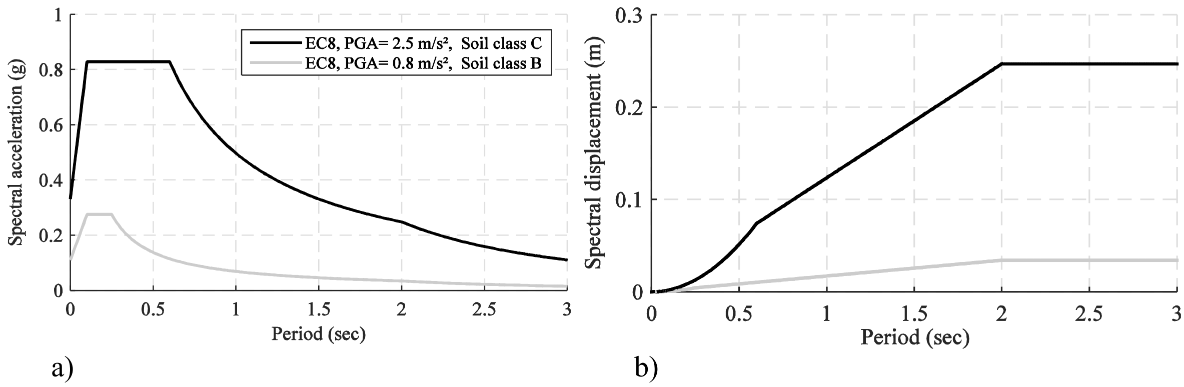

Fig. 5.12. EC8 elastic response spectra for the two seismic intensity levels: a) acceleration and b) displacement.

A simple floor plan was selected for the buildings studied herein (Fig. 5.13). For the CFS-SWP system, rectangular buildings with perimeter shear walls that resist lateral forces for each direction intending to represent a typical CFS framed structure where the length of the lateral load resisting system is proportional to the lateral demand (Fig. 5.13a). As for the MRF system, the structural configuration in plan is shown in Fig. 5.13b. The buildings consist of three MRFs spaced at 6 m. Resistance to seismic loads is provided by the three frames in the longitudinal direction and by a bracing system in the transverse direction. As depicted in Fig. 5.13, the building structures are analysed in the longitudinal (horizontal) direction.

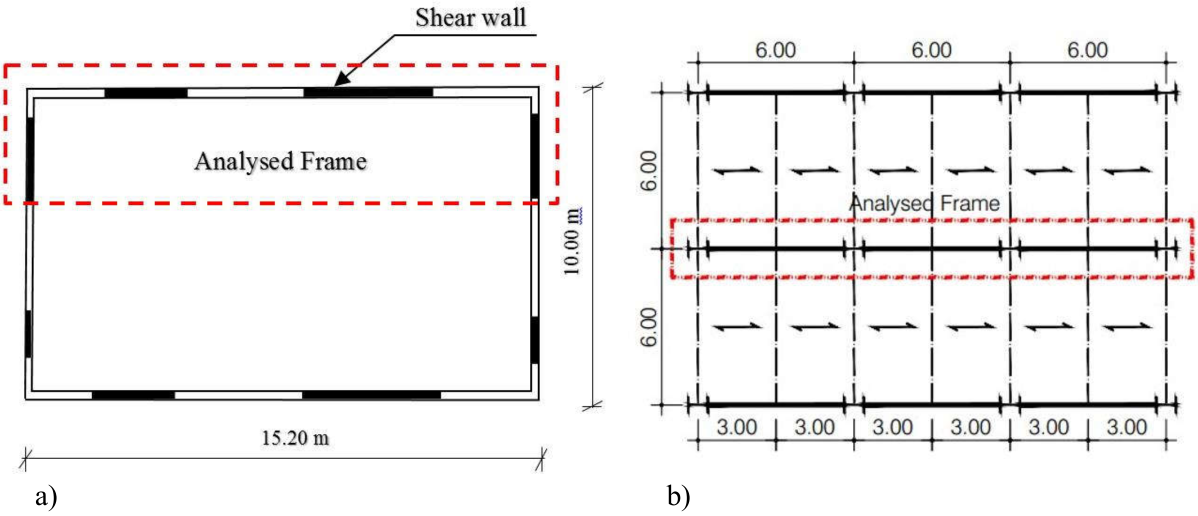

Fig. 5.13. Plan views of: a) CFS-SWP and b) MRF buildings.

Live loads of 2.0 kN/m² and 1.0 kN/m² were applied on the intermediate and roof floors, respectively. The seismic mass was derived through conversion of the vertical loads corresponding to the quasi-permanent combination.

European HEB and IPE sections were adopted for the columns and beams sections for MRFs, respectively, assuming a yield strength of 275 N/mm². The calculated cross-sections sizes, obtained based on the design procedure detailed in Section 5.5.1, are listed in Table 5.2. Moreover, the structural period-based ductility (μ_T) and lateral overstrength (Ω_0) were evaluated according to the FEMA P695 criteria [6] for all buildings of both structural systems from nonlinear static analyses (see Section 5.5.4a).

Table 5.2. MRFs design parameters.

Building	**T_1 (sec)**	**Floors**	**Beams**	**Interior columns**	**Exterior columns**	**Design criterion**	**Ω[b]**	**μ[b]**
1/4[a]	0.81	1	IPE300	HEB 240	HEB 200	P-Δ/ resistance	21.97/3.04[c]	6.56
		2	IPE300	HEB 240	HEB 200			
2/5	1.07	1	IPE330	HEB 360	HEB 300	P-Δ	22.26/3.13	5.56
		2	IPE330	HEB 360	HEB 300			
		3	IPE300	HEB 320	HEB 280			
		4	IPE300	HEB 320	HEB 280			
3/6	1.18	1	IPE400	HEB 360	HEB 320	P-Δ	20.16/3.12	6.52
		2	IPE360	HEB 360	HEB 320			
		3	IPE330	HEB 340	HEB 320			
		4	IPE300	HEB 340	HEB 320			
		5	IPE300	HEB 320	HEB 300			

[a] Similar design (columns and beams cross-section) for both buildings;
[b] Static pushover analysis outcomes;
[c] Two separated numbers correspond to the results of buildings having same number of storeys design for low and moderate-to-high seismicity.

The design procedure for the MRFs at both seismic intensity levels led to similar structural element sizes (beams and columns cross-sections). The main reason behind these design outcomes is the fact that the second order stability effect (P-Δ) was the governing design criterion rather than strength requirements as opposed to CFS-SWP structures, where their design was mostly governed by strength demands. Particularly, in the case of buildings designed for a low seismicity site (Porto), the calculated shear demand was much smaller than the minimum possible SWP shear capacity, which resulted in a relatively higher lateral overstrength (stiffness) of the whole system in comparison to those of the same system (CFS-SWP) designed for the sites corresponding to moderate-to-high seismicity (Tables 3.4). Since the governing design criterion of the MRFs is primarily a drift restriction (P-Δ) due to their relatively high ductility, the resulted static overstrength factors (Table 5.2) are much higher than those of CFS-SWP structures.

The obtained solutions for both structural systems are now compared in terms of their weight. Fig. 5.14 shows the weight of each solution.

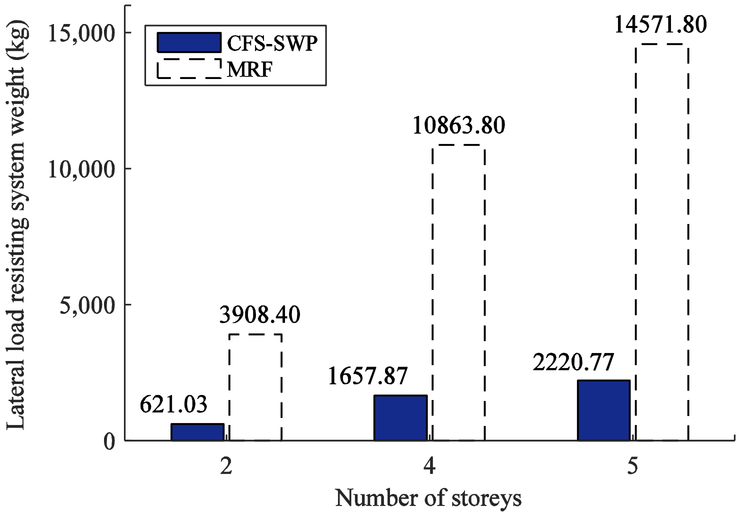

Fig. 5.14. Lateral load resisting system weight of CFS-SWP and MRF systems designed for Lagos site.

It is clear from Fig. 5.14 the difference in steel weight between CFS-SWP and MRF systems. From these results, it is possible to conclude that CFS-SWP system uses approximately 15% of the steel weight found in its MRF counterpart. It is worth noting that the above-mentioned weight ratio was determined on the basis of merely the lateral load resisting system components rather than all building components such as the floor diaphragms, vertical load bearing walls, partition walls, exterior and interior finishes, fire protection etc. Moreover, it should be noted that this significant difference in weight resulted in structures with very different dynamic characteristics, as demonstrated by the fundamental periods of vibration listed in Tables 3.4 and 5.2. In general, CFS-SWP structures have lower periods of vibration than MRFs (particularly those designed for Lagos) and hence are expected to develop lower levels of deformations.

5.5.3. Numerical modelling

The key aspect in conducting a probabilistic seismic performance assessment is the accurate estimation of the nonlinear structural response with the least rate of uncertainty which is a twofold issue: (*i*) the formulation of reliable numerical models, and (*ii*) the adoption of ground motion records that are consistent with the seismic hazard of the site for which the seismic design was carried out. The OpenSees finite element (FE) software [76] has been adopted in this study to model the structural systems and to conduct nonlinear static and dynamic analyses.

For MRFs, beams and columns are represented with an elasticBeamColumn element. The material nonlinear behaviour is considered through a concentrated plasticity hinge approach in which column and beam ends are assigned a hysteresis behaviour that takes into account strength and stiffness deterioration effect (Lignos and Krawinkler (2011)) [141]. Fig. 5.15 illustrates an example of a backbone curve and hysteresis loops for a European HEB 300 profile along with the stiffness and deterioration parameters that have been calibrated following the procedure proposed by Araújo et al. (2017) [142]. The effect of the axial load on the flexural capacity of the columns was taken in an approximate way. A preliminary pushover analysis has been conducted first in order to evaluate the expected average axial force under the combined actions of gravity and lateral loading as follows: $P_{grav} + 0.5 \text{ x } P_E^{max}$, where P_{grav} and P_E^{max} are the axial force due to gravity loads and the maximum axial force due to lateral loading, respectively (Zareian et al. (2010) [143]). Consequently, the backbone curve is adapted by reducing the flexural strength according to interaction equations proposed in EC3-1-1 [5]. However, no modification of the stiffness and deterioration parameters is made in this approach. On the other hand, the panel zones are modelled using a beam-column joint element "Joint2D" that is available in OpenSees. The rotational spring utilised to represent the panel zone is assigned the Helmut Krawinkler (1978) [144] tri-linear moment-distortion behaviour. It is worth noting that no deterioration has been considered for the panel zone behaviour. Fig. 5.16 illustrates the adopted modelling strategy for the performance assessment of MRFs. Gravity loads were applied to the model as initial loads.

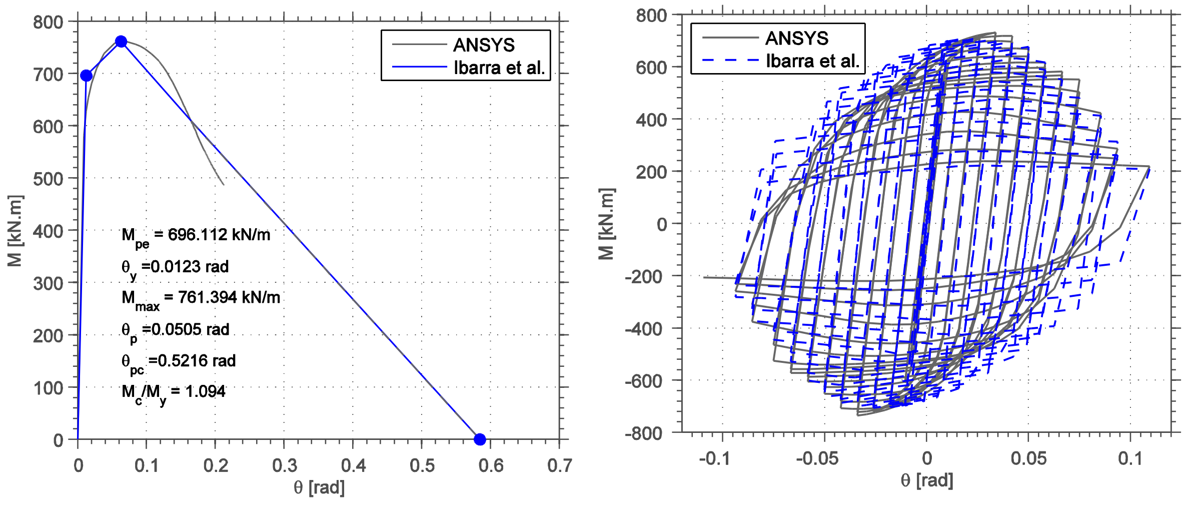

a) b)

Fig. 5.15. Calibration of the Modified Ibarra–Krawinkler deteriorating model for an HEB 300 steel profile: a) monotonic and b) cyclic behaviour.

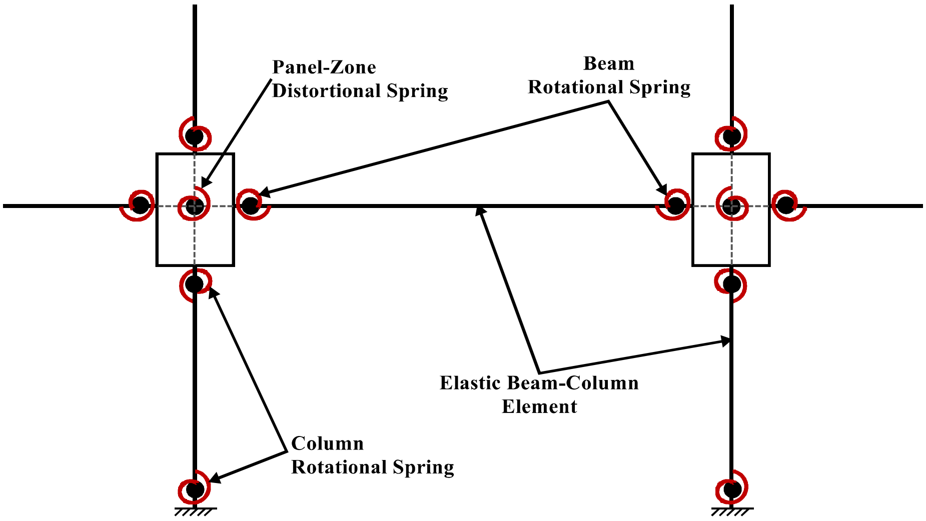

Fig. 5.16. OpenSees FE model of steel MRF: joint zone, column and beam ends represented by rotational springs [145].

5.5.4. Intensity-based assessment

a) Nonlinear lateral behaviour

Nonlinear static analysis (pushover) was carried out under displacement control on all structures of both systems in order to evaluate their lateral behaviour. To initiate the analysis, the lateral loads were distributed along the height of the structures following a lateral load pattern proportional to the first-mode of vibration of the structures. Before running the analysis, the models have been subjected to initial loads corresponding to the gravity loads. Fig. 5.17 shows an example of pushover curves of CFS-SWP and MRF 5-storey structures designed for the Lagos site.

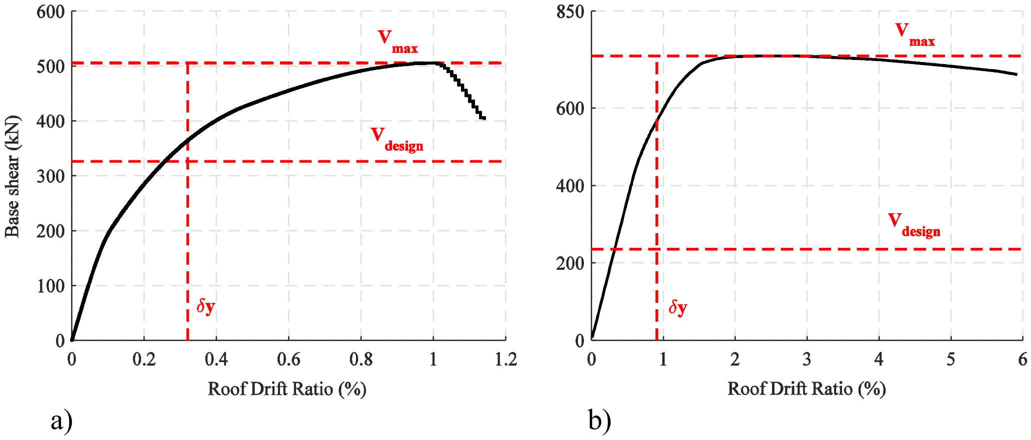

Fig. 5.17. Pushover capacity curves of building 6: a) CFS-SWP and b) MRF systems.

As opposed to the MRF system, for which the behaviour is linear elastic at low loading level, Fig. 5.17a shows that the CFS-SWP system exhibits nonlinear behaviour at very low lateral displacements. This characteristic is due to the behavioural complexity of the SWP components and their interaction (see Fig. 2.11). The difference in ductility between the two systems is obvious in Fig. 5.17. This can be attributed, in part, to the design and modelling assumption made for CFS-SWP system, where the chord studs are not continuous along the height of the structure [137]. Additionally, the fact that SWPs are the only lateral load resisting elements of CFS-SWP building system, a clear post-peak drop of the structure's lateral capacity is observed. This contributes to a low level of redundancy of the structural system, which significantly results in a concentration of inelastic demands, notably after failure of one SWP, which ultimately triggers the development of global collapse. Conversely, the capacity curve of the MRF system (Fig. 5.17b) after global yielding is much more stable where plasticity develops gradually in its elements (beams and columns) which lead to a high level of global ductility. The source and level of lateral overstrength observed for both structural systems has been discussed in Section 5.5.2.

b) Nonlinear dynamic response history analyses

The characterisation of the seismic performance of the structures is carried out based on a large number of nonlinear dynamic response history analyses (*e.g.*, 1000 runs for building 1 of the CFS-SWP system) under the sets of ground motion records previously selected, scaled to several intensity levels, known as IDA [105]. Accordingly, various response characteristics under low- and high-shaking intensities are represented.

In this study, and in order to generate the response parameters required for the derivation of the fragility curves, the building models have been subjected to ground motion records sets (40 records per set following the selection procedure described in Section 5.3) scaled for increasing intensity levels until collapse of the structures. Additional analyses are typically performed within the last interval of intensities to determine, as accurately as possible, the collapse intensity within a certain tolerance. In this paper, the 5% damped first mode pseudo-spectral acceleration $Sa(T_1, 5\%)$ (as an abbreviation, $Sa(T_1)$ will be used hereafter) is used as the intensity measure (IM). The term collapse adopted in this study, for both lateral load resisting systems, corresponds to the attainment of 10% of the initial slope of the median of the IDA curves. Since in CFS buildings the SWP is the primary element for resisting the lateral loads, the engineering demand parameter (EDP) was defined as the lateral drift of the SWP which coincides with the inter-storey drift. Values of inter-storey drift equal to 1.0% and 2.1% were adopted for the definition of the DL and NLC limit states (performance levels), respectively.

These values were based on the study performed by Joel Martinez (2007) [106]. Moreover, the lateral drift of a SWP might be lower than the limit value for a given performance level but the internal forces installed on the chord studs might exceed their capacity. Therefore, to determine whether or not the lateral capacity of the SWP has been exceeded, both the SWP lateral drift and strength demand on chord studs have been monitored in all response history analyses. As for MRFs, to be consistent in the comparison and to avoid bias in the results, the inter-storey drift ratio has also been adopted as the EDP. Inter-storey drift ratio limits of 1.0% and 2.5% were considered as per ASCE 41-13 [146] corresponding to the above described two limit states.

The PoE was calculated, based on the IDA results, as the ratio of ground motion records that caused the exceedance of a given performance level at each IM to the total number of ground motion records (40 records). A lognormal cumulative distribution function (CDF) was used to define a fragility curve. The evaluation of the fragility function parameters was based on the maximum likelihood estimation method proposed by Jack Baker (2015) [108]. Figs. 5.18 and 5.19 show the fragility curves obtained for the DL limit state for both CFS-SWP and MRF structures, respectively, in which the x-axis is normalised to Sa (T_1) of the EC8 elastic response spectrum for the serviceability limit state level.

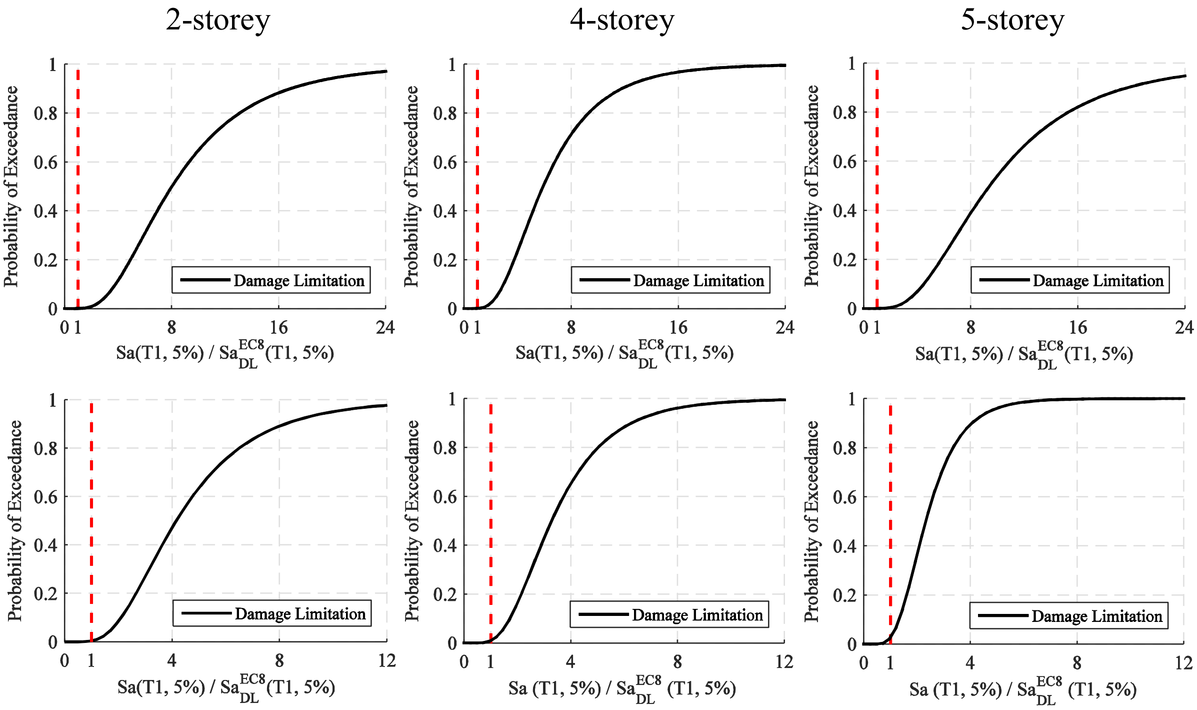

Fig. 5.18. DL limit state fragility curves of the CFS-SWP structures designed for: Porto (top) and Lagos (bottom).

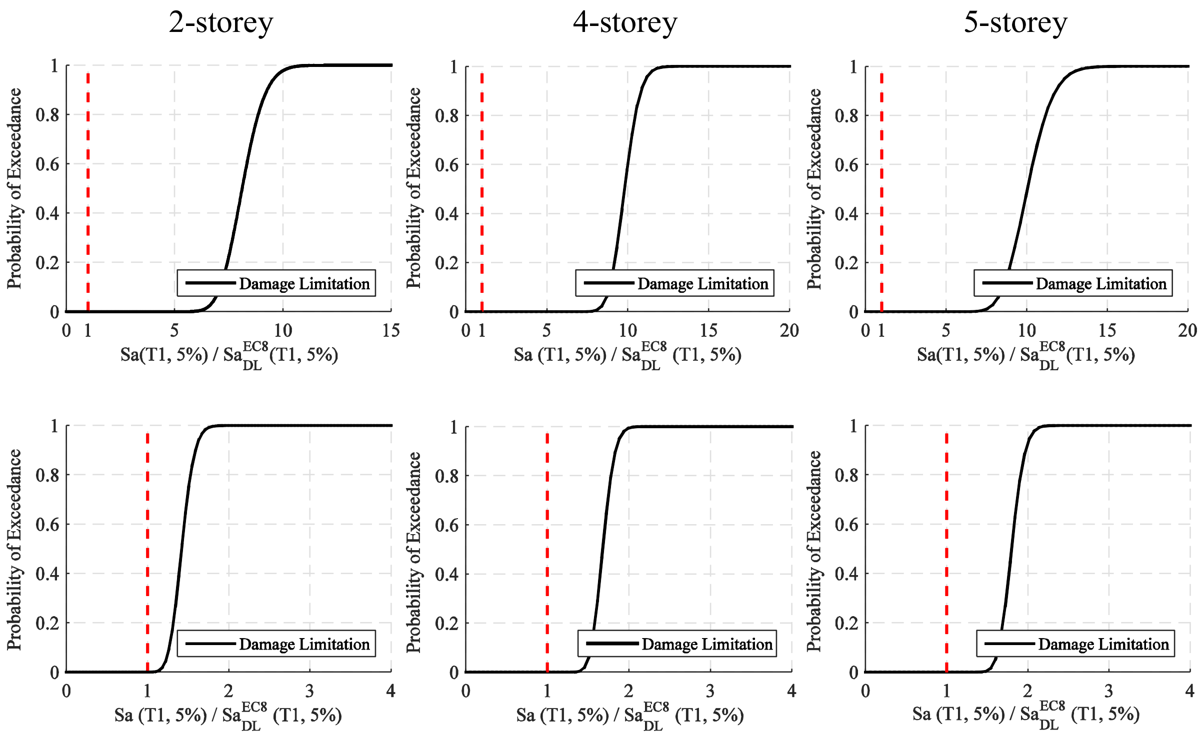
2-storey

4-storey

5-storey

Fig. 5.19. DL limit state fragility curves of the MRF structures designed for: Porto (top) and Lagos (bottom).

The results presented in Figs. 5.18 and 5.19 show that the probability of both structural systems exceeding the limit imposed at the design stage (EC8, 1% inter-storey drift) is extremely low. They also indicate that, for low- to mid-rise buildings, located in low and moderate-to-high seismicity regions, the CFS-SWP system provides an acceptable serviceability (functionality) performance.

Fig. 5.19 shows a reduced standard deviation in the fragility curves of MRFs corresponding to DL limit state. This is explained with the low levels of plasticity that develop in the structures for the seismic intensity level considered, with the regularity of the structural system which has more than 90% of the effective modal mass being mobilised at the first-mode period of vibration (this holds true for CFS-SWP system as well), and, importantly, with the reduced spectral variability of the selected ground motion records at the fundamental period of vibration. On the other hand, for the CFS-SWP system, the fragility curves for the DL limit state are characterised by relatively higher standard deviations (Fig. 5.18). This is justified with the inelastic behaviour of the structural system for low levels of lateral deformation, as discussed in Section 5.5.4a, in addition to the deteriorating characteristics of the hysteresis behaviour of the CFS-SWP system, which results in the lengthening of the fist-mode period of vibration from early stages of the earthquake response. Therefore, the PoE are more sensitive to the spectral shape effect in the case of CFS-SWP system than in the MRF structural system. This emphasises the fact that the impact of adopting the CS, as a target spectrum for ground motion record selection, on the structural response varies depending on the characteristics of the structures being analysed in this study. Nevertheless, the generalisation of this conclusion can only be made based on a detailed study conducted over different building types and intensity measures. As for the NLC and NC limit states, the corresponding results are shown in Figs. 5.20 and 5.21 for CFS-SWP and MRF structures, respectively, in which the x-axis is normalised to Sa (T_1) of the EC8 elastic response spectrum.

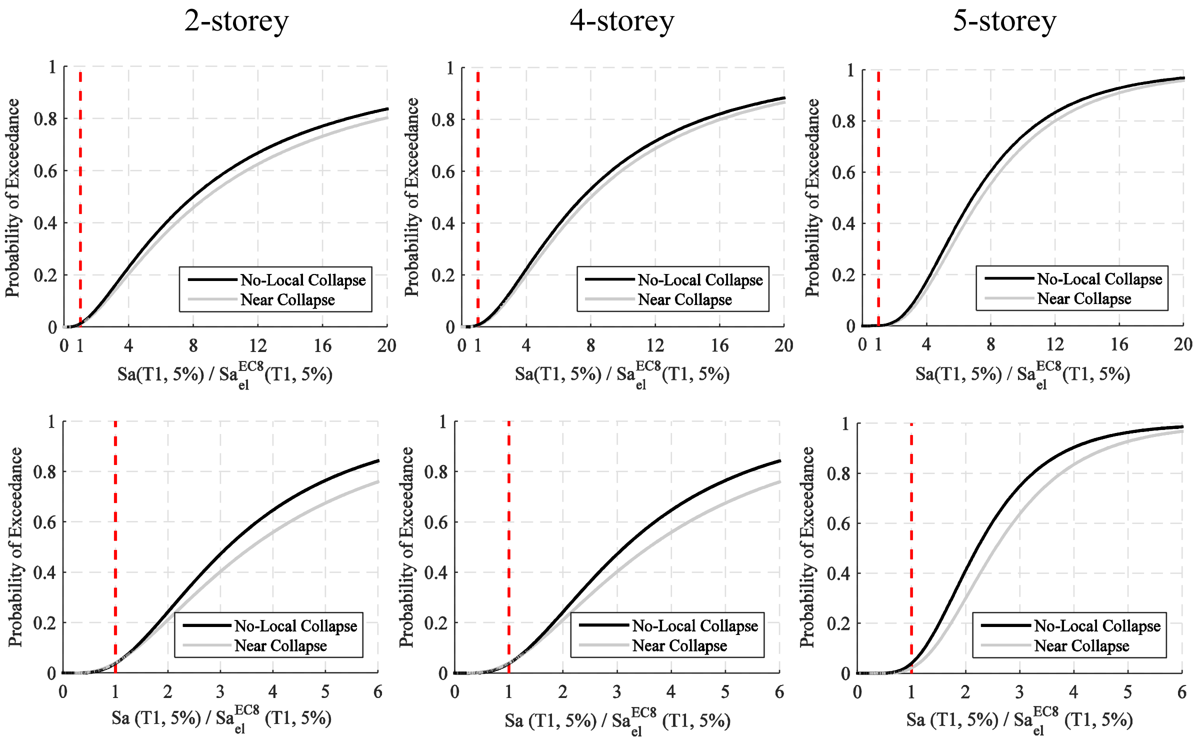

Fig. 5.20. NLC and NC limit states fragility curves of the CFS-SWP structures designed for: Porto (top) and Lagos (bottom).

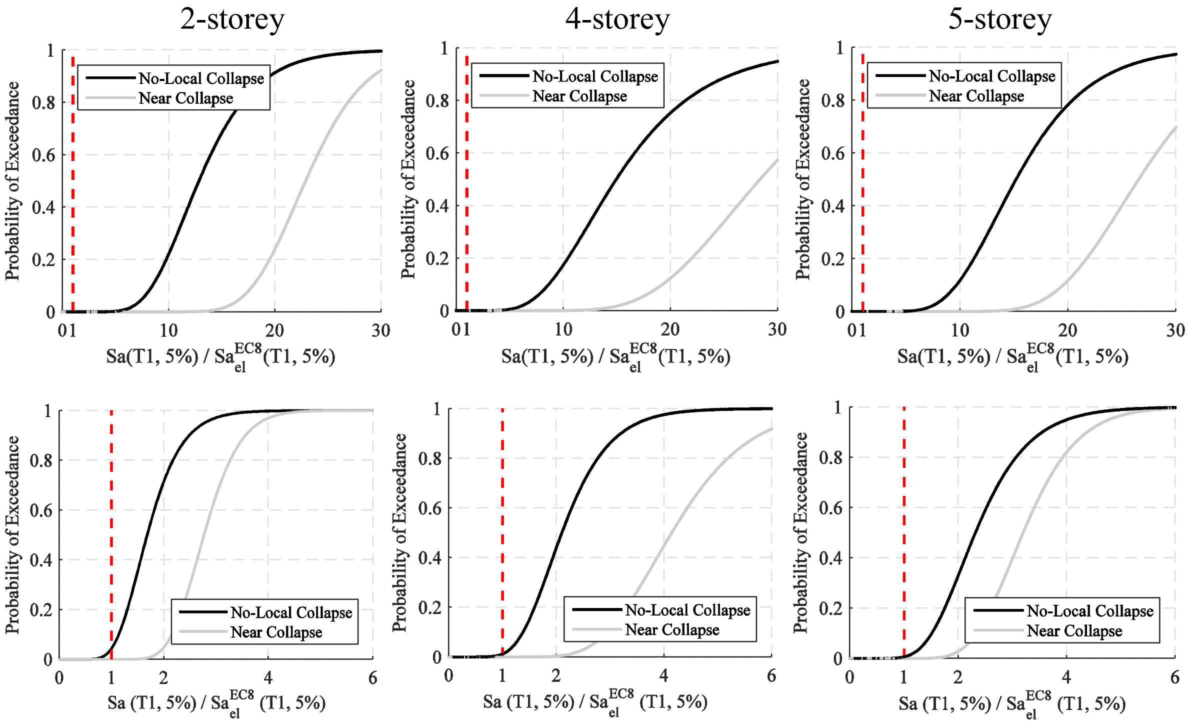

Fig. 5.21. NLC and NC limit states fragility curves of the MRF structures designed for: Porto (top) and Lagos (bottom).

Similarly, when the performance of both systems is compared for the NLC and NC limit states, low levels of PoE are observe. Slightly higher values are obtained for the CFS-SWP system in comparison to the MRF system. The reason behind this observation is found on the different values of inter-storey drift that were adopted to characterise the NC limit state for both structural systems (5% inter-storey drift for the MRF as opposed to 2.5% for the CFS-SWP system). It is worth noting that there is also a clear difference in terms of the global ductility of both structural systems (see Section 5.5.4a). Moreover, the fragility curves of CFS-SWP system for NLC and NC limit states are similar in terms of mean and standard deviation, which indicates that the EDP adopted in this study represents, jointly, the local and global collapse for this structural system, which reveals once more the low level of redundancy of the CFS-SWP system as discussed in Section 5.5.4a.

The results depicted in Figs. 5.20 and 5.21 illustrate the consequence of a drift-controlled seismic design. It is clear that the MRFs exhibit a reserve of strength which is reflected in a resistance against collapse for seismic intensities corresponding to more than two times the design earthquake intensity level (Fig. 5.21). A similar good performance is also observed for the CFS-SWP system (Fig. 5.20).

All the observations made above regarding the fragility curves are expected to have an important impact on the quantification of the seismic risk, which is presented in the following section.

5.5.5. Risk-based assessment

Despite the differences in the fragility curves that have been identified in the previous section, the effectiveness of each structural system for seismic resistance can only be fully assessed based on the evaluation of the seismic risk. The fragility curves of the studied structures are combined with site-specific hazard curves representing the probability of occurrence of earthquake intensities within a specific timeframe (Fig. 5.2). The seismic risk is quantified in terms of the mean annual probability of exceeding the above described limit states (λ_{DL}, λ_{NLC} and λ_{NC}). Computing λ_i involves the integration of the fragility curve over the seismic hazard curve at the design site (the interval of integration adopted herein is from 0.005 g to 3.00 g) using the following integration:

$$\lambda_{\mathrm{i}} = \int_{0}^{+\infty} \mathrm{P}(E_i|S_a) \cdot |\, \mathrm{d}\lambda_{\mathrm{IM}}(S_a) \,| \tag{5.6}$$

Where $\mathrm{P}(E_i|S_a)$ is the probability that the structure will exceed a given limit state when subjected to an earthquake with ground motion intensity level Sa, and $\lambda_{\mathrm{IM}}(S_a)$ is the mean annual probability of exceeding ground motion intensity Sa.

A risk-based assessment is also known as the first step of the “PEER Integral” in Cornell and Krawinkler (2000) [147], “drift hazard” calculation in Krawinkler and Miranda (2004) [34] and “time-based assessment” in ATC-58 (2011) [148]. The SAC/FEMA closed-form probabilistic framework proposed by Cornell et al. (2002) [111] was adopted assuming a biased hazard fitting using a second-order power-law function as proposed by Dimitrios Vamvatsikos (2014) [112].

Fig. 5.22 shows a comparison of the annual PoE of different limit states, between the CFS-SWP and MRF structures. As far as the structures designed for Porto are concerned, the results are uniform in terms of trend, where the risk of exceeding any limit state is, as expected, lower for MRF than for CFS-SWP structures. This results from the higher lateral overstrength of the MRFs which leads to lower PoE of a given limit state in comparison to CFS-SWP structures. A similar conclusion has been drawn by previous researchers [16, 137] based on a sensitivity study in which the lateral overstrength had a significant effect on the fragility data. However, in the case of structures designed for Lagos, particularly the 2-storey building, the MRFs exhibited higher risk of exceeding the DL limit state in comparison to the CFS-SWP structures. This observation may be justified by the fact that the CFS-SWP structures are stiffer, and hence develop lower lateral deformation for the seismic intensity corresponding to the DL limit state. As illustrated in Fig. 5.23, the evaluation of the seismic risk, which involves the convolution of the PoE of the DL limit state and the hazard, results in a larger area for the 2-storey MRF in comparison to the CFS-SWP system. Disaggregation of the annual PoE of the DL limit state (Fig. 5.23) reveals that the lower half of the fragility curve contributed most to the annual PoE for the CFS structure. Conversely, for the MRF structure, the upper half of the fragility curve contributed most to the annual PoE. This observation stems from the lower standard deviation that characterises the fragility curve of the MRF structure.

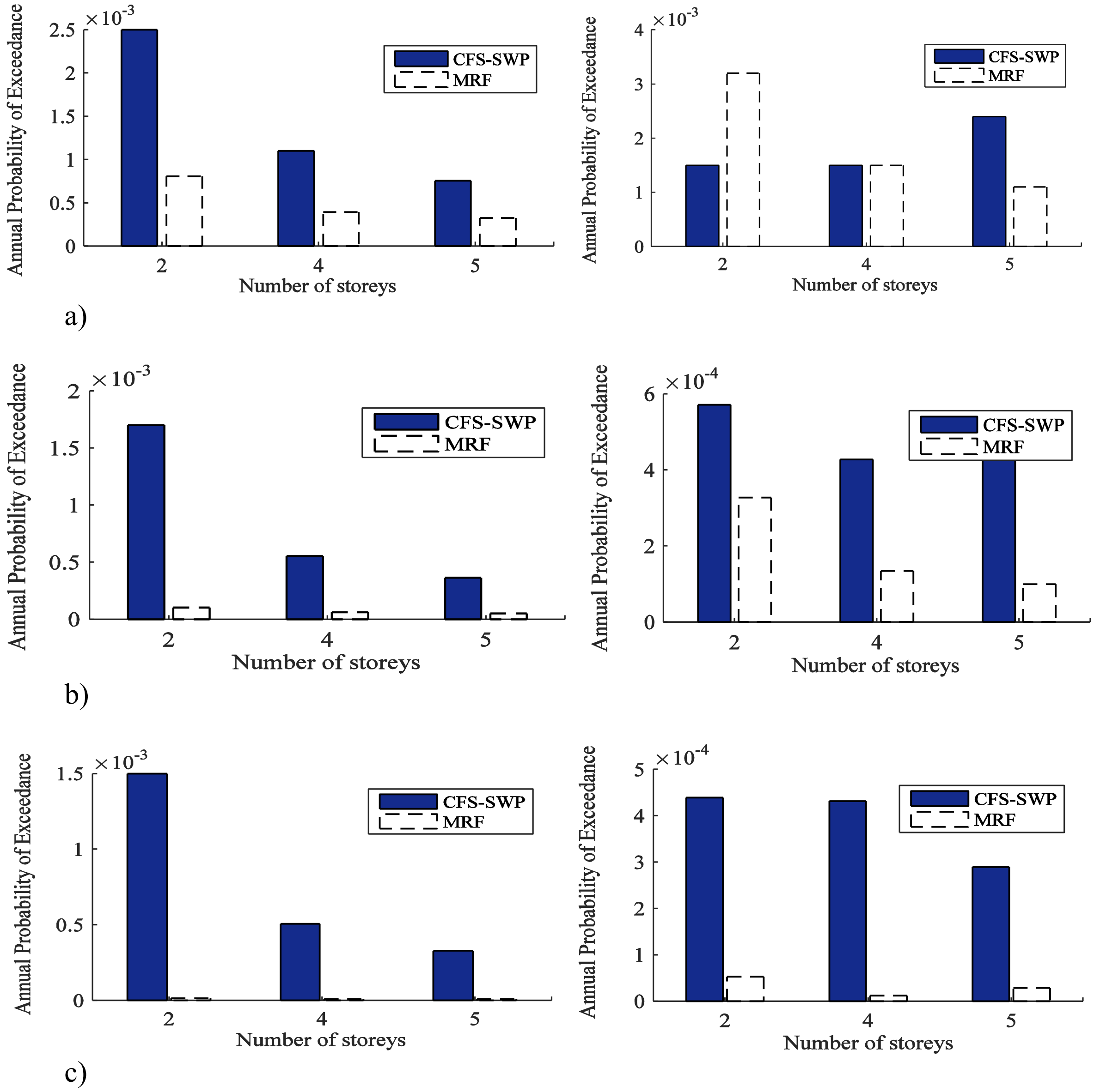

Fig. 5.22. Annual probability of exceeding: a) DL, b) NLC and c) NC limit states for regions of low (left) and moderate-to-high (right) seismicity. (Scales vary per limit state and region).

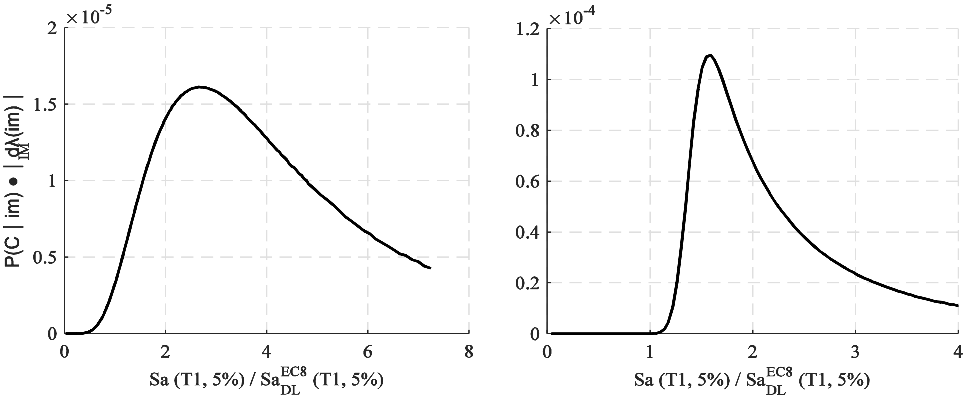

a) b)

Fig. 5.23. λ_{DL}disaggregation curves of the 2-storey buildings located in Lagos: a) CFS-SWP and b) MRF systems.

Disaggregation of the annual PoE of the NC limit state reveals that the intensities corresponding to the lower half of the fragility curve govern the amplitude of the annual PoE. The dominance of intensities lower than the median intensity is driven by the steep slope of the seismic hazard curve at these intensities (Fig. 5.2). Therefore, the Sa (T_1) levels that most contributed to the estimation of the annual PoE values are located towards the left tail of the fragility curve [149]. This is due to the fact that small magnitude earthquakes are more frequent than large magnitude earthquakes. Therefore, when quantifying the annual PoE related to any limit state, it is more important to accurately estimate the left side of the fragility function, where the design Sa(T_1) level is located, than the right side of the function. This represents a good index to reduce uncertainty in the assessment of the annual PoE. Consequently, adopting a state-of-the-art characterisation of the target response spectrum (the exact CS) for the selection of ground motion records fits well with the above described criterion since the absence of variability of Sa(T_1) for all the selected ground motion records and the consistency with the seismic hazard of the site, for all relevant periods, is ensured. This is in line with the recommendation made by Lin et al. (2013) [150] where the CS, for a risk-based assessment purpose, is considered as the most accurate target spectrum among UHS and CMS for the selection of ground motion records.

The annual PoE (risk) associated to the three limit states over the lifetime of the CFS-SWP and MRF structures are summarised in Table 5.3. Following the approach proposed by Pinto and Franchin (2014) [151] for extracting general limits of the annual probability of failure for different building classes and limit states, a simplified expression 2.25/T_R (where T_R is the return period), which is based on the hazard curve fitting, is adopted. Since the structures studied in this chapter were designed for residential building occupancy, Class II buildings (ordinary) was considered which led to values of 4.5E-02, 4.7E-03 and 2.3E-03 for DL, NLC and NC limit states, respectively.

Table 5.3. Annual probability of the CFS-SWP and MRF structures exceeding different performance limit states.

Building	**DL**			**NLC**			**NC**		
	CFS-SWP	**MRF**	$\overline{\lambda_{DL}}$	**CFS-SWP**	**MRF**	$\overline{\lambda_{NLC}}$	**CFS-SWP**	**MRF**	$\overline{\lambda_{NC}}$
1	2.50E-3	8.06E-4	3.0E-2	1.70E-3	1.02E-4	4.7E-3	1.50E-3	1.34E-5	2.3E-3
2	1.10E-3	3.92E-4		5.54E-4	6.21E-5		5.06E-4	7.41E-6	
3	7.55E-4	3.24E-4		3.63E-4	4.96E-5		3.28E-4	7.92E-6	
4	1.50E-3	3.20E-3		5.71E-4	3.27E-4		4.39E-4	5.30E-5	
5	1.50E-3	1.50E-3		4.27E-4	1.34E-4		4.31E-4	1.17E-5	
6	2.40E-3	1.10E-3		4.35E-4	9.94E-5		2.89E-4	2.83E-5	

As illustrated in Table 5.3, all the structures considered in this study fulfil the prescribed limits. It is worth noting that the calculation of seismic risk is dependent on many factors and the associated uncertainty is substantial, where a small change in the hazard curve fitting could induce a significant increase or decrease on the seismic risk. Moreover, the approximation in the fit of the lognormal distribution that was adopted to derive the fragility curves also contributes to an uncertainty in the estimation of the seismic risk. This is deemed relevant, even when the parameters of the lognormal distribution are estimated using the maximum likelihood fitting method [108]. Therefore, special care should be devoted to this source of uncertainty in risk-based assessment studies, as also referred in previous works [152, 153]. Moreover, it is worth noting that, in this study, only the aleatory uncertainties have been taken into account through the consideration of the record-to-record variability. On the other hand, the epistemic uncertainties are knowledge-based and are most related to the physical properties of the structure and its modelling parameters. Since the level of knowledge in modelling the two types of structural systems is similar, the introduction of these uncertainties would affect the absolute value of the seismic risk, but would not have a significant impact on the relative comparison of the seismic performance of the two structural systems.

Annexes B and C of Eurocode 0 [154] prescribe a general limit of 1.E-04 probability of failure over 50 years for buildings under ULS effect; as illustrated in Table 5.3, some structures do not fulfil the prescribed limit. Note that it would be only possible to achieve this limit if the designed structure would not certainly collapse from ground motions with 1% probability of occurrence in 50 years (return period of 4975 years). Such a ground motion is extremely rare which is, from the author's perspective, not economical to design a residential structure to withstand such rare events. This observation is consistent with what has been concluded by other researchers [117, 155, 156].

5.6. Conclusion

The main objective of the research presented in this chapter is the quantification of the seismic risk of the CFS-SWP adopting the more common conventional steel MRF as a benchmark system. Two-, 4- and 5-storey building of both structural systems have been designed for two different sites located in Portugal and for two seismic intensity levels. Seismic design was conducted based on the European seismic provisions, taking into consideration some recommendations previously proposed by the author regarding the design of CFS-SWP systems for seismic resistance. The structures were modelled using the OpenSees software adopting novel deteriorating hysteresis models that are capable of reasonably capturing the structural response up to the onset of collapse. PSHA was conducted to characterise the seismic hazard. IDA was performed using site-specific ground motion records sets selected based on a realistic target response spectrum (CS) derived from PSHA disaggregation data. For both structural system types, the annual PoE for predefined limit states were determined. The main conclusions drawn from this study are listed as follows:

- The results showed the potential benefit of using lightweight cold-formed structural members to withstand lateral loads in low- and mid-rise buildings which favours the economical aspect without a significant cost in the structural performance.
- The values of the annual PoE shed light on the need for adopting a realistic target response spectrum for the selection of a ground motion record set. The obtained results reveal a non-negligible influence of the spectral shape of the ground motion records on the structural response, particularly for structural systems that have a deteriorating lateral behaviour and develop inelastic behaviour at low levels of deformation.
- The analyses conducted in this research showed that the probability of violating any limit state (DL, NLC and NC) falls within the prescribed limits. In general, MRFs are associated to lower levels of seismic risk. Nevertheless, the seismic risk associated to CFS-SWP system is still acceptable. Therefore, the latter can be considered as a reliable structural solution in achieving performance-based objectives for low- and mid-rise buildings located in low and moderate-to-high seismic areas.

CHAPTER 6

NUMERICAL STUDY ON THE BEHAVIOUR AND DESIGN OF SCREW CONNECTED BUILT-UP COLD-FORMED STEEL COLUMNS VALIDATED BY EXPERIMENTAL RESULTS

6.1. Introduction

Built-up cold-formed steel (CFS) members are often assembled and used in low to mid-rise CFS framed buildings where higher axial capacity or greater local system rigidity is required. Typical examples include chord studs in CFS framed shear walls (see Figs. 1.2 and 2.11), as end studs on orthogonally intersecting walls, headers/jambs in window and doorway openings, and roof truss members. Although they can be composed of many different cross-section types and assembled in many different configurations, typical built-up sections include the back-to-back "I" and toe-to-toe "box" sections, which are doubly symmetric and are assembled using traditional CFS lipped channel sections. These built-up sections can offer an axial compression capacity more than twice that of the individual members if composite action is developed through the stud connectors, which can be screws, bolts, welds, or battens.

The motivation for the experimental and numerical work presented in this chapter is to study the composite action, prevailing buckling modes, post-peak behaviour, and failure modes of a series of built-up CFS column specimens. The aim is to specifically understand which components of a column, as constructed and installed in CFS structures, affect the composite action under concentrically-applied compressive loads. The two back-to-back channel sections used (362S162-68 and 600S137-54 using AISI-S100 (2016) [60] nomenclature) are studied as single and double studs with varying web interconnection layouts (using screws), with all columns built with or without oriented strand board (OSB) sheathing. Further, advanced shell finite element (FE) models, validated with test results, are completed in ABAQUS [8] with nonlinear geometry, material, fastener, and contact behaviour. Model complementary results that are not available experimentally such as quantifying individual fastener forces, exploring friction and contact in full details, are examined as well. The ultimate goal of this study is to improve existing design guidelines in which all relevant failure modes are considered in the design of built-up CFS columns.

6.2. Current built-up CFS column design provisions

The AS/NZS 4600 Standard (2005) [157] for CFS members limits only the maximum fastener spacing along the column length by ensuring that flexural buckling of the individual studs between fasteners will not occur prior to global flexural buckling of the built-up section. In North America, AISI S100 (2016) Section I1.2 [60] requires the calculation of axial capacity using the modified slenderness ratio approach, which was adopted from AISC 360 (2010) [158] and assumes only minor-axis flexural buckling in the estimation of strength, Fe. Equations (6.1) and (6.2) show the basis for these calculations.

$$F_e = \frac{\pi^2 E}{\left(\frac{KL}{r}\right)_m^2} \tag{6.1}$$

$$\left(\frac{KL}{r}\right)_m = \sqrt{\left(\frac{KL}{r}\right)_o^2 + \left(\frac{a}{r_i}\right)^2} \tag{6.2}$$

In Equation (6.2), $(KL/r)_o$ is the slenderness ratio of the entire built-up section about its minor axis, a is the intermediate fastener spacing along the column's height, and r_i is the minimum radius of gyration of each single stud in the built-up section. This modified slenderness method estimates a loss of shear rigidity at the discrete fasteners and increases the slenderness ratio of the built-up section to reduce its capacity accordingly. The method cannot predict the effects of fastener spacing/layouts on torsional, flexural-torsional, local, or distortional buckling modes. For a complete design, local and distortional strengths are also required to be determined using the Effective Width Method or the Direct Strength Method (DSM) on either the individual sections or the fully-composite built-up cross-sections. The governing strength is the minimum stress: F_e (nominal global strength), F_l (nominal local strength) or F_d (nominal distortional strength).

$$\frac{a}{r_i} \leq \frac{1}{2}\left(\frac{KL}{r}\right)_0 \tag{6.3}$$

Like the requirements in the AS/NZ code, a limitation on the fastener spacing along the height is used to ensure that individual stud buckling does not occur before the entire built-up section buckles. Equation (6.3) is used to determine this maximum spacing. If the modified slenderness ratio is used in Equation (6.3), an iterative calculation must be performed to obtain an optimal spacing. Although the specification does not clarify whether the fasteners should be single or double for each fastener longitudinal spacing increment, the double configuration is conservatively assumed in the work presented in this chapter. AISI S100-16 also requires a prescriptive fastener grouping at the member ends, but its impact on the modified slenderness is not treated directly. As per section I1.2, if screws are used as fasteners in these end fastener groups (EFGs), they must be longitudinally spaced no more than 4 diameters apart and for a distance equal to 1.5 times the maximum width of the built-up section.

6.3. Experimental tests on built-up CFS columns

Seventeen built-up CFS column tests have been conducted by the research group of Professor Benjamin William Schaffer at Johns Hopkins University (JHU) [7] to which was associated the numerical modelling developed in this study in a collaborative manner. The experiments focused on the composite action, fastener spacing/layout, and column end conditions, in addition to an extensive comparison to code-based strength predictions. A 445 kN MTS universal testing rig has been used to perform monotonic concentric compression loading during the test series. The column specimens were installed within tracks, which rested on fixed platen supports. Prevailing deformation modes were sought, as they develop under a certain fastener layout, end conditions, and presence of sheathing. The recommended fastener spacing and layout per AISI S100-16 was used for all trials. The column height was 1.83 m which is the maximum height allowed in the MTS rig setup, in this test series. It is worth noting that all tests have been conducted by Dave Fratamico a PhD student at JHU [159].

6.3.1. Test matrix and instrumentation

Section types were selected to differ in local slenderness, but still be globally slender. The 362S162-68 is a popular cross-section in CFS framed buildings, but is not slender enough when compared to the other selected cross-section, the 600S137-54. Both sections have also been previously tested by Luiz Vieira (2011) [74] and Torabian et al. (2015) [160]. Fig. 6.1 shows the typical arrangement of the built-up "I" sections and typical screw arrangements.

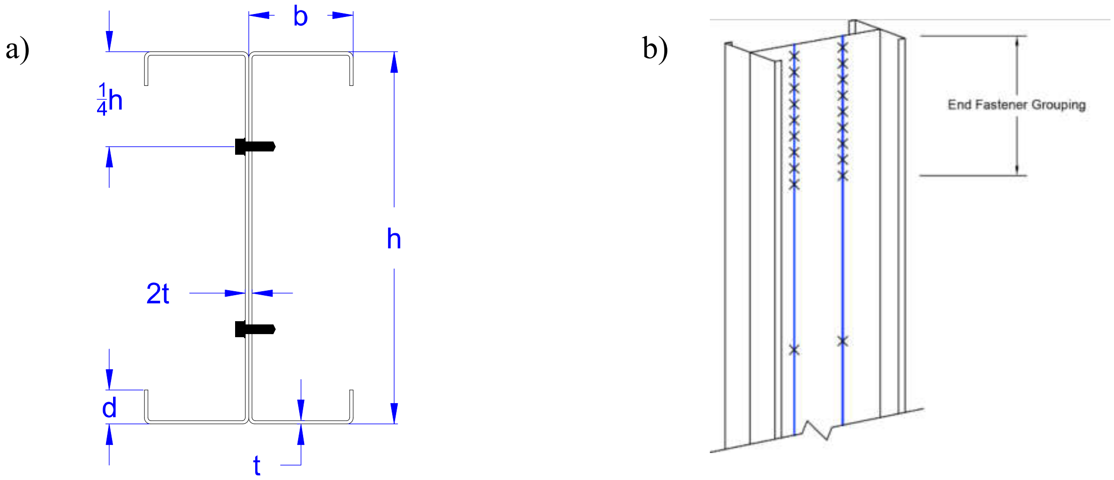

Fig. 6.1. a) The built-up, back-to-back section studied, showing the location of the web interconnections via screws and b) an example of the AISI-recommended fastener layout at the column ends.

The test matrix is shown in Table 6.1, where at least 8 unique test cases are performed on the two types of sections used (see Fig. 6.2 for illustrations of the cases). The goal is to understand the effect of the incremental addition of assembly components that can contribute to composite action. The true stud-to-track semi-rigid end condition is tested via single stud tests A1 and B1. The back-to-back stud end condition with the track when no fasteners are present in the webs is tested via A2 and B2. The effect of intermediate fasteners whose spacing is designed according to AISI S100-12 D1.2 and E4.2 (see Fig. 6.2, case 3) is studied via trials A3 and B3. Lastly, the effect of end fastener groups on the developed composite action is studied in trials A4 and B4, with details on screw layouts in Fig. 6.2 (see case 4). The length of the end fastener groups per AISI, were: α = 138 mm and 229 mm for the 362S162-68 and 600S137-54 section trials, respectively; α is the maximum width of the column multiplied by 1.5. All trials are then repeated (as A5-A8 and B5-B8) with OSB sheathing of 11.1 mm thickness, attached on both sides of the studs and in contact with the stud flanges and track lips. Isolation plates (12.7 mm thick) were installed between the tracks and their adjacent platens, at the top and bottom of the column, to prevent bearing on the OSB ends. The purpose of the sheathed tests is to understand and quantify the achievable, upper bound composite action with the added effect of bracing and confinement of the sheathing on the built-up studs; local deformation modes are sought as well.

As per industry standard, studs are connected with steel-to-steel hex washer head screws (self-drilling #10) and between studs and tracks as well. For the specimens with OSB, the hex washer head screw is replaced with a steel-to-steel flat pancake head screw (Simpson FPHSD #10) so as to not bow the OSB as it is fastened over the track. OSB sheathing is attached with Simpson #10 PPSD wood-to-steel screws.

Table 6.1. Test matrix.

Trial	**Section used**		**Sheathing**	**Single stud**	**Built-up screw layout**		
	362S162-68	**600S137-54**			**None**	**Even**[a]	**AISI**[b]
A1	X			X			
A2	X				X		
A3	X					X	
A4	X						X
A5	X		X	X			
A6	X		X		X		
A7	X		X			X	
A8	X		X				X
B1		X		X			
B2		X			X		
B3		X				X	
B4		X					X
B5/B5b[c]		X	X	X			
B6		X	X		X		
B7		X	X			X	
B8		X	X				X

[a] Evenly-spaced screw spacing;
[b] Prescriptive AISI-based screw spacing;
[c] Staggered screw layout (illustrated in Fig. 6.2c).

All tests were displacement-controlled quasi-static loading. The load rate did not exceed 1.52 mm/min for single studs or 0.76 mm/min for back-to-back studs. Loading platens were made of low-carbon steel with an appropriate hardness and yield strength as required for the tests; they were installed parallel (+/- 0.05° off the horizontal plane). The dimensions and setup are shown in Fig. 6.3. Measurements of load are made through the load cell on the MTS rig (Fig. 6.3), and the MTS's LVDT measures the applied displacements. To track specimen deformations, 17 position transducers (PTs) are installed. Lateral bi-planar displacements and overall rotation at the mid-section can be tracked throughout the test using 11 PTs at mid-height (see Fig. 6.3). In addition, 1 PT is installed on the top and bottom tracks, orthogonal to the web of the studs in order to track the out-of-plane deformation of the webs due to local buckling or localised failures at the ends. To monitor stud engagement to the track during the tests, 2 PTs are installed: one at the top and one on the bottom track. Lastly, for unsheathed specimens, if flexural buckling is expected, a special "shear slip" PT is installed at the top and bottom to monitor the web slip for trials with different levels of composite action (see Figs. 6.4 and 6.5 for the slip mechanism and setup). LabVIEW software and National Instruments hardware are used to coordinate all data acquisition. The error of eccentricity of the applied loads and out-of-plumb are recorded for each column as they are loaded into the rig. Specifically, measurements were taken near the top, bottom, and mid-height of the columns in two planar directions to endure that the centroid of each column's section were within the line of action of the applied load in the rig. Upon final positioning, error values are recorded, but considered negligible since eccentricities were calculated as never larger than 0.64 mm.

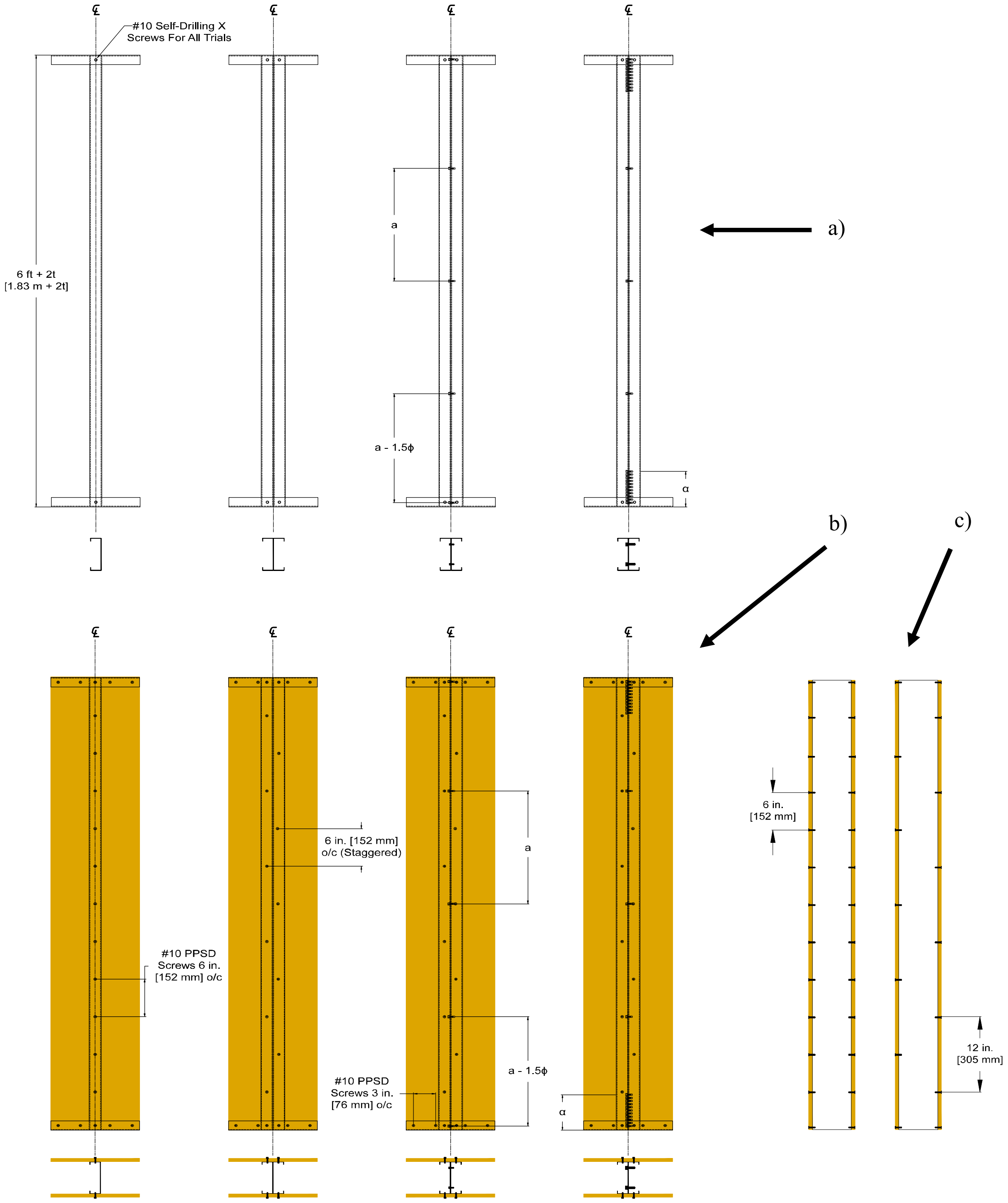

Fig. 6.2. All 8 test specimens per section type: a) unsheathed, b) sheathed and c) screw spacings for B5 and B5b.

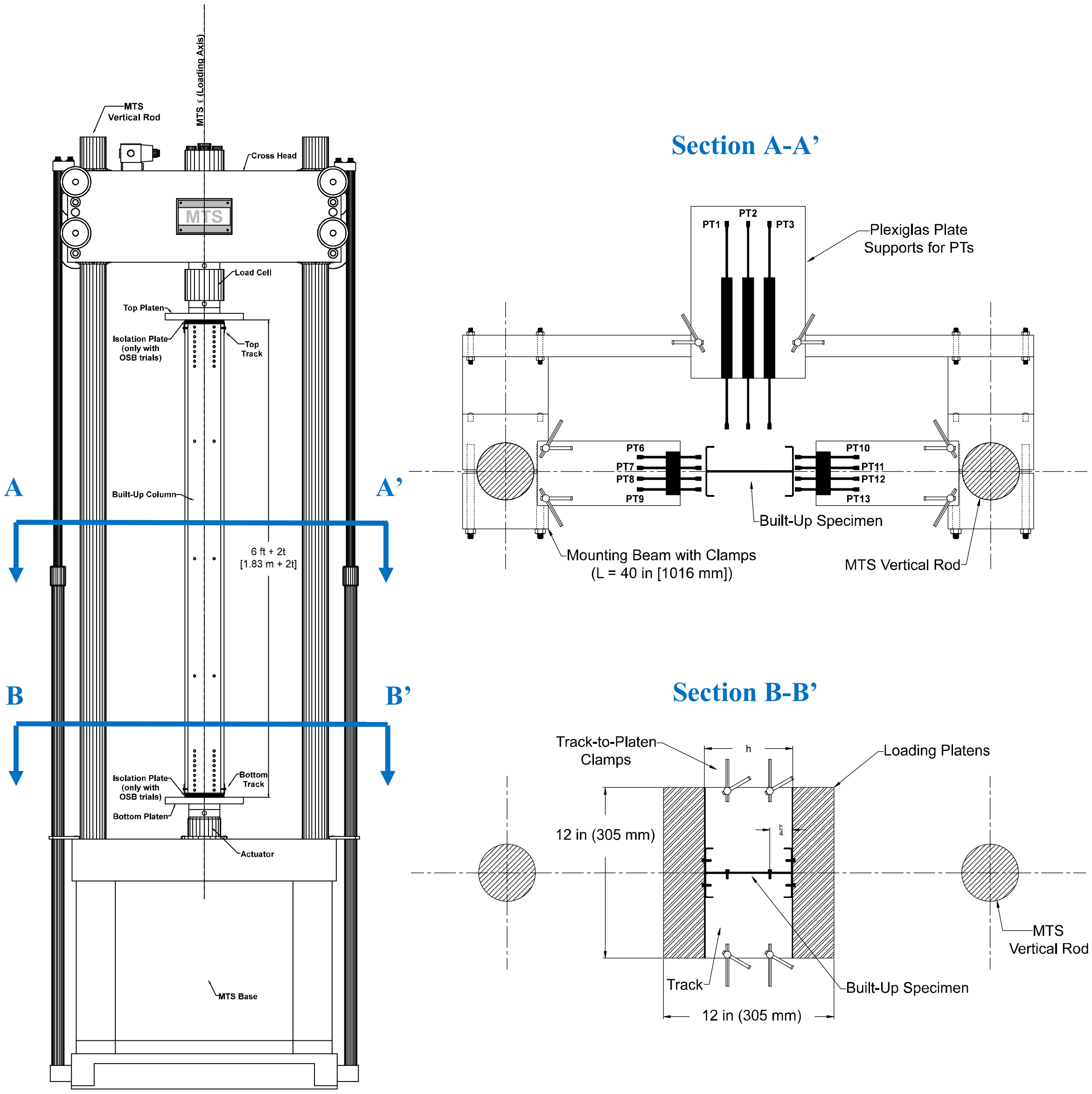

Fig. 6.3. MTS testing rig with specimen installed (left), position transducer arrangement at mid-height (Section A-A’), and specimen positioning on loading platens (Section B-B’).

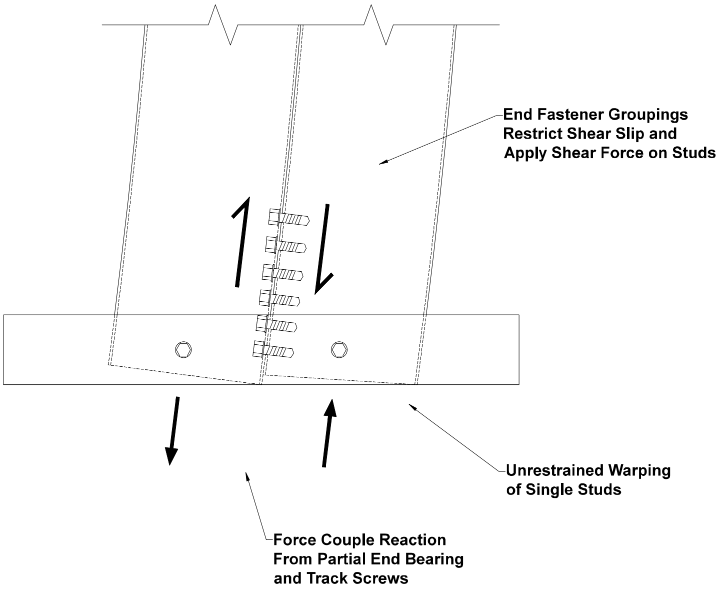

Fig. 6.4. Shear slip expected when columns undergo flexural buckling.

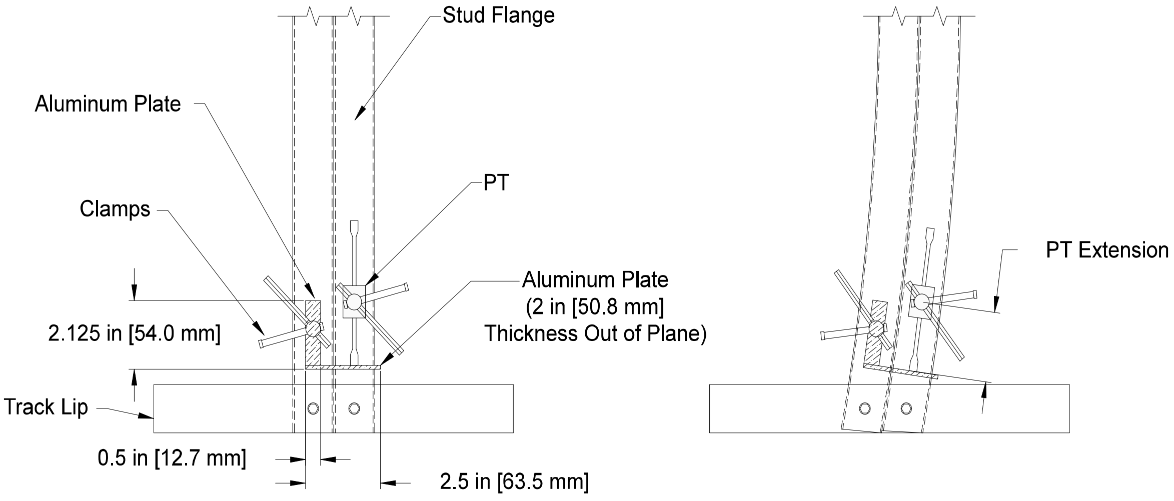

Fig. 6.5. Setup for the "shear slip" position transducers in an undeformed (left) and a deformed state (right).

6.3.2. Laser scanning for geometric imperfections

Measurements for specimen dimensions and quantification of geometric imperfections were completed using a novel laser scanning method. The laser scanner, shown in Fig. 6.6, uses a 2D line laser that generates 800 points per reading (longitudinal to the column) and a rotary stage allows for angled readings (Zhao et al. (2015)) [161]. Full-field 3D geometric information is obtained as a point cloud of stitched longitudinal scan readings from different scan angles. Example output data for cross-section dimensions are shown in Fig. 6.7. Average plate thickness for each specimen was measured by hand using a calibrated micrometer, and the results are used in finite-strip analyses and in the reconstruction of the 3D geometry for each specimen.

Fig. 6.6. Laser scanner setup with built-up specimen installed.

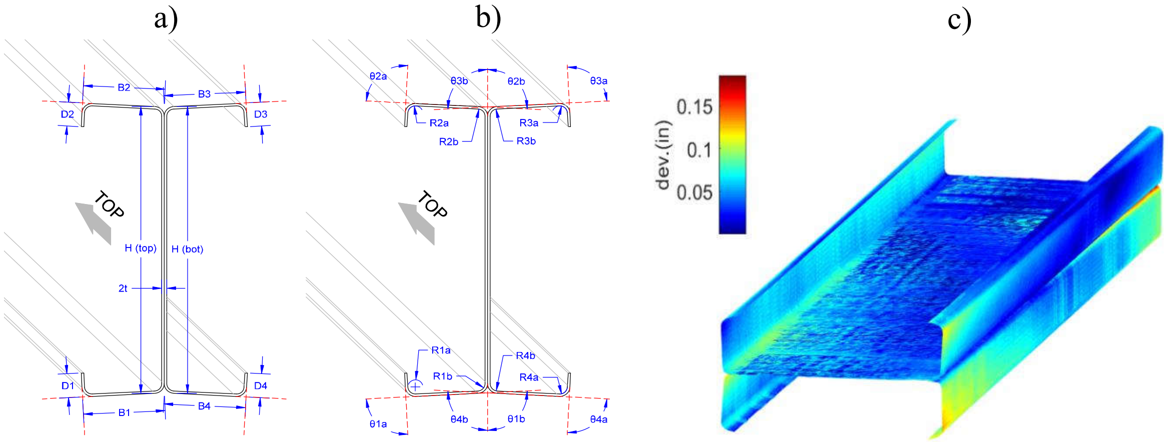

Fig. 6.7. Results from laser scan: a) imperfect cross-section linear dimensions averaged over full length: a) lengths, b) averaged imperfect cross-section angles and radii and c) full-field 3D reconstruction of true geometry for FE analyses.

6.3.3. Coupon testing for material characterisation

To quantify basic material properties of the CFS used for the test specimens, a series of 12 coupon tests, using CNC milled longitudinal cuts of the webs and flanges for the channel sections and of the webs and lips of the track section, were performed. Fig. 6.8 shows the locations of the coupons. Testing was completed in accordance with ASTM A370-12a (2012) [162], and results are shown in Table 6.2 and plotted in Appendix D. To remove the zinc coating, both ends of all coupons were put in a 1M HCl solution until the coating was removed; uncoated steel measurements (namely uncoated thickness) could then be made. Fig. 6.9 shows the ASTM-dictated coupon dimensions for steel sheet thicknesses used in the tests herein. Yield (at 0.2% offset) and ultimate tensile strengths for the 362S162-68 and 362T125-68 sections were similar and recorded with a mean of 419.3 MPa and 543.0 MPa, respectively. Similarly, for the 600S137-54 and 600T150-54 sections, yield and ultimate tensile strengths were recorded with a mean of 397.8 MPa and 483.0 MPa, respectively. All yield stress values are considerably above the nominal 344.7 MPa. Young's modulus was not estimated from the linear data in the test results and is assumed to be 203400 MPa as prescribed in AISI S100-12.

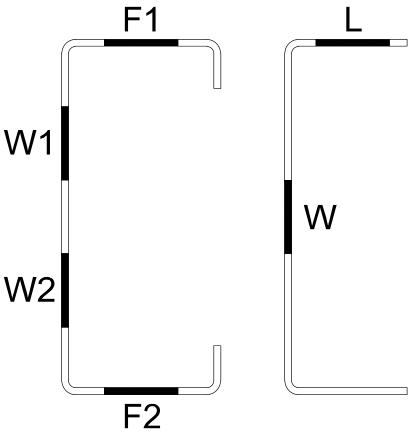

Fig. 6.8. Location of coupon taken from the lipped channel (left) and track sections (right).

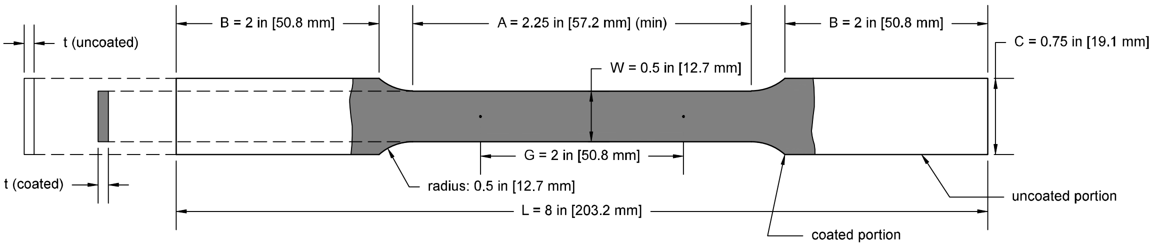

Fig. 6.9. Tensile coupon dimensions.

Table 6.2. Tensile coupon test results.

ID	Specimen	Base metal thickness t (mm)	Gauge length elongation ΔL_g (%)	Yield stress[a] $F_{y,0.2}$ (MPa)	Yield stress[b] $F_{y,\text{ auto}}$ (MPa)	Upper yield stress $F_{y,\text{ upper}}$ (MPa)	Tensile strength F_u (MPa)	Strain at tensile strength ε_u (mm/mm)	Strain at rupture ε_r (mm/mm)
1	362S162-68-W1	1.82	17.50	426.3	428.8	431.6	550.9	0.1304	>0.17
2	362S162-68-W2	1.83	17.40	420.7	421.1	422.0	540.1	0.1324	>0.17
3	362S162-68-F1	1.85	17.78	428.6	425.9	433.3	546.7	0.1230	>0.17
4	362S162-68-F2	1.81	18.30	402.4	407.4	402.7	535.9	0.1322	>0.17
Mean		**1.83**		**419.5**	**420.8**	**422.4**	**543.4**		
STDEV		**0.01**		**10.28**	**8.211**	**12.16**	**5.794**		
5	600S137-54-W1	1.40	21.61	402.3	404.0	406.1	484.5	0.1541	>0.20
6	600S137-54-W2	1.40	23.51	398.1	395.6	399.0	481.0	0.1772	>0.22
7	600S137-54-F1	1.39	23.25	389.4	390.8	391.5	481.8	0.1798	>0.22
8	600S137-54-F2	1.38	23.65	389.4	389.9	391.7	480.7	0.1783	>0.22
Mean		**1.39**		**394.8**	**395.1**	**397.1**	**482.0**		
STDEV		**0.01**		**5.600**	**5.590**	**6.023**	**1.498**		
9	362T125-68-W	1.81	18.68	406.2	408.5	407.1	537.2	0.1325	>0.18
10	362T125-68-L	1.83	18.90	431.2	431.5	431.9	547.4	0.1289	>0.17
11	600T150-54-W	1.38	21.95	410.6	408.6	411.3	491.6	0.1710	>0.21
12	600T150-54-L	1.39	23.58	405.4	404.2	405.7	487.2	0.1675	>0.22
Mean		**1.60**		**413.4**	**413.2**	**414.0**	**515.9**		
STDEV		**0.22**		**10.49**	**10.71**	**10.54**	**26.74**		

[a] The 0.2% offset method is used here;

[b] The autographic method used was the averaging of the stress levels at the 0.4% and 0.8% offset intercepts.

6.4. Summary of test results

6.4.1. Unbraced columns

The purpose of the single stud tests was to provide a baseline and explore the end condition formed between the studs and tracks. Although not expected to buckle with a globally pinned end condition due to the end bearing and screw connections with the track, global buckling was observed as the primary limit state. Fig. 6.10 shows the results for all trials of both cross-section types, without sheathing; note that for the loading data for the single stud trials (A1 and B1), a scale factor of 2 was applied to allow for comparison with the other trials that employ doubled studs. With the addition of another stud in the track, but no screw connections between the studs (A2 and B2), an increase in capacity is observed when compared to the scaled single stud capacities. Although the buckling modes were similar, a more rigid end condition is expected as the studs buckled sympathetically and friction may develop between the two studs. With the addition of the fasteners in the web the capacity increased, but was limited by local buckling in the case of the B-series 600S137-54 specimens, as summarised in Table 6.3.

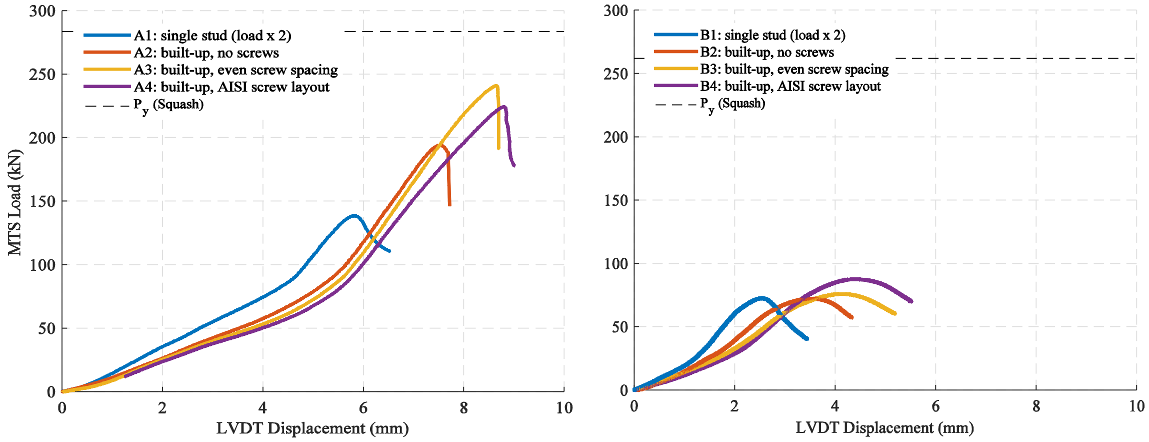

a) b)

Fig. 6.10. Test data (P-δ) for all unsheathed column trials: a) 362S162-68 and b) 600S137-54 specimens.

Table 6.3. Unsheathed specimen experimental results.

Trial	Specimen type	Observed elastic buckling mode	P_u (kN)	Failure mode at the peak load
A1	Single 362S162-68	FT	69.35	FT
A2	Back-to-Back 362S162-68	FT[a]	194.3	FT[a]
A3	Back-to-Back 362S162-68	D[b]	241.2	L (web, mid-height)[a]
A4	Back-to-Back 362S162-68	D[b]	224.4	L (web, mid-height)[a]
B1	Single 600S137-54	F (minor axis)/FT	36.38	L (lips, mid-height)
B2	Back-to-Back 600S137-54	F (minor axis)[b]	72.15	D/L (lips, mid-height)[a]
B3	Back-to-Back 600S137-54	F (minor axis)[b]	75.98	D/L (lips, mid-height)[b]
B4	Back-to-Back 600S137-54	L (web)[b]	87.63	D/L (lips, mid-height)[b]

[a] Non-sympathetic buckling mode (generally symmetric about the minor axis);

[b] Sympathetic buckling mode between the two studs (non-symmetric about minor axis);

Note: FT = flexural-torsional, F = flexural, D = distortional, and L = local.

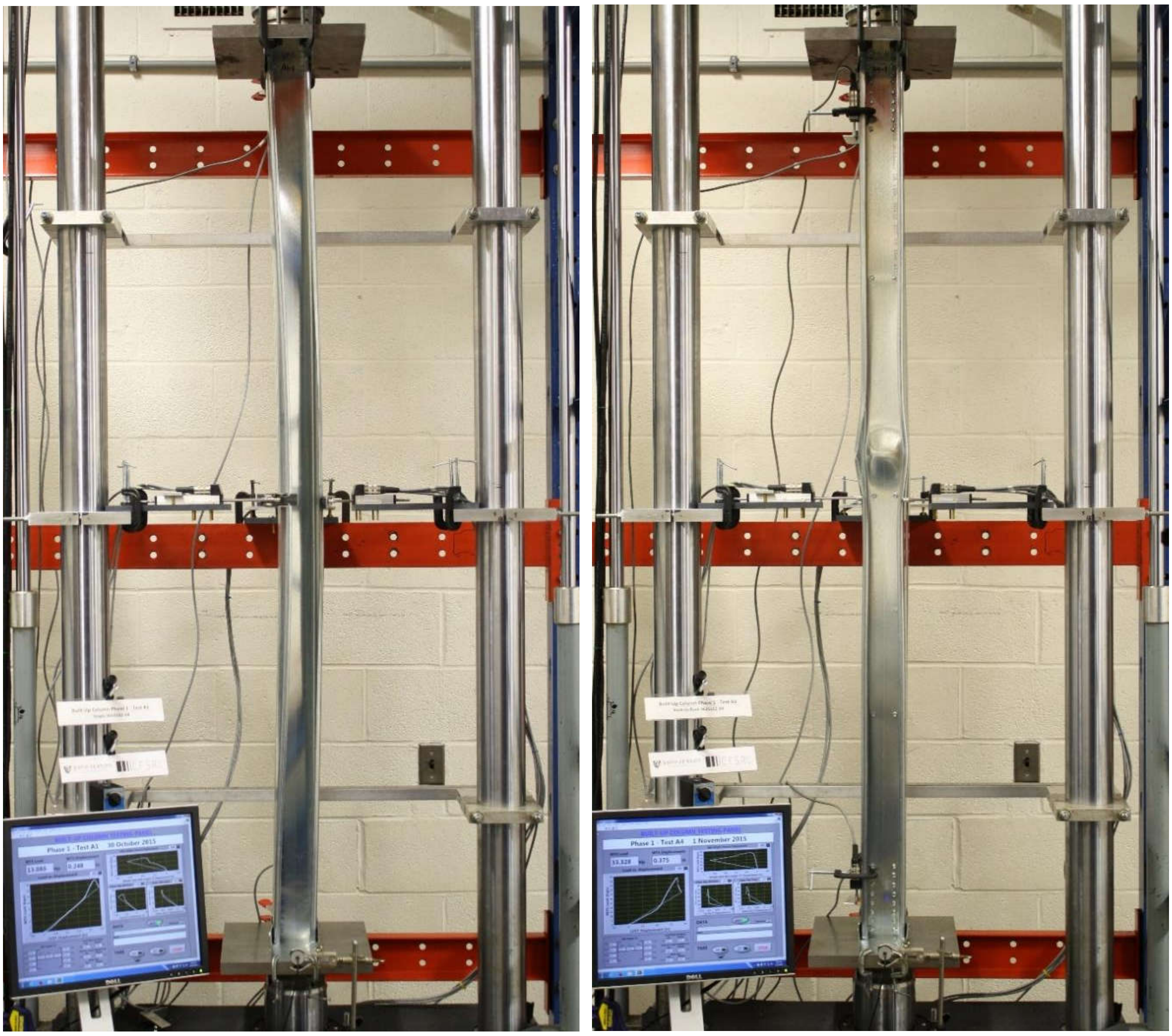

Fig. 6.11. Typical flexural-torsional (left, trial A1) and interacting local/flexural (right, trial A4) buckling failures.

Figs. 6.11 and 6.12 show typical modes of failure reported in Table 6.3 for the unsheathed columns. Note that the change in initial stiffness in the plots of Fig. 6.10 are caused by the seating of the column ends in the tracks upon loading. At 1.83 m length, the 362S162-68 stud buckles in a flexural-torsional mode. With the addition of fasteners, the increase in capacity is evident (up to 74% as shown in Fig. 6.10a) due to the increase in composite action, and the mode shifts from a global to a local mode. Also evident is that the strength of column A4 (with a denser fastener spacing on the web) is less than the strength of column A3; the presence of the EFGs had little to no effect on the buckling deformation and peak capacity, and the observed difference could be attributed to geometric imperfections or stud-to-track end conditions. Luiz Vieira (2011) [74] also studied the same 362S162-68 columns at the same length, and results compare reasonably well. In Vieira (2011) [74], the unsheathed 1.83 m column failed in flexural-torsional buckling at a load of 60.46 kN, a capacity 13% less than the comparable specimen tested in trial A1. Differences in delivered thickness, material yield stress, geometric imperfections, or stud-to-track engagement could account for the discrepancy. The 600S137-54 stud (specimen B1) buckled in a minor-axis flexural mode, as did columns B2 and B3. Surprisingly, neither stiffness nor strength varied substantially for the back-to-back sections with the addition of the web fasteners. However, an increase in capacity was observed for this stud with the addition of the EFGs, and their presence enforced a sympathetic web local buckling mode. Although the benefit of the EFG is assumed to be to limit end slip and thus maximise composite action in global (flexural) buckling, such a substantial number of fasteners also has an impact on local buckling as observed in this case.

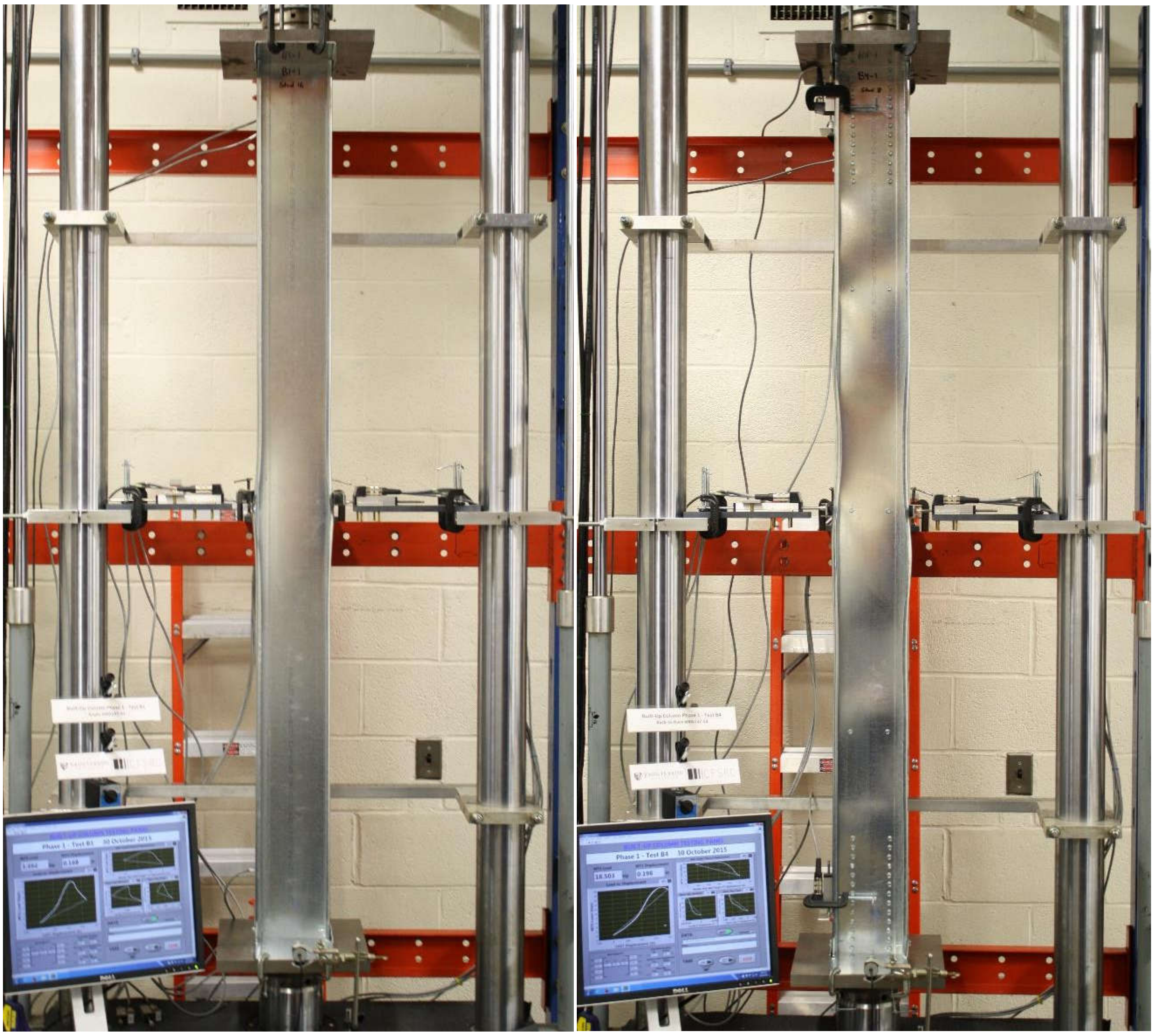

Fig. 6.12. Typical flexural (left, trial B1) and interacting local/flexural (right, trial B4) buckling failures.

6.4.2. Southwell estimation of column end conditions

Also sought from the results was an estimate of the end conditions. For trials A1 and B1 with single studs and a single fastener connecting each flange between the stud and track, end conditions closer to the pin-pin case can be expected. However, bearing is also possible and thus it is difficult to know the end condition prior to testing. In the built-up cases (*e.g.*, trials A4 and B4), a shear force couple exists via the stud-to-track screws (see Fig. 6.4), and in conjunction with the EFGs connecting the webs, a more rigid end condition is expected. The Southwell method was used to estimate the elastic, minor-axis flexural buckling loads of the columns using position transducer displacement at mid-height, specifically the out-of-plane deflection of the specimens' webs. The critical load is estimated using Equation (6.4), with notation similar to Southwell's original form (1932) [163]:

$$\delta = P_{cr}\left(\frac{\delta}{P}\right) - \delta_o \tag{6.4}$$

where δ is the lateral deflection at mid-height, Pcr is the estimated elastic minor-axis flexural buckling load (calculated as the slope of the line in a plot of δ/P vs. δ), P is the applied load, and δ_o is any initial deflection in the column, which is ignored when determining the critical load. The method is approximate, but provides some insight.

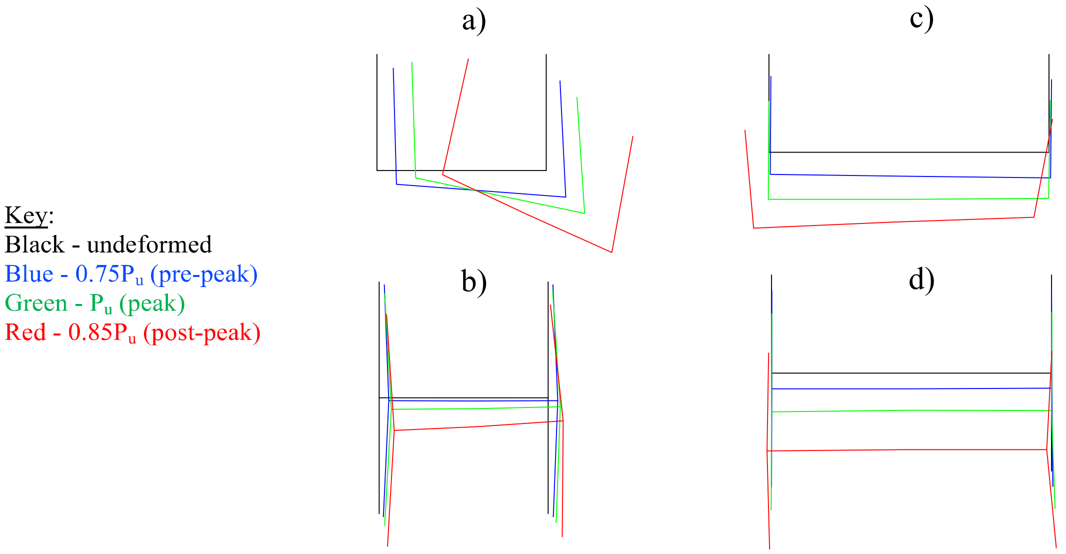

Fig. 6.13. Plots of mid-height cross-section displacements/rotations (to scale, from position transducers) for unsheathed trials: a) A1, b) A4, c) B1 and d) B4.

Note, that although some columns deformed in a torsional mode at peak load (such as A1), the initial displacements were of flexural type in the linear elastic range of loading. Also, linear P-δ data was extracted from the overall test data for each trial after the point at which the studs' cross-sections were recorded to be fully engaged to the tracks by the stud-to-track PTs. Fig. 6.13 provides the cross-section deformation as recorded by the mid-height PTs at the web (from one end) and the flanges. The different colours represent various stages of loading, with black indicating the base, undeformed state. For each trial, the data before reaching 75% of peak load (the blue cross-sections in Fig. 6.13) was used in the Southwell estimations. Table 6.4 shows the effective length factors, back-calculated from the Euler formula for critical buckling load, where the critical load is the slope from the Southwell plot. Calculations are performed assuming non-composite action. The presence of local buckling, distortional buckling, torsional buckling, and partially composite action complicate the approximation. Nonetheless, under the stated assumptions, K is between 0.8 and 1.0 for the single studs and 0.5 and 0.6 for the composite studs.

Table 6.4. Estimation of column end conditions.

Specimen	P_{Euler} with K=0.5 (kN)	P_{Euler} with K=1.0 (kN)	$P_{cr,Southwell}$ (kN)	Effective length factor, K
A1 (single)	46.48	185.9	44.90	1.00
A4 (built-up)*	92.92	371.7	329.0	0.53
B1 (single)	26.23	104.9	40.50	0.81
B4 (built-up)*	52.44	209.9	129.0	0.64

*A non-composite calculation is used.

6.4.3. Sheathing-braced columns

Specimens A5-A8 and B5-B8 repeat the previous tests but now with OSB sheathing attached to the flanges of the studs. The results as shown in Fig. 6.14 and Table 6.5 are that the impact of the sheathing is more important than the detailing of the all steel back-to-back specimens. Again, the single stud loads are scaled by 2 to compare more directly with the other trials.

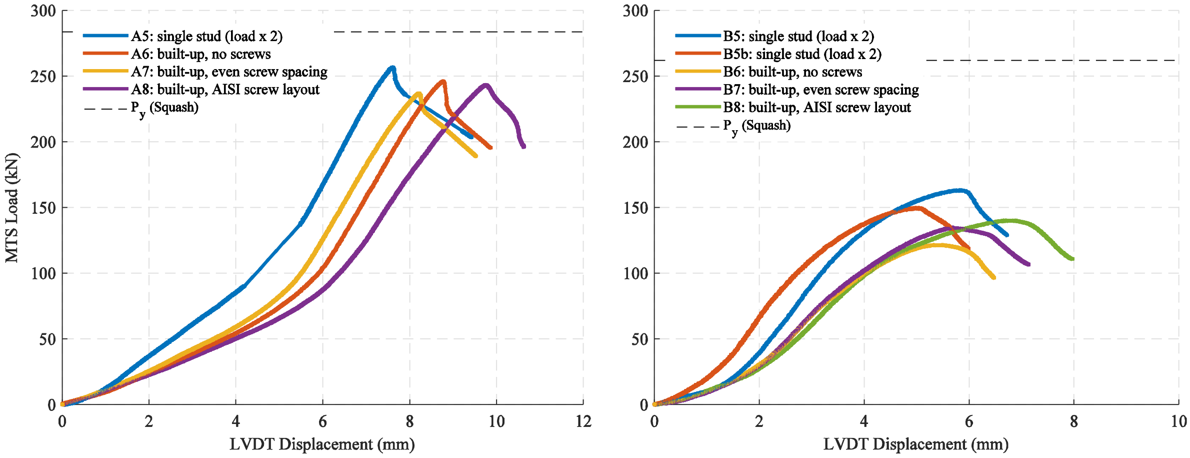

a) b)

Fig. 6.14. Test data (P-δ) for all sheathed column trials: a) 362S162-68 and b) 600S137-54 specimens.

Table 6.5. Sheathed specimen experimental results.

Trial	Specimen type	Buckling mode	P_u (kN)	Failure mode
A5	Single 362S162-68	L (web, top)	128.4	L (web, top)
A6	Back-to-Back 362S162-68	L (web, top)[a]	246.0	L (web, top)[a]
A7	Back-to-Back 362S162-68	L (web, top)[a]	236.9	L (web, top)[a]
A8	Back-to-Back 362S162-68	L (web, bottom)[b]	243.1	L (web, bottom)[b]
B5	Single 600S137-54	L (web)[a]	81.62	L (web, top)
B5b[c]	Single 600S137-54	L (web)[a]	75.08	L (web, top)
B6	Back-to-Back 600S137-54	L (web)[a]	121.5	L (web, top)[a]
B7	Back-to-Back 600S137-54	L (web)[a]	134.6	L (web, top)[a]
B8	Back-to-Back 600S137-54	L (web)[a]	140.3	L (web, bottom)[b]

[a] Non-sympathetic buckling mode;
[b] Sympathetic buckling mode;
[c] Staggered screw layout;
Note: L = local.

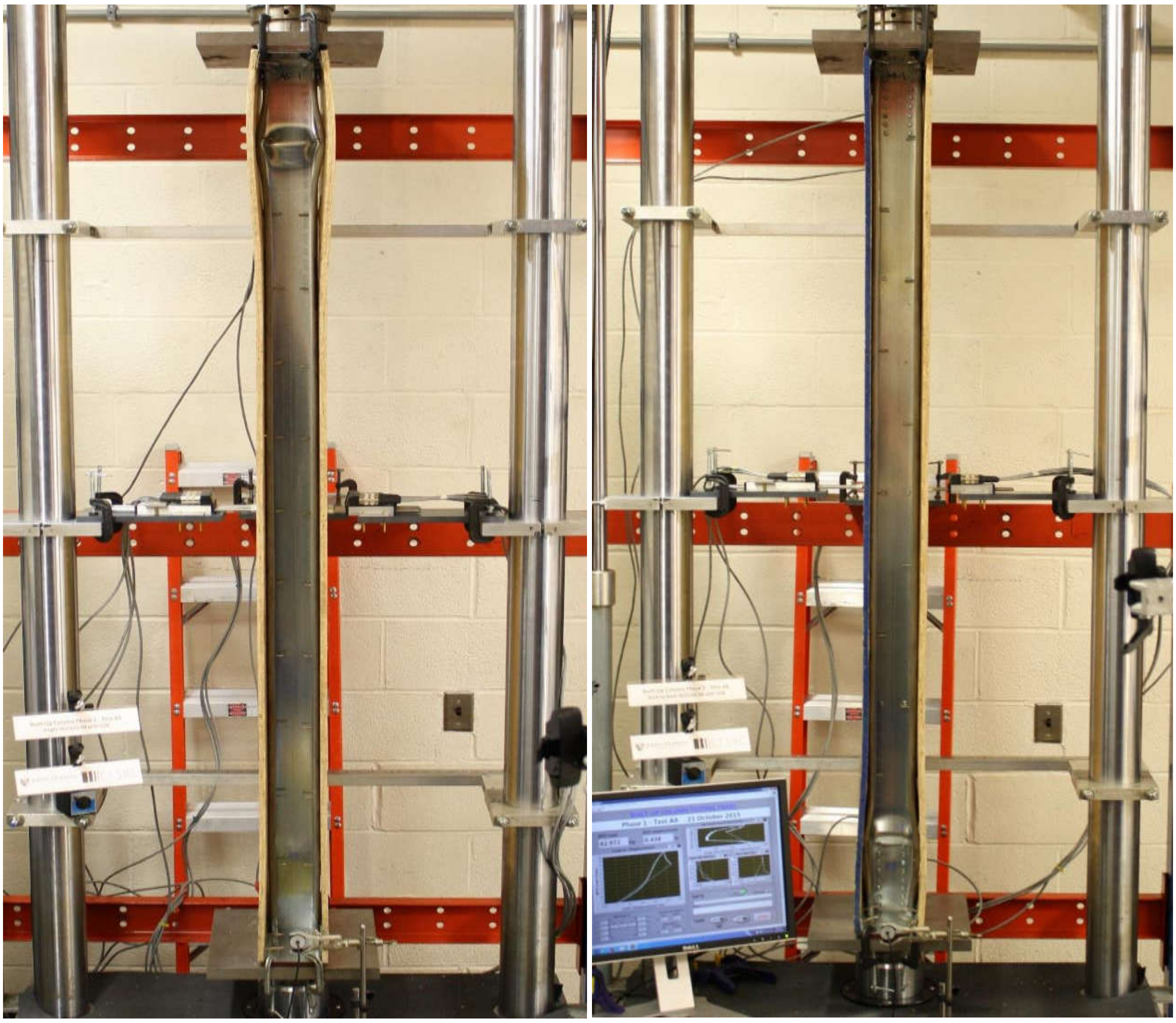

Fig. 6.15. Typical single stud (left, trial A5) and built-up column (right, trial A8) web local buckling failures.

Table 6.5 shows all sheathed trial test results. As shown in Fig. 6.14, the strength of the screw-fastened columns (A7, A8, B7, and B8) is not significantly larger, since local buckling controlled and the fastener spacings consistently allowed for the local buckling half-wavelengths to develop. The local buckling mode (sympathetic or non-sympathetic) generally yielded the same column strength. Also, evident in the plots is the increased stiffness of the single sheathed studs. This is due in part to the 152.4 mm screw longitudinal spacing, which connect the flanges to the OSB on the single studs. The spacing difference between single and back-to-back sheathed columns is shown in Figs. 6.15 and 6.16; in the back-to-back studs, the spacing is the same, but staggered on one flange at each 152.4 mm increment. The highest strength of the 362S162-68 sheathed series was recorded in A6 at 246.0 kN, in which a non-sympathetic local buckling half-wave developed near the upper end.

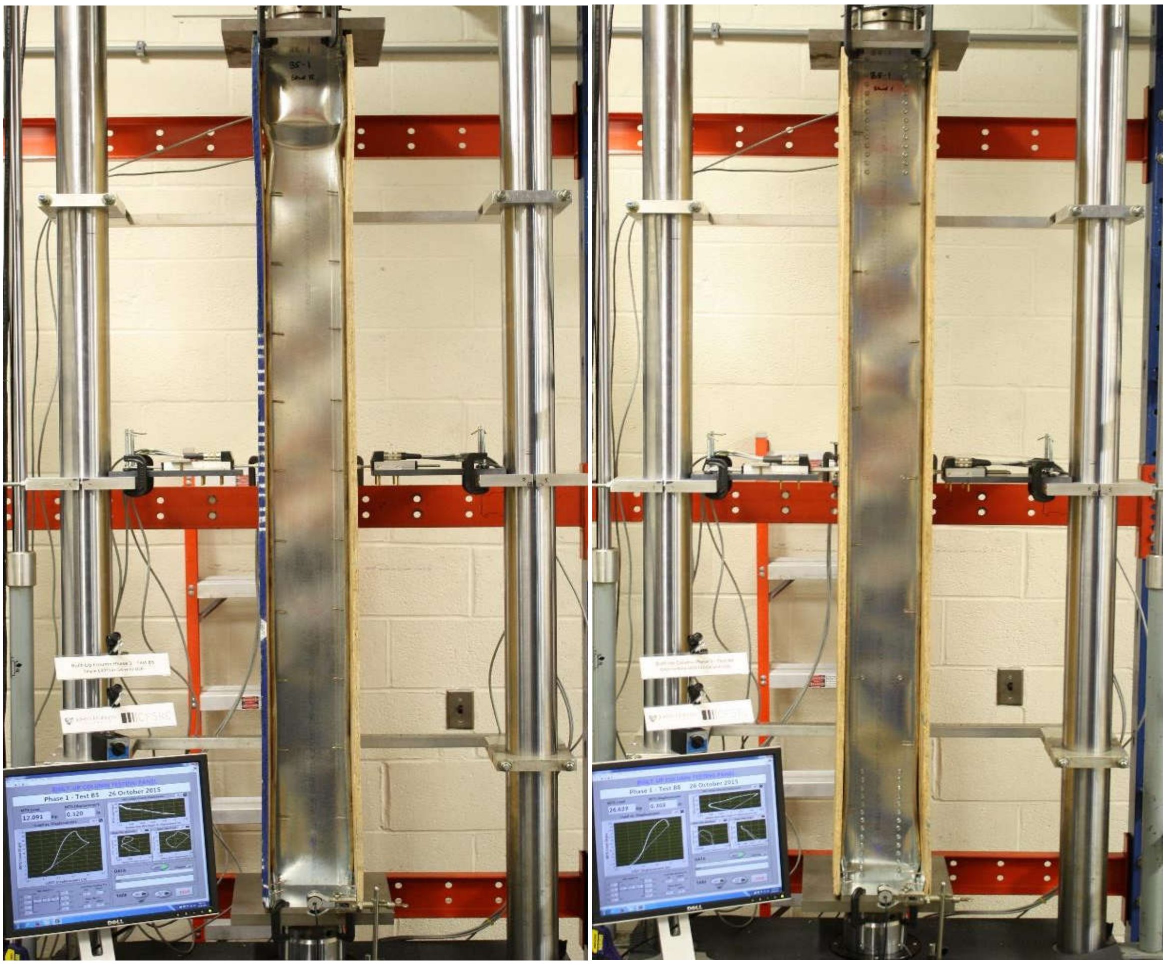

Fig. 6.16. Typical single stud (left, trial B5) and built-up column (right, trial B8) web local buckling failures.

Similar buckling and failure modes were observed in the sheathed 600S137-54 series tests (B5-B8). For the built-up specimens B6-B8 the strength increases with the additional detailing. However, the stiffness remains essentially constant across B6-B8. The single stud specimen B5 exhibits the highest stiffness and strength when multiplied by 2 to compare with the back-to-back test results. As in the A5 specimen the stud-to-sheathing spacing is 152.4 mm, but since there is only one stud it is not staggered as is the case for built-up members and thus the individual flange in the B5 tests has a 152.4 mm stud-to-sheathing fastener spacing. Another are less than 1.0, DSM tends to deliver non-conservative estimates of nominal strength using the current CUFSM modelling method. The problem of choosing an appropriate end condition for unsheathed columns also persists in this method. However, using a clamped end condition tends to deliver ratios closer to 1.0 for the single stud analyses. Although accurate predictions of built-up CFS column capacities using CUFSM and DSM are not always possible, this numerical method of design is promising if discrete fasteners are modelled and appropriate treatment of end conditions is included in CUFSM. Future numerical work aims to efficiently model fastener connections in built-up sections for beams and columns in a finite-strip modelling framework for calculation of elastic buckling loads and modes for use in determining strength.

As for the semi-analytical approach (*i.e.*, modified slenderness ratio), additional study is needed as it depends significantly on the end conditions and does not capture the local, distortional, torsional and flexural-torsional buckling modes.

6.10. Conclusion

Built-up columns are frequently used as end studs in SWP in CSF framed buildings. Therefore, understanding the behaviour and strength of screw-fastened built-up CFS columns with and without sheathing is important, for design specifications in order to provide efficient solutions in this common scenario. The tests associated to this work show that without sheathing, an all-steel built-up column is influenced by its end attachment (*e.g.*, to a track) nearly as much as interconnections between the built-up members. Also, friction and end conditions can play an important role in composite action of an all-steel built-up column. With sheathing present, the tests show that the sheathing influences composite action and bracing conditions. The restraint of the flanges provided by OSB sheathing engages composite action in the built-up member, largely restricts global buckling modes, partially restricts distortional modes, and modestly changes observed local buckling modes. Preliminary evaluation of potential design methods indicates that care must be taken to correctly approximate the end boundary conditions and the impact of sheathing and inter-connections on the buckling modes.

Subsequently, the intent of the numerical study presented herein were to introduce new and advanced techniques of FE modelling for CFS members, specifically applied to built-up CFS columns. Particularly, user-defined elements “UELs” are useful for modelling screw fasteners cyclic behaviour using empirical fastener data and a Pinching4 framework. Output of force and displacement for each fastener is possible and can be useful when considering optimal fastener arrangements; this method of modelling fasteners can be more effective than using simple constraints or linear springs, as is typical in most previous modelling work. A simple approach to model stud-to-track connections compares well with tested behaviour, and overall, the modelling protocol is shown to accurately simulate tested conditions and behaviour. Screw fasteners are shown to only increase capacity and enforce compatible buckling modes among individual studs in a built-up section if sheathing is not present. However, in CFS framing, sheathing is nearly unavoidable in order to provide proper architectural finish. Built-up columns in CFS are often designed ignoring this sheathing even though the impact is significant through the restriction of the potential buckling modes and the demands on the built-up section. Design should endeavour to easily include these benefits.

The current modified slenderness ratio approach assumes that flexural buckling controls, but it does not prohibit the use of other analyses to determine distortional and local buckling strength of single studs which can also be used in the determination of nominal built-up column strength. The approach currently considers even fastener spacings; it does not account for the effect of EFGs and semi-rigid end conditions, which are necessary for the proper calculation of strength. Considering these design code limitations, a new methodology should be developed in which numerical solutions for the elastic buckling capacity of any built-up CFS member can be obtained using optimal fastener layouts and connections to sheathing. An existing DSM framework can then be used to estimate strength.

CONCLUSIONS AND RECOMMENDATIONS

This research developed seismic design provisions in accordance with the Eurocode requirements for frames with sheathed shear wall panels (SWPs) made of cold-formed steel (CFS), and investigated the seismic performance factors of a set of building archetypes using Incremental Dynamic Analyses (IDA) following the Federal Emergency Management Agency (FEMA) P695 methodology. The main observations and conclusions of the work were discussed in each chapter, the most relevant findings alongside important conclusions, limitations and future work are highlighted in the following sections.

1. Deteriorating hysteresis models for cold-formed steel shear wall panels

Two hysteresis models for steel- and wood-sheathed CFS-SWP incorporating a load path dependent strength (cyclic and in-cycle) and stiffness deterioration as well as pinching, have been developed. The models input parameters are explicitly introduced in terms of the SWP physical and mechanical characteristics. The deteriorating models are integrated into the finite element (FE) software OpenSees as uniaxialMaterials through scripts written in C++ programming language. The accuracy and efficiency of the models is validated through a correlation with available experimental results using a modelling technique of the SWP. Therefore, these models are considered to be reliable and computationally efficient for the purposes of the research aims of this thesis.

2. Seismic design procedure for cold-formed steel sheathed shear wall frames: proposal and evaluation

A proposal and validation of a seismic design and verification procedure for CFS frames using sheathed SWP as a lateral load resisting system, are presented. The approach involved the definition of a set of design provisions consistent with current European design standards, the selection and design of 54 archetype buildings considering three different levels of seismic intensity and two different types of occupancy. It was observed that the median interstorey drift was always less than the drift limit of 2.5% when the buildings were subjected to the design level earthquakes. Each ground motion record was then scaled to different intensities from 0.2 to 3.0 (in some cases up to 5.0) as part of the IDA. The results of the IDA were used to evaluate the performance of the archetype buildings and to validate the q values used in design according to the FEMA P695 methodology.

Based on the evaluation results, it is proposed that a behaviour factor *q* equal to 2 can be adopted for the type of CFS-SWP system addressed in this study, but limited to structures located in regions of low-to-moderate seismicity. An extension of this proposal to structures located in moderate-to-high seismicity regions can be made based on additional research addressing the issues of spectral shape of ground motion records and the contribution of non-structural components.

3. Seismic risk assessment of cold-formed steel shear wall systems located in low and moderate-to-high seismicity regions

A comparison between CFS-SWP and conventional steel moment-resisting frame (MRF) systems based on a detailed assessment of the seismic risk, has been carried out. IDA was performed using site-specific ground motion records sets selected based on a realistic target response spectrum "Conditional Spectrum" (CS) derived from PSHA disaggregation data. For both structural system types, the annual probability of exceedance for predefined limit states were determined. The obtained results reveal a non-negligible influence of the spectral shape of the ground motion records on the structural response, particularly for structural systems that have a deteriorating lateral behaviour and develop inelastic behaviour at low levels of deformation. Additionally, following the CS approach in selecting ground motion records showed a superior structural performance when compared to FEMA P695 based results where performance groups designed for moderate-to-high were then able to meet the FEMA P695 acceptance criteria despite the fact that they had not passed the minimum requirements when the effect of spectral shape of ground motion records was not adequately taken into account.

The analyses conducted in this research showed that the probability of violating any limit state (Damage Limitation, No-Local Collapse and Near Collapse) falls within the prescribed limits. In general, MRFs are associated to lower levels of seismic risk. Nevertheless, the seismic risk associated to CFS-SWP system is still acceptable. Therefore, the latter can be considered as a reliable structural solution in achieving performance-based objectives for low- and mid-rise buildings located in low and moderate-to-high seismic areas.

4. Numerical study on the behaviour and design of screw connected built-up back-to-back cold-formed steel columns validated by experimental results

A new, advanced method of FE modelling of CFS members, for analyses of screw connected and axially-loaded back-to-back, built-up CFS-SWP chord studs, has been developed and validated based on column test data from displacement controlled experiments conducted at

Johns Hopkins University. For more accurate representation of screw nonlinear shear behaviour, user-defined elements "UELs" are used in lieu of standard springs or constraints in FE modelling. The FE modelling protocol is shown to accurately simulate tested conditions and behaviour. Output of force and displacement for each fastener is shown to be useful when considering optimal and simpler fastener arrangements for better built-up chord stud design. Results indicate that under the tested end boundary conditions there is a little boost in axial capacity with the addition of member end fastener groups at the top and bottom of the columns in common sheathed columns; further, the response of screw fasteners remained elastic up until the post-peak regime which reveals the conservatism in built-up column fastener layout and design as currently required by the Design of Cold-Formed Steel Structural Members AISI S100 (2016) section I1.2. As a consequence, these results are very important and may be the basis for future numerical parametric investigations with the purpose of improving/presenting available/new design guidelines for CFS columns with built-up cross-sections.

5. Recommendations for future research

Several numerical works based on experimental results have been carried out by researchers with the objective of deriving seismic performance factors for CFS framed structures, in which, it has been found that the non-structural components of CFS light framed building have an important influence on the lateral stiffness and strength of the structure. It is therefore crucial to incorporate the influence of such components when assessing the response of CFS buildings. Furthermore, non-structural components make up a considerable rate of the building's total construction cost, a more detailed study involving loss calculations of both structural and non-structural components is considered as a topic worthy of future study.

The ultimate goal of the experimental and numerical studies presented in the last chapter of this thesis is to improve/present available/new design guidelines for CFS columns with built-up cross-sections, in which, all relevant failure modes (local, distortional and global buckling) are considered. Future work will aim to consider perforations in the lipped channel built-up sections, use new modelling approaches for geometric imperfections, and propose improvements for fastener layouts and overall column design. In addition, the characterisation of monotonic and cyclic behaviour of built-up CFS columns is sought so that chord stud buckling limit states could be captured in seismic simulations of CFS framed shear walls.

APPENDIX A

LIST OF SYMBOLS AND ABBREVIATIONS

The main symbols and abbreviations used in this thesis are as follows:

A_f : Chord stud cross-section area

C_ϕ : Calibration coefficient

C_p : Correction factor

Ei : Hysteresis energy dissipated in the i^{th} excursion

$E_{monotonic}$: Total hysteresis energy dissipation capacity under monotonic load

Et : Total hysteresis energy dissipation capacity

Fi+ : Positive intercept strength of a screw fastener at zero displacement

F_b : Design base shear

F_i : Horizontal force acting on floor i

Fi- : Negative intercept strength of a screw fastener at zero displacement

F_m : Mean value of fabrication factor

F_u : Tensile strength

F_y : Yield strength

$F_{y,0.2}$: Yield strength calculated using the 0.2% offset method

$F_{y,auto}$: Yield strength calculated using the autographic method

$F_{y,upper}$: Upper yield strength

I_x : Chord stud moment of inertia per x-axis

I_y : Chord stud moment of inertia per y-axis

K_ϕ : Rotational stiffness

K_e : Elastic stiffness

K_r : Re-loading stiffness

K_u : Un-loading stiffness

K_x : Lateral translational stiffness

K_y : Out-of-plane translational stiffness

$M_{cx,Rd,com}$: Cross-section resistance to moment about x-axis

$M_{cy,Rd,com}$: Cross-section resistance to moment about y-axis

M_m : Mean value of material factor

M_y : Yield moment
$M_{y,Ed}$: Design bending moment about y-axis
$M_{x,Ed}$: Design bending moment about x-axis
$N_{c,Rd}$: Cross-section resistance to axial force
N_{Ed} : Design axial force
P_{cr} : Estimated elastic minor-axis flexural buckling load
P_m : Mean value of professional factor
P_{tot} : Total cumulative gravity load
q : Behaviour factor
R_0 : Overstrength factor
R_d : Ductility factor
R_n : Nominal shear capacity of the SWP
$S_{0.4u}$: Strength corresponding to 40% of the ultimate shear strength
$S_{0.8u}$: Strength corresponding to 80% of the ultimate shear strength
Sa : Spectral acceleration
Sc : Screw spacing
$S_d\,(T_1)$: Design spectral acceleration at the fundamental period
S_u : Ultimate shear strength
S_y : Yield strength limit idealized as 85% of the ultimate shear strength
T : Period of vibration
T_1 : Fist-mode period of vibration
T_R : Return period
V_{design} : Design base shear
V_F : Coefficient of variation of fabrication factor
V_{max} : Maximum base shear
V_M : Coefficient of variation of material factor
V_P : Coefficient of variation of test results
V_Q : Coefficient of variation of load factor
d_r : Inter-storey drift developing for the earthquake intensity corresponding to the SLS
d_s : Screw diameter
e : Natural logarithmic base
e_{xw} : Shift of the x-axis due to the loss of effective area of the cross-section
e_{yw} : Shift of the y-axis due to the loss of effective area of the cross-section

h : Inter-storey height

m : Mass of the structure

β : Reliability index

βi : Deteriorated rate after the i^{th} excursion

β_{DR} : Design requirement uncertainty in the seismic performance analysis

β_{TD} : Test data uncertainty in the seismic performance analysis

β_{MDL} : Modelling uncertainty in the seismic performance analysis

β_{RTR} : Record-to-record uncertainty in the seismic performance analysis

β_{TOT} : Total uncertainty in the seismic performance analysis

δ_0 : Initial deflection in the column

δ_i^k : Un-loading stiffness damage index

δ_i^f : Strength damage index

δ_i^d : Re-loading stiffness damage index

δ_u : Displacement at tensile strength

δ_y : Yield displacement

$\Delta_{0.4u}$: Displacement corresponding to $s_{0.4u}$

$\Delta_{0.8u}$: Displacement corresponding to $s_{0.8u}$

$\Delta M_{x,Ed}$: Additional moment about x-axis

$\Delta M_{y,Ed}$: Additional moment about y-axis

Δ_u : Displacement corresponding to s_u

Δ_y : Displacement corresponding to s_y

$\varepsilon_{plastic}$: Plastic strain

ε_r : Strain at rupture

ε_u : Strain at tensile strength

λ_i : Annual probability of exceedance of different performance limit states

$\rho(T, T^*)$: Correlation coefficient between pairs of ε values at two periods

μ_T : Period-based ductility

Ω_0 : Lateral overstrength

Ω_{max} : Maximum structural overstrength factor

Ω_{min} : Minimum structural overstrength factor

ν : Reduction factor

θ : Inter-storey sensitivity coefficient

ϕ : Resistance factor

ξ : Damping ratio
ACMR : Adjusted Collapse Margin Ratio
AISI : American Iron and Steel Institute
ASCE : American Society of Civil Engineers
ASD : Allowable Stress Design
ASTM : American Society for Testing and Materials
ATC : Applied Technology Council
CBF : Concentrically-Braced Frame
CFS : Cold-Formed Steel
CFS-SWP : Cold-Formed Steel Shear Wall Panel
CFSSSWP : Cold-Formed Steel-Sheathed Shear Wall Panel
CFSWSWP : Cold-Formed Wood-Sheathed Shear Wall Panel
CDF : Cumulative Distribution Function
CMR : Collapse Margin Ratio
CMS : Conditional Mean Spectrum
CNC : Computer Numerical Control
CS : Conditional Spectrum
CSP : Canadian soft plywood
CUREE : Consortium of Universities for Research in Earthquake Engineering
DFP : Douglas fir plywood
DL : Damage Limitation
DM : Damage Measure
DOF : Degree of Freedom
DSM : Direct Strength Method
E : Young’s modulus
EC3 : Eurocode 3
EC8 : Eurocode 8
EDP : Engineering Demand Parameter
EEEP : Equivalent Energy Elastic-Plastic
EFG : End Fastener Grouping
EWM : Effective Width Method
FE : Finite Element
FEA : Finite Element Analysis

FEMA : Federal Emergency for Management Agency
FEUP : Faculty of Engineering of the University of Porto
FPHSD : Fastener Pan Head Self-Drilling
FSM : Finite Stripe Method
GMPE : Ground Motion Prediction Equation
H : Height of a shear wall
H/W : Height-to-Width aspect ratio
ID : Identity
IDA : Incremental Dynamic Analyses
IM : Intensity Measure
IMK : Ibarra-Medina-Krawinkler
JHU : John Hopkins University
LRFD : Load Resistance Factor Design
LVDT : Linear Variable Differential Transformer
M : Magnitude
MCE : Maximum Considered Earthquake
MID : Modal Imperfection Decomposition
MRF : Moment-Resisting Frame
NC : Near Collapse
NLC : No-Local Collapse
OpenSees : Open System for Earthquake Engineering Simulation
OSB : Oriented Strand Board
P-Δ : Second-order effects
PBEE : Performance-Based Earthquake Engineering
PBSD : Performance-Based Seismic Design
PEER : Pacific Earthquake Engineering Research Centre
PG : Performance Group
PGV : Peak Ground Velocity
PGA : Peak Ground Acceleration
PoE : Probability of Exceedance
PSHA : Probabilistic Seismic Hazard Analysis
PT : Position Transducer
W : Width of a shear wall

APPENDIX B

C++ SOURCE CODES OF CFSSSWP AND CFSWSWP UNIAXIALMATERIALS

Note: for a brevity, only C++ source codes of CFSSSWP uniaxialMaterial are presented in this appendix. As for the C++ source codes of CFSWSWP uniaxialMaterial, the reader is referred to the following website links:

http://opensees.berkeley.edu/WebSVN/filedetails.php?repname=OpenSees&path=%2Ftrunk%2FSRC%2Fmaterial%2Funiaxial%2FCFSWSWP.h

http://opensees.berkeley.edu/WebSVN/filedetails.php?repname=OpenSees&path=%2Ftrunk%2FSRC%2Fmaterial%2Funiaxial%2FCFSWSWP.cpp

B.1. Header file « CFSSSWP.h »

```
/* ****************************************************************** **
**    OpenSees - Open System for Earthquake Engineering Simulation    **
**          Pacific Earthquake Engineering Research Center            **
**                                                                    **
**                                                                    **
** (C) Copyright 1999, The Regents of the University of California    **
** All Rights Reserved.                                               **
**                                                                    **
** Commercial use of this program without express permission of the   **
** University of California, Berkeley, is strictly prohibited.  See   **
** file 'COPYRIGHT' in main directory for information on usage and    **
** redistribution, and for a DISCLAIMER OF ALL WARRANTIES.            **
**                                                                    **
** Developed by:                                                      **
**   Frank McKenna (fmckenna@ce.berkeley.edu)                         **
**   Gregory L. Fenves (fenves@ce.berkeley.edu)                       **
**   Filip C. Filippou (filippou@ce.berkeley.edu)                     **
**                                                                    **
** ****************************************************************** */

// $Revision: 2.0 $
// $Date: 12-10-2015 $

// written by Smail KECHIDI, Ph.D. student at University of Blida 1
(s_kechidi@univ-blida.dz), PhD mobility Student at University of Porto FEUP
(smail.kechidi@fe.up.pt)
// Created: 12-10-2015 10:24:20 $
//
// Description: This file contains the class implementation for CFSSSWP
// CFSSSWP is based on Pinching4 uniaxialMaterial

#ifndef CFSSSWP_h
#define CFSSSWP_h
```

```
 #include <UniaxialMaterial.h>
 #include <OPS_Stream.h>
 #include <Vector.h>
 #include"CubicSpline.h"

 class CFSSSWP : public UniaxialMaterial
 {
 public :

   CFSSSWP(int tag,
         double hight, int width, double fuf, double fyf,
         double tf, double Af, double fus, double fys, double ts,
         double np, double ds, double Vs, double screw_Spacing, double A,
double L);

   CFSSSWP();
   ~CFSSSWP();

   double GetTangentFromCurve(double Strain);
   double GetTangentFromCurve3(double Strain);
   double GetTangentFromCurve4(double Strain);
   double GetStressFromCurve(double Strain);
   double GetStressFromCurve3(double Strain);
   double GetStressFromCurve4(double Strain);
   int setTrialStrain(double strain, double strainRate = 0.0);
   double getStrain(void);
   double getStress(void);
   double getTangent(void);
   double getInitialTangent(void);
   int commitState(void);
   int revertToLastCommit(void);
   int revertToStart(void);

   UniaxialMaterial *getCopy(void);

   int sendSelf(int commitTag, Channel &theChannel);
   int recvSelf(int commitTag, Channel &theChannel,
            FEM_ObjectBroker &theBroker);
   void Print(OPS_Stream &s, int flag = 0);

 protected:

 private:

   // BSpline Adds
   void SetSpline(void);

   double* BSplineXs,*BSplineYs,*BSplinePosDamgdYs, *BSplineNegDamgdYs;
   int BSplineXLength,BSplineYLength;
   CubicSpline Spline3,Spline4;

   // Physical and mechanical characteristics of the panel
   // Shear Wall Panel's Dimensions
   double hight; int width, Precision; double A; double L;

   // Characteristics and material properties of the steel framing studs
   double fuf; double fyf; double tf; double Ife; double Ifi; double E;
   double Af;

   // Characteristics and material properties of sheathing
```

```
double fus; double fys; double ts; double np; double type;

// Characteristics of the screw fasteners
double ds; double screw_Spacing; double nc; double Vs;

// Backbone parameters
double stress1p; double strain1p; double stress2p; double strain2p;
double stress3p; double strain3p; double stress4p; double strain4p;
double stress1n; double strain1n; double stress2n; double strain2n;
double stress3n; double strain3n; double stress4n; double strain4n;
double Dy; double ke;

Vector envlpPosStress; Vector envlpPosStrain;
Vector envlpNegStress; Vector envlpNegStrain;

// material tag
int tagMat;

// Damage parameters
double gammaDLimit;
double gammaFLimit;
double gammaE;
double TnCycle, CnCycle;

// unloading-reloading parameters
double rDispP; double rForceP; double uForceP;
double rDispN; double rForceN; double uForceN;

Vector state3Stress; Vector state3Strain; Vector state4Stress;
Vector state4Strain;

Vector envlpPosDamgdStress; Vector envlpNegDamgdStress;

// Trial State Variables
double Tstress;
double Tstrain;
double Ttangent;

// Converged Material History parameters
int Cstate;
double Cstrain;
double Cstress;
double CstrainRate;
double lowCstateStrain;
double lowCstateStress;
double hghCstateStrain;
double hghCstateStress;
double CminStrainDmnd;
double CmaxStrainDmnd;
double Cenergy;
double CgammaD;
double CgammaDN;
double CgammaF;
double CgammaFN;
double gammaFUsed;

// Trial Material History Parameters
int Tstate;
double dstrain;
double TstrainRate;
double lowTstateStrain;
```

```
   double lowTstateStress;
   double hghTstateStrain;
   double hghTstateStress;
   double TminStrainDmnd;
   double TmaxStrainDmnd;
   double Tenergy;
   double TgammaD;
   double TgammaDN;
   double TgammaF;
   double TgammaFN;

   // strength and stiffness parameters
   double kElasticPos;
   double kElasticNeg;
   double uMaxDamgd;
   double uMinDamgd;

   // energy parameters
   double energyCapacity;
   double kunload;
   double elasticStrainEnergy;
   void lateralShearStrength(void);
   void SetEnvelope(void);
   void getstate(double, double);
   double posEnvlpStress(double);
   double posEnvlpTangent(double);
   double negEnvlpStress(double);
   double negEnvlpTangent(double);
   void getState3(Vector& , Vector& , double);
   void getState4(Vector& , Vector& , double);
   double Envlp3Tangent(Vector , Vector , double);
   double Envlp3Stress(Vector , Vector , double);
   double Envlp4Tangent(Vector , Vector , double);
   double Envlp4Stress(Vector , Vector , double);
   void updateDmg(double, double);
 };
 #endif
```

B.2. C++ file « CFSSSWP.cpp »

```
/* ****************************************************************** **
**    OpenSees - Open System for Earthquake Engineering Simulation    **
**          Pacific Earthquake Engineering Research Center            **
**                                                                    **
**                                                                    **
** (C) Copyright 1999, The Regents of the University of California    **
** All Rights Reserved.                                               **
**                                                                    **
** Commercial use of this program without express permission of the  **
** University of California, Berkeley, is strictly prohibited.  See   **
** file 'COPYRIGHT' in main directory for information on usage and    **
** redistribution, and for a DISCLAIMER OF ALL WARRANTIES.            **
**                                                                    **
** Developed by:                                                      **
**   Frank McKenna (fmckenna@ce.berkeley.edu)                         **
**   Gregory L. Fenves (fenves@ce.berkeley.edu)                       **
**   Filip C. Filippou (filippou@ce.berkeley.edu)                     **
**                                                                    **
** ****************************************************************** */

// $Revision: 1.0 $
```

```
// $Date: 12-10-2015 $

// Written by Smail KECHIDI, Ph.D. student at University of Blida 1
(s_kechidi@univ-blida.dz), PhD mobility Student at University of Porto FEUP
(smail.kechidi@fe.up.pt)
// Created: 12-10-2015 12:24:20 $
//
// Description: This file contains the class implementation for CFSSSWP
// CFSSSWP is based on Pinching4 uniaxialMaterial

#include <elementAPI.h>
#include "CFSSSWP.h"
#include <OPS_Globals.h>
#include <stdlib.h>
#include <math.h>
#include <float.h>
#include <OPS_Stream.h>
#include <stdio.h>
#include <string.h>
#include "CubicSpline.h"
#include "TriMatrix.h"


static int numCFSSSWP = 0;

#ifdef _WIN32
#define isnan _isnan
#endif

void *
OPS_CFSSSWP(void)
{
  // print out some KUDO's
  if (numCFSSSWP == 0) {
    opserr << "Cold Formed Steel Steel-Sheathed Shear Wall Panel
uniaxialMaterial - Written by Smail KECHIDI Ph.D Student at University of
Blida 1 - Please when using this make reference as: Smail Kechidi and
Nouredine Bourahla (2016), Deteriorating hysteresis model for cold-formed
steel shear wall panel based on its physical and mechanical
characteristics, Journal of Thin-Walled Structures, DOI:
10.1016/j.tws.2015.09.022\n";
    numCFSSSWP =1;
  }

  // Pointer to a uniaxial material that will be returned
  UniaxialMaterial *theMaterial = 0;

  //
  // parse the input line for the material parameters
  //

  int    iData[1];
  double dData[16];
  int numData;
  numData = 1;
  if (OPS_GetIntInput(&numData, iData) != 0) {
    opserr << "WARNING invalid uniaxialMaterial CFSSSWP tag" << endln;
    return 0;
  }

  numData = 15;
```

```
  if (OPS_GetDoubleInput(&numData, dData) != 0) {
    opserr << "WARNING invalid Material parameters\n";
    return 0;
  }

  //
  // create a new material
  //

theMaterial = new CFSSSWP(iData[0], dData[0], dData[1], dData[2], dData[3],
dData[4], dData[5], dData[6], dData[7], dData[8], dData[9], dData[10],
dData[11], dData[12], dData[13], dData[14]);

  if (theMaterial == 0) {
   opserr << "WARNING could not create uniaxialMaterial of type CFSSSWP\n";
    return 0;
  }

  // return the material
  return theMaterial;
}

CFSSSWP::CFSSSWP(int tag, double H, int B, double fuf, double fyf, double
tf, double Af, double fus, double fys, double ts, double np, double ds,
double Vs, double sc, double A, double L):
UniaxialMaterial(tag, MAT_TAG_Pinching4), hight(H), width(B), fuf(fuf),
fyf(fyf), tf(tf), Af(Af), fus(fus), fys(fys), ts(ts), np(np), ds(ds),
Vs(Vs), screw_Spacing(sc), A(A), L(L), (7), envlpPosStrain(7),
envlpNegStress(7), envlpNegStrain(7), tagMat(tag),
gammaDLimit(0.0),
gammaFLimit(0.0),
gammaE(10.0),
TnCycle(0.0), CnCycle(0.0),
rDispP(0.488), rForceP(0.183), uForceP(-0.08), rDispN(0.488),
rForceN(0.244), uForceN(-0.08),
state3Stress(4), state3Strain(4), state4Stress(4), state4Strain(4),
envlpPosDamgdStress(7), envlpNegDamgdStress(7)

    {

       double ddeg;
       ddeg = 0.1*((hight/(2*width))*(screw_Spacing/152.0));
       gammaDLimit = ddeg;

// set envelope slopes
this->lateralShearStrength();
this->SetEnvelope();
envlpPosDamgdStress = envlpPosStress; envlpNegDamgdStress = envlpNegStress;
state3Stress.Zero(); state3Strain.Zero(); state4Stress.Zero();
state4Strain.Zero();

// Initialize history variables
this->revertToStart();
this->revertToLastCommit();
}

void CFSSSWP :: lateralShearStrength(void)
{
Precision=100;
```

```
double Alpha,Alpha1,Alpha2,Beta,Beta1,Beta2,Beta3,Lambda,Wmax,Pns,Pns1,
Pns2,Pns3,Pnsed,We,rho,V,V1,V2,Gs,Omega1,Omega2,Omega3,Omega4,Delta1,
Delta2,Delta3,Delta4,DeltaV,MinPns,MinPns1,MinPns2,N,Pn; Pns=0; MinPns=0;
double mu=0.3; E=203000.00; Dy=0;
Alpha=hight/width;
Alpha1=fus/310.27;
Alpha2=fuf/310.27;
Beta1=ts/0.4572;
Beta2=tf/0.4572;
Beta3=screw_Spacing/152.4;
Lambda=1.736*(Alpha1*Alpha2)/(Beta1*Beta2*pow(Beta3,2)*Alpha);
Wmax=width/(hight/(sqrt(pow(hight,2)+(width*width))));
            if (tf/ts<=1.0)
            {
                  Pns1=4.2*sqrt(pow(tf,3)*ds)*fuf;
                  Pns2=2.7*ts*ds*fus;
                  Pns3=2.7*tf*ds*fuf;
                  MinPns=Pns1;
                  MinPns=(Pns2<MinPns)? Pns2:MinPns;
                  MinPns=(Pns3<MinPns)? Pns3:MinPns;
            }
            else if (tf/ts>=2.5)
            {
                  Pns1=2.7*ts*ds*fus;
                  Pns2=2.7*tf*ds*fuf;
                  MinPns=(Pns1<Pns2)? Pns1:Pns2;
            }
            else if ((tf/ts)>1.0 && (tf/ts)<2.5)
            {
                  Pns1=4.2*sqrt(pow(tf,3)*ds)*fuf;
                  Pns2=2.7*ts*ds*fus;
                  Pns3=2.7*tf*ds*fuf;
                  MinPns1=Pns1;
                  MinPns1=(Pns2<MinPns)? Pns2:MinPns1;
                  MinPns1=(Pns3<MinPns)? Pns3:MinPns1;
                  MinPns2=(Pns1<Pns2)? Pns2:Pns3;
                  MinPns=MinPns1+(MinPns2-MinPns1)*((tf/ts)-1)/1.5;
         }
                  double dis=3*ds;
                  Pnsed=0.5*dis*ts*fus;
                  if (Lambda<=0.0819)
                  We=Wmax;
            else
            {
                  rho=(1-0.05*pow((Lambda-0.08),0.12))/pow(Lambda,0.12);
                  We=rho*Wmax;
            }
                  Pn=(MinPns<Pnsed)? MinPns:Pnsed;
V1=(((We/(2*screw_Spacing))*Pn)+((We*width)/(2*screw_Spacing*hight)*Pn)+Vs*
(width/(sqrt(pow(hight,2)+(width*width)))));
                  V2=(We*ts*fys)*(width/sqrt(pow(hight,2)+(width*width)));
                  V=(V1<V2)? V1:V2;
                  double r,fo;
                  r=1/(1+A/(hight*(width-L)));
                  fo=r/(3-2*r);
                  stress3p=fo*V*np;
                  Beta=500*(ts/0.457);
                  Gs=E/(2*(1+mu));
                  Omega4=sqrt(227.53/fyf);
                  rho=0.075*(ts/0.457);
      Delta1=(2*(stress3p/(width*np))*pow(hight,3)/(3*E*Af*width));
```

```
      Omega1=screw_Spacing/152.4;
      Omega2=0.838/tf;

      Delta2=Omega1*Omega2*((stress3p/(width*np))*hight)/(rho*Gs*ts);
      Omega3=sqrt(hight/(2*width));

      Delta3=pow(Omega1,(5/4))*Omega2*Omega3*Omega4*pow((stress3p/(width*np
)/(0.0029*Beta)),2);
                  Delta4=2.5*hight/width;
                  strain3p=(Delta1+Delta2+Delta3+Delta4)/(1000);
                  stress4p=0.8*stress3p;
                  strain4p=1.4*strain3p;
                  stress1p=0.4*stress3p;
                  strain1p=strain3p/9.25;
                  ke=stress1p/strain1p;
                  stress2p=0.85*stress3p;
                  Dy=(stress2p/ke);
strain2p=(stress2p*(strain3p+Dy-2*strain4p-
strain1p)+stress3p*strain4p+stress4p*(strain4p-strain3p))/(0.6*stress3p);
stress1p=stress1p; stress2p=stress2p; stress3p=stress3p; stress4p=stress4p;
strain1p=strain1p; strain2p=strain2p; strain3p=strain3p; strain4p=strain4p;
strain1n = -strain1p; stress1n = -stress1p; strain2n = -strain2p; stress2n
= -stress2p;
strain3n = -strain3p; stress3n = -stress3p; strain4n = -strain4p; stress4n
= -stress4p;
envlpPosStress.Zero(); envlpPosStrain.Zero(); envlpNegStress.Zero();
envlpNegStrain.Zero();
energyCapacity = 0.0; kunload = 0.0; elasticStrainEnergy = 0.0;
}

 CFSSSWP::CFSSSWP():
 UniaxialMaterial(0, MAT_TAG_Pinching4),
   stress1p(0.0), strain1p(0.0), stress2p(0.0), strain2p(0.0),
   stress3p(0.0), strain3p(0.0), stress4p(0.0), strain4p(0.0),
   stress1n(0.0), strain1n(0.0), stress2n(0.0), strain2n(0.0),
   stress3n(0.0), strain3n(0.0), stress4n(0.0), strain4n(0.0),

   gammaDLimit(0.0),
   gammaFLimit(0.0),
   gammaE(0.0),
   rDispP(0.0), rForceP(0.0), uForceP(0.0), rDispN(0.0), rForceN(0.0),
   uForceN(0.0)
 {

 }

 CFSSSWP::~CFSSSWP()
 {

 }

int CFSSSWP::setTrialStrain(double strain, double CstrainRate)
 {
         Tstate = Cstate;
         Tenergy = Cenergy;
         Tstrain = strain;
         lowTstateStrain = lowCstateStrain;
         hghTstateStrain = hghCstateStrain;
         lowTstateStress = lowCstateStress;
         hghTstateStress = hghCstateStress;
         TminStrainDmnd = CminStrainDmnd;
```

```
         TmaxStrainDmnd = CmaxStrainDmnd;
         TgammaF = CgammaF;
         TgammaFN = CgammaFN;
         TgammaD = CgammaD;
         TgammaDN = CgammaDN;

         dstrain = Tstrain - Cstrain;
         if (dstrain<1e-12 && dstrain>-1e-12){
                 dstrain = 0.0;
         }

         // determine new state if there is a change in state
         getstate(Tstrain,dstrain);

         switch (Tstate)
         {

         case 0:
                 Ttangent = envlpPosStress(0)/envlpPosStrain(0);
                 Tstress = Ttangent*Tstrain;
                 break;
         case 1:
                 Tstress = posEnvlpStress(strain);
                 Ttangent = posEnvlpTangent(strain);
                 break;
         case 2:
                 Ttangent = negEnvlpTangent(strain);
                 Tstress = negEnvlpStress(strain);
                 break;
         case 3:
                 kunload = (hghTstateStrain<0.0) ? kElasticNeg:kElasticPos;
                         state3Strain(0) = lowTstateStrain;
                         state3Strain(3) = hghTstateStrain;
                         state3Stress(0) = lowTstateStress;
                         state3Stress(3) = hghTstateStress;

                 getState3(state3Strain,state3Stress,kunload);
                 SetSpline();
Ttangent = Envlp3Tangent(state3Strain,state3Stress,strain);
Tstress = Envlp3Stress(state3Strain,state3Stress,strain);
                 break;
         case 4:
                 kunload = (lowTstateStrain<0.0) ? kElasticNeg:kElasticPos;
                         state4Strain(0) = lowTstateStrain;
                         state4Strain(3) = hghTstateStrain;
                         state4Stress(0) = lowTstateStress;
                         state4Stress(3) = hghTstateStress;

                 getState4(state4Strain,state4Stress,kunload);
                 SetSpline();
Ttangent = Envlp4Tangent(state4Strain,state4Stress,strain);
Tstress = Envlp4Stress(state4Strain,state4Stress,strain);
                 break;
         }

         double denergy = 0.5*(Tstress+Cstress)*dstrain;
         elasticStrainEnergy = (Tstrain>0.0) ?
0.5*Tstress/kElasticPos*Tstress:0.5*Tstress/kElasticNeg*Tstress;
Tenergy = Cenergy + denergy;
updateDmg(Tstrain,dstrain);
             return 0;
```

```
 }

static int
getIndex(Vector v,double value)
{
      for(int i = 0; i < v.Size(); i++)
      {
            if(v[i] > value) return i;
      }
      return -1;
}
static int
getIndexNeg(Vector v,double value)
{
      for(int i = 0; i < v.Size(); i++)
      {
            if(v[i] < value) return i;
      }
      return -1;
}

 void CFSSSWP::SetSpline(void)
 {
                  int Size = 5;
                  double *X = new double[Size], *Y = new double[Size];

                  int fifth = getIndexNeg(envlpNegStrain,state3Strain(0));
                  if(fifth == -1)
                  {
                        printf("erreur fifth");
                        exit(5);
                  }

                  X[0] = state3Strain(0) - 20;
                  X[1] = state3Strain(0);
                  X[2] = state3Strain(1);
                  X[3] = state3Strain(2);
                  X[4] = state3Strain(3);


                  Y[0] = state3Stress(0) - 1;
                  Y[1] = state3Stress(0);
                  Y[2] = state3Stress(1);
                  Y[3] = state3Stress(2);
                  Y[4] = state3Stress(3);

                  if(X[3] - X[0] < 0)
                  {
                        printf("erreur1\n");
                  }

                  float a0,an,b0,bn;

                  a0 = GetTangentFromCurve(state3Strain(0));
                  an = GetTangentFromCurve(state3Strain(3));
                  b0 = state3Stress(0) - a0*state3Strain(0);
                  bn = state3Stress(3) - an*state3Strain(3);

                  Spline3.Fit(X,Size,Y,Size);

                  fifth = getIndex(envlpPosStrain,state4Strain(3));
```

```
                 if(fifth == -1)
                 {
                       printf("erreur fifth1");
                       exit(5);
                 }

                 X[0] = state4Strain(0);
                 X[1] = state4Strain(1);
                 X[2] = state4Strain(2);
                 X[3] = state4Strain(3);
                 X[4] = state4Strain(3) + 20;

                 Y[0] = state4Stress(0);
                 Y[1] = state4Stress(1);
                 Y[2] = state4Stress(2);
                 Y[3] = state4Stress(3);
                 Y[4] = state4Stress(3) + 1;

                 if(X[3] - X[0] < 0)
                 {
                       printf("erreur2\n");
                       while(1);
                 }

                 a0 = GetTangentFromCurve(state4Strain(0));
                 an = GetTangentFromCurve(state4Strain(3));
                 b0 = state4Stress(0) - a0 * state4Strain(0);
                 bn = state4Stress(3) - an * state4Strain(3);

                 Spline4.Fit(X,Size,Y,Size);
}

double CFSSSWP::getStrain(void)
{
        return Tstrain;
}

double CFSSSWP::getStress(void)
{
        return Tstress;
}

double CFSSSWP::getTangent(void)
{
        return Ttangent;
}

double CFSSSWP::getInitialTangent(void)
{
        return envlpPosStress(0)/envlpPosStrain(0);
}

int CFSSSWP::commitState(void)
{
        Cstate = Tstate;

        if (dstrain>1e-12||dstrain<-(1e-12)) {
                CstrainRate = dstrain;}
        else {
        CstrainRate = TstrainRate;}
        lowCstateStrain = lowTstateStrain;
```

```
        lowCstateStress = lowTstateStress;
        hghCstateStrain = hghTstateStrain;
        hghCstateStress = hghTstateStress;
        CminStrainDmnd = TminStrainDmnd;
        CmaxStrainDmnd = TmaxStrainDmnd;
        Cenergy = Tenergy;
        Cstress = Tstress;
        Cstrain = Tstrain;
        CgammaD = TgammaD;
        CgammaDN = TgammaDN;
        CgammaF = TgammaF;
        CgammaFN = TgammaFN;
        CnCycle = TnCycle;

        // define adjusted strength and stiffness parameters

        uMaxDamgd = TmaxStrainDmnd*(1 + CgammaD);
        uMinDamgd = TminStrainDmnd*(1 + CgammaDN);

        envlpPosDamgdStress = envlpPosStress*(1-gammaFUsed);
        envlpNegDamgdStress = envlpNegStress*(1-gammaFUsed);

        return 0;
}

int CFSSSWP::revertToLastCommit(void)
{

        Tstate = Cstate;

        TstrainRate = CstrainRate;

        lowTstateStrain = lowCstateStrain;
        lowTstateStress = lowCstateStress;
        hghTstateStrain = hghCstateStrain;
        hghTstateStress = hghCstateStress;
        TminStrainDmnd = CminStrainDmnd;
        TmaxStrainDmnd = CmaxStrainDmnd;
        Tenergy = Cenergy;

        Tstrain = Cstrain; Tstress = Cstress;

        TgammaD = CgammaD;
        TgammaDN = CgammaDN;
        TgammaF = CgammaF;
        TgammaFN = CgammaFN;
        TnCycle = CnCycle;

        return 0;
}

int CFSSSWP::revertToStart(void)
{
        Cstate = 0;
        Cstrain = 0.0;
        Cstress = 0.0;
        CstrainRate = 0.0;
        lowCstateStrain = envlpNegStrain(0);
        lowCstateStress = envlpNegStress(0);
        hghCstateStrain = envlpPosStrain(0);
        hghCstateStress = envlpPosStress(0);
```

```
         CminStrainDmnd = envlpNegStrain(1);
         CmaxStrainDmnd = envlpPosStrain(1);
         Cenergy = 0.0;
         CgammaD = 0.0;
         CgammaDN = 0.0;
         CgammaF = 0.0;
         CgammaFN = 0.0;
         TnCycle = 0.0;
         CnCycle = 0.0;
         Ttangent = envlpPosStress(0)/envlpPosStrain(0);
         dstrain = 0.0;
         gammaFUsed = 0.0;
         uMaxDamgd = CmaxStrainDmnd;
         uMinDamgd = CminStrainDmnd;

         return 0;
 }

 UniaxialMaterial* CFSSSWP::getCopy(void)
 {
CFSSSWP *theCopy = new CFSSSWP (this->getTag(),hight,  width,  fuf,  fyf,
tf,  Af,  fus, fys,  ts, np,  ds,  Vs,  screw_Spacing, A, L);

         theCopy->rDispN = rDispN;
         theCopy->rDispP = rDispP;
         theCopy->rForceN = rForceN;
         theCopy->rForceP = rForceP;
         theCopy->uForceN = uForceN;
         theCopy->uForceP = uForceP;

         // Trial state variables
         theCopy->Tstress = Tstress;
         theCopy->Tstrain = Tstrain;
         theCopy->Ttangent = Ttangent;

         // Coverged material history parameters
         theCopy->Cstate = Cstate;
         theCopy->Cstrain = Cstrain;
         theCopy->Cstress = Cstress;
         theCopy->CstrainRate = CstrainRate;
         theCopy->lowCstateStrain = lowCstateStrain;
         theCopy->lowCstateStress = lowCstateStress;
         theCopy->hghCstateStrain = hghCstateStrain;
         theCopy->hghCstateStress = hghCstateStress;
         theCopy->CminStrainDmnd = CminStrainDmnd;
         theCopy->CmaxStrainDmnd = CmaxStrainDmnd;
         theCopy->Cenergy = Cenergy;
         theCopy->CgammaD = CgammaD;
         theCopy->CgammaDN = CgammaDN;
         theCopy->CgammaF = CgammaF;
         theCopy->CgammaFN = CgammaFN;
         theCopy->CnCycle = CnCycle;
         theCopy->gammaFUsed = gammaFUsed;

         // trial material history parameters
         theCopy->Tstate = Tstate;
         theCopy->dstrain = dstrain;
         theCopy->lowTstateStrain = lowTstateStrain;
         theCopy->lowTstateStress = lowTstateStress;
         theCopy->hghTstateStrain = hghTstateStrain;
         theCopy->hghTstateStress = hghTstateStress;
```

```
        theCopy->TminStrainDmnd = TminStrainDmnd;
        theCopy->TmaxStrainDmnd = TmaxStrainDmnd;
        theCopy->Tenergy = Tenergy;
        theCopy->TgammaD = TgammaD;
        theCopy->TgammaDN = TgammaDN;
        theCopy->TgammaF = TgammaF;
        theCopy->TgammaFN = TgammaFN;
        theCopy->TnCycle = TnCycle;

        // Strength and stiffness parameters
        theCopy->kElasticPos = kElasticPos;
        theCopy->kElasticNeg = kElasticNeg;
        theCopy->uMaxDamgd = uMaxDamgd;
        theCopy->uMinDamgd = uMinDamgd;

        for (int i = 0; i<7; i++)
        {
                theCopy->envlpPosStrain(i) = envlpPosStrain(i);
                theCopy->envlpPosStress(i) = envlpPosStress(i);
                theCopy->envlpNegStrain(i) = envlpNegStrain(i);
                theCopy->envlpNegStress(i) = envlpNegStress(i);
                theCopy->envlpNegDamgdStress(i) = envlpNegDamgdStress(i);
                theCopy->envlpPosDamgdStress(i) = envlpPosDamgdStress(i);
        }

        for (int j = 0; j<4; j++)
        {
                theCopy->state3Strain(j) = state3Strain(j);
                theCopy->state3Stress(j) = state3Stress(j);
                theCopy->state4Strain(j) = state4Strain(j);
                theCopy->state4Stress(j) = state4Stress(j);
        }

        theCopy->energyCapacity = energyCapacity;
        theCopy->kunload = kunload;
        theCopy->elasticStrainEnergy = elasticStrainEnergy;

        return theCopy;
}

int CFSSSWP::sendSelf(int commitTag, Channel &theChannel)
{
        return -1;
}

int CFSSSWP::recvSelf(int commitTag, Channel &theChannel,

FEM_ObjectBroker & theBroker)
{
        return -1;
}

void CFSSSWP::Print(OPS_Stream &s, int flag)
{
        s << "CFSSSWP, tag: " << this-> getTag() << endln;
        s << "Displacement: " << Tstrain << endln;
        s << "Strength: " << Tstress << endln;
        s << "state: " << Tstate << endln;
}

void CFSSSWP::SetEnvelope(void)
```

```
 {
         double kPos = stress1p/strain1p;
         double kNeg = stress1n/strain1n;
         double k = (kPos>kNeg) ? kPos:kNeg;
         double u = (strain1p>-strain1n) ? 1e-20*strain1p:-1e-20*strain1n;

         envlpPosStrain(0) = u;
         envlpPosStress(0) = u*k;
         envlpNegStrain(0) = -u;
         envlpNegStress(0) = -u*k;

         envlpPosStrain(1) = strain1p;
         envlpPosStrain(2) = strain2p;
         envlpPosStrain(3) = strain3p;
         envlpPosStrain(4) = strain4p;

         envlpNegStrain(1) = strain1n;
         envlpNegStrain(2) = strain2n;
         envlpNegStrain(3) = strain3n;
         envlpNegStrain(4) = strain4n;

         envlpPosStress(1) = stress1p;
         envlpPosStress(2) = stress2p;
         envlpPosStress(3) = stress3p;
         envlpPosStress(4) = stress4p;

         envlpNegStress(1) = stress1n;
         envlpNegStress(2) = stress2n;
         envlpNegStress(3) = stress3n;
         envlpNegStress(4) = stress4n;

         double k1 = (stress4p - stress3p)/(strain4p - strain3p);
         double k2 = (stress4n - stress3n)/(strain4n - strain3n);

         envlpPosStress(5) =0.05*stress3p;
         envlpPosStrain(5) = strain4p + 3.75*(strain4p-strain3p);
         envlpNegStress(5) = 0.05*stress3n;
         envlpNegStrain(5) = strain4n + 3.75*(strain4n-strain3n);

         envlpPosStrain(6) = 1e+6*envlpPosStress(5);
         envlpPosStress(6) = (k1>0.0)?
         envlpPosStress(5)+k1*(envlpPosStrain(6)-
         envlpPosStrain(5)):envlpPosStress(5)*1.1;
         envlpNegStrain(6) = 1e+6*strain4n;
         envlpNegStress(6) = (k2>0.0)?
envlpNegStress(5)+k1*(envlpNegStrain(6)-
envlpNegStrain(5)):envlpNegStress(5)*1.1;

         // define crtical material properties
         kElasticPos = envlpPosStress(1)/envlpPosStrain(1);
         kElasticNeg = envlpNegStress(1)/envlpNegStrain(1);

         double energypos = 0.5*envlpPosStrain(0)*envlpPosStress(0);

         for (int jt = 0; jt<4; jt++){
         energypos += 0.5*(envlpPosStress(jt) +
envlpPosStress(jt+1))*(envlpPosStrain(jt+1)-envlpPosStrain(jt));
         }

         double energyneg = 0.5*envlpNegStrain(0)*envlpNegStress(0);
```

```
         for (int jy = 0; jy<4; jy++){
         energyneg += 0.5*(envlpNegStress(jy) +
envlpNegStress(jy+1))*(envlpNegStrain(jy+1)-envlpNegStrain(jy));
         }

         double max_energy = (energypos>energyneg) ? energypos:energyneg;

         energyCapacity = gammaE*max_energy;

             // BSpline Adds

             int Size = 9;
             double *X = new double[Size], *Y = new double[Size];

             for(int i = 0;i < 2;i++)
             {
                   X[i] = envlpPosStrain(0);
                   Y[i] = envlpPosStress(0);
                   X[Size - i - 1] = envlpPosStrain(4);
                   Y[Size - i - 1] = envlpPosStress(4);
             }

             for(int i = 0;i < Size - 4;i++)
             {
                   X[i + 2] = envlpPosStrain(i);
                   Y[i + 2] = envlpPosStress(i);
             }
double *XFit = new double[(Size-3)*Precision+2],*YFit = new double[(Size-
3)*Precision+2];
            double *a = new double[4], *b = new double[4];

            double p1X,p1Y,p2X,p2Y,p3X,p3Y,p4X,p4Y;

            for(int i = 0;i < Size-3;i++)
      {
          p1X = X[i];
          p1Y = Y[i];
          p2X = X[i + 1];
          p2Y = Y[i + 1];
          p3X = X[i + 2];
          p3Y = Y[i + 2];
          p4X = X[i + 3];
          p4Y = Y[i + 3];
          a[0] = (-p1X + 3 * p2X - 3 * p3X + p4X) / 6.0f;
          a[1] = (3 * p1X - 6 * p2X + 3 * p3X) / 6.0f;
          a[2] = (-3 * p1X + 3 * p3X) / 6.0f;
          a[3] = (p1X + 4 * p2X + p3X) / 6.0f;
          b[0] = (-p1Y + 3 * p2Y - 3 * p3Y + p4Y) / 6.0f;
          b[1] = (3 * p1Y - 6 * p2Y + 3 * p3Y) / 6.0f;
          b[2] = (-3 * p1Y + 3 * p3Y) / 6.0f;
          b[3] = (p1Y + 4 * p2Y + p3Y) / 6.0f;
          for (int j = 0; j < Precision; j++)
          {
               float t = (float)(j) / (float)(Precision);
XFit[i*Precision+j] = ((a[2] + t * (a[1] + t * a[0])) * t + a[3]);
YFit[i*Precision+j] = ((b[2] + t * (b[1] + t * b[0])) * t + b[3]);
          }
      }

double XAdvance = XFit[Precision*(Size-3)-1] - XFit[Precision*(Size-3)-2];
double YAdvance = YFit[Precision*(Size-3)-1] - YFit[Precision*(Size-3)-2];
```

```
double Tangente = (YFit[Precision*(Size-3)-1] - YFit[Precision*(Size-3)-
2])/(XFit[Precision*(Size-3)-1] - XFit[Precision*(Size-3)-2]);

      double Epsilon = 0.1f;

      YFit[Precision*(Size-3)] = Epsilon;
      XFit[Precision*(Size-3)] = XFit[Precision*(Size-3) - 1] + (Epsilon -
YFit[Precision*(Size-3) - 1]) / Tangente;

      YFit[Precision*(Size-3)+1] = Epsilon;
      XFit[Precision*(Size-3)+1] = 10000;

      BSplineXs = XFit;
      BSplineYs = YFit;

      BSplineXLength = Precision*(Size-3) + 2;
      BSplineYLength = Precision*(Size-3) + 2;

 }

 double CFSSSWP::GetTangentFromCurve(double Strain)
 {
            int i = 0;
            int Neg = 0;
            while(i < BSplineXLength && BSplineXs[i] < Strain)
            {
                  i++;
            }
            if(i == BSplineXLength && BSplineXs[i-1] < Strain)
            {
                  if(Neg == 0) return 1;
                  return -1;
                  exit(0);
            }
            if(BSplineXs[i] == Strain)
            {
return (BSplineYs[i+1] - BSplineYs[i-1]) / (BSplineXs[i+1] - BSplineXs[i-
1]);
            }
            else if (i < BSplineXLength - 2 && BSplineXs[i+1] == Strain)
            {
return (BSplineYs[i+2] - BSplineYs[i]) / (BSplineXs[i+2] - BSplineXs[i]);
            }
            else
            {
return (BSplineYs[i] - BSplineYs[i-1]) / (BSplineXs[i] - BSplineXs[i-1]);
            }
 }

 double CFSSSWP::GetStressFromCurve(double Strain)
 {
            int i = 0;
            int Neg = 0;
            if (Strain < 0)
            {
                  Neg = 1;
                  Strain = -Strain;
            }
            while(i < BSplineXLength && BSplineXs[i] < Strain)
            {
                  i++;
```

```
            }
            if(i == BSplineXLength && BSplineXs[i-1] < Strain)
            {
                  if(Neg == 0) return -1;
                  return 1;
            }
            if(BSplineXs[i] == Strain)
            {
                  if(Neg == 1)
                        return BSplineYs[i];
                        return BSplineYs[i];
            }
            else if (i < BSplineXLength - 1 && BSplineXs[i+1] == Strain)
            {
                  return BSplineYs[i+1];
            }
            else
            {
double Stress = BSplineYs[i-1] + (BSplineYs[i] - BSplineYs[i-1]) /
(BSplineXs[i] - BSplineXs[i-1]) * (Strain - BSplineXs[i-1]);
                  if(Neg == 1)
                  return -Stress;
                  return  Stress;
                  }
 }

 void CFSSSWP::getstate(double u,double du)
 {
         int cid = 0;
         int cis = 0;
         int newState = 0;
         if (du*CstrainRate<=0.0){
                 cid = 1;
         }
         if (u<lowTstateStrain || u>hghTstateStrain || cid) {
                 if (Tstate == 0) {
                         if (u>hghTstateStrain) {
                                 cis = 1;
                                 newState = 1;
                                 lowTstateStrain = envlpPosStrain(0);
                                 lowTstateStress = envlpPosStress(0);
                                 hghTstateStrain = envlpPosStrain(5);
                                 hghTstateStress = envlpPosStress(5);
                         }
                         else if (u<lowTstateStrain){
                                 cis = 1;
                                 newState = 2;
                                 lowTstateStrain = envlpNegStrain(5);
                                 lowTstateStress = envlpNegStress(5);
                                 hghTstateStrain = envlpNegStrain(0);
                                 hghTstateStress = envlpNegStress(0);
                         }
                 }
                 else if (Tstate==1 && du<0.0) {
                         cis = 1;
                         if (Cstrain>TmaxStrainDmnd) {
                                 TmaxStrainDmnd = u - du;
                         }
                         if (TmaxStrainDmnd<uMaxDamgd) {
                                 TmaxStrainDmnd = uMaxDamgd;
                         }
```

```
                         if (u<uMinDamgd) {
                                 newState = 2;
                                 gammaFUsed = CgammaFN;
                                 for (int i=0; i<=6; i++) {
         envlpNegDamgdStress(i) = envlpNegStress(i)*(1.0-gammaFUsed);
                                 }
                                 lowTstateStrain = envlpNegStrain(6);
                                 lowTstateStress = envlpNegStress(6);
                                 hghTstateStrain = envlpNegStrain(0);
                                 hghTstateStress = envlpNegStress(0);
                         }
                         else {
                                 newState = 3;
                                 lowTstateStrain = uMinDamgd;
                                 gammaFUsed = CgammaFN;
                                 for (int i=0; i<=6; i++) {
         envlpNegDamgdStress(i) = envlpNegStress(i)*(1.0-gammaFUsed);
                                 }
                         lowTstateStress = negEnvlpStress(uMinDamgd);
                                 hghTstateStrain = Cstrain;
                                 hghTstateStress = Cstress;
                         }

                 }
                 else if (Tstate ==2 && du>0.0){
                         cis = 1;
                         if (Cstrain<TminStrainDmnd) {
                                 TminStrainDmnd = Cstrain;
                         }
                         if (TminStrainDmnd>uMinDamgd) {
                                 TminStrainDmnd = uMinDamgd;
                         }
                         if (u>uMaxDamgd) {
                                 newState = 1;
                                 gammaFUsed = CgammaF;
                                 for (int i=0; i<=6; i++) {
         envlpPosDamgdStress(i) = envlpPosStress(i)*(1.0-gammaFUsed);
                                 }
                                 lowTstateStrain = envlpPosStrain(0);
                                 lowTstateStress = envlpPosStress(0);
                                 hghTstateStrain = envlpPosStrain(5);
                                 hghTstateStress = envlpPosStress(5);
                         }
                         else {
                                 newState = 4;
                                 lowTstateStrain = Cstrain;
                                 lowTstateStress = Cstress;
                                 hghTstateStrain = uMaxDamgd;
                                 gammaFUsed = CgammaF;
                                 for (int i=0; i<=6; i++) {
         envlpPosDamgdStress(i) = envlpPosStress(i)*(1.0-gammaFUsed);
                                 }
         hghTstateStress = posEnvlpStress(uMaxDamgd);
                         }

                 }
else if (Tstate ==3) {
if (u<lowTstateStrain){
cis = 1;
newState = 2;
lowTstateStrain = envlpNegStrain(5);
```

```
hghTstateStrain = envlpNegStrain(0);
lowTstateStress = envlpNegDamgdStress(5);
hghTstateStress = envlpNegDamgdStress(0);
                      }
else if (u>uMaxDamgd && du>0.0) {
cis = 1;
newState = 1;
lowTstateStrain = envlpPosStrain(0);
lowTstateStress = envlpPosStress(0);
hghTstateStrain = envlpPosStrain(5);
hghTstateStress = envlpPosStress(5);
                                 }
else if (du>0.0) {
cis = 1;
newState = 4;
lowTstateStrain = Cstrain;
lowTstateStress = Cstress;
hghTstateStrain = uMaxDamgd;
gammaFUsed = CgammaF;
for (int i=0; i<=6; i++) {
envlpPosDamgdStress(i) = envlpPosStress(i)*(1.0-gammaFUsed);
                         }
hghTstateStress = posEnvlpStress(uMaxDamgd);

                         }
                         }
else if (Tstate == 4){
if (u>hghTstateStrain){
cis = 1;
newState = 1;
lowTstateStrain = envlpPosStrain(0);
lowTstateStress = envlpPosDamgdStress(0);
hghTstateStrain = envlpPosStrain(5);
hghTstateStress = envlpPosDamgdStress(5);
                      }
else if (u<uMinDamgd && du <0.0) {
cis = 1;
newState = 2;
lowTstateStrain = envlpNegStrain(5);
lowTstateStress = envlpNegDamgdStress(5);
hghTstateStrain = envlpNegStrain(0);
hghTstateStress = envlpNegDamgdStress(0);
                                 }
else if (du<0.0) {
cis = 1;
newState = 3;
lowTstateStrain = uMinDamgd;
gammaFUsed = CgammaFN;
for (int i=0; i<=6; i++) {
envlpNegDamgdStress(i) = envlpNegStress(i)*(1.0-gammaFUsed);
                         }
lowTstateStress = negEnvlpStress(uMinDamgd);
hghTstateStrain = Cstrain;
hghTstateStress = Cstress;

                         }
                         }
                         }
if (cis) {
Tstate = newState;
```

```
         }
         }

double CFSSSWP::posEnvlpStress(double u)
                 {
                         double k = 0.0;
                         int i = 0;
                         double f = 0.0;
                                     f = GetStressFromCurve(u);
                                     f = f*(1-gammaFUsed);
                                     return f;
                         while (k==0.0 && i<=5){

if (u<=envlpPosStrain(i+1)){
k = (envlpPosDamgdStress(i+1)-envlpPosDamgdStress(i))/(envlpPosStrain(i+1)-
envlpPosStrain(i));
f = envlpPosDamgdStress(i) + (u-envlpPosStrain(i))*k;
                           }
i++;
                           }


if (k==0.0){
k = (envlpPosDamgdStress(6) - envlpPosDamgdStress(5))/(envlpPosStrain(6) -
envlpPosStrain(5));
f = envlpPosDamgdStress(6) + k*(u-envlpPosStrain(6));
                           }
                         return f;

                           }

 double CFSSSWP::posEnvlpTangent(double u)
                           {
                         double k = 0.0;
                         int i = 0;
while (k==0.0 && i<=5){
if (u<=envlpPosStrain(i+1)){
k = (envlpPosDamgdStress(i+1)-envlpPosDamgdStress(i))/(envlpPosStrain(i+1)-
envlpPosStrain(i));
                         }
                                  i++;
                         }

                         if (k==0.0){
k = (envlpPosDamgdStress(6) - envlpPosDamgdStress(5))/(envlpPosStrain(6) -
envlpPosStrain(5));
                                     }
k = GetTangentFromCurve(u);

                         return k;

                 }

 double CFSSSWP::negEnvlpStress(double u)
                 {
                         double k = 0.0;
                         int i = 0;
                         double f = 0.0;
                                     f = GetStressFromCurve(u);
                                     f = f*(1-gammaFUsed);
                                     return f;
```

```
while (k==0.0 && i<=5){
if (u>=envlpNegStrain(i+1)){
k = (envlpNegDamgdStress(i)-envlpNegDamgdStress(i+1))/(envlpNegStrain(i)-
envlpNegStrain(i+1));
f = envlpNegDamgdStress(i+1)+(u-envlpNegStrain(i+1))*k;
                           }
i++;
                           }

if (k==0.0){
k = (envlpNegDamgdStress(5) - envlpNegDamgdStress(6))/(envlpNegStrain(5)-
envlpNegStrain(6));
f = envlpNegDamgdStress(6) + k*(u-envlpNegStrain(6));
                           }
return f;

                 }

 double CFSSSWP::negEnvlpTangent(double u)
                 {
                         double k = 0.0;
                         int i = 0;
                         while (k==0.0 && i<=5){

if (u>=envlpNegStrain(i+1)){
k = (envlpNegDamgdStress(i)-envlpNegDamgdStress(i+1))/(envlpNegStrain(i)-
envlpNegStrain(i+1));
                           }
                                  i++;
                           }

if (k==0.0){
k = (envlpNegDamgdStress(5) - envlpNegDamgdStress(6))/(envlpNegStrain(5)-
envlpNegStrain(6));
                           }
k = GetTangentFromCurve(u);
                         return k;

                           }

 void CFSSSWP::getState3(Vector& state3Strain, Vector& state3Stress, double
kunload)
                 {

double kmax = (kunload>kElasticNeg) ? kunload:kElasticNeg;

if (state3Strain(0)*state3Strain(3) <0.0){

// trilinear unload reload path expected, first define point for reloading
state3Strain(1) = lowTstateStrain*rDispN;
if (rForceN-uForceN > 1e-8) {
state3Stress(1) = lowTstateStress*rForceN;
                                  }
                                 else {
if (TminStrainDmnd < envlpNegStrain(3)) {
double st1 = lowTstateStress*uForceN*(1.0+1e-6);
double st2 = envlpNegDamgdStress(4)*(1.0+1e-6);
state3Stress(1) = (st1<st2) ? st1:st2;
                                          }
else {
double st1 = envlpNegDamgdStress(3)*uForceN*(1.0+1e-6);
```

```
double st2 = envlpNegDamgdStress(4)*(1.0+1e-6);
state3Stress(1) = (st1<st2) ? st1:st2;
                                        }
                                }

// if reload stiffness exceeds unload stiffness, reduce reload stiffness to
make it equal to unload stiffness
if ((state3Stress(1)-state3Stress(0))/(state3Strain(1)-state3Strain(0)) >
kElasticNeg) {
state3Strain(1) = lowTstateStrain + (state3Stress(1)-
state3Stress(0))/kElasticNeg;
                                }

// check that reloading point is not behind point 4
if (state3Strain(1)>state3Strain(3)) {

// path taken to be a straight line between points 1 and 4
double du = state3Strain(3) - state3Strain(0);
double df = state3Stress(3) - state3Stress(0);
state3Strain(1) = state3Strain(0) + 0.33*du;
state3Strain(2) = state3Strain(0) + 0.67*du;
state3Stress(1) = state3Stress(0) + 0.33*df;
state3Stress(2) = state3Stress(0) + 0.67*df;
                                }
else {
if (TminStrainDmnd < envlpNegStrain(3)) {
state3Stress(2) = uForceN*envlpNegDamgdStress(4);
                                        }
else {
state3Stress(2) = uForceN*envlpNegDamgdStress(3);
                                        }
state3Strain(2) = hghTstateStrain - (hghTstateStress-
state3Stress(2))/kunload;

if (state3Strain(2) > state3Strain(3)) {

// point 3 should be along a line between 2 and 4
double du = state3Strain(3) - state3Strain(1);
double df = state3Stress(3) - state3Stress(1);
state3Strain(2) = state3Strain(1) + 0.5*du;
state3Stress(2) = state3Stress(1) + 0.5*df;
                                        }
else if ((state3Stress(2) - state3Stress(1))/(state3Strain(2) -
state3Strain(1)) > kmax) {

linear unload-reload path expected
double du = state3Strain(3) - state3Strain(0);
double df = state3Stress(3) - state3Stress(0);
state3Strain(1) = state3Strain(0) + 0.33*du;
state3Strain(2) = state3Strain(0) + 0.67*du;
state3Stress(1) = state3Stress(0) + 0.33*df;
state3Stress(2) = state3Stress(0) + 0.67*df;
                                        }
else if ((state3Strain(2) < state3Strain(1))||((state3Stress(2)-
state3Stress(1))/(state3Strain(2)-state3Strain(1))<0)) {
if (state3Strain(2)<0.0) {

// pt 3 should be along a line between 2 and 4
double du = state3Strain(3)-state3Strain(1);
double df = state3Stress(3)-state3Stress(1);
state3Strain(2) = state3Strain(1) + 0.5*du;
```

```
state3Stress(2) = state3Stress(1) + 0.5*df;
                                                 }
else if (state3Strain(1) > 0.0) {

// pt 2 should be along a line between 1 and 3
double du = state3Strain(2)-state3Strain(0);
double df = state3Stress(2)-state3Stress(0);
state3Strain(1) = state3Strain(0) + 0.5*du;
state3Stress(1) = state3Stress(0) + 0.5*df;
                                                 }
else {
double avgforce = 0.5*(state3Stress(2) + state3Stress(1));
double dfr = 0.0;
if (avgforce < 0.0){
dfr = -avgforce/100;
                                                 }
else {
dfr = avgforce/100;
                                                  }
double slope12 = (state3Stress(1) - state3Stress(0))/(state3Strain(1) -
state3Strain(0));
double slope34 = (state3Stress(3) - state3Stress(2))/(state3Strain(3) -
state3Strain(2));
state3Stress(1) = avgforce - dfr;
state3Stress(2) = avgforce + dfr;
state3Strain(1) = state3Strain(0) + (state3Stress(1) -
state3Stress(0))/slope12;
state3Strain(2) = state3Strain(3) - (state3Stress(3) -
state3Stress(2))/slope34;
                                                }
                                         }
                                 }
                         }
else {

// linear unload reload path is expected
double du = state3Strain(3)-state3Strain(0);
double df = state3Stress(3)-state3Stress(0);
state3Strain(1) = state3Strain(0) + 0.33*du;
state3Strain(2) = state3Strain(0) + 0.67*du;
state3Stress(1) = state3Stress(0) + 0.33*df;
state3Stress(2) = state3Stress(0) + 0.67*df;
                                 }

double checkSlope = state3Stress(0)/state3Strain(0);
double slope = 0.0;

// final check
int i = 0;
while (i<3) {
double du = state3Strain(i+1)-state3Strain(i);
double df = state3Stress(i+1)-state3Stress(i);
if (du<0.0 || df<0.0) {
double du = state3Strain(3)-state3Strain(0);
double df = state3Stress(3)-state3Stress(0);
state3Strain(1) = state3Strain(0) + 0.33*du;
state3Strain(2) = state3Strain(0) + 0.67*du;
state3Stress(1) = state3Stress(0) + 0.33*df;
state3Stress(2) = state3Stress(0) + 0.67*df;
slope = df/du;
i = 3;
```

```
                                         }
if (slope > 1e-8 && slope < checkSlope) {
state3Strain(1) = 0.0; state3Stress(1) = 0.0;
state3Strain(2) = state3Strain(3)/2; state3Stress(2) = state3Stress(3)/2;
                                         }
                                         i++;
                                 }


                         }

void CFSSSWP::getState4(Vector& state4Strain,Vector& state4Stress, double
kunload)
                 {

double kmax = (kunload>kElasticPos) ? kunload:kElasticPos;

if (state4Strain(0)*state4Strain(3) <0.0){

// trilinear unload reload path expected
state4Strain(2) = hghTstateStrain*rDispP;
if (uForceP==0.0){
state4Stress(2) = hghTstateStress*rForceP;
                                 }
else if (rForceP-uForceP > 1e-8) {
state4Stress(2) = hghTstateStress*rForceP;
                                 }
else {
if (TmaxStrainDmnd > envlpPosStrain(3)) {
double st1 = hghTstateStress*uForceP*(1.0+1e-6);
double st2 = envlpPosDamgdStress(4)*(1.0+1e-6);
state4Stress(2) = (st1>st2) ? st1:st2;
                                         }
                                         else {
double st1 = envlpPosDamgdStress(3)*uForceP*(1.0+1e-6);
double st2 = envlpPosDamgdStress(4)*(1.0+1e-6);
state4Stress(2) = (st1>st2) ? st1:st2;
                                         }
                                 }

// if reload stiffness exceeds unload stiffness, reduce reload stiffness to
make it equal to unload stiffness
if ((state4Stress(3)-state4Stress(2))/(state4Strain(3)-state4Strain(2)) >
kElasticPos) {
state4Strain(2) = hghTstateStrain - (state4Stress(3)-
state4Stress(2))/kElasticPos;
                                 }

// check that reloading point is not behind point 1
if (state4Strain(2)<state4Strain(0)) {

// path taken to be a straight line between points 1 and 4
double du = state4Strain(3) - state4Strain(0);
double df = state4Stress(3) - state4Stress(0);
state4Strain(1) = state4Strain(0) + 0.33*du;
state4Strain(2) = state4Strain(0) + 0.67*du;
state4Stress(1) = state4Stress(0) + 0.33*df;
state4Stress(2) = state4Stress(0) + 0.67*df;
                                }
                                 else {
if (TmaxStrainDmnd > envlpPosStrain(3)) {
```

```
state4Stress(1) = uForceP*envlpPosDamgdStress(4);
                                            }
else {
state4Stress(1) = uForceP*envlpPosDamgdStress(3);
                                            }
state4Strain(1) = lowTstateStrain + (-
lowTstateStress+state4Stress(1))/kunload;

if (state4Strain(1) < state4Strain(0)) {

// point 2 should be along a line between 1 and 3
double du = state4Strain(2) - state4Strain(0);
double df = state4Stress(2) - state4Stress(0);
state4Strain(1) = state4Strain(0) + 0.5*du;
state4Stress(1) = state4Stress(0) + 0.5*df;
                                            }
else if ((state4Stress(2) - state4Stress(1))/(state4Strain(2) -
state4Strain(1)) > kmax) {

// linear unload-reload path expected

double du = state4Strain(3) - state4Strain(0);
double df = state4Stress(3) - state4Stress(0);
state4Strain(1) = state4Strain(0) + 0.33*du;
state4Strain(2) = state4Strain(0) + 0.67*du;
state4Stress(1) = state4Stress(0) + 0.33*df;
state4Stress(2) = state4Stress(0) + 0.67*df;
                                           }
else if ((state4Strain(2) < state4Strain(1))||((state4Stress(2)-
state4Stress(1))/(state4Strain(2)-state4Strain(1))<0)) {
if (state4Strain(1)>0.0) {

// pt 2 should be along a line between 1 and 3
double du = state4Strain(2)-state4Strain(0);
double df = state4Stress(2)-state4Stress(0);
state4Strain(1) = state4Strain(0) + 0.5*du;
state4Stress(1) = state4Stress(0) + 0.5*df;
                                                  }
else if (state4Strain(2) < 0.0) {

// pt 2 should be along a line between 2 and 4
double du = state4Strain(3)-state4Strain(1);
double df = state4Stress(3)-state4Stress(1);
state4Strain(2) = state4Strain(1) + 0.5*du;
state4Stress(2) = state4Stress(1) + 0.5*df;
                                                  }
else {
double avgforce = 0.5*(state4Stress(2) + state4Stress(1));
double dfr = 0.0;
if (avgforce < 0.0){
dfr = -avgforce/100;
                                                          }
else {
dfr = avgforce/100;
                                                          }
double slope12 = (state4Stress(1) - state4Stress(0))/(state4Strain(1) -
state4Strain(0));
double slope34 = (state4Stress(3) - state4Stress(2))/(state4Strain(3) -
state4Strain(2));
state4Stress(1) = avgforce - dfr;
state4Stress(2) = avgforce + dfr;
```

```
state4Strain(1) = state4Strain(0) + (state4Stress(1) -
state4Stress(0))/slope12;
state4Strain(2) = state4Strain(3) - (state4Stress(3) -
state4Stress(2))/slope34;
                                                 }
                                         }
                                 }
                         }
                                else {

// linear unload reload path is expected
double du = state4Strain(3)-state4Strain(0);
double df = state4Stress(3)-state4Stress(0);
state4Strain(1) = state4Strain(0) + 0.33*du;
state4Strain(2) = state4Strain(0) + 0.67*du;
state4Stress(1) = state4Stress(0) + 0.33*df;
state4Stress(2) = state4Stress(0) + 0.67*df;
                                 }

double checkSlope = state4Stress(0)/state4Strain(0);
double slope = 0.0;

// final check
int i = 0;
while (i<3) {
double du = state4Strain(i+1)-state4Strain(i);
double df = state4Stress(i+1)-state4Stress(i);
if (du<0.0 || df<0.0) {
double du = state4Strain(3)-state4Strain(0);
double df = state4Stress(3)-state4Stress(0);
state4Strain(1) = state4Strain(0) + 0.33*du;
state4Strain(2) = state4Strain(0) + 0.67*du;
state4Stress(1) = state4Stress(0) + 0.33*df;
state4Stress(2) = state4Stress(0) + 0.67*df;
i = 3;
                                         }
if (slope > 1e-8 && slope < checkSlope) {
state4Strain(1) = 0.0; state4Stress(1) = 0.0;
state4Strain(2) = state4Strain(3)/2; state4Stress(2) = state4Stress(3)/2;
                                         }

                                         i++;
                                 }
                         }

 double CFSSSWP::Envlp3Tangent(Vector s3Strain, Vector s3Stress, double u)
                         {
                                              double k = 0.0;
                                                k = Spline3.EvalT(u);
                                                if(k != 10e8)
                                                 {
                                                       return k;
                                                }
                                                 int i = 0;
                                 while ((k==0.0||i<=2) && (i<=2))
                                 {
                                         if (u>= s3Strain(i)) {
k = (s3Stress(i+1)-s3Stress(i))/(s3Strain(i+1)-s3Strain(i));
                                         }
                                         i++;
                                 }
```

```
                                 if (k==0.0) {
                                         if (u<s3Strain(0)) {
                                                 i = 0;
                                         }
                                         else {
                                                 i = 2;
                                         }
k = (s3Stress(i+1)-s3Stress(i))/(s3Strain(i+1)-s3Strain(i));

                                 }
printf("Tangente = %f\n",k);
                                 return k;
                         }

 double CFSSSWP::Envlp4Tangent(Vector s4Strain, Vector s4Stress, double u)
                         {
                                 double k = 0.0;
                                int i = 0;
                                                k = Spline4.EvalT(u);
                                                if(k != 10e8)
                                                {
                                                return k;
                                                }
                                 while ((k==0.0||i<=2) && (i<=2))
                                 {
                                         if (u>= s4Strain(i)) {
k = (s4Stress(i+1)-s4Stress(i))/(s4Strain(i+1)-s4Strain(i));
                                         }
                                         i++;
                                 }
                                 if (k==0.0) {
                                         if (u<s4Strain(0)) {
                                                 i = 0;
                                         }
                                         else {
                                                 i = 2;
                                         }
k = (s4Stress(i+1)-s4Stress(i))/(s4Strain(i+1)-s4Strain(i));

                                 }
printf("Tangente = %f\n",k);
                                 return k;
                         }


 double CFSSSWP::Envlp3Stress(Vector s3Strain, Vector s3Stress, double u)
{
  double k = 0.0;
  int i = 0;
  double f = 0.0;
  f = Spline3.Eval(u);
  if(isnan(f))
    {
      printf("erreur3");
      while(1);
    }
  if(f != 10e8)
    {
      return f;
      return GetStressFromCurve(u);
    }
```

```
  while ((k==0.0||i<=2) && (i<=2))
    {
      if (u>= s3Strain(i)) {
      k = (s3Stress(i+1)-s3Stress(i))/(s3Strain(i+1)-s3Strain(i));
      f = s3Stress(i)+(u-s3Strain(i))*k;
      }
      i++;
    }
  if (k==0.0) {
    if (u<s3Strain(0)) {
      i = 0;
    }
    else {
      i = 2;
    }
    k = (s3Stress(i+1)-s3Stress(i))/(s3Strain(i+1)-s3Strain(i));
    f = s3Stress(i)+(u-s3Strain(i))*k;
  }
  printf("Strain = %f   Stress = %f Min = %f, Max =
%f\n",u,f,s3Strain(0),s3Strain(3));
  if(u > s3Strain(3))
    {
      while(1);
    }
  return f;
}

double CFSSSWP::Envlp4Stress(Vector s4Strain, Vector s4Stress, double u)
{
  double k = 0.0;
  int i = 0;
  double f = 0.0;
  f = Spline4.Eval(u);
  if(isnan(f))
    {

printf("erreur4");
                                                             while(1);
    }
  if(f != 10e8)
                                                 {
                                                   return f;
                                                   return
GetStressFromCurve(u);
                                                 }
  while ((k==0.0||i<=2) && (i<=2))
    {
      if (u>= s4Strain(i)) {
k = (s4Stress(i+1)-s4Stress(i))/(s4Strain(i+1)-s4Strain(i));
f = s4Stress(i)+(u-s4Strain(i))*k;
                                         }
                                         i++;
                                 }
                                 if (k==0.0) {
                                         if (u<s4Strain(0)) {
                                                 i = 0;
                                         }
                                         else {
                                                 i = 2;
                                         }
k = (s4Stress(i+1)-s4Stress(i))/(s4Strain(i+1)-s4Strain(i));
```

```
f = s4Stress(i)+(u-s4Strain(i))*k;
                                }
printf("Strain = %f     Stress = %f Min = %f, Max =
%f\n",u,f,s4Strain(0),s4Strain(3));
                                                if(u > s4Strain(3))
                                                {
                                                      while(1);
                                                }
                                return f;
                        }

void CFSSSWP::updateDmg(double strain, double dstrain)
         {
double tes = 0.0;
double umaxAbs = (TmaxStrainDmnd>-TminStrainDmnd) ? TmaxStrainDmnd:-
TminStrainDmnd;
double uultAbs = (envlpPosStrain(1)>-envlpNegStrain(1)) ?
envlpPosStrain(1):-envlpNegStrain(1);
TnCycle = CnCycle;
if ((strain<uultAbs && strain>-uultAbs) && Tenergy < elasticStrainEnergy)
                 {

TgammaD += TnCycle;
TgammaF += TnCycle;

                 }
if (Tenergy>elasticStrainEnergy) {
tes = ((Tenergy-elasticStrainEnergy)/energyCapacity);
TgammaD += tes;
TgammaF += tes;
                 }

TgammaDN = TgammaD;
TgammaD = (TgammaD<gammaDLimit) ? TgammaD:gammaDLimit;
TgammaFN = TgammaF;
TgammaF = (TgammaF<gammaFLimit) ? TgammaF:gammaFLimit;
                 }
```

APPENDIX C

DETAILED RESULTS FOR CFS ARCHETYPE BUILDINGS

The following figures summarise the results of the design procedure evaluation explained in Chapter 4. Maximum interstorey drift values are plotted for each response history analysis for each archetype ($q = 2$) on the so-called IDA curves and the median response is highlighted with a red curve. The corresponding fragility curves are also displayed for each archetype. The black curve is based on the results of dynamic analysis. The red curve is shifted to take into account the influence of spectral shape (using the so-called Spectral Shape Factor) as well as total uncertainty.

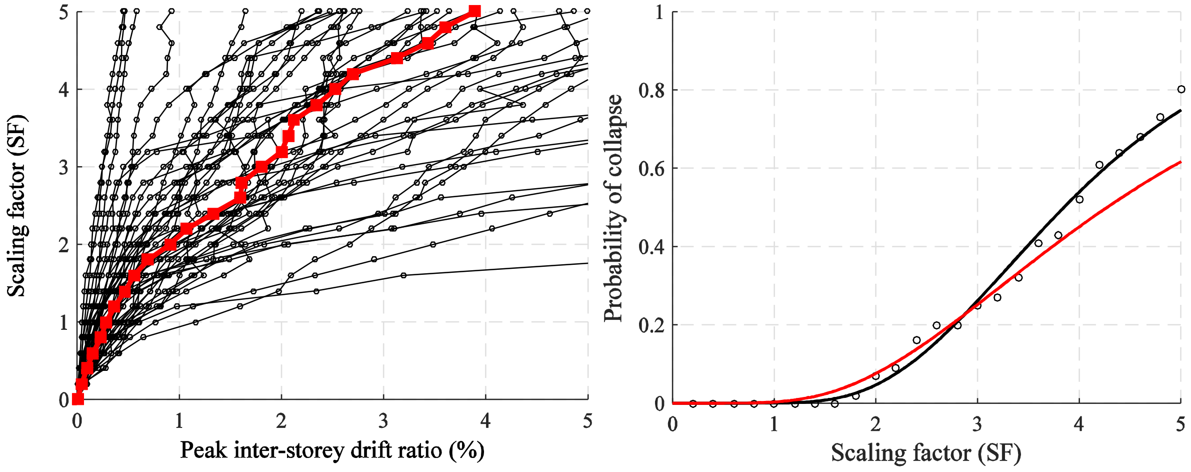

IDA curves (left) and fragility curves (right) for archetype 1.

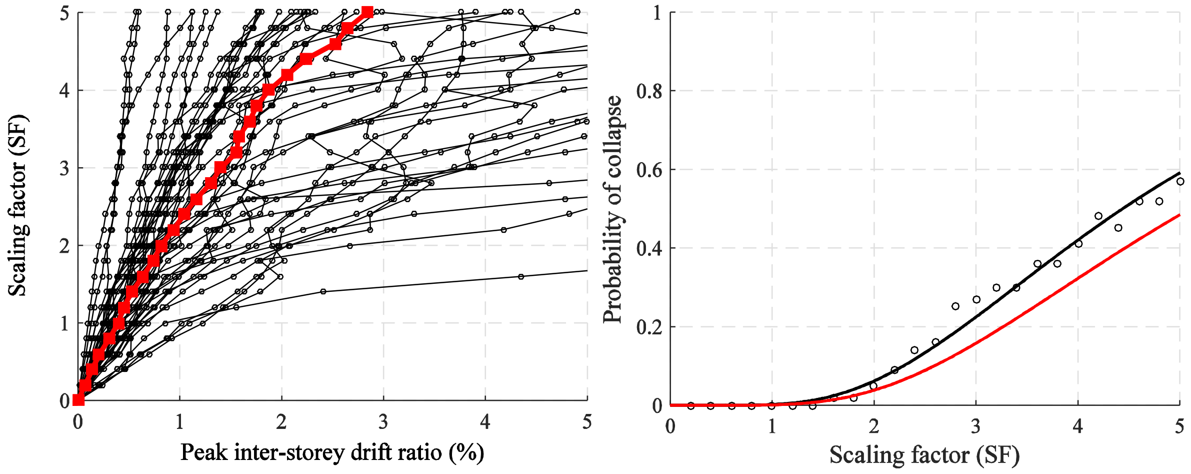

IDA curves (left) and fragility curves (right) for archetype 2.

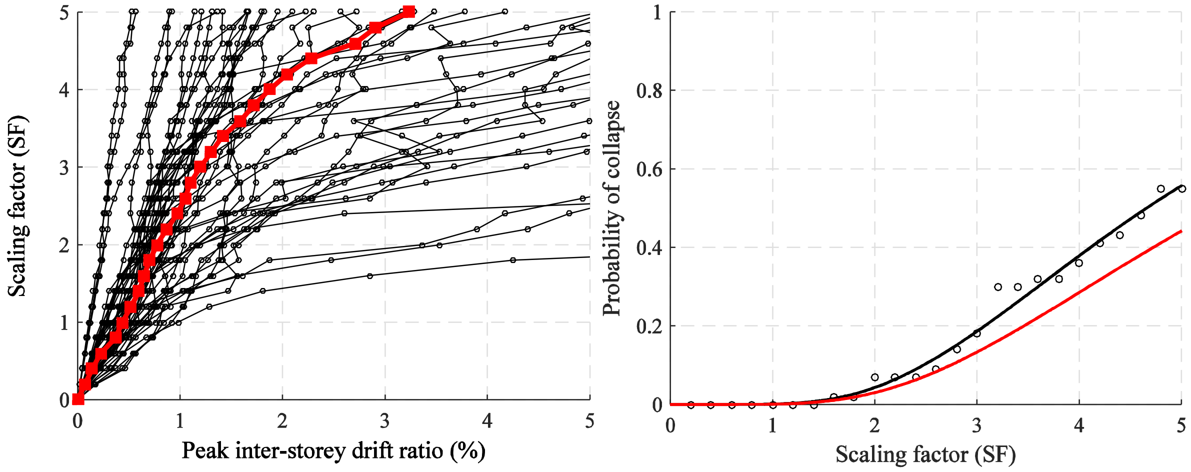

IDA curves (left) and fragility curves (right) for archetype 3.

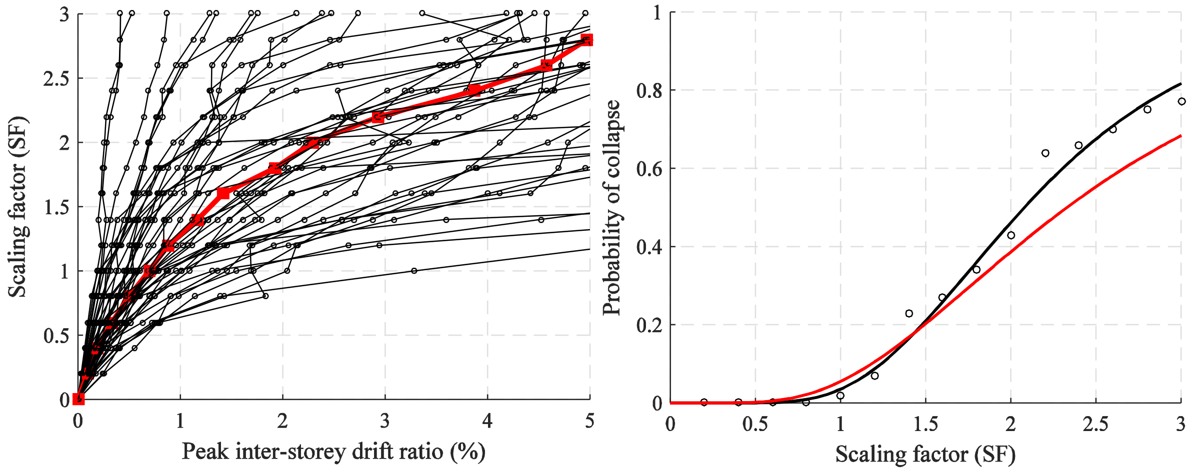

IDA curves (left) and fragility curves (right) for archetype 4.

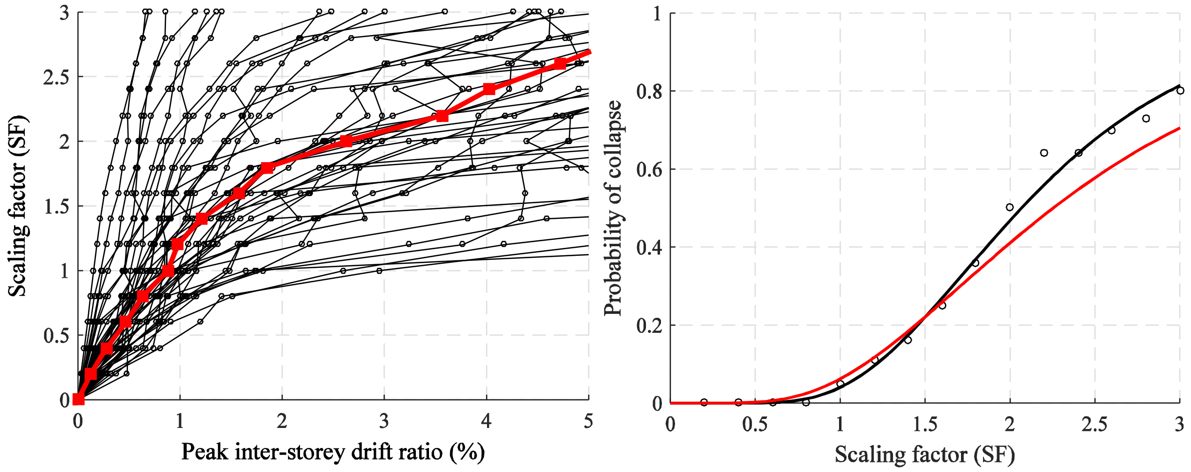

IDA curves (left) and fragility curves (right) for archetype 5.

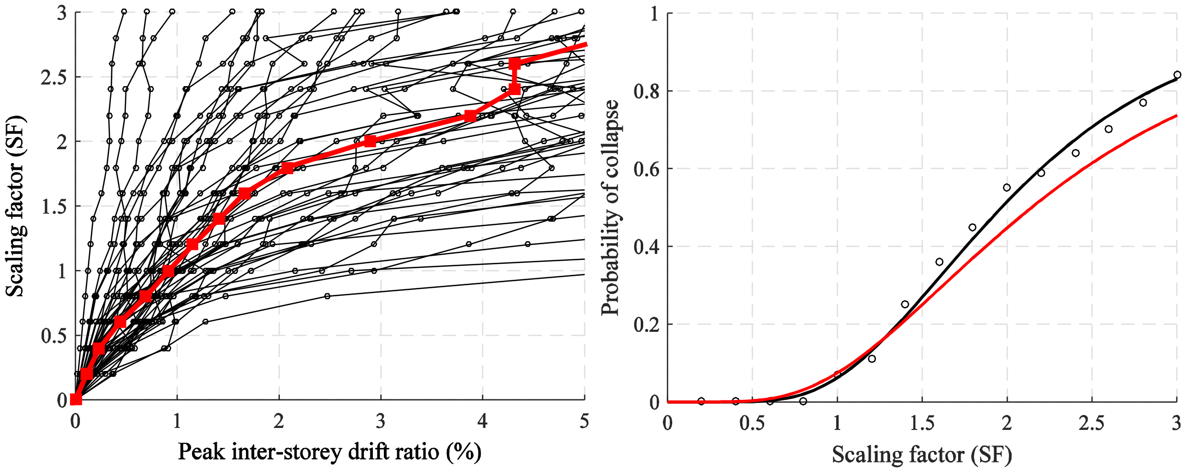

IDA curves (left) and fragility curves (right) for archetype 6.

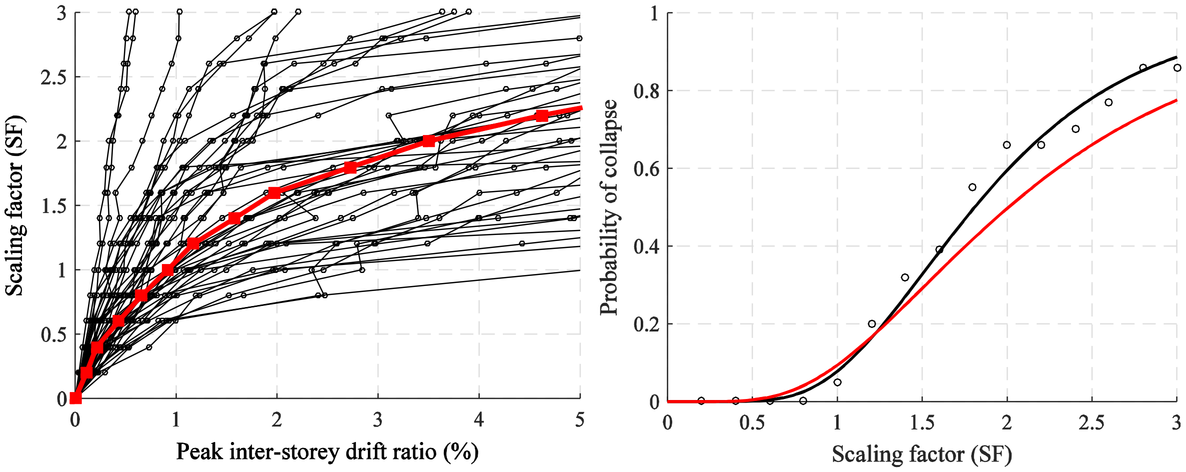

IDA curves (left) and fragility curves (right) for archetype 7.

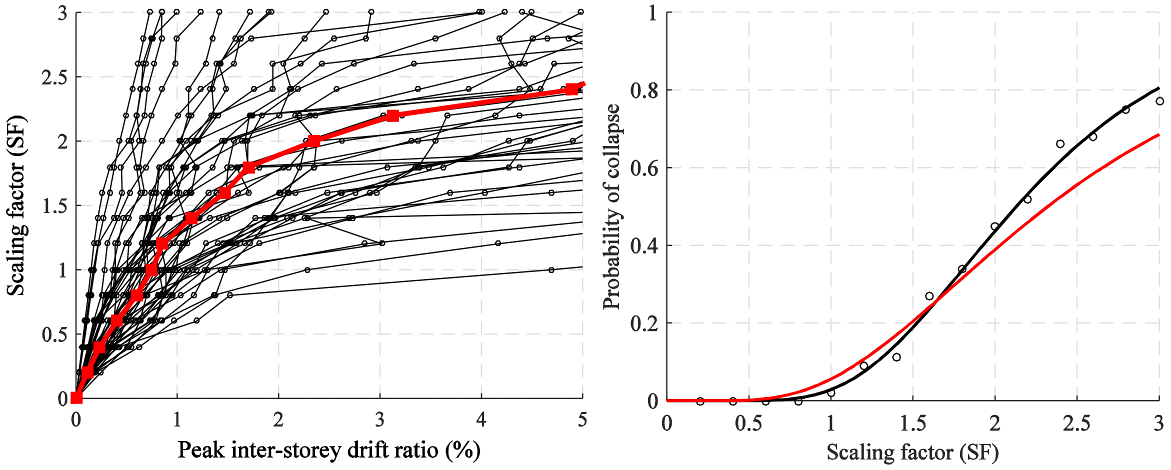

IDA curves (left) and fragility curves (right) for archetype 8.

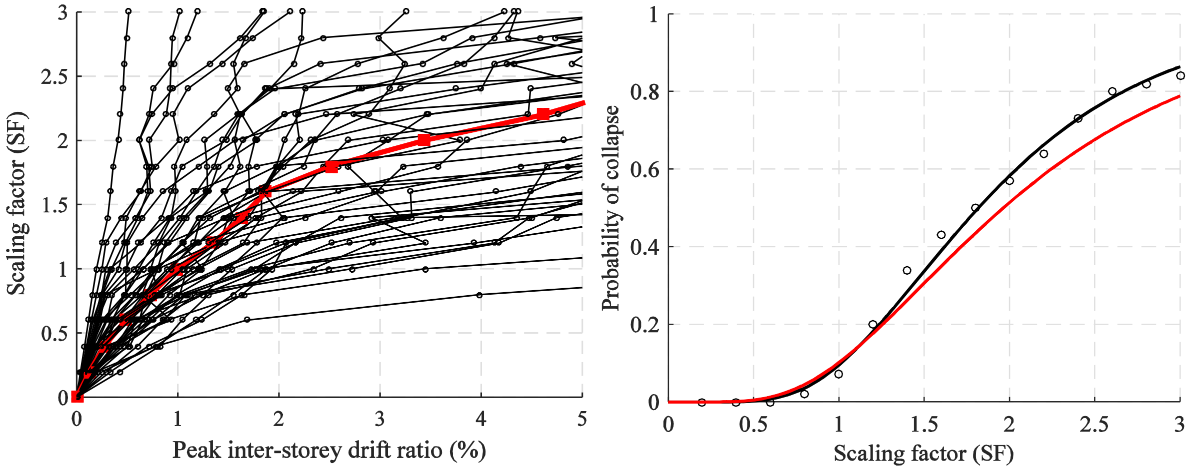

IDA curves (left) and fragility curves (right) for archetype 9.

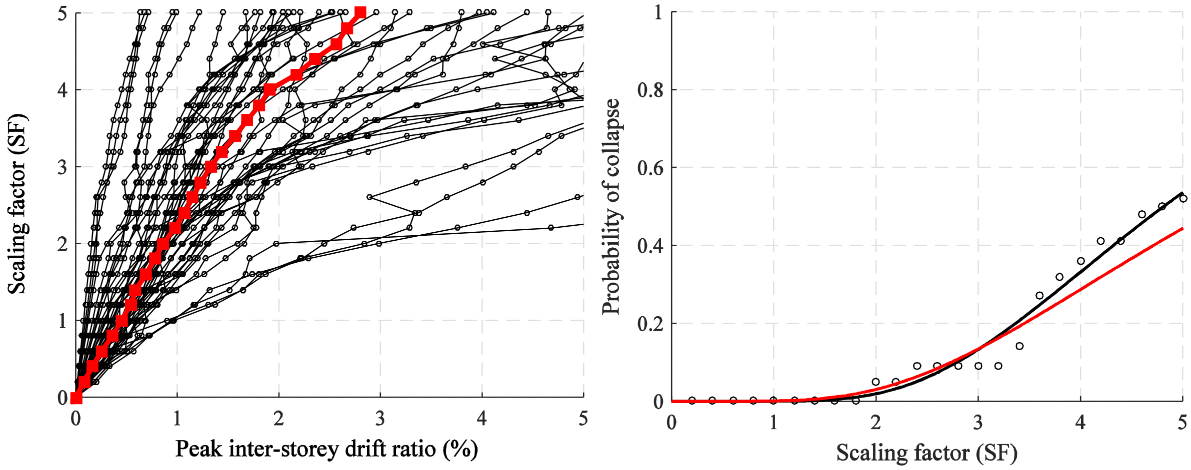

IDA curves (left) and fragility curves (right) for archetype 10.

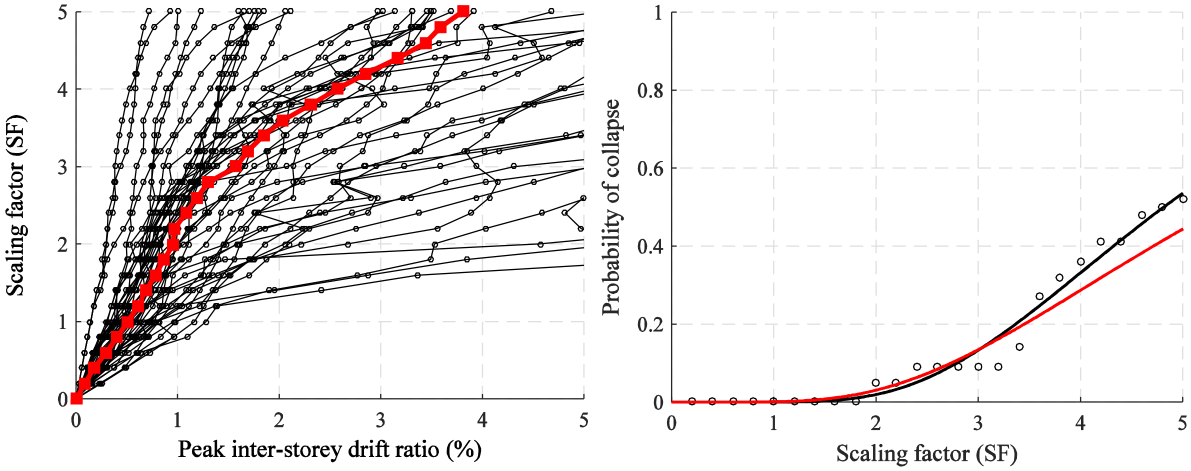

IDA curves (left) and fragility curves (right) for archetype 11.

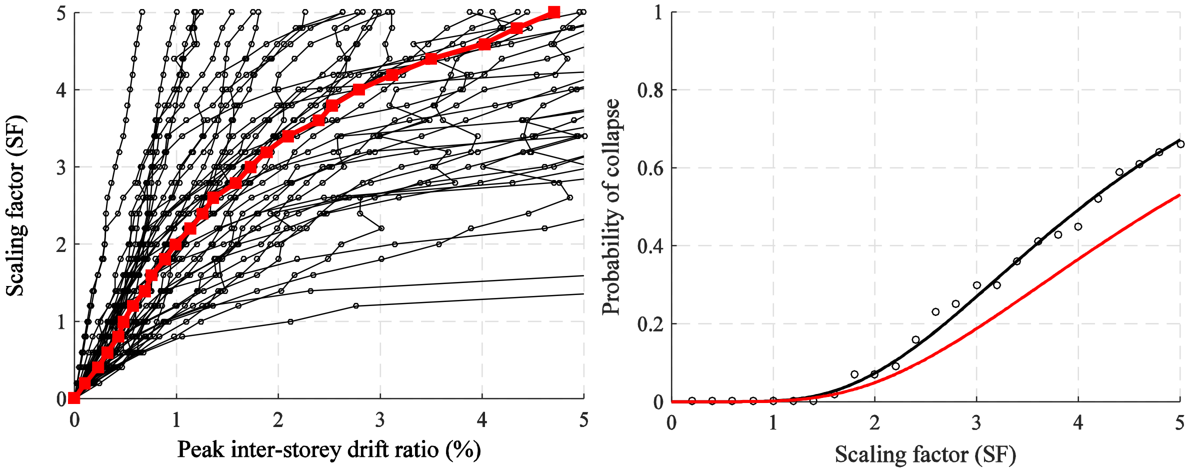

IDA curves (left) and fragility curves (right) for archetype 12.

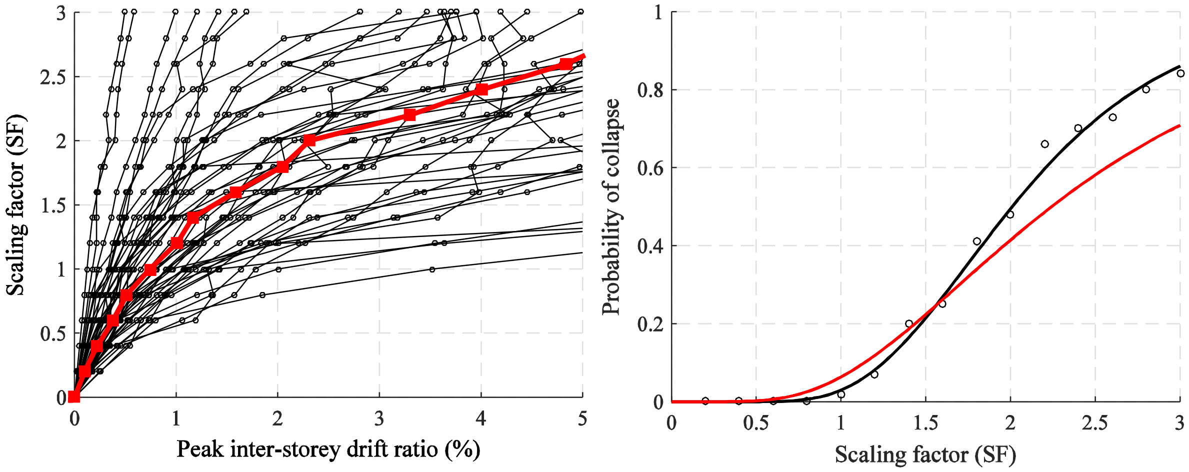

IDA curves (left) and fragility curves (right) for archetype 13.

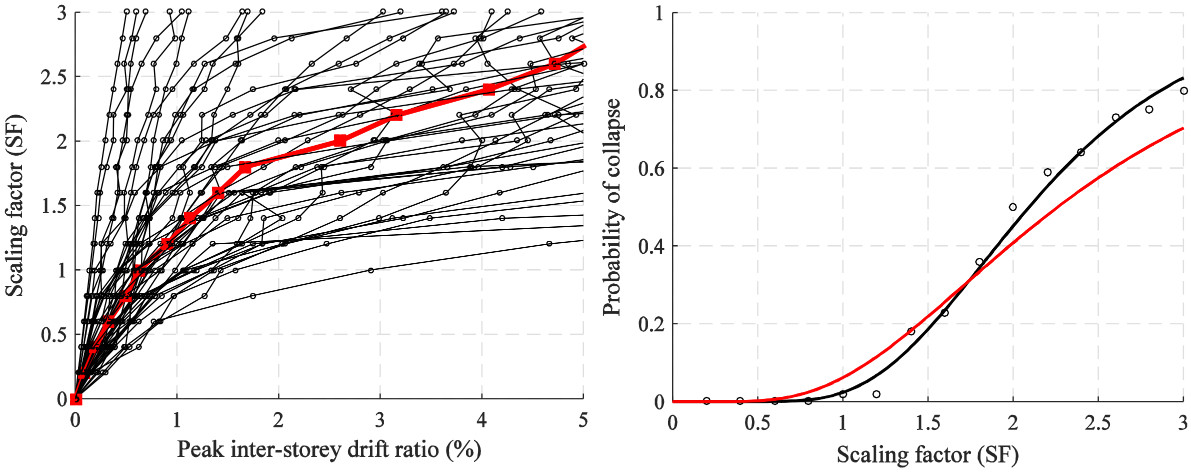

IDA curves (left) and fragility curves (right) for archetype 14.

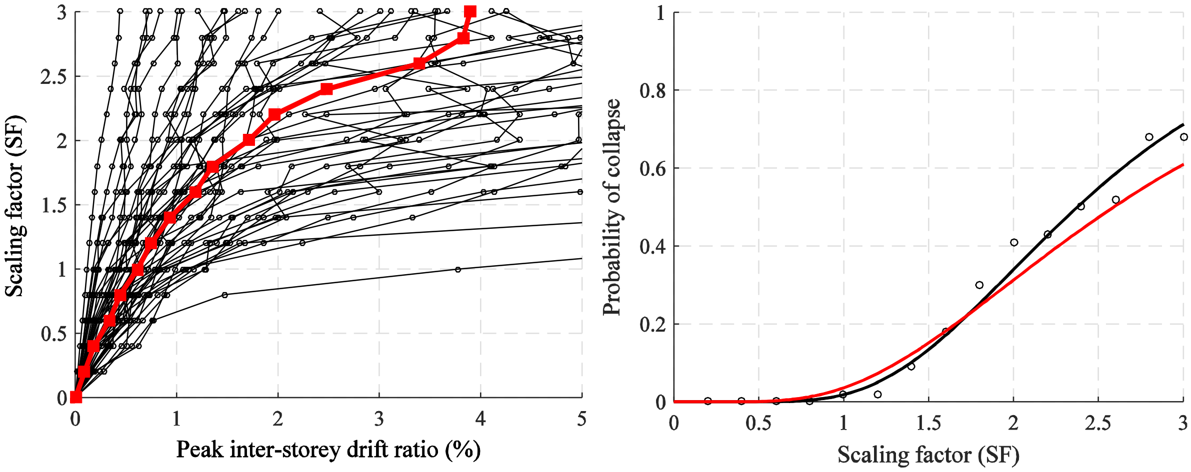

IDA curves (left) and fragility curves (right) for archetype 15.

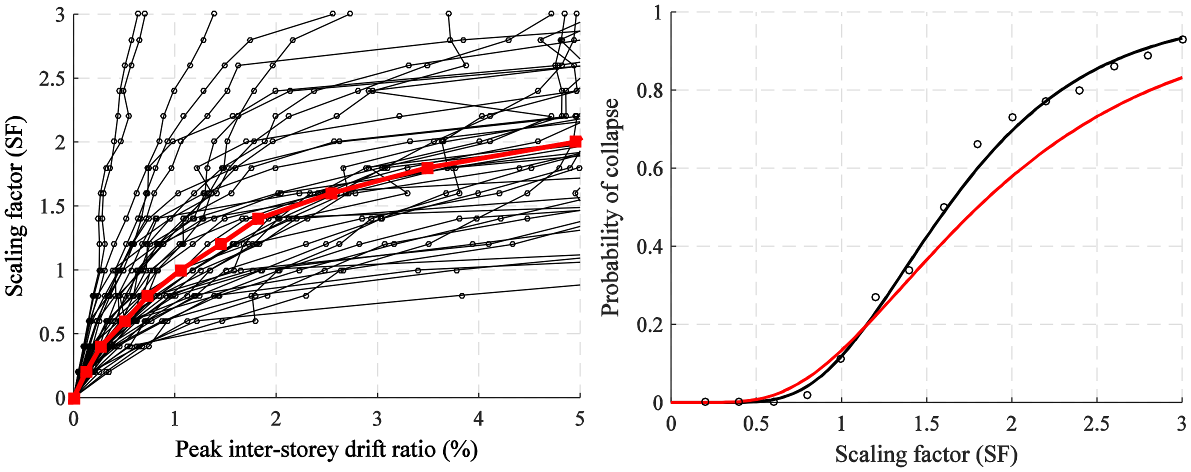

IDA curves (left) and fragility curves (right) for archetype 16.

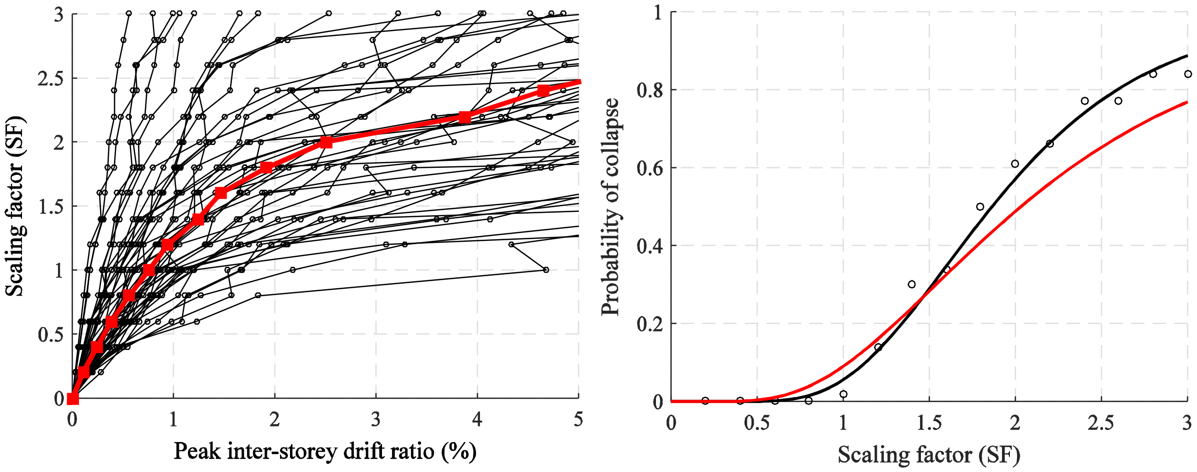

IDA curves (left) and fragility curves (right) for archetype 17.

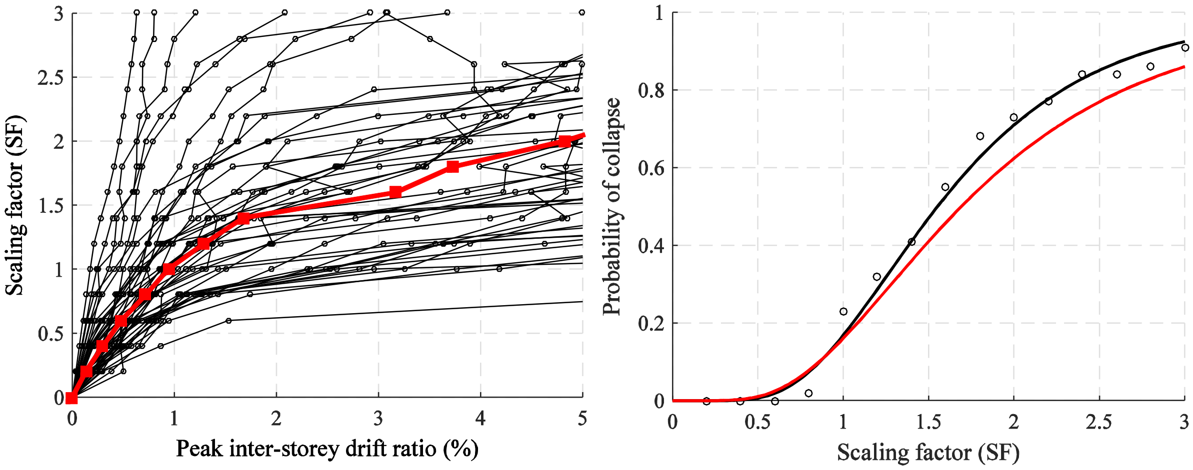

IDA curves (left) and fragility curves (right) for archetype 18.

APPENDIX D

COUPON TEST RESULTS

This appendix includes all the coupon test curves (engineering stress-strain) for chord studs and tracks composing specimens that are presented in Chapter 6. The black curve represents the engineering stress-stress relationship. The dashed red, blue and green lines are, respectively, the 2%, 4% and 8% (red, blue and green, respectively) offset methods adopted for the assessment of the yield stress.

T1

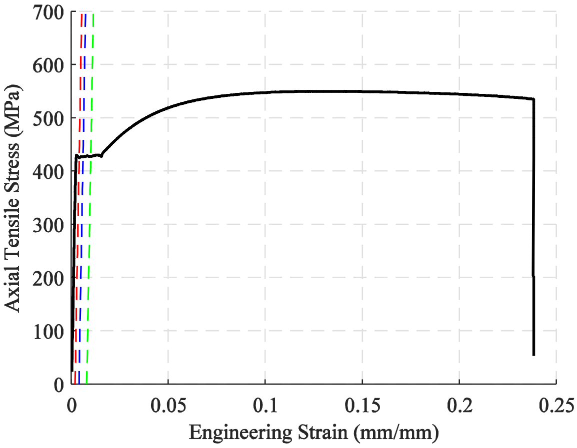

T2

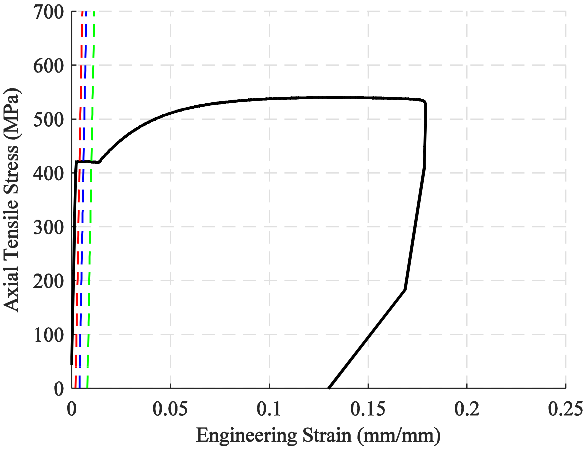

T3

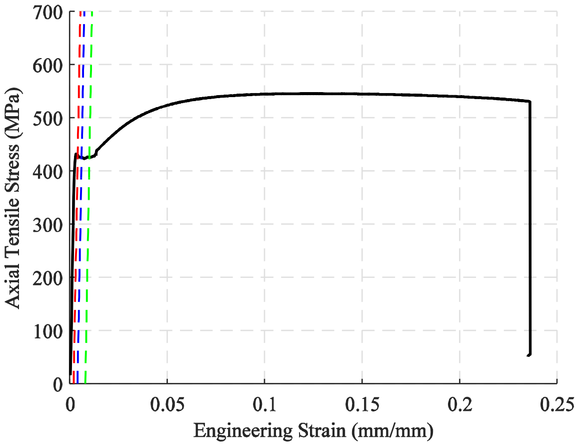

T4

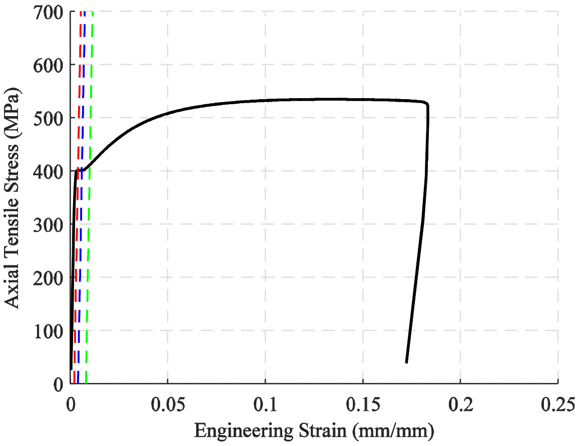

T5

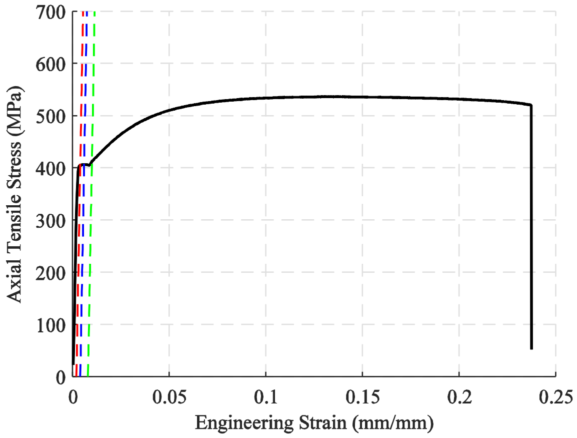

T6

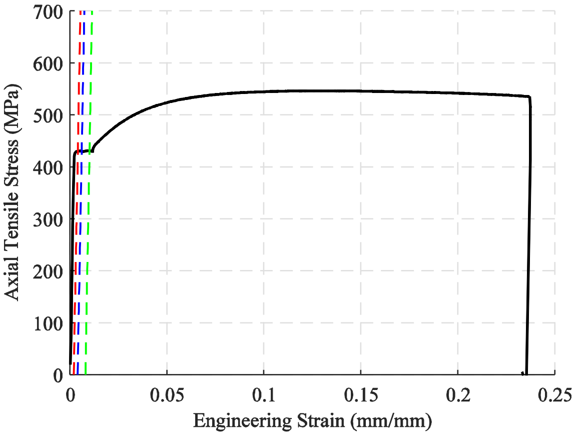

T7

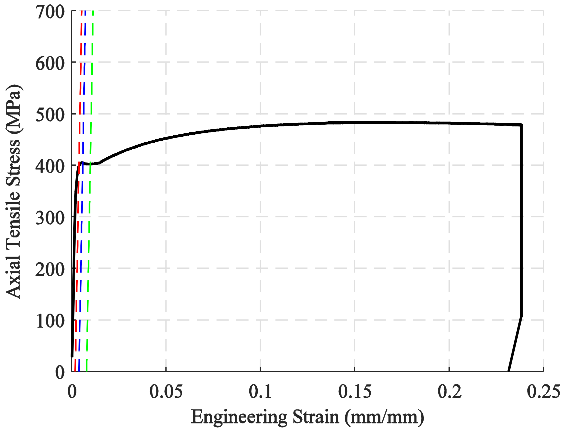

T8

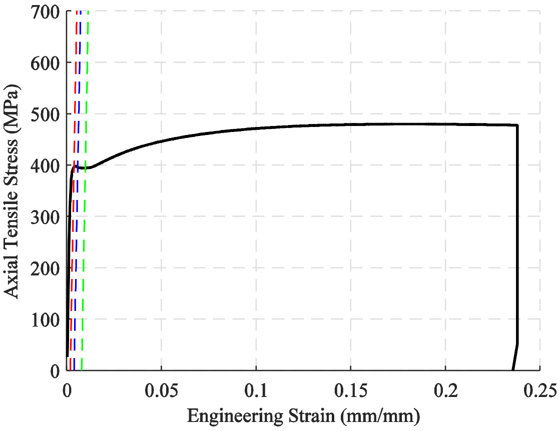

T9

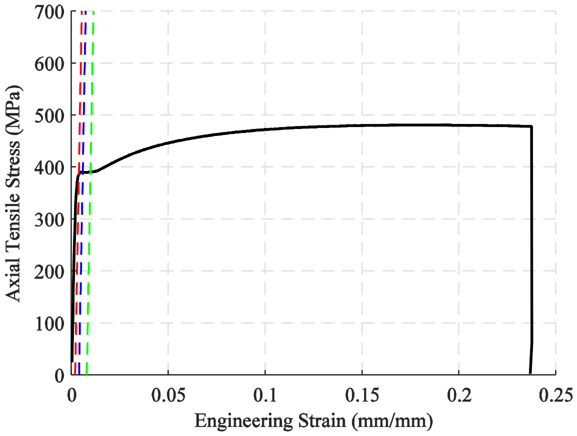

T10

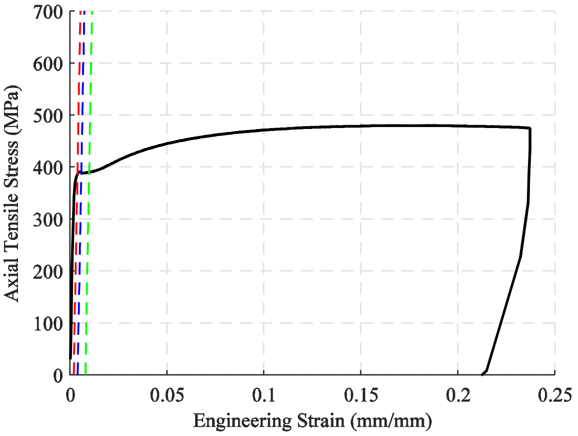

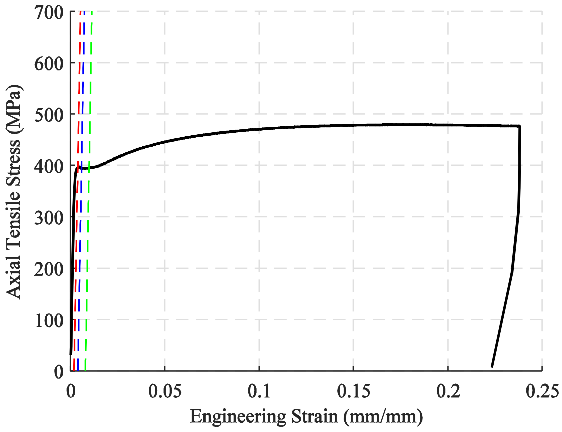
T11
Axial Tensile Stress (MPa)
700
600
500
400
300
200
100
0
0
0.05
0.1
0.15
0.2
0.25
Engineering Strain (mm/mm)

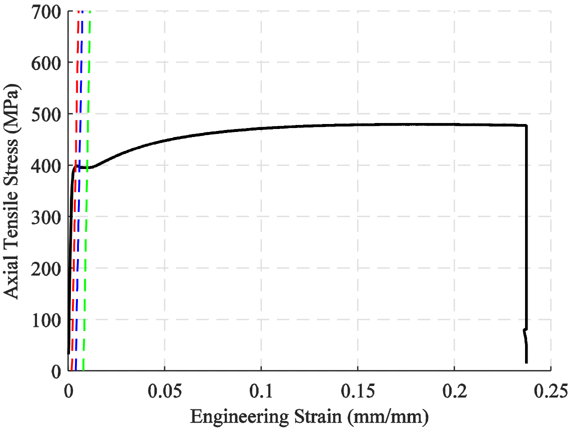
T12
Axial Tensile Stress (MPa)
700
600
500
400
300
200
100
0
0
0.05
0.1
0.15
0.2
0.25
Engineering Strain (mm/mm)

REFERENCES

1. EN 1998-1, Eurocode 8. Design of structures for earthquake resistance, Part 1: general rules, seismic actions and rules for buildings, European Committee for Standardization, Brussels, CEN (2005).

2. American Iron and Steel Institute (AISI), North American standard for seismic design of cold-formed steel structural systems, AISI S400, Washington, D.C., USA, (2015).

3. DTR BC 2.48, "RPA99 V2003 : Règles Parasismiques Algériennes", Centre National de Recherche Appliquée en Génie Parasismique, Alger, (2003).

4. DTR BC 2.44, "CCM97 : Règles de conception et de calcul des structures métalliques", Centre National de Recherche Appliquée en Génie Parasismique, Alger, (1997).

5. EN 1993-1-1, "Eurocode 3: Design of steel structures - Part 1.1: General rules and rules for buildings", European Committee for Standardization, Brussels, CEN, (2005).

6. FEMA P695, Quantification of building system performance and response parameters. FEMA P695, (2009).

7. http://www.ce.jhu.edu/bschafer/, [last accessed on 27/10/2017].

8. ABAQUS 6.14-5, Dassault Systems Simulia Corp., Providence, RI, (2014).

9. Schafer, B. W., "Cold-formed steel structures around the world", Steel Construction, V. 4, n° 3, (2011), 141-149.

10. Shamim, I., "Seismic Design of Lateral Force Resisting Cold-Formed Steel Framed (CFS) Structures", Doctor of Philosophy Thesis, Department of Civil Engineering and Applied Mechanics, McGill University, Montreal, Québec, Canada, (2012), 447 p.

11. Branston, A.E., Chen, C.Y., Boudreault, F.A. and Rogers, C.A., "Testing of light-gauge steel frame wood structural panel shear walls", Canadian Journal of Civil Engineering, V. 33, n° 9, (2006), 561-572.

12. Gad, E. F., “Performance of brick-veneer cold-formed steel framed domestic structures subjected to earthquake loading”, PhD thesis, Department of Civil and Environment Engineering, University of Melbourne, Australia, (1997).

13. Stewart, W.G., “The Seismic Design of Plywood Sheathed Shear Walls”, PhD Thesis, University of Canterbury, New Zealand, (1987).

14. Dolan, J.D., “The dynamic response of timber shear walls”, PhD thesis, Department of Civil Engineering, University of British Columbia, Vancouver, BC, Canada, (1989).

15. Ibarra, F.L., Medina, R.A. and Krawinkler, H., “Hysteretic Models That Incorporate Strength and Stiffness Deterioration”, Earthquake Engineering and Structural Dynamics, V. 34, n° 6, (June 2005), 1489-1511.

16. Vigh, L.G., Deierlein, G.G., Miranda, E., Liel, A.B. and Tipping, S., “Seismic performance assessment of steel corrugated shear wall system using nonlinear analysis”, Journal of Constructional Steel Research, V. 85, (2013), 48-59.

17. Balh, N., “Development of seismic design provisions for steel-sheathed shear walls”, Master thesis, McGill University, Montreal, Québec, Canada, (2010).

18. Yu, C., “Shear Resistance of Cold-Formed Steel Framed Shear Walls with 0.681 mm, 0.762 mm, and 0.838 mm Steel Sheet Sheathing”, Engineering Structures, V. 32, (2010), 1522-1529.

19. Yu, C. and Chen, Y., “Detailing Recommendations for 1.83 m Wide Cold-Formed Steel Shear Walls with Steel Sheathing”, Journal of Constructional Steel Research, V. 67, n° 7, (2011), 93-101.

20. Liu, P., Peterman, K.D. and Schafer, B.W., “Impact of construction details on OSB-sheathed cold-formed steel framed shear walls”, Journal of Constructional Steel Research, V. 101, (2014), 114-123.

21. DaBreo, J., “Impact of Gravity Load on the Lateral Performance of Cold-Formed Steel Frame/Steel Sheathed Shear Walls”, Master of thesis, Department of Civil Engineering and Applied Mechanics, McGill University, Montreal, Québec, Canada, (2012).

22. Mohebbi, S., Mirghaderi, R., Farahbod, F. and Sabbagh, A.B., “Experimental work on single and double-sided steel sheathed cold-formed steel shear walls for seismic actions”, Thin-Walled Structures, V. 91, (2015), 50-62.

23. Fülöp, L. and Dubina, D., “Performance of wall-stud cold-formed shear panels under monotonic and cyclic loading Part I: Experimental research”, Thin-Walled Structures, V. 42, (2004), 321-338.

24. Berediafe-Bourahla, M., Allal, N., Meddah, H. and Bourahla, N., “Retour d’expérience en conception, réalisation et activité de recherche”, La 1ère Conférence Internationale de Construction Métallique et Mixte CICOMM’2015, October 12-13, 2015, Tlemcen, Algeria.

25. Gad, E.F., Chandler, A.M., Duffield, C.F. and Stark, G., “Lateral Behaviour of Plasterboard-Clad Residential Steel Frames”, Journal of Structural Engineering, (January 1999), 32-39.

26. Serrette, R. L., Morgan, K. A. and Sorhouet, M. A., “Performance of Cold-Formed Steel-Framed Shear Walls: Alternative Configurations”, Santa Clara University, Final Report LGSRG-06-02; (2002).

27. Peterman, K.D., “Behavior of full-scale cold-formed steel buildings under seismic excitations”, PhD thesis, John Hopkins University, Baltimore, United States, (2014); 307 p.

28. National Association of Home Builders (NAHB) Research Center for The American Iron and Steel Institute, “Monotonic Tests of Cold-Formed Steel Shear Walls with Opening”, (1997).

29. Rahnama, M. and Krawinkler, H., “Effects of soft soil and hysteresis model on seismic demands”, John A. Blume Earthquake Engineering Center Report No. 108. Department of CEE, Stanford University, (1993).

30. Lowes, L.N. and Altoontash, A., “Modeling the Response of Reinforced Concrete Beam-Column Joints”, Journal of Structural Engineering, V. 129, (2003), 1686-1697.

31. Park, Y. and Ang, A., “Mechanistic seismic damage model for reinforced concrete”, Journal of Structural Engineering, V. 111, (1985), 722-739.

32. NEHRP guidelines for the seismic rehabilitation of buildings, FEMA-273, (1997).

33. Seismic Evaluation and Retrofit of existing concrete buildings, ATC-40, (1996).

34. Krawinkler, H. and Miranda, E., “Performance-Based Earthquake Engineering”, Chapter 9 of Earthquake Engineering: From engineering seismology to performance based engineering, edited by Y. Bozorgnia and V. Bertero, CRC press, (2004).

35. Deierlein, G.G., “Overview of a comprehensive framework for earthquake performance assessment”, Performance-Based Seismic Design Concepts and Implementation-Proceedings of an International Workshop, Bled, Slovenia, (2004), 15-26.

36. SEAOC, Vision 2000-Performance Based Seismic Engineering of Buildings. Structural Engineers Association of California, Sacramento, California, (1995).

37. Shamim, I., DaBreo, J. and Rogers, C.A., “Dynamic testing of single- and double-story steel sheathed cold-formed steel framed shear walls”, Journal of Structural Engineering, V. 139, n° 5, (May 2013), 807-817.

38. Fülöp, L. and Dubina, D., “Performance of wall-stud cold-formed shear panels under monotonic and cyclic loading Part II: numerical modelling and performance analysis”, Thin-Walled Structures, V. 42, n° 2, (2004), 339-349.

39. Landolfo, R., Fiorino, L. and Corte, D.G., “Seismic behavior of sheathed cold-formed structures: Physical tests”, Journal of Structural Engineering, V. 132, n° 4, (2006), 570-581.

40. Iuorio, O., Fiorino, L. and Landolfo, R., “Testing CFS structures: The new school BFS in Naples”, Thin-Walled Structures, V. 84, (2014), 275-288.

41. Fiorino, L., Iuorio, O., Macillo, V., Terracciano, M.T., Pali, T. and Landolfo, R., “Seismic Design Method for CFS Diagonal Strap-Braced Stud Walls: Experimental Validation”, Journal of Structural Engineering”, V. 142, n° 3, (2016).

42. Leng, J., “Simulation of cold-formed steel structures”, PhD thesis, John Hopkins University, Baltimore, United States, (2015), 827 p.

43. Foliente, G.C., "Stochastic dynamic response of wood structural systems", PhD thesis, Virginia polytechnic institute and state university, Blacksburg, Virginia, United States, (1993).

44. Nithyadharan, M. and Kalyanaraman, V., "Modelling hysteretic behaviour of cold-formed steel wall panels", Thin-Walled Structures", V. 46, (2013), 643-652.

45. Shamim. I. and Rogers, C.A., "Steel sheathed/CFS framed shear walls under dynamic loading: Numerical modelling and calibration", Thin-Walled Structures, (2013), V. 71, 57-71.

46. Vigh, L.G., Liel, A.B., Deierlein, G.G., Miranda, E. and Tipping, S., "Component model calibration for cyclic behavior of a corrugated shear wall", Thin-Walled Structures, V. 75, (2014), 53-62.

47. Buonopane, S.G., Bian, G., Tun, T.H. and Schafer, B.W., "Computationally efficient fastener-based models of cold-formed steel shear walls with wood sheathing", Journal of Constructional Steel research, V. 110, (2015), 137-148.

48. Padilla-Llano, D.A., "A framework for cyclic simulation of thin-walled cold-formed steel members in structural systems", PhD thesis, Virginia Polytechnic Institute and State University, Blacksburg, United States, (2015), 226 p.

49. Martinez, J.M. and Xu L., "Simplified Nonlinear Finite Element Analysis of Buildings with CFS Shear Wall Panels", Journal of Constructional Steel Research, V. 67, n° 12, (December 2010), 565-575.

50. Morello, D., "Seismic performance of multi-storey structures with cold-formed steel wood sheathed shear walls", Master thesis, Department of Civil Engineering and Applied Mechanics, McGill University, Montreal, Québec, Canada, (2009).

51. American Iron and Steel Institute (AISI), Standard for cold-formed steel framing-lateral design 2007 edition, AISI S213, Washington, D.C., USA, (2007).

52. Shamim, I. and Rogers, C.A., "Numerical evaluation: AISI S400 steel-sheathed CFS framed shear wall seismic design method", Thin-Walled Structures, V. 95, (2015), 48-59.

53. American Society of Civil Engineers (ASCE), “Minimum design loads for buildings and other structures”, ASCE/SEI 7-10, Reston, USA, (2013).

54. Corte, D.G., Fiorino, L. and Landolfo, R., “Seismic behavior of sheathed cold-formed structures: Numerical study”, Journal of Structural Engineering, V. 132, (2006).

55. Vincenzo, M., Iuorio, O., Terracciano, M.T., Fiorino, L. and Landolfo, R., “Seismic response of CFS strap-braced stud walls: theoretical study”, Thin-Walled Structures, V. 85, (2014), 301-312.

56. Fiorino, L., Iuorio, O. and Landolfo, R., “Sheathed cold-formed steel housing: A seismic design procedure”, Thin-Walled Structures, V. 47, n° 8-9, (2009), 919-930.

57. Landolfo, R., Fiorino, L. and Iuorio, O., “A specific procedure for seismic design of cold-formed steel housing”, Advanced Steel Construction, V. 6, n° 1, (2010), 603-618.

58. Fiorino, L., Iuorio, O., Macillo, V. and Landolfo, R., “Performance based design of sheathed CFS buildings in seismic area”, Thin-Walled Structures, V. 61, (2012), 248-257.

59. Fiorino, L., Iuorio, O. and Landolfo, R., “Designing CFS structures: The new school BFS in Naples”, Thin-Walled Structures, V. 78, (2014), 37-47.

60. American Iron and Steel Institute (AISI), North American Specification for the Design of Cold-Formed Steel Structural Members, AISI S100, Washington, D.C., USA, (2016).

61. EN 1993-1-3, Eurocode 3. Design of steel structures, Part 1.3: general rules for cold formed thin gauge members and sheeting, European Committee for Standardization, Brussels; CEN (2007).

62. Stone, T.A. and LaBoube, R.A., “Behavior of cold-formed steel built-up I-sections”, Thin-Walled Structures, V. 43, n° 12, (2005), 1805-1817.

63. Young, B. and Chen, J., “Design of Cold-Formed Steel Built-Up Closed Sections with Intermediate Stiffeners”, Journal of Structural Engineering, V. 134, (2008), 727-737.

64. Georgieva, I., Schueremans, L., Pyl, L. and Vandewalle, L., “Experimental investigation of built-up double-Z members in bending and compression”, Thin-Walled Structures, V. 53, (2012), 48-57.

65. Georgieva, I., Schueremans, L., Pyl, L. and Vandewalle, L., “Numerical study of built-up double-Z members in bending and compression”, Thin-Walled Structures, V. 60, (2012), 85-97.

66. Zhang, J., “Cold-formed steel built-up compression members with longitudinal stiffeners”, PhD Thesis, The University of Hong Kong, (2014).

67. Loughlan, J. and Yidris, N., “The local-overall flexural interaction of fixed-ended plain channel columns and the influence on behaviour of local conditions at the constituent plate ends”, Thin-Walled Structures, V. 81, (2014),132-137.

68. Anbarasu, M., Kanagarasu, K. and Sukumar, S., “Investigation on the behaviour and strength of cold-formed steel web stiffened built-up battened columns”, Materials and Structures, V. 48, n° 12, (2015), 4029-4038.

69. Dabaon, M., Eloobody, E. and Ramzy, K., “Experimental investigation of built-up cold-formed steel section battened columns”, Thin-Walled Structures, V. 92, (2015), 137-145.

70. Dabaon, M., Eloobody, E. and Ramzy, K., “Nonlinear behaviour of built-up cold-formed steel section battened columns”, Journal of Constructional Steel Research, V. 110, (2015), 16-28.

71. Reyes, W. and Guzmán, A., “Evaluation of the slenderness ratio in built-up cold-formed box sections”, Journal of Constructional Steel Research, V. 67, (2011), 929-935.

72. American Iron and Steel Institute (AISI), North American specification for the design of cold-formed steel structural members, AISI S100, Washington, D.C., USA, (2012).

73. Li, Y., Li, Y., Wang, S. and Shen, Z., “Ultimate load-carrying capacity of cold-formed thin-walled columns with built-up box and I section under axial compression”, Thin-Walled Structures, V. 79, (June 2014), 202-217.

74. Vieira, L.C.M., “Behavior and design of sheathed cold-formed steel stud walls under compression”, PhD thesis, John Hopkins University, Baltimore, United States, (2011).

75. Ye, J., Feng, R., Chen, W. and Liu, W., “Behavior of cold-formed steel wall stud with sheathing subjected to compression”, Journal of Constructional Steel Research, V. 116, (2016), 79-91.

76. PEER, OpenSees: Open system for earthquake engineering simulation, Pacific Earthquake Engineering Research Center, University of California, Berkeley, CA, (2006).

77. Peterman, K.D., Nakata, N. and Schafer, B.W., "Hysteretic characterization of cold-formed steel stud-to-sheathing connections", Journal of Constructional Steel Research, V. 101, (2014), 254-264.

78. Kechidi, S., "Développement d'un modèle hystérésis pour les panneaux de contreventement en profiles d'acier formés à froid", Mémoire de Magister, Université de Blida 1, Algérie, (2014).

79. Yanagi, N. and Yu, Y., "Effective strip method for the design of cold-formed steel framed shear wall with steel sheet sheathing", Journal of Structural Engineering, V. 140(4), (2014).

80. Xu, L. and Martinez, J., "Strength and stiffness determination of shear wall panels in cold-formed steel framing", Thin-Walled Structures, V. 44, (2006), 1084-1095.

81. Serrette, R., David, P. and Nolan, P.E., "Reversed cyclic performance of shear walls with wood panels attached to cold-formed steel with pins", Journal Structural Engineering, V. 135, (2009), 959-967.

82. Uriz, P. and Mahin, S., "Toward Earthquake-resistant Design of Concentrically Braced Steel-frame Structures", PEER Report, University of California, Berkeley, (2008).

83. Scott, M. H. and Fenves, G. L., "How to Introduce a New Material into OpenSees" PEER report, Version 1.1, University of California, Berkeley, (2001).

84. Hubard, J.R., "Theory and Problems Programming with C++ Second Edition, Schaum's Outlines", University of Richmond Virginia, United State, (2000).

85. Ousterhout, J., "Tcl and the Tk Toolkit", Addison-Wesley, Reading Massachusetts, (1994), 460 pages.

86. Welch, B., Jones, K. and Hobbs, J., "Practical Programming in Tcl and Tk", 4th Edition ISBN: 0-13-038560-3, (June 2003).

87. Bourahla N., El-Djouzi B. and Allal N., Nonlinear seismic behaviour of experimentally identified stiffness and damping characteristics of cold formed steel infill frames,

Proceeding of the eleventh Conference on Structures Under Shock and Impact, WIT Transaction on the built and environment, vol. 113, (2010), 277-285.

88. Bourahla N., Boukhamacha T., Allal N. and Attar A., Equivalent shear link modeling and performance of cold formed steel structures under earthquake loadings, Proceedings of the 9th US and 10th Canadian Conference on Earthquake Engineering, paper 1063, Toronto, (2010).
89. American Society for Testing and Materials (ASTM), "Standard Practice for Static Load Test for Shear Resistance of Framed Walls for Buildings (E564-12)", West Conshohocken, PA., (2012).
90. Branston, A.E., "Developments of a Design Methodology for Steel Frame/wood Panel Shear Walls", Master thesis, Department of Civil Engineering & Applied Mechanics, McGill University Montreal, Canada, (2004).
91. Chen, C.Y., "Testing and performance of steel frame/wood panel shear walls", Master thesis, Department of Civil Engineering & Applied Mechanics, McGill University Montreal, Canada, (2004).
92. American Society for Testing and Materials (ASTM), "Standard Test Methods for Cyclic (Reversed) Load Test for Shear Resistance of Vertical Elements of the Lateral Force Resisting Systems for Buildings (E2126-12)", West Conshohocken, PA., (2012).
93. Balh, N., DaBreo, J., Ong-Tone, C., El-Saloussy, K., Yu, C. and C.A. Rogers, "Design of steel sheathed cold-formed steel framed shear walls", Thin-Walled Structures, V. 75, (2014), 76-86.
94. Elghazouli, A.Y. and Castro, J.M., "Design of steel structures in seismic design of buildings to Eurocode 8", Taylor and Francis, UK, 2009, pp. 175-214.
95. Kumar, M., Stafford, P.J. and Elghazouli, A.Y., "Seismic shear demands in multi-storey steel frames designed to Eurocode 8", Engineering Structures, V. 52, (2013), 69-87.
96. Peterman, K.D. and Schafer, B.W., "Cold-Formed Steel Studs under Axial and Lateral Load", Journal of Structural Engineering, V. 140, n° 10, (2014).

97. Kechidi, S. and Bourahla, N., “Deteriorating hysteresis model for cold-formed steel shear wall panel based on its physical and mechanical characteristics”, Thin-Walled Structures, V. 98(Part B), (2016), 421-430.

98. EN1991-1-1, “Eurocode 1 - Actions on structures, Part 1-1: General actions - Densities, self-weight, imposed loads for buildings”, 250. Brussels, Technical Commission, (2005).

99. American Iron and Steel Institute (AISI), North American Standard for Cold-Formed Steel Framing-General Provisions, AISI S200-12, Washington, D.C., USA, (2012).

100. Kechidi, S. and Bourahla, N., “CFSWSWP uniaxialMaterial”. http://opensees.berkeley.edu/wiki/index.php/CFSWSWP/, [last accessed on 27/10/2017].

101. Dubina, D., “Behavior and performance of cold-formed steel-framed houses under seismic action”, Journal of Constructional Steel Research, V. 64, n° 7-8, (2008), 896–913.

102. Chiou, B., Darragh, R., Gregor, N. and Silva, W., “NGA Project Strong-Motion Database”, Earthquake Spectra, V. 24, n° 1, (2008), 23-44.

103. MATLAB 2016a, The MathWorks, Inc., Natick, MA, United States, (2016).

104. Flores, F., Charney, F. and Lopez-Garcia, D., “The influence of gravity column continuity on the seismic performance of special steel moment frame structures”, Journal of Constructional Steel Research, V. 118, (2016), 217-230.

105. Vamvatsikos, D. and Cornell, C.A., “Incremental dynamic analysis”, Earthquake Engineering and Structural Dynamics, V. 31, n° 3, (2002), 491-514.

106. Martinez, J.M., “Seismic performance assessment of multi-storey buildings with cold formed steel shear wall systems”, PhD thesis, University of Waterloo, Ontario, Canada, (2007).

107. Fardis, M., Carvalho, E., Elnashai, A., Faccioli, E., Pinto, P. and Plumier, A., “Designers’ guide to EN 1998-1 and EN 1998-5 Eurocode 8: Design of structures for earthquake resistance, General rules, seismic actions, design rules for buildings, foundations and retaining structures”, Thomas Telford Publishing, London, (2005).

108. Baker, J.W., “Efficient analytical fragility function fitting using dynamic structural analysis”, Earthquake Spectra, V. 31, n° 1, (2015), 579-599.

109. Baker, J.W., “Conditional Mean Spectrum: Tool for Ground-Motion Selection”, Journal of Structural Engineering, V. 137, n° 3, (2011), 322-331.

110. Macedo, L. and Castro, J.M., “SelEQ: An advanced ground motion record selection and scaling framework”, Advances in Engineering Software, V. 114, (2017), 32-47.

111. Cornell, C. A., Jalayer, F., Hamburger, R.O. and Foutch, D.A., “Probabilistic basis for 2000 SAC Federal Emergency Management Agency steel moment frame guidelines”, Journal of Structural Engineering. V. 128, n° 4, (2002), 526-533.

112. Vamvatsikos, D., “Accurate application and Second-Order improvement of SAC/FEMA probabilistic formats for seismic performance assessment”, Journal of Structural Engineering, V. 140, n° 2, (2014).

113. Baker, J.W. and Cornell, C.A., “Spectral shape, epsilon and record selection”, Earthquake Engineering and Structural Dynamics, V. 35, (2006), 1077-1095.

114. Bojórquez, E. and Iervolino, I., “Spectral shape proxies and nonlinear structural response”, Soil Dynamics and Earthquake Engineering, V. 31, (2011), 996-1008.

115. Iervolino, I., De Luca, F. and Cosenza, E., “Spectral shape-based assessment of SDOF nonlinear response to real, adjusted and artificial accelerograms”, Engineering Structures, V. 32, (2010), 2776-2792.

116. Bradley, B.A., “A generalized conditional intensity measure approach and holistic ground-motion selection”, Earthquake Engineering and Structural Dynamics, V. 39, (2010), 1321-1342

117. Zsarnóczay, Á., “Experimental and numerical investigation of Buckling Restrained Braced frames for Eurocode conform design procedure development”, PhD thesis, Budapest University of Technology and Economics, Budapest, Hungary, (2013), 147 p.

118. Haselton, C.B., “Assessing Seismic Collapse Safety of Modern Reinforced Concrete Moment Frame Buildings”, PhD Thesis, Department of Civil and Environmental Engineering, Stanford University, Stanford, California, (2006).

119. Haselton, C.B. and Deierlein, G.G., "Assessing Seismic Collapse Safety of Modern Reinforced Concrete Moment-Frame Buildings, PEER report", University of California, Berkeley, CA (2007).

120. Sato, A. and Uang, C.M., "A FEMA P695 study for the proposed seismic performance factors for cold formed steel special bolted moment frames", Earthquake Spectra, V. 29, (2013), 259-282.

121. Miyamoto, H., Gilani, A., Wada, A. and Ariyaratana, C., "Identifying the Collapse Hazard of Steel Special Moment-Frame Buildings with Viscous Dampers Using the FEMA P695 Methodology", Earthquake Spectra, V. 27, (2011), 1147-1168.

122. Lee, J. and Kim, J., "Seismic performance evaluation of staggered wall structures using FEMA P695 procedure", Magazine of Concrete Research, V. 65, (2013), 1023-1033.

123. Farahi, M. and Mofid, M., "On the quantification of seismic performance factors of Chevron Knee Bracings in steel structures", Engineering Structures, V. 46, (2013), 155-164.

124. Purba, R. and Breneau M., "Seismic performance of steel plate shear walls considering two different design philosophies of infill plates. II: Assessment of collapse potential", Journal of Structural Engineering, V. 141, n° 6, (2015).

125. https://paginas.fe.up.pt/~jmcastro/, [last accessed on 27/10/2017].

126. OpenQuake GEM OpenQuake Manual, http://www.globalquakemodel.org/openquake/, [last accessed on 27/10/2017].

127. European Facility for Earthquake Hazard and Risk (EFEHR), http://www.efehr.org:8080/jetspeed/portal/, [last accessed on 03/09/2017].

128. https://en.wikipedia.org/wiki/Poisson_distribution/, [last accessed on 27/10/2017].

129. Baker, J. W. and Jayaram, N., "Correlation of spectral acceleration values from NGA ground motion models", Earthquake Spectra, V. 24, n° 1, (2008), 299-317.

130. Lin, T., Harmsen, S.C., Baker, J.W. and Luco, N., "Conditional spectrum computation incorporating multiple causal earthquakes and ground-motion prediction models", Bulletin of the Seismological Society of America, V. 103, n° 4, (2013), 1103-1116.

131. Vilanova, S.P. and Fonseca, J.F., "Probabilistic seismic-hazard assessment for Portugal", Bulletin of the Seismological Society of America, V. 97, n° 5, (2007), 1702-1717.

132. Atkinson, G.M. and Boore, D.M., "Earthquake ground-motion prediction equations for eastern North America", Bulletin of the Seismological Society of America, V. 96, (2006), 2181-2205.

133. Akkar, S. and Bommer, J.J., "Empirical equations for the Prediction of PGA, PGV, and spectral accelerations in Europe, the Mediterranean Region, and the Middle East", Seismological Research Letters, V. 81, (2010), 195-206.

134. Silva, V., "Development of open models and tools for seismic risk assessment: application to Portugal", PhD thesis, Department of Civil Engineering, University of Aveiro, (2013).

135. Abrahamson, N.A., "Non-stationary spectral matching", Seismological Research Letters, V. 63, n° 1, (1992).

136. Hancock, J., Watson-Lamprey, J., Abrahamson, N.A., Bommer, J.J., Markatis A., McCoy, E. and Mendis, R., "An improved method of matching response spectra of recorded earthquake ground motion using wavelets", Journal of Earthquake Engineering, V. 10, (2006), 67-89.

137. Kechidi, S., Bourahla, N. and Castro, J.M., "Seismic design procedure for cold-formed steel sheathed shear wall frames: Proposal and evaluation", Journal of Constructional Steel Research, V. 128, (2017), 219-232.

138. Haselton, C.B. and Baker, J.W., Ground motion intensity measures for collapse capacity prediction: choice of optimal spectral period and effect of spectral shape. 8th National Conference on Earthquake Engineering, April 18-22, (2006), San Francisco, CA, United States.

139. Elghazouli, A.Y., "Assessment of European seismic design procedures for steel framed structures", Bulletin of Structural Engineering, V. 8, (2010), 65-89.

140. Castro, J.M., Dávila-Arbona, F.J. and Elghazouli, A.Y., “Seismic design approaches for panel zones in steel moment frames”, Journal of Earthquake Engineering, V. 12, (2008), 34-51.

141. Lignos, D.G. and Krawinkler, H., “Deterioration modeling of steel components in support of collapse prediction of steel moment frames under earthquake loading”, Journal of Structural Engineering, V. 137, n° 11, (2011), 1291-1302.

142. Araújo, M., Macedo, L. and Castro J.M., “Evaluation of the rotation capacity limits of steel members defined in EC8-3”, Journal of Constructional Steel Research, V. 135, (2017), 11-29.

143. Zareian, F., Lignos, D.G. and Krawinkler, H., “Evaluation of seismic collapse performance of steel special moment resisting frames using FEMA P695 (ATC-63) methodology”, Proceedings of Structures Congress ASCE, Orlando, Florida, May 12-14, (2010).

144. Krawinkler, H., “Shear in beam-column joints in seismic design of steel frames”, Engineering Journal, V. 15, n° 3, (1978), 82-91.

145. Macedo L. Improved performance-based seismic design methodologies for steel moment-resisting frames (PhD thesis), University of Porto, Portugal 2017.

146. Seismic Evaluation and Retrofit of Existing Buildings (ASCE 41-13), (2013), 555 p.

147. Cornell, C. and Krawinkler, H., “Progress and challenges in seismic performance assessment”. PEER News 3(2), (2000).

148. Applied Technology Council, ATC-58, Guidelines for Seismic Performance Assessment of Buildings. Applied Technology Council, Redwood City, California, (2011), 266p.

149. Eads, L., Miranda, E., Krawinkler, H. and Lignos, D.G., “An efficient method for estimating the collapse risk of structures in seismic regions”, Earthquake Engineering & Structural Dynamics, V. 42, (2013), 25-41.

150. Lin, T., Haselton, C.B. and Baker, J.W., “Conditional spectrum-based ground motion selection. Part II: Intensity-based assessments and evaluation of alternative target spectra”, Earthquake Engineering & Structural Dynamics, V. 42, (2013), 1867-1884.

151. Pinto, P.E. and Franchin, P., “Existing buildings: the new Italian provisions for probabilistic seismic assessment”, Perspectives on European Earthquake Engineering and Seismology, Geotechnical, Geological and Earthquake Engineering, V. 34, (2014), 97-130.

152. Bradley, B.A., “The seismic demand hazard and importance of the conditioning intensity measure”, Earthquake Engineering & Structural Dynamics, V. 41, n° 11, (2012), 1417-1437.

153. Marques, M., Macedo, L., Araújo, M., Martins, L., Castro, J.M., Sousa, L., Silva, V. and Delgado, R., “Influence of Record Selection Procedures on Seismic Loss Estimations”, Vulnerability, Uncertainty, and Risk, (2014), 1756-1766.

154. EN 1990:2002 Eurocode: Basis of structural design, CEN, (2002).

155. Joint Committe on Structural Safety (JCSS). Probabilistic Model Code Part 1 - Basis of Design, (2001).

156. Popov, E.P. and Engelhardt, M.D., “Seismic eccentrically braced frames”, Journal of Constructional Steel Research, V. 10, (1988), 321-354.

157. Standards Australia, Cold-formed Steel Structures, AS/NZS 4600, Standards Australia/ Standards New Zealand, (2005).

158. AISC 360, Specification for Structural Steel Buildings, American Institute of Steel Construction, Chicago, IL, (2010).

159. http://www.davefratamico.com/, [last accessed on 27/10/2017].

160. Torabian, S., Zheng, B. and Schafer, B.W., “Experimental response of cold-formed steel lipped channel beam-columns”. Thin-Walled Structures, V. 89, (2015), 152-168.

161. Zhao, X., Tootkaboni, M. and Schafer, B.W., “Development of a Laser-Based Geometric Imperfection Measurement Platform with Application to Cold-Formed Steel Construction”, Experimental Mechanics, V. 55, (2015), 1779-1790.

162. American Society for Testing and Materials (ASTM), “Standard Test Methods and Definitions for Mechanical Testing of Steel Products (ASTM370-12a)”, West Conshohocken, PA., (2012).

163. Southwell, R.V. “On the analysis of experimental observations in problems of elastic stability”, Proceedings of the Royal Society of London A: Mathematical, Physical and Engineering Sciences. V. 135, n° 828, (1932), 601-616.

164. Schafer, B.W., Li, Z. and Moen, C.D., “Computational modeling of cold-formed steel.” Thin-Walled Structures, V. 48, (2010), 752-762.

165. Schafer, B.W. and Ádàny, S., “Buckling analysis of cold-formed steel members using CUFSM: conventional and constrained finite strip methods”, Proceedings of the 18th International Specialty Conference on Cold-Formed Steel Structures, Orlando, FL, (2006).

166. Zhao, X., “Measurement and Application of Geometric Imperfections in Cold-Formed Steel Members”, PhD Thesis, The Johns Hopkins University, (2016).

167. Zeinoddini, V.M. and Schafer, B.W., “Simulation of geometric imperfections in cold-formed steel members using spectral representation approach”, Thin-Walled Structures, V. 60, (2012), 105-117.

168. Fratamico, D., “Experiments, Analysis, and Design of Built-Up Cold-Formed Steel Columns”, PhD thesis, John Hopkins University, Baltimore, United States, (2017).

169. Ding, C., “Monotonic and Cyclic Simulation of Screw-Fastened Connections for Cold-Formed Steel Framing”, MSc Thesis, Virginia Polytechnic and State University, (2015).

170. Lowes, L.N., Mitra, N. and Altoontash, A., “A Beam-Column Joint Model for Simulating the Earthquake Response of Reinforced Concrete Frames (Report #2003/10)”, Retrieved from the Pacific Earthquake Engineering Research Center (PEER), Berkeley, CA, (2004).

171. Moen, C.D., Tao, F. and Cole, R., “Monotonic and Cyclic Backbone Response of Single Shear Cold-Formed Steel Screw-Fastened Connections”, Proceedings of the International Colloquium on Stability and Ductility of Steel Structures, Timisoara, Romania, (2016).

172. Tao, F., Cole, R. and Moen, C.D., “Monotonic and Cyclic Backbone Response of Single Shear Sheathing-to-Cold-Formed Steel Screw-Fastened Connections”, Proceedings of the Wei-Wen Yu International Specialty Conference on Cold-Formed Steel Structures, Baltimore, MD, (2016).

173. Ye, J., “Performance based optimisation of novel lightweight steel frame systems for rapid, economical and sustainable construction”, PhD thesis, University of Sheffield, UK, (2017).

174. A. A1003-15, “Standard Specification for Steel Sheet, Carbon, Metallic- and Nonmetallic-Coated for Cold-Formed Framing Members”, West Conshohocken, PA., (2015).

175. American Iron and Steel Institute (AISI), North American Specification for Cold-Formed Steel Framing - Wall Stud Design, AISI S211, Washington, D.C., USA, (2012).

176. Li, Z. and Schafer, B.W., “Buckling analysis of cold-formed steel members with general boundary conditions using CUFSM: conventional and constrained finite strip methods”, 20th International Specialty Conference on Cold-Formed Steel Structures, St. Louis, MO, (2010a).

177. Vieira, L.C.M. and Schafer, B.W., “Behavior and Design of Sheathed Cold-Formed Steel Stud Walls under Compression”, Journal of Structural Engineering, V. 139, n° 5, (2013), 772-786.

PUBLICATIONS RECORD

Peer-Reviewed Journal Articles:

1. Smail Kechidi and Nouredine Bourahla, Deteriorating hysteresis model for cold-formed steel shear wall panel based on its physical and mechanical characteristics. *Thin-Walled Structures*. 98 (2016); 421-430. Impact Factor (2016): 2.829.

2. Smail Kechidi, Nouredine Bourahla and José Miguel Castro, Seismic design procedure for cold-formed steel shear wall frames: Proposal and evaluation. *Journal of Constructional Steel Research*. 128 (2017); 219-232. Impact Factor (2016): 2.028.

3. Smail Kechidi, Luís Macedo, José Miguel Castro and Nouredine Bourahla, Seismic risk assessment of cold-formed steel shear wall systems. *Journal of Constructional Steel Research*. 138 (2017); 565-579. Impact Factor (2016): 2.028.

Articles in Conference Proceedings:

1. Smail Kechidi, Luís Macedo, José Miguel Castro and Nouredine Bourahla (2018), Design and Assessment of Cold-Formed Steel Shear Wall Systems Located in Moderate-to-High Seismicity Regions, the 9th International Conference on Behaviour of Steel Structures in Seismic Areas STESSA, February 14-17, 2018, Christchurch, New Zealand.

2. Smail Kechidi, David C. Fratamico, José M. Castro, Nouredine Bourahla, Benjamin W. Schafer (2017), Numerical study of screw fasteners in built-up CFS chord studs, the 8th European conference on steel and composite structures EUROSTEEL, September 13-15, 2017, Copenhagen, Denmark.

3. Smail Kechidi, David C. Fratamico, José M. Castro, Nouredine Bourahla, Benjamin W. Schafer (2017), Numerical study on the behavior and design of screw connected built-up CFS chord studs, Proceedings of the Annual Stability Conference, Structural Stability Research Council SSRC, March 21-24, 2017, San Antonio, Texas, USA.

4. Smail Kechidi and Nouredine Bourahla (2015), Seismic behaviour assessment of cold-formed steel five storeys building, La 1ère Conférence Internationale de Construction Métallique et Mixte CICOMM'2015, October 12-13, 2015, Tlemcen, Algeria.

5. Smail Kechidi and Nouredine Bourahla (2014), Seismic performance of a multi-storey cold-formed steel lateral load resisting system, Colloque International Caractérisation et Modélisation des Matériaux et Structures CMMS, November 12-13, 2014, Tizi-Ouzou, Algeria.

6. Nouredine Bourahla and **Smail Kechidi** (2014), Seismic Performance of Multi-storey Cold-Formed Steel Shear Wall Panel with Different Height-to-Width Aspect Ratios, Second European Conference on Earthquake Engineering and Seismology 2ECEES, August 24-29, 2014, Istanbul, Turkey.

7. Smail Kechidi and Nouredine Bourahla (2014), Deteriorating Hysteresis Model for Cold-Formed Steel Shear Wall Panel based on physical and mechanical characteristics, OpenSeesDays Portugal, Workshop on Multi-Hazard Analysis of Structures using OpenSees, July 3-4, 2014, Porto, Portugal.